ABSTRACT

Title of Document: A METHODOLOGY FOR DETERMINING THE FIRE PERFORMANCE EQUIVALENCY AMONGST SIMILAR MATERIALS DURING A FULL-SCALE FIRE SCENARIO BASED ON BENCH-SCALE TESTING

Chad Michael Lannon, Master of Science, 2015

Directed By: Dr. Stanislav Stoliarov, Associate Professor, Department of Fire Protection Engineering

A methodology was developed for determining the equivalency amongst materials during a full-scale fire scenario. This procedure utilizes milligram-scale and or bench-scale tests to obtain the effective physical and chemical properties of individual materials through an optimization procedure. A flame heat feedback model was developed for corner-wall flame spread and implemented into a two-dimensional pyrolysis model, ThermaKin2D. ThermaKin2D was utilized to simulate upward flame spread during the room corner test. A criterion was created that determines the fire performance of similar materials during this full-scale fire scenario and compares how each material performed relative to one another. A fire investigator will be able to better select materials for their reconstructive fire test based on the modeled full-scale fire performance of candidate materials compared to the exemplar material found during the fire investigation. Overall, this procedure is expected to improve a fire investigator's ability to perform accurate reconstructive fire tests.

A METHODOLOGY FOR DETERMINING THE FIRE PERFORMANCE EQUIVALENCY AMONGST SIMILAR MATERIALS DURING A FULL-SCALE FIRE SCENARIO BASED ON BENCH-SCALE TESTING

By

Chad Michael Lannon

Thesis submitted to the Faculty of the Graduate School of the
University of Maryland, College Park, in partial fulfillment
of the requirements for the degree of
Master of Science
2015

Advisory Committee:
Professor Stanislav I. Stoliarov, Ph.D., Chair
Professor James A. Milke, Ph. D., P.E.
Professor Arnaud Trouve, Ph.D.

Acknowledgements

Working on this project was a great honor and an amazing learning opportunity! The success of this thesis would not have been possible without the tremendous support of those around me. I am very grateful to you all!

Dr. Stas, thank you for taking me under your wing and being my advisor! This project was only possible because of your visionary guidance! The countless hours you spent meeting with me, reviewing my work and guiding my way was invaluable. You took on a raw engineer, a challenging project and crafted a great project approach. You kept me focused and motivated and you were always willing to pass on your brilliance. The fire engineering community is extremely fortunate to have you because you will be a major contributor to the progression of fire science.

Jamie Lord deserves an amazing amount of credit for this project. I went to the Bureau of Alcohol, Tobacco, Firearms and Explosives Fire Research Lab (ATF FRL) looking to obtain a potential thesis topic related to fire investigations. During my visit, I met with Jamie while he was conducting a reconstructive fire test. Seeing some of the innovative tests the ATF FRL was involved in was impressive and alluring. The talk we had the day was the origin of this project. Throughout the year and a half that I worked with you, you've been a great role model, mentor and friend! You've been incredibly supportive, and always willing to go the extra mile to accommodate me or answer any of my questions. I hope to work alongside you one day!

I must also thank the ATF FRL for hosting me as a student researcher. All of the bench-scale and large-scale experiments were completed at the ATF FRL. Every time I had tests to complete, it felt like I had an army of engineers and technicians there to assist me. Brian Grove opened the door for me at the ATF FRL and allowed me to work at the lab. Jason Dress helped me complete over 50 cone calorimeter experiments. A truly great and intelligent guy! Cory Runyon and Jon Butta supported me on numerous large-scale tests. Many of which would not have been successful without them. I also owe a lot of gratitude to Mark Gratkowski, Rob Wulff, Steve Little, Stevie Little, James Zurenko and Adam St. John.

My experience as a fire protection student at the University of Maryland (UMD) was remarkable! The fire protection engineering school is small community filled with brilliant professors, motivated students and endless opportunities. I'd like to thank all the students and faculty who crafted this experience. I owe a lot of thanks to everyone in my research group; Xi Ding, Xuan Liu, Fernando Raffan, Adam Friedman, Geri Martin, Cara Hamel, Yan Ding & Josh Swann. I'd like to specially acknowledge Mark Mckinnon and Isaac Leventon, two future Ph.D's that have an amazing career ahead of them! Both of you guys were a wealth of knowledge and always willing to share it.

I owe a lot of thanks to Dr. Milke and Dr. Trouve for being on my thesis committee and reviewing this long thesis! Dr. Milke has been a great mentor to me throughout my tenure at UMD. He is someone I've always trusted and went to for guidance! I've also learned so much from Dr. Trouve. You spurred my interested in fire modeling.

Most importantly, I owe everything to my family! I would not be who I am today without you all! Throughout my life, both my parents and brother have always been incredibly supportive and pushed me to pursue my dreams. And even though, our family is growing and moving away, we will always be connected through the love you show us.

Last but not least, I owe the most love to my best friend Ola Bienkowski! I'm looking forward to the adventures and memories we will share together!

Table of Contents

List of Tables

List of Figures

1. Introduction

1.1 Motivation

A structure fire initiates once a combustible item is ignited. The fire will propagate beyond the ignition source after it spreads to adjacent flammable fuels. As the fire develops inside a compartment, it produces a tremendous amount of heat and toxic smoke, which can lead to the loss of property and lives. In 2013, there were 487,500 reported structure fires in the United States. These structure fires led to 2,855 deaths, 14,075 injuries and 9.5 billion dollars worth of property damage [1].

Devastating structures fires require fire investigators to visit the scene of the incident and determine the cause and origin of the fire. This is often difficult to determine due to fire's destructive nature. The most effective method in determining the cause, origin and progression of a fire is to perform reconstructive fire tests. A reconstructive fire test strives to recreate the fire scenario by building a full scale replica of the structure in a laboratory, and using it to test hypotheses regarding the cause, origin and propagation of the fire. A reconstructive fire test is critical in defining the fire development time line.

When building these structures, it is necessary to substitute materials that can be purchased at building supply stores for the original materials that were found during the fire investigation because the original materials are either destroyed or there is an insufficient quantity to conduct large scale tests. Section 22.5.2 of NFPA 921: Guide for

Fire and Explosion Investigations states that the test is only credible when the materials utilized in the test assembly are “suitable exemplars of the actual materials” [2]. Accurate reconstructive fire testing requires the laboratory structure to be outfitted with building materials that possess similar fire performance ability as the original materials that were collected during the investigation. Typically, materials are chosen for use in reconstruction tests based on the information available about the construction of the building, or through post-fire visual examination of the remaining building materials. Since there is no standard method for selecting materials for reconstructive fire tests, materials are often chosen based on visual appearance and without appropriate scientific reasoning. The fire forensic field needs a scientific method for comparing various materials and predicting how they perform relative to one another in a full-scale fire scenario so that reconstructive fire tests can be accurately performed.

1.2 Background

Bench scale tests have been used for decades to compare the fire performance of different materials [3][4][5][6]. The downfall of bench scale testing is that the fire performance of those materials is only applicable to that specific scenario. It is unclear how to relate the various parameters determined during bench-scale testing to the dynamics of a full-scale fire.

There are many different types of full-scale fire scenarios. The one analyzed in this project is the room corner test. The standard room corner test is a large-scale test used to evaluate the flammability of combustible materials that are installed along the walls and ceiling [7][8][9][10]. The room corner test seeks to create a realistic

compartment fire scenario by placing a square propane burner on the floor, in the corner of a room and subjecting the walls and ceiling to a large flame. The gas burner produces a fire with a heat release rate (HRR) specific to the test standard. A fire in the corner of a room is a severe fire scenario that will typically ignite the wall and ceiling materials. Once ignition occurs, the flames will spread vertically and horizontally along the walls and ceiling. A smoke layer is formed that continuously transfers heat to the surrounding surfaces. Once the compartment fire is large enough, it will transition to flashover and flames will extend beyond the doorway to maximize oxidation. During the experiment, the products of combustion are captured by the hood and the compartment HRR is determined based on the principal of oxygen consumption calorimetry. The compartment temperature, heat flux to the floor and the doorway velocity are also measured. A diagram of the room corner test is shown in Figure 1.

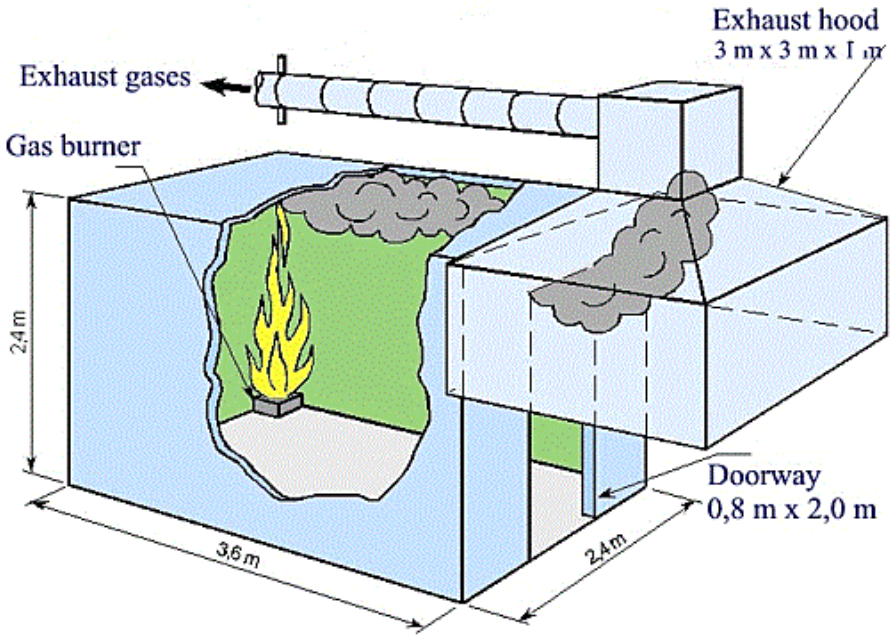

Figure 1. Room Corner Test Setup [11]

The room corner test is used to evaluate the fire performance of the materials in this project. This test incorporates the fire dynamics of a realistic compartment fire scenario and it also creates a scenario that is very similar to the full-scale reconstructive fires analyzed by investigators. This test determines the acceptability of wall and or ceiling materials for use in building construction based on the time it takes for the room to transition to flashover. The time to flashover is highly dependent upon the materials ability to support flame spread along the walls and ceiling. In forensic fire investigation, the time to flashover is a critical component that signifies a definitive moment when conditions are untenable within a structure. This is a standard test that best demonstrates how materials perform during an actual fire. Typically, it is used to evaluate interior finishes and determine whether they pass the flammability regulations. These tests are very expensive to perform and require up to 30 m^2 of product to test. This makes it impractical to perform multiple tests that are intended to compare the fire performance of various materials.

Over the past couple decades, many researchers have attempted to develop room corner fire models as a replacement for the actual full-sized test [12][13][14][15][16][17][18][19][20]. Most of these models require input data from bench-scale tests, such as the cone calorimeter or the LIFT test. The goal of the room corner models is to provide an inexpensive and efficient solution for evaluating multiple materials and predicting their relative performance during the room corner test. Many of the room corner models were successful at predicting full-scale room corner test results for the materials they tested. But most of these models were not validated for all types of materials, especially ones that char, melt, drip and or delaminate from surfaces.

At the moment, computational fluid dynamics (CFD) solvers are not validated to accurately simulate full-scale flame spread in a variety of configurations. Current computers are not powerful enough to efficiently run direct numerical simulations (DNS) for engineering applications. In addition to this, most of the room corner models were not developed for commercial use and are not readily available to the public. The publically available room corner models were not used in this project because one of the project goals was to explore the use of milligram-scale testing as a potential source for obtaining the material properties needed during modeling. The current room corner models rely on properties obtained through bench-scale testing, rather than milligram-scale testing. Therefore, a pyrolysis model, ThermaKin2D was developed to simulate upward flame spread during the room corner test. This model was used to predict the fire performance of similar materials in the room corner scenario.

1.3 Project Approach

In this project, four different types of medium density fiberboard (MDF) wall-paneling were tested in milligram-scale, bench-scale, and full-scale experiments to determine their performance under various fire conditions. A procedure was developed to determine the key material properties required for pyrolysis modeling. This procedure utilizes milligram-scale and or bench-scale testing to obtain the effective physical and chemical properties of the individual materials. The micro-scale combustion calorimeter (MCC) was the milligram-scale experiment and the cone calorimeter was the bench-scale experiments. Models simulating the MCC experiments and the cone calorimeter experiments were developed in ThermaKin2D. The temperature independent material properties were obtained through an optimization procedure where each material property

was manually changed to inversely model the experimental HRR results. The MCC experiments and optimization procedure provided the essential kinetic parameters that describe the decomposition of the material, while the cone calorimeter experiment and optimization procedure provided the thermal and optical properties of the virgin sample and the char it produces.

Once the material's properties were obtained for each of the four samples, full-scale experiments were performed in an open corner-wall test and the room corner test. Two types of experiments were performed in the open corner-wall test. The first was to measure and characterize the heat flux conditions from an exposure fire produced by a square propane gas burner. The second set of tests measured the flame spread dynamics of a corner-wall fire. Quantitative measurements were made so that a model could be developed for upward flame spread in the corner of a room. The corner-wall flame heat feedback model is incorporated into ThermaKin2D and a model is developed that simulates upward flame spread during the room corner test. The ThermaKin2D room corner model is utilized to simulate the room corner test for each of the materials and the models predictions are compared to the experimental results. A set of criteria has been developed to compare each material's fire performance during the room corner simulations to determine which materials perform similarly. Overall, the objective of this project is to develop a standard methodology and criteria for determining the equivalency amongst materials during a full-scale fire scenario so that fire investigators can more accurately perform reconstructive fire tests.

1.4 Literature Review

1.4.1 Thermal Model for Upward Flame Spread

The generalized thermal model for upward flame spread is shown in Figure 2 [21]. The combustible surface where flame spread occurs is divided into three regions: pyrolysis zone, flame extension zone and burnout zone. In the pyrolysis zone (y_p), flames continuously exist over the surface of the combustible material. The flames transfer convective and radiative heat to the surface of the material, in the form of heat flux. The flame heat flux ($q"_f$) is the strongest within the pyrolysis region. As the combustible material pyrolyzes, it produces gaseous fuel ($\dot{m}"$), which is consumed by the fire. This closed loop cycle continues as the fire develops and spreads along the surface of the material. The flame heat flux is relatively steady within the pyrolysis zone and decreases vertically in the flame extension zone (δ_f). The flame height (y_f) fluctuates in the flame extension zone. The heat transfer rate from the fire to the combustible surface is lower because the combustion gases cool as they entrain air and rise. The combustible solid is pre-heated in this zone. Flame spreads vertically once the material in the flame extension zone heats up, pyrolyzes and ignites. Flames do not exist over the burnout zone (y_b) because the material is no longer producing sufficient fuel to sustain combustion.

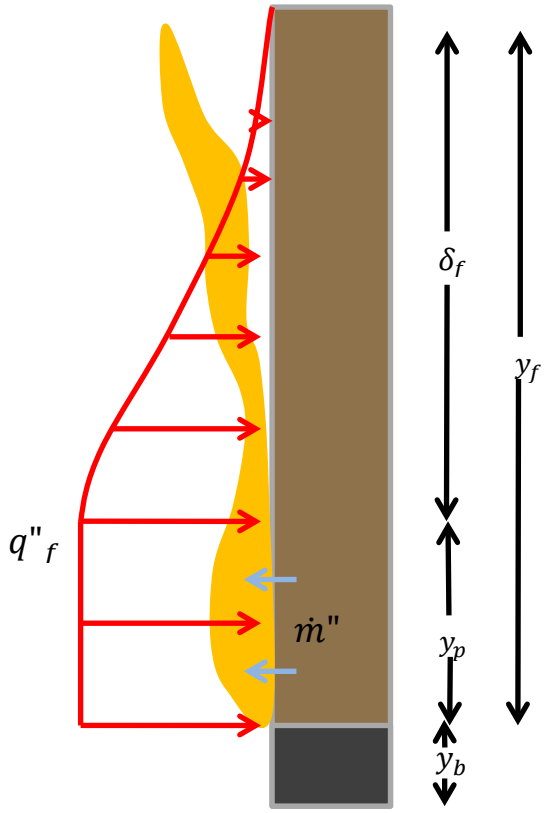

Figure 2. Thermal Model for Upward Flame Spread

1.4.2 Fire in the Corner of the Room

A fire in the corner of a room is the most hazardous compartment fire scenario due to the corner-wall reradiation effects and the reduced entrainment rate [2][22]. In a corner fire scenario, both walls and the ceiling are exposed to the fire. As their temperatures increase, they reradiate heat back to the combustible surface and this increases the burning rate of the combustible material. Air entrainment rate and fire location has a significant effect on the flame height and the flame spread rate. As shown in Figure 3, corner wall fires are only exposed to a fraction of the environment compared to an axisymmetric fire and a wall fire. When the fire is located in the corner of a room or against a vertical wall, the fire is only able to draw air in from the exposed side. This causes there to be an imbalance of airflow on the flame, which results in the flame tilting

and attaching itself to the wall surface [2]. Compared to an axisymmetric fire, a fire against a flat wall has half the entrainment rate, and a corner wall fire has quarter of the entrainment rate [23], which can be seen in Figure 3. The air being entrained to the plume convectively cools the surrounding surfaces and the upper layer. At the same time, a corner wall fire increases its flame height to maximize the amount of air being entrained to the exposed flame sheet. In the corner fire scenario, the decreased entrainment rate and taller flame height results in a greater heat transfer rate to the surrounding surfaces and upper layer. When a fuel package is placed in the corner, it will lead to a 70 % higher upper layer temperature than the same fire away from the walls or corner [2]. All of these effects cause the fire to develop at a faster rate compared to other compartment fire scenarios.

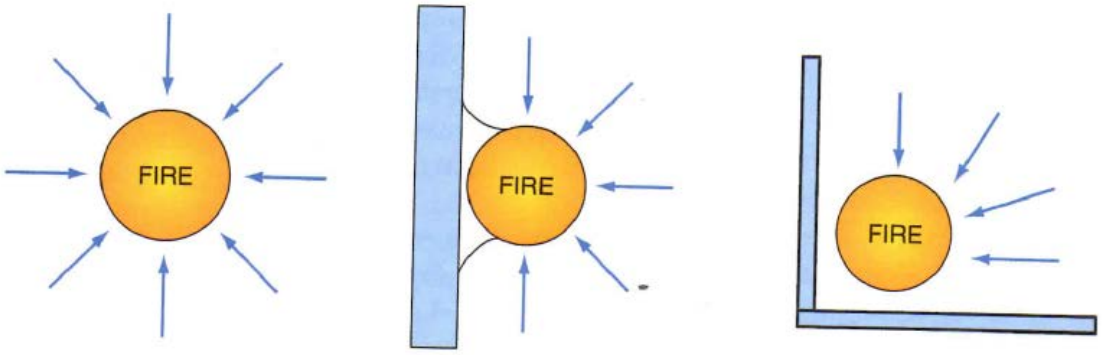

Figure 3. Fire location in a compartment [22]

There are three corner fire scenarios: an exposure fire from a nearby fuel source, a corner-wall fire and a combination of the two [24]. An example of an exposure fire is a burning Christmas tree in the corner of a room. An exposure fire can be represented by a square gas burner located in or near the corner of two perpendicular walls. A corner-wall fire involves spreading flames along a combustible wall lining. During the room corner test, these two scenarios are combined together.

1.4.3 Corner-wall Flame Heat Feedback Models

Over the past few decades, researchers have been motivated to study fires in the corner of a room because of their hazardous potential. Significant efforts have been made to study the thermal conditions along the corner walls and ceiling due to an exposure fire or a corner wall fire. Experiments were performed in either a compartment similar to the room corner test or in an open corner-wall configuration. A majority of the researchers perform their experiments using either a square burner or thin line gas burner. A square gas burner represents an exposure fire, while the line burners simulate a burning vertical wall. Very few researchers have performed tests using combustible wall linings.

Williamson, Revenaugh and Mowrer performed several full-scale room corner tests where the heat flux from the flames to the corner walls were measured at various fire sizes and propane burner standoff distances [25]. Kokkala performed corner fire tests in an open environment with two walls and no ceiling [26]. He varied the size of the square propane gas burner and the HRR, while measuring the gas temperature, flame height and the total heat flux to the Gardon-type total heat flux gauge. Kokkala proposed flame height and gas temperature correlations based on the dimensionless heat release rate of the fire (Q^*). Tran and Janssens performed experiments using a square methane burner along two corner-walls without a ceiling [27]. They created correlations for the flame height, temperature, velocity and mass flux of the burner used during the ASTM room corner test. Soon after, Quintiere and Cleary performed a dimensional analysis to determine the dimensionless variables that influence the flame height and heat flux to a surface in various configurations: line fire against a wall, square burner against a wall, square burner in the corner and window flames impinging on a wall [28]. The burner fire

was propane fed. Ohlemiller, Cleary and Shields performed flame spread experiments along two corner walls composed of a composite material [29]. They measured the heat flux from the square propane burner and wall fire. In Dillon's thesis, he conducted experiments to quantify the flame height and heat flux from the flame of ISO 9705 burner within the compartment of the room corner test [30].

Hasemi et al. were the first to mount L-shaped propane line burners to the walls, simulating the fuel production from a burning wall surface [31]. They performed experiments in an open-corner wall with and without a ceiling. The experimentalists measured the heat flux from the flame, HRR from the burner and flame height visually using video cameras. For all the experiments, the propane burner HRR was less than 100×10^3 W. Equation 1 is an empirical correlation for the flame height in the corner of two walls without a ceiling is based on the Q^* and the height of the gas burner (D). Hasemi et al. also demonstrated potential scaling methods for the vertical and horizontal heat flux distribution from the corner wall fire.

$$y_f/D = 6.0\ Q^{*0.60} \tag{1}$$

Qian and Saito measured the flame height and heat flux from a corner wall fire, as opposed to an exposure fire from a gas burner [32]. In their experiments, PMMA lined the walls of an open corner-wall test configuration that had a noncombustible ceiling. The PMMA was ignited using a propane torch and the fire was allowed to propagate to the ceiling. Qian and Saito proposed an empirical correlation for the flame height and heat flux distribution of a PMMA corner wall fire. The proposed flame height equation is a function of the time after ignition. This flame height equation is highly dependent on

the ignition scenario. The flame heat flux was found to be steady in the pyrolysis zone at 32.5×10^3 W m^{-2} based on measurements obtained by the Gardon-type heat flux gauge. The vertical heat flux distribution in the flame extension zone is provided in Equation 2. Equation 2 is a function of the vertical height (y) and flame height and it is reported in units of W cm^{-2}.

$$q''_f = 0.822\left(y/y_f\right)^{-2.3} \quad (2)$$

Lattimer and Sorathia performed the most detailed experiments characterizing the steady state thermal conditions felt at the surface of the walls and ceiling during a fire in the corner of a room [33]. Many of the room corner fire models rely on the correlations developed in their paper to define the flame height and thermal conditions produced by the corner-wall fire. Lattimer and Sorathia performed full-scale experiments within an open room corner test apparatus and they measured gas temperature, flame height and total incident heat flux to the wall and ceiling. The surface heat flux was measured using Schmidt-Boelter total heat flux gauges with hot tap water circulating through them. During the experiments, either a square or L-shaped line propane gas burner was located in the corner of room. The square burner simulates an exposure fire, which is similar to the room corner test. While the line burner simulates a wall fire located in the corner of the room. Both propane gas burners varied in width (0.17 m, 0.30 m and 0.50 m) and fire size (25×10^3 W, 50×10^3 W, 100×10^3 W, 200×10^3 W and 300×10^3 W). The walls and ceiling were lined with a noncombustible material and the height of the ceiling was 2.25 m above the top of the burner. Based on the experimental measurements, Lattimer and Sorathia provide empirical correlations for the flame length, gas temperature and the vertical and horizontal heat flux distribution along three regions; the corner walls, the

upper wall-ceiling region and the ceiling. These correlations were developed for the two fire scenarios: corner exposure fire and the corner wall fire. Equation 3 solves for Q^*, which is used to calculate the flame height in Equation 4. These equations can be used to solve for the flame height of either a corner-wall fire or an exposure fire.

$$Q^* = \frac{Q}{\rho c T_\infty \sqrt{g} d^{\frac{5}{2}}} \tag{3}$$

$$y_f/d = C Q^{*\frac{1}{2}} \tag{4}$$

Equation 3 solves for Q^*, which is function of the heat release rate (Q), single side flame burning width or the square burner width (d), acceleration of gravity (g)and properties of air at ambient conditions: density (ρ), heat capacity (c) and temperature (T_∞). Equation 4 can be used to determine the flame height of an exposure fire in the corner of a room and a corner-wall fire. The flame height equation can be determined using Q^* and an empirical constant (C). To calculate the flame tip height ($y_{f,tip}$), C is equal to 5.9 for both the corner-wall fire and the exposure fire. The continuous flame height ($y_{f,cont}$) for the corner-wall fire and the exposure fire requires a C value equal to 4.3 and 3.9, respectively.

Equation 5 is used to determine the vertical heat flux distribution of a corner-wall flame. Equation 6 and Equation 7 are a set of equations used to determine the vertical heat flux distribution of an exposure fire produced by a square propane burner.

$$q''_f = \begin{cases} 70, & y/y_{f,tip} < 0.5 \\ 10\left(y/y_{f,tip}\right)^{-2.8}, & y/y_{f,tip} \geq 0.5 \end{cases} \tag{5}$$

$$q"_{peak} = 120[1 - e^{(-4*d)}] \quad (6)$$

$$q"_b = \begin{cases} q"_{peak}, \ y/y_{f,tip} \leq 0.40 \\ q"_{peak} - 4\left(y/y_{f,tip} - 2/5\right)\left(q"_{peak} - 30\right), \ 0.4 < y/y_{f,tip} < 0.65 \\ 7.2\left(y/y_{f,tip}\right)^{-\frac{10}{3}}, \ y/y_{f,tip} \geq 0.65 \end{cases} \quad (7)$$

The vertical heat flux distribution (Equation 5) states that the heat flux from the corner-wall flame ($q"_f$) is 70 kW/m^2 over the first half of the flame tip height. The heat flux decays vertically as a function of the vertical height divided by the flame tip height. In Equation 6 and Equation 7, the peak heat flux ($q"_{peak}$) is used to determine the heat flux from the burner ($q"_b$). The $q"_{peak}$ occurs over 40% of the flame tip height and then the heat flux decays above that.

Later, Lattimer and Sorathia performed flame spread experiments where combustible materials lined the walls and ceiling in the open corner wall configuration that contained a ceiling [34]. An ISO 9705 gas burner was ignited and produced a 100×10^3 W fire for 600 s, followed by a 300×10^3 W fire for the next 600 s. The experimental measurements of flame height, heat flux and gas temperature were compared to the correlations developed in their previous work. The flame height correlation provided strong predictions of the experimental data, while the wall heat flux and gas temperature correlations over predicted the experimental results.

1.4.4 Room Corner Models

Many researchers have furthered the understanding of compartment fire dynamics by developing correlations and models to simulate the room corner test [35]. Both of these rely on input data from bench-scale tests. The room corner correlations are

based on a statistical analysis that relates bench-scale test data to room corner test results, such as time to flashover and smoke production. The physics-based room corner models predict the time dependent compartment HRR and smoke production of the room corner test by incorporating fire dynamic equations. Often times, physics-based models implement flame spread equations into a zone fire model to best predict fire propagation in a compartment. Some models account for lateral flame spread, burnout and smoke layer/compartment reradiation. All current room corner correlations and models rely on the input data from bench-scale tests, such as the cone calorimeter and LIFT apparatus. Examples of the room corner correlations and physics-based models are provided in the following sections.

Ostman and Tsantaridis developed a simple correlation to predict the time to flashover in the room corner test [13]. The model is a function of time to ignition, total heat release during 300 s after ignition and the mean density. The first two variables are obtained from cone calorimeter testing at incident heat flux conditions of 25×10^3 and 50×10^3 W m^{-2}. This correlation can predict the relative time to flashover for the materials they tested, only if the room corner test reaches flashover within the first ten minutes. This model cannot predict time to flashover for materials that take longer than 600 s to flashover. This model is only valid for predicting the time to flashover in one set of room corner conditions. The model is limited in that once the gas burner dimensions, fire size and duration is changed from the ISO standard, the correlation is no longer valid.

Quintiere and Lian discuss four parameters that dictate a materials performance during a flammability scenario and more specifically the room corner test [18]. These parameters are the materials critical heat flux (CFH), ratio of heat of combustion to heat

of gasification (HRP), thermal response parameter (TRP) and available energy per unit area (AEP). The HRP is the ratio of energy production during combustion to the energy required to cause the material to vaporize. TRP characterizes a thermally thick materials propensity to ignite. The CFH is the minimum heat flux required to ignite the material. The AEP is the amount of available energy during combustion and it is dependent on a materials thickness and combustion efficiency. These material flammability parameters are constant, independent of external heat flux and can be obtained from the cone calorimeter test. Material burning characteristics such as melting, bubbling, delamination are not considered. An empirical correlation is developed that utilizes these four parameters to predict the time to flashover during the ISO room corner test. The correlations over predicts the time to flashover for a majority of the materials. Also, this correlation is only applicable to testing conditions of the ISO Room Corner Test.

Quintiere created one of the first physics-based models for the purpose of simulating the ISO Room-Corner test [14]. Quintiere's model utilizes several governing equations that solve for the upward flame spread and lateral/downward flame spread. The model incorporates empirical correlations that determine the fire to surface heat flux and it also attempts to account for thermal feedback effects within the compartment. These equations allow the model to determine material ignition, burning area, material burnout, the upper-layer temperature and room HRR. The model relies on input data determined through the LIFT and cone calorimeter tests. Model simulations of the room-corner were performed on several different materials and the predictions of these models were compared to the results of the actual room-corner tests by Dillion [36]. Dillon found that the Quintiere model accurately predicted the results for only a few of the

materials. The Quintiere model was shown to be extremely sensitive to changes in the effective heat of vaporization and HRRPUA.

Another physics-based model was developed by Hughes Associates, Inc. that predicts material performance during the ISO 9705 room corner test using data obtained from the cone calorimeter test [16]. This group developed a more general fire growth model which couples a flame spread model together with a zone model. The flame spread model incorporates a detailed vertical flame spread model [37]. The flame spread model also incorporates the flame height and heat flux correlations developed by Lattimer for both the propane gas exposure fire and the corner-wall fire, which were discussed in Section 1.4.3 [33]. During the period of time when the gas burner fire is on and the wall material has ignited, they specify the higher surface heat flux value of the two correlations. The fire growth model is able to track the gas temperature, burning area, HRR and smoke production. This model requires the input of fire properties that must be acquired from cone calorimeter experiments at various incident heat flux conditions. The model was found to be sensitive to the following material properties: thermal inertia, material HRR curve, upper layer temperature. The validation study was only completed for 8 materials. The model sufficiently predicts the compartment HRR curve for most of the materials. The model was not validated for use outside of the standard room corner test conditions and it is currently not available to the public.

BRANZFIRE is a state-of-the-art compartment fire model, created at WPI and developed at the Building Research Association of New Zealand that simulates flame spread and fire growth with an enclosure [15]. This model can be used to evaluate material fire performance during the room corner test. The model requires input data

acquired from the bench-scale cone calorimeter tests. The flame spread and fire growth model utilized in the BRANZFIRE model is based on a previous room corner model developed by Quintiere [14]. BRANZFIRE couples the flame spread and fire growth model together with a zone model that simultaneously solves the mass and energy conservation equations. The BRANZFIRE model was validated by comparing the model's prediction of compartment HRR to the experimental results for 11 materials [38]. It appears that the models adequately predicts the compartment HRR curve, but is unable to accurately simulate upward flame spread along the corner-walls. During the initial stages of the simulation, the model over predicts the rate at which the fire develops along the combustible materials. BRANZFIRE utilizes Lattimer's square gas burner correlations to characterize the thermal conditions from a fire in the corner of a room. BRANZFIRE utilizes Equation 3 and Equation 4 to determine the flame tip height. The heat flux from the fire to the wall surfaces is based on the peak heat flux from a square gas burner, Equation 6 and prescribed along the height of the wall. The surface heat flux is between 59×10^3 W m^{-2} to 83×10^3 W m^{-2} when the square gas burner is 0.17 m to 0.30 m wide. In the BRANZFIRE model, the high surface heat flux conditions are believed to be the source of error in the upward flame spread rate.

In 2009, the Southwest Research Institute (SWRI) published a paper discussing their room corner model [19]. The SWRI attempted to improve Quintiere's original room corner model by modifying correlations for the gas burner flame height and heat flux, tracking the burning area with combination of rectangular shapes and making the emissivity of the upper layer gases based on smoke production rate. This model was validated by comparing the model's prediction of room HRR and smoke production for

four marine composite materials. The authors of this report found that the model over predicts the room HRR and subsequently the time to flashover for these products due to the high heat of gasification value representing the material.

Over the past couple decades, many room corner models have been developed, but a majority of these models are not publically available. BRANZFIRE is the only state of the art room corner model currently available. It was not utilized in this project because it does an inadequate job of predicting upward flame spread along the corner-walls of the room corner test. The large-scale upward flame spread experiments conducted in this project will demonstrate that the Lattimer's square burner and corner-wall correlations over estimate the total heat flux to the surface of the corner-walls. Thus, a flame heat feedback model is developed in this project capable of predicting the flame height and heat flux distribution of a spreading corner-wall fire. It is implemented into ThermaKin2D to simulate the room corner tests conducted in this project.

2. Materials, Experiments and Methods

2.1 *Materials*

2.1.1 Material of Interest

Common building materials and interior linings utilized during reconstructive fire tests are: MDF wood paneling, carpet, carpet padding, oriented strand board, plywood and gypsum wallboard [39]. MDF was installed in legacy homes and is currently used in modern construction. MDF wood-paneling will be the focus of this project because the ATF FRL commonly uses during their reconstructive fire tests.

Currently, MDF wood-paneling is the most prevalent type of wood-paneling product commercial available. MDF wood-paneling is an engineered wood product consisting of various types of wood fibers held together by an adhesive. Previous researchers have performed milligram-scale, bench-scale and intermediate-scale flammability tests on MDF [40][41][42][43]. MDF has been shown to have a Class C flame spread rating during ASTM E-84, which means that it is an acceptable interior finish according to the building codes in the United States [44].

Several different manufacturers produce MDF wood-paneling. In this project, four different types of MDF wood-paneling are analyzed. A generic naming convention is used to describe each material. This naming convention describes each material as a "Sample" followed by a letter of the alphabet.

In the built environment, MDF paneling is typically glued or stapled to the gypsum wallboard, which makes up the walls. Therefore, in the bench-scale and full-scale experiments, the MDF samples were stapled to the gypsum wallboard to replicate common installation practices. Stapling the MDF samples to the gypsum wallboard prevented swelling during the cone calorimeter experiments and delamination from the walls during the full-scale tests.

Prior to all the bench-scale and large-scale experiments, the MDF samples and the gypsum wallboard were placed in a conditioning chamber set to 296 K and 50 % humidity for an extended period of time. Bench-scale testing would not occur until the mass of the samples reached equilibrium.

2.1.2 Material Description

Sample A is produced by Georgia-Pacific LLC, it is titled PurImpression and it has a Universal Product Code (UPC) = 81999-56073 [45]. Sample A is thickest MDF wood-paneling product analyzed in this project. It is a white board that is 6.2×10-3 m thick, with a bead line located along the top surface. The density of the sample at room temperature is 1089.4 kg m-3. Figure 4 provides an image of Sample A prepared for the cone calorimeter experiment.

Figure 4. Sample A

Sample B is produced by Decorative Panels International, it is titled Prefinished Panel Paintable Beaded White and it has a UPC = 65096-00139 [46]. Sample B is the second thickest wood-paneling product. Sample B is also a white board with a bead. Sample B is 4.1×10^{-3} m thick, with a density of 889.3 kg m^{-3} at room temperature. Figure 5 provides an image of Sample B prepared for the cone calorimeter experiment.

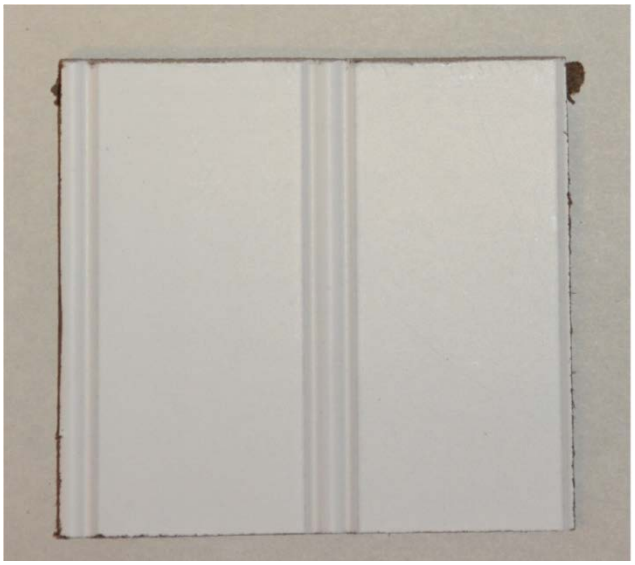

Figure 5. Sample B

Sample C is produced by Georgia-Pacific LLC, it is titled Springfield Hickory and it has a UPC = 81999-55039 [47]. Sample C is 3.6×10^{-3} m thick, 888.8 kg m^{-3} dense at room temperature and it has a light brown color. Figure 6 provides an image of Sample C.

Figure 6. Sample C

Sample D is produced by Eucatex of North America and it is titled Eucaboard [48]. Eucaboard is 3.2×10^{-3} m thick and it has a dark brown color. At room temperature, Sample D has a density of 1080.2 kg m^{-3}. Figure 7 provides an image of Sample D.

Figure 7. Sample D

The gypsum wallboard used during the bench-scale and full-scale experiments was produced by United States Gypsum Company. It is titled SHEETROCK Brand Ultralight Panels and has a UPC = 69606009220 [49]. The gypsum wallboard was 1.26×10^{-2} m thick and had a density of 480.6 kg m^{-3} at room temperature. Figure 8 provides an image of the gypsum wallboard.

Figure 8. Gypsum wallboard

2.2 Milligram-Scale Testing

2.2.1 MCC

The MCC was developed by the Federal Aviation Administration (FAA) to determine the flammability characteristics of combustible polymers [50]. The MCC uses the principal of pyrolysis-combustion flow calorimetry (PCFC) which decouples the condensed phase and gas phase reactions to determine a specimen's HRR, char yield, temperature of decomposition, and the heat of complete combustion of the gaseous volatiles. Figure 9 provides an image of the MCC that was constructed at the University of Maryland (UMD) by the research team and a diagram of the MCC apparatus.

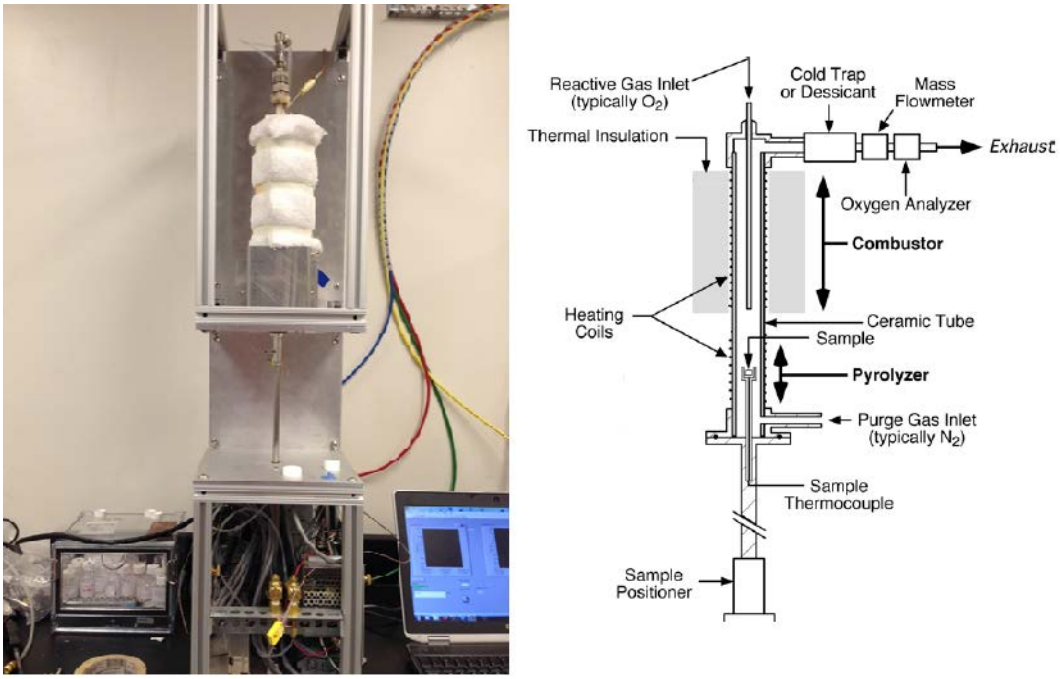

(a) (b)

Figure 9. An image of the MCC constructed at UMD is provided in image a. A diagram of the MCC is depicted in figure b [50]

During the MCC test, a milligram sized sample is inserted into the pyrolyzer, where it is linearly heated in an inert environment. As the sample heats up and pyrolyzes, nitrogen flows around the pyrolyzer and transports the volatiles into the combustion

chamber. Excess oxygen is delivered into the combustion chamber, which is maintained at an elevated temperature. Complete combustion occurs within the superheated chamber once the volatiles mix with oxygen. The products of combustion are analyzed after they exit the combustion chamber. The MCC uses the principal of oxygen consumption calorimetry to determine the heat released as a function of time and the pyrolysis temperature. The MCC experiments were performed according to ASTM D7309 [51].

The samples tested in the MCC typically weigh between 2×10^{-6} kg and 5×10^{-6} kg. To create each sample, the MDF wallboard was drilled using a drill press containing a 1.6×10^{-3} m sized drill bit. MDF fibers and saw dust were pulled to the surface as the drill pierced and circulated within the MDF wallboard. A sufficient quantity of the sample saw dust was collected and placed in a clean glass vial. The glass vial was then placed in a desiccator which contained Drierite. Doing this minimized the moisture content of the sample. Figure 10 provides an image of the MCC samples prior to testing.

Figure 10. Pre-test images of Samples A, B, C and D in their respected glass vial and sample holders

The MCC was calibrated according to ASTM D7309 by testing metals with a known melting temperature. Each metal is heated at 1 K/s. The temperature at which the metal reacts is noted and the calibration is performed by equating the measured melting temperature to the known melting temperature. This calibration is done periodically. To ensure that the MCC was properly functioning each day, a system performance test was conducted by testing a reference polymer with known flammability characteristics according to [52].

Prior to each test, the sample is placed in a clean ceramic pan with a known weight and the mass of the sample is determined using a microbalance. All of the samples tested in the MCC weighed 2.5×10^{-6} kg $\pm$ 0.15×10^{-6} kg. After the sample is weighed, the ceramic pan containing the specimen is placed on top of the hydraulic pedestal and it is loaded into the pyrolyzer. The experiment is started once the temperature and gas flow rates stabilize at their specified values. Once the test begins, the sample is heated at 1 K/s until it reaches 1023 K, a value well above the material pyrolysis temperature. After each test, the mass of the char residue is measured. The char is then discarded and the sample holder is cleaned using a torch. Each sample was tested 5 times.

2.3 Bench-Scale Experiments

2.3.1 Cone Calorimeter

The cone calorimeter is a popular bench-scale test used to measure the flammability of combustible materials. During the cone calorimeter test, a 0.1 m $\times$ 0.1 m sample rests on top a mass scale and underneath a conical radiant heater which subjects

the specimen to a steady radiant heat flux. An ignition source is placed above the sample to ignite the combustible products. Throughout the test, the exhaust hood has several pieces of instrumentation which measure the flow and temperature of the smoke, as well as the concentration of oxygen, carbon monoxide and carbon dioxide.

The cone calorimeter is able to measure the ignitability, effective heat of combustion and soot production of the combustible material. The cone calorimeter also measures the heat release rate per unit area (HRRPUA) based on the principle of oxygen consumption calorimetry which assumes that the amount of energy produced per unit mass of oxygen consumed is nearly constant at 13.1×10^6 J kg^{-1} [53]. HRR is calculated in Equation 8 based on the pressure difference (ΔP) and temperature (T_e) of the combustion products flowing through the exhaust system, the difference in the volumetric fraction of oxygen (X_{O_2}), a calibration constant (C), and the oxygen heat of combustion ($\frac{\Delta h_c}{r_0}$) [3]. The effective heat of combustion is calculated using Equation 9 by dividing the integral of the HRR by the mass loss during combustion (Δm). Several testing standards exist that define the cone calorimeter testing procedures [3] [54].

$$\dot{Q}(t) = \left(\frac{\Delta h_c}{r_0}\right)(1.10)\, C \sqrt{\frac{\Delta P}{T_e}\,\frac{\left(X_{O_2}^0 - X_{O_2}(t)\right)}{1.105 - 1.5\, X_{O_2}(t)}} \tag{8}$$

$$\Delta H_{eff} = \frac{\int \dot{Q}(t)}{\Delta m} \tag{9}$$

It was important to expose the samples to a wide range of thermal conditions which best represent the conditions a combustible solid may experience during vertical flame spread. The samples were exposed to a low incident heat flux (20×10^3 or 25×10^3

W m^{-2}), a medium incident heat flux (50×10^3 W m^{-2}) and a high incident heat flux (80×10^3 W m^{-2}). Each test was performed three times. At lower conditions, the sample was first exposed to 20×10^3 W m^{-2}. If the sample did not ignite, a new test was performed where the sample was exposed to 25×10^3 W m^{-2}.

2.3.2 Cone Calorimeter Sample Preparation and Testing Procedure

For all of the cone calorimeter experiments, the tested specimen consisted of the MDF samples placed upon 0.0126 m of gypsum wallboard. Once the samples were conditioned, the mass of the MDF sample and gypsum was measured. The sample was restrained to the gypsum wallboard and the sides and bottom of the specimen were then wrapped in one layer of aluminum foil. FiberFrax Durablanket insulation was positioned at the bottom of the sample holder and the specimen was placed on top of the insulation. An image of the cone calorimeter sample setup is provided in Figure 11. The edge frame was then positioned on top of the sample and securely fastened to the sample holder so that the top of the sample was flush with the edge frame. The sample had an exposed surface area of 88.4×10^{-4} m^2.

Figure 11. Cone calorimeter sample preparation

Prior to testing each day, the following items were set and calibrated according to [3]: exhaust flow rate, radiant heater, mass scale, smoke meter and the oxygen, carbon monoxide and carbon dioxide gas analyzers. The calibration constant was then obtained by igniting the methane burner under the cone, producing a 5×10^{3} W fire for 720 s. Once the cone calorimeter was calibrated and sample was prepared, the sample was placed into position, 25×10^{-3} m underneath the heater. The test began once the ignitor was set in place and the shield was removed. Throughout the test, photos were taken and all observable events were marked. The test concluded 120 s after yellow flames were no longer visible. After the tests, the sample holder was removed from the cone calorimeter and placed underneath an exhaust hood until the specimen was cool.

2.3.3 Cone Calorimeter Sample Restraining Method

One of the objectives in this project is to develop a cone calorimeter model in ThermaKin2D. In order to model these tests, a boundary condition must be specified that replicates the thermal conditions created by the cone calorimeter, specifically the incident heat flux from the radiant heater. Prior to the cone calorimeter experiments, the incident heat flux is set based on the temperature of the radiant heater and the distance from the bottom of the heater to the surface of the sample, which is 25×10^{-3} m. During testing, materials often deform and swell, which causes the distance between the radiant heater and the surface of the sample to decrease. The incident heat flux increases once the distance between the sample and the radiant heater decreases. Modeling the changing incident heat flux is difficult and very complicated. Therefore the goal is to prevent the sample from swelling by restraining the sample surface to its original location. This

allows the model to assume that the incident heat flux from the heater to the sample's surface is uniform.

ASTM E1354 provides two methods for holding the sample in place: edge frame or wire grid. A stainless steel edge frame provides a way to encapsulate the edges of the sample so that a small amount of force is applied to the top edges of the specimen. The edge frame is intended to maintain the surface height and reduce edge burning [55]. The intention of the wire grid is to prevent the vertical expansion of intumescent materials. A third restraining method was also developed in this project. It entailed stapling the MDF sample to the gypsum wallboard and using the edge frame to secure the sample inside the sample holder. One staple was embedded at the center of the sample, while the other four staples were placed equidistant from the corner to the center. Figure 12 provides an image of the three different restraining methods.

(a) Edge frame only

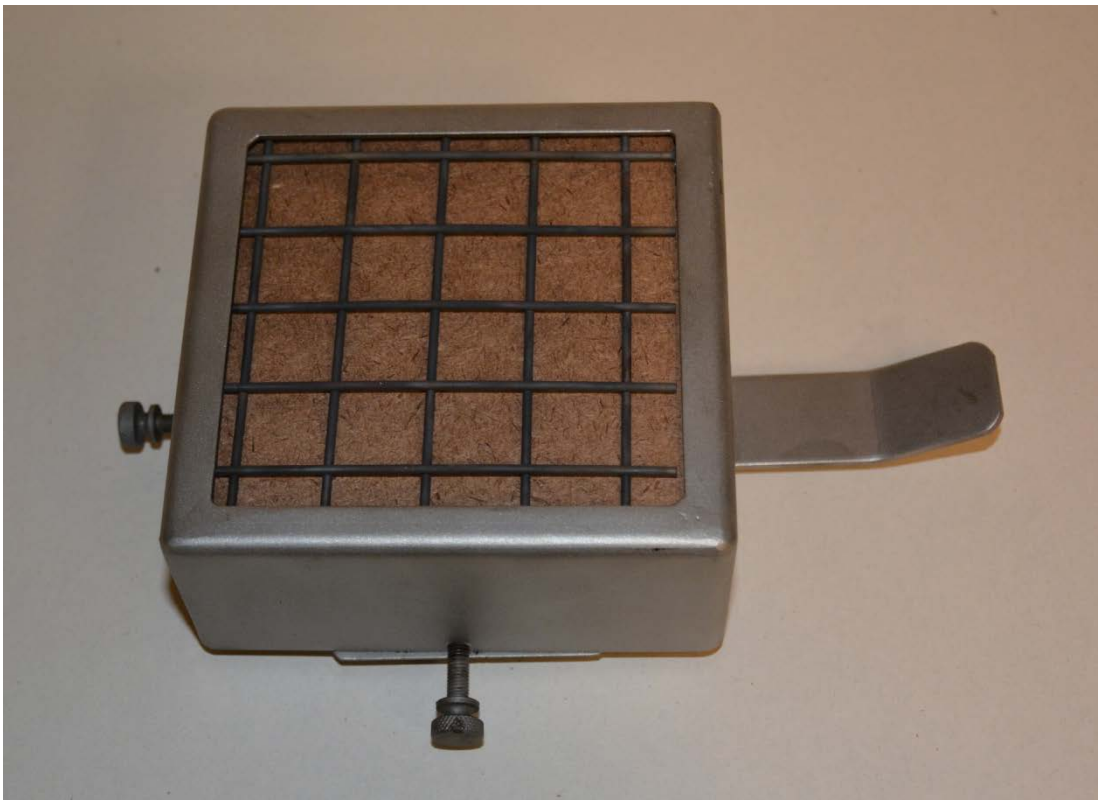

(b) Edge frame and wire grid

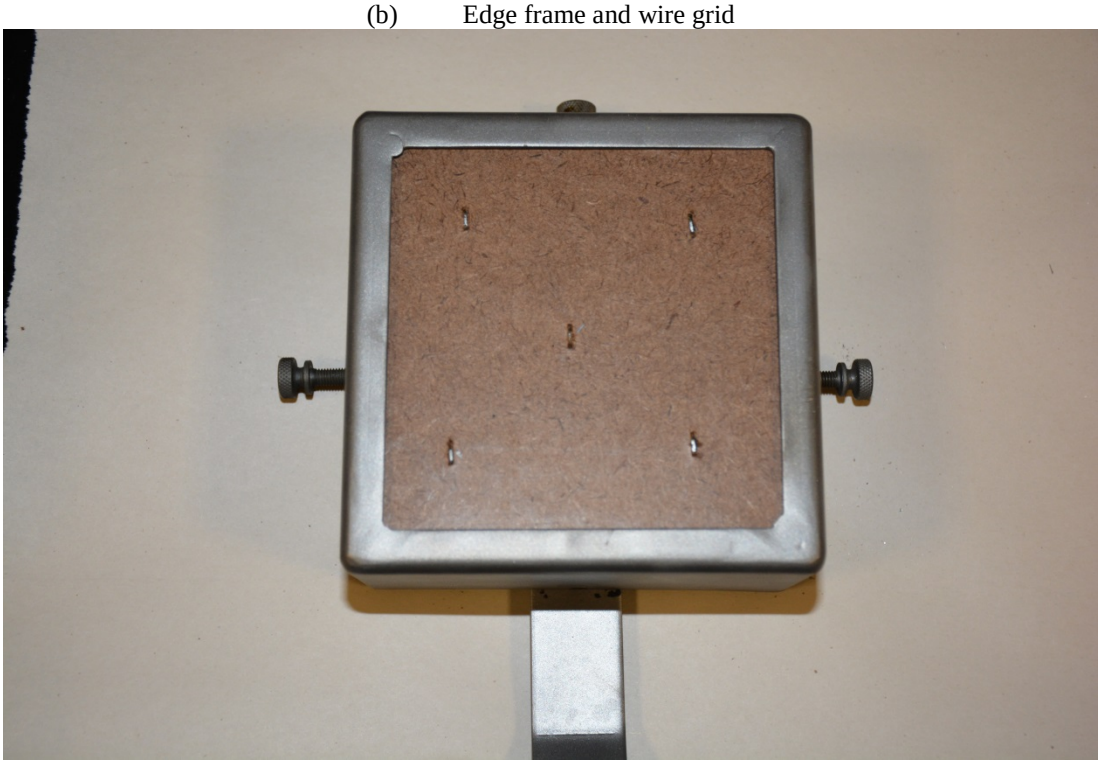

(c) Edge frame and five staples

Figure 12. Three cone calorimeter restraining methods: edge frame, edge frame with wire grid and edge frame with staples

Of all the materials, Sample A had the tendency to swell the most, which caused it to challenge the various restraining methods. Preliminary testing on Sample A was performed at an incident heat flux of 50×10^3 W m^{-2} to determine the most effective restraining method. The results of the preliminary cone calorimeter tests on Sample A using the various restraining methods are displayed in Figure 13.

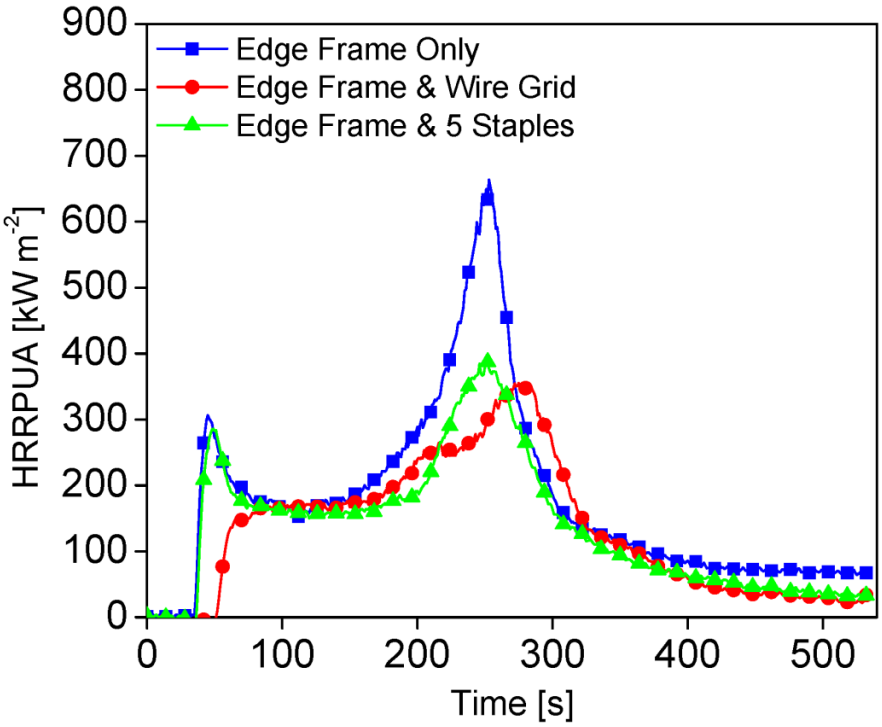

Figure 13. Preliminary cone calorimeter testing of Sample A at 50 kW/m^2 using three different restraining methods

Qualitatively, Sample A produces two HRR peaks. The first peak is due to the initial energy production from the flame upon ignition. While the secondary peak occurs after heat has transferred through the material, the internal temperature has rose and the sample begins to deform and swell. The first restraining method employed was the edge frame only. It was the least invasive method but the sample did swell past the top of the sample holder around 140 s, which is when the second HRR peak is beginning to

develop. Upon completion of the test, it was observed that the sample had bowed into a convex shape, significantly decreasing the distance between the sample surface and the cone heater. The second restraining method attempted was the wire grid in addition to the edge frame. The wire grid was the most invasive method. As shown in Figure 13, ignition occurred 20 s after the ignition time of the other two methods. After ignition, small flamlets appeared between each square grid, rather then one large solid flame. The wire grid reduces the exposed surface area and the metal grid acts as a heat sink which causes the ignition time and HRR curve to vary compared to the other methods. The wire grid was successful at preventing surface expansion. The third technique used to restrain the sample was stapling the sample to the gypsum and utilizing the edge frame. This method was able to adequately prevent surface expansion. Figure 13 demonstrates that the staple method is able to consistently predict ignition according to the sample preparation technique where only edge frame was used. At the same time, this restraining method prevents the sample from swelling which may be why the second HRR peak is less severe.

MDF wallboard is commonly installed using staples. In this project, the MDF wallboard was installed using staples in the large-scale tests. Using staples to restrain the sample during the cone calorimeter tests will maintain installation uniformity amongst the bench-scale tests and full-scale tests. This is the best restraining method to use in this project because it prevents surface expansion, while maintaining realistic measurements of the HRR.

2.3.4 Additional Cone Calorimeter Experiments

One of the goals of this project is to model the cone calorimeter tests using ThermaKin2D. In order to perform pyrolysis modeling, the char density must be prescribed for each material and a boundary condition must be specified that represents the additional heat flux from the flame to the surface of the sample, upon ignition. Mistakenly, the char was never analyzed during the previous cone calorimeter tests. For pyrolysis modeling, the char density must be specified, as well as the heat flux from the flame to the surface of the material upon ignition. Therefore, more cone calorimeter experiments were performed on each sample at an incident heat flux of 50×10^{3} W m^{-2} and the dimensions and mass of the char were measured post-test. In addition to this, cone calorimeter experiments were performed in which the heat flux from the flame to the surface of the material was measured in the cone configuration.

The cone calorimeter apparatus had to be modified slightly to perform the flame heat flux experiments. As shown in Figure 14, the load cell and the sample mounting assembly had to be removed so that the heat flux gauge could be positioned within the sample. Prior to these experiments, the samples were conditioned and prepared in the same manner as discussed in Section 2.3.3. The only difference was that a 0.95×10^{-2} m hole was drilled through the MDF and gypsum sample. A 0.95×10^{-2} m diameter water-cooled Schmidt Boelter heat flux gauge was placed inside the sample so that the surface of the heat flux gauge was flush with the sample surface as shown in Figure 15. Three tests were performed where the heat flux gauge was positioned at the center of the sample and three tests were performed where the heat flux gauge was positioned at side of the

sample. The fifth center staple was not installed when the heat flux gauge was positioned at the center.

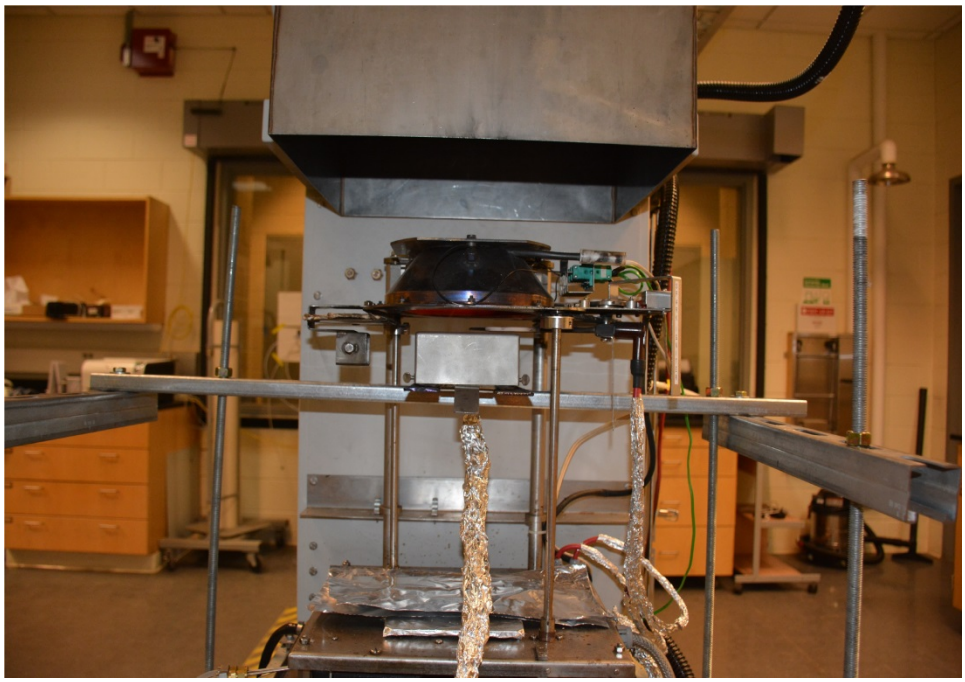

Figure 14. Modified cone calorimeter apparatus for the flame heat flux experiments

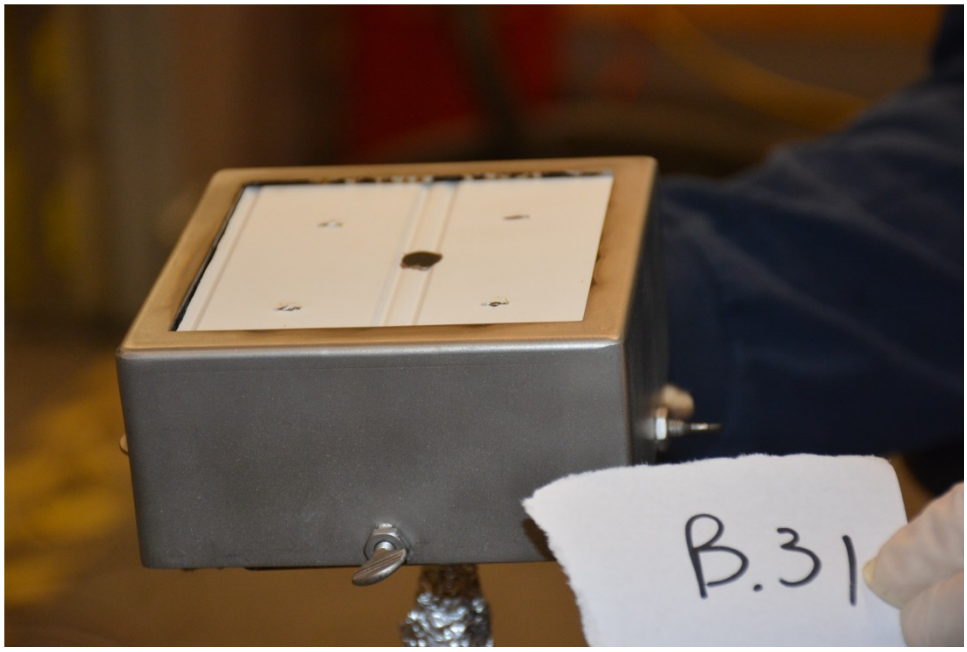

(a)

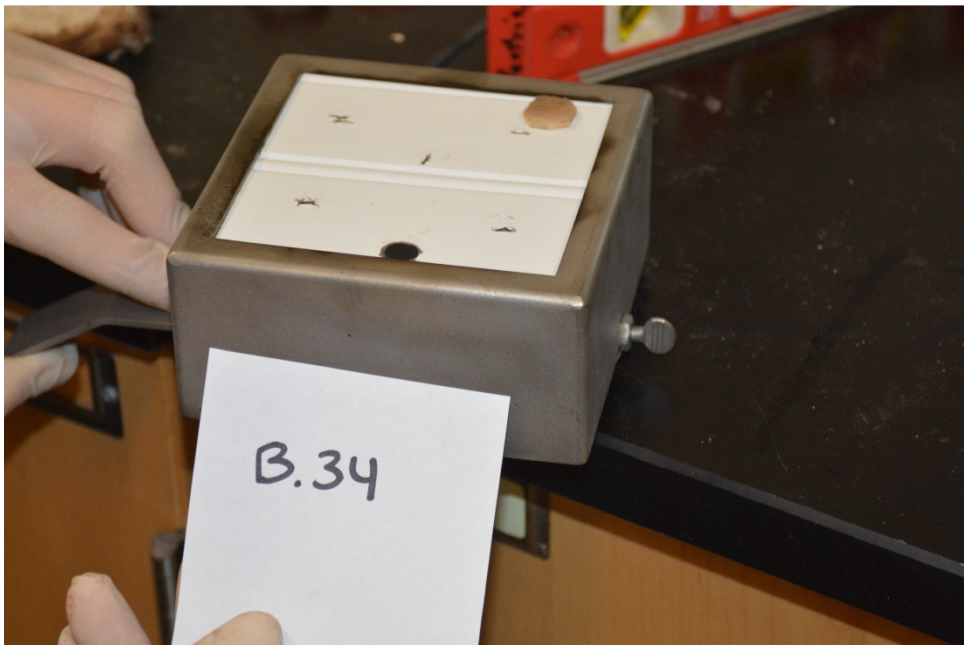

(b)

Figure 15. Flame heat flux cone calorimeter experiments. Image (a) shows the test where the heat flux gauge is centered, while image (b) shows the test where the heat flux gauge is located at the side.

The gauge was calibrated by placing the experimental heat flux gauge next to a reference heat flux gauge 0.25 m underneath the radiant heater as shown in Figure 16. Next, the voltage reading from the experimental heat flux gauge was plotted against the reference heat flux gauge reading at 25×10^3 W m^{-2}, 35×10^3 W m^{-2} and 55×10^3 W m^{-2}. The calibration constant was determined by fitting the data with a linear line. Subsequently, the calibration constant is used to convert voltage measurements to heat flux. After each test the heat flux gauge was removed from the sample, cleaned, repainted and recalibrated. The heat flux gauge was cleaned to remove the unwanted residue from the surface of the gauge.

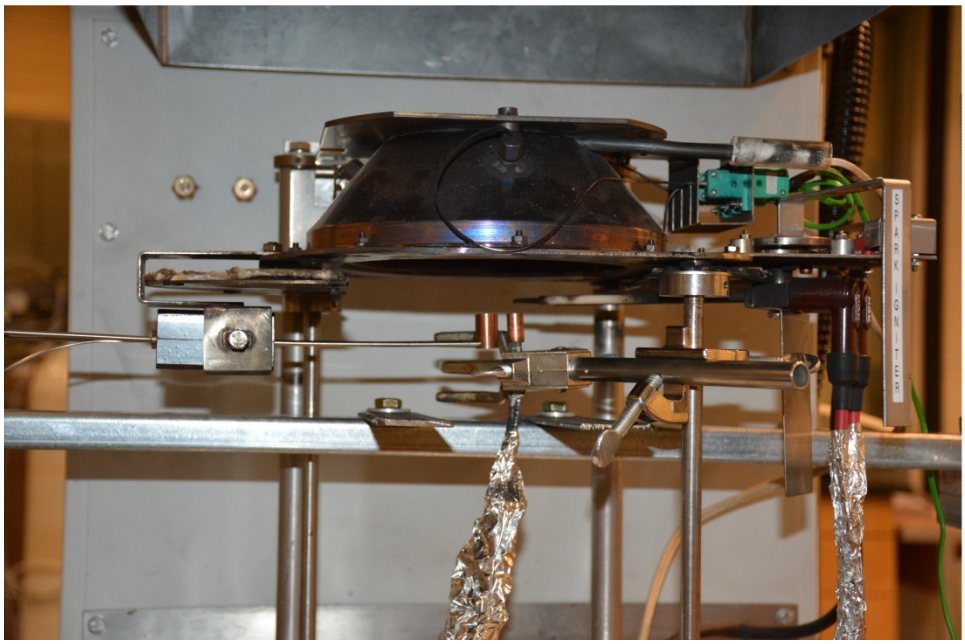

Figure 16. Flame heat flux experiments - heat flux gauge calibration

Since the four samples have similar compositions, the effective heat of combustion values are assumed to be very similar amongst the four samples. Therefore, it is further assumed that the flame structure and the heat flux it produces are similar amongst the four samples for all the cone calorimeter experiments. Thus, Sample A and Sample B were the only materials tested during the flame heat flux experiments. Six tests were conducted. Prior to all of these experiments, a shield made of 6×10^{-3} m thick Kaowool PM Insulation was place over top of the heat flux gauge. The shield can be seen in Figure 15b. The sample holder was placed 0.25 m underneath the cone calorimeter as shown in Figure 14. Similar to the standard [3], the spark ignitor was positioned above the sample, the radiation shield was removed and the radiant heater exposed the sample to an incident heat flux of 35×10^{3} W m^{-2}. 45 s after ignition, the shield covering the heat flux gauge was removed to measure the additional heat flux from the flame. Figure 17 shows an image of test B.3 were the heat flux gauge is still protected by the shield and an another image where the shield has been removed.

(a)

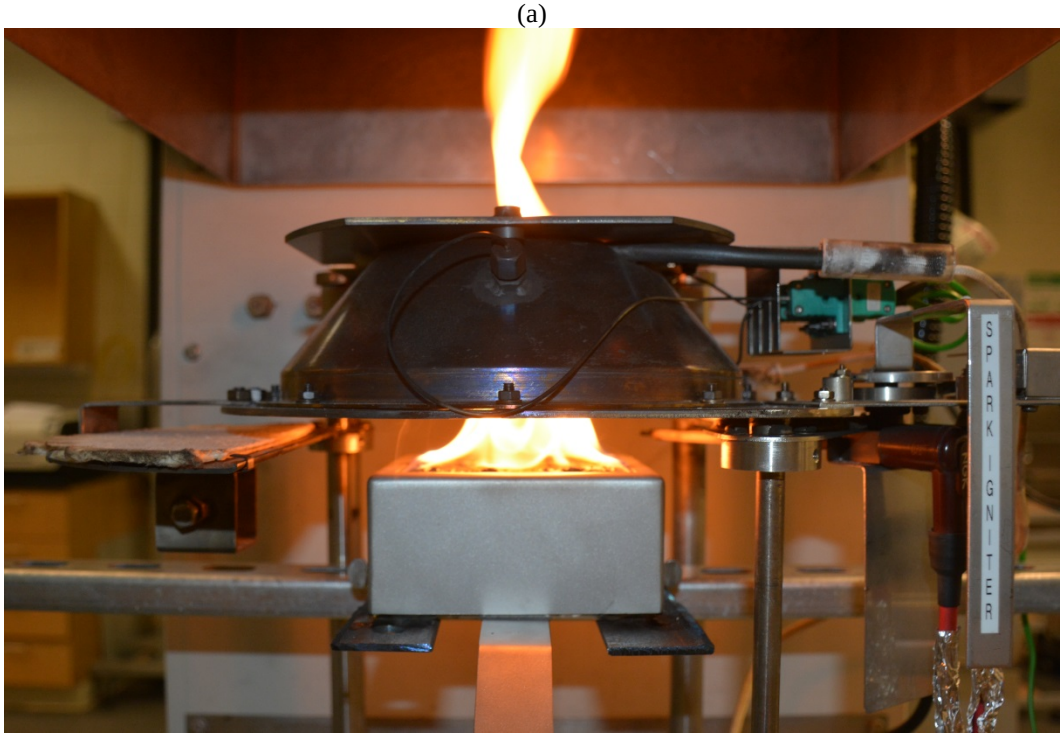

(b)

Figure 17. Flame heat flux test B.3. Image (a) shows the cone calorimeter experiment once ignition has occurred but prior to the heat flux gauge shield being removed. Image (b) shows a zoomed-out photo of test B.3 once the heat flux gauge shield has been removed.

2.4 Full-Scale Experiments

2.4.1 Open Corner-Wall Tests

The room corner test is difficult to perform because it is expensive, time consuming and requires a lot of instrumentation. Thus an assembly was constructed which mimics the corner-wall and ceiling of the room corner test so that multiple tests could be conducted in this scaled scenario.

Three different types of tests were performed in this assembly. First, a set of preliminary tests were conducted to determine the appropriate burner fire size and burner duration during the full-scale tests. Next, actual experiments were performed that involved installing the MDF sample along the corner-walls and exposing the samples to a propane burner fire. Once the material ignited, the burner was turned off and the fire was allowed to spread upwards, in order to measure the heat flux from the spreading flame to the burning surface. The last set of experiments entailed subjecting a noncombustible surface to the square propane fire in order to characterize the heat flux from the exposure fire.

A corner-wall assembly was constructed under the 1 MW Hood at the ATF Fire Research Lab. The 1 MW hood can measure HRR with a reported uncertainty of 10 % at 50×10^{3} W and 5% at 500×10^{3} W [56]. This assembly was built with wood framing and the walls were composed of gypsum wallboard similar to the room corner tests. Figure 18 provides an image of the open corner-wall testing assembly. All of the walls were 2.4 m tall and 1.2 m wide. The ceiling extended 1.7 m from the corner and it covered the area above the walls. A 30.5×10^{-2} m × 30.5×10^{-2} m × 35.375×10^{-2} m square propane gas

burner was located on the floor in the corner of the assembly. The burner was filled with stone gravel up to 30.375×10^{-2} m above the floor. During the experiments, CP grade propane with a 99% purity was released from the burner. The propane flow rate was controlled using an Alicat Scientific Mass and Volume Gas Flow Meter specified for 100 SLPM. The propane burner HRR was then specified by multiplying the propane flow rate by propane's effective heat of combustion, which was 46.4×10^{6} J/kg. The propane HRR was verified by comparing the hood HRR measurements to the specified burner fire size. During the flame spread and burner characterization tests, seven water-cooled Schmidt-Boelter Heat Flux Transducers that were 2.54×10^{-2} m in diameter with a 100×10^{3} W m^{-2} capacity were imbedded in the walls to characterize the heat flux distribution from the flame to the surface of the wall. The holes the heat flux gauges occupied were sealed using FiberFrax Durablanket insulation. Water was heated to 313 K and was circulated through the heat flux gauges to prevent condensation from forming on the heat flux gauges.

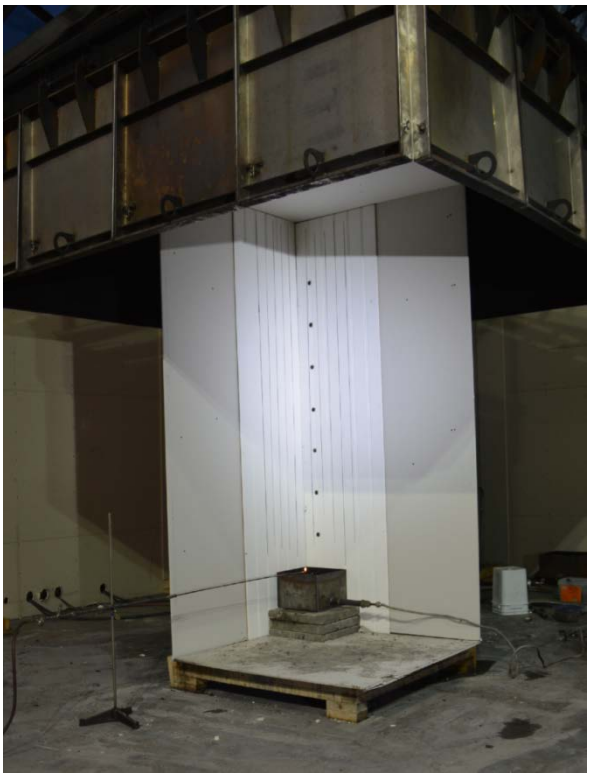

Figure 18. Open corner-wall testing assembly

Two video cameras simultaneously recorded each flame spread test. The center-view video camera was directed at the corner walls to record flame propagation along both walls, while the side-view video camera faced only the right wall to record the burning width. The two video camera perspectives are shown in Figure 19.

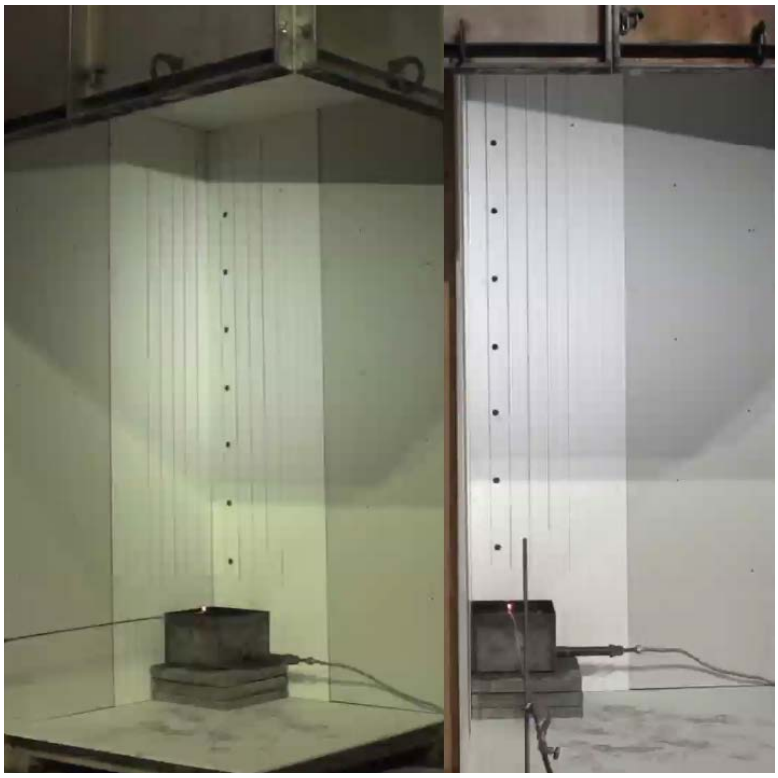

(a) (b)

Figure 19. Video camera perspectives during the flame spread tests. The images shown are from the center-view camera perspective (a) and the side-view camera perspective (b)

2.4.2 Open-Corner Wall Preliminary Testing

Two sets of preliminary experiments were conducted in the open corner-wall configuration. Both preliminary tests were intended to determine the appropriate burner fire size and burner duration that would achieve material ignition and sustain flame spread during the open corner-wall experiments and the room corner tests. The goal of the open corner-wall flame spread experiments was to achieve optimal flame spread along the MDF samples in the corner-walls. A flame heat feedback model for corner-wall flame spread was developed based on the HRR and heat flux measurements recorded during these tests. This flame heat feedback model was incorporate into ThermaKin2D to simulate full-scale flame spread.

Preliminary testing in the open corner-wall configuration was performed on all of the samples and it was found that each of the samples reacted differently to the same exposure fire. Two of the samples took a couple of minutes to ignite and therefore, the fire slowly propagates up of the surface of the walls. These samples had the propensity to self-extinguish if the burner was not left on for a long enough duration. While the other materials ignited quickly and they enabled fast vertical flame spread. If the burner was left on for too long, the flames would quickly spread to the ceiling. This scenario was not desired because the burner would control the rate of flame spread rather than the material itself. Therefore, preliminary testing was conducted on each sample to determine the minimum fire size and exposure duration needed to sustain ignition and achieve controlled vertical flame spread. It was found that a 25×10^3 W fire was able to ignite all the materials, but each sample had to be exposed to the burner fire for a different duration. Table 1 provides the propane burner exposure duration for each sample which sustained flame spread once the burner is turned off. Sample A required the longest burner exposure time, while sample B required the shorted burner exposure duration.

Table 1: Flame Spread Experiments - Propane Burner Exposure Duration

Sample	Exposure Duration (s)
A	345
B	227
C	293
D	250

During the standard room corner test, the gas burner subjects the tested specimen to extreme thermal conditions. The ISO and ASTM standards for the room corner test require the gas burner to produce a 100×10^3 W fire for the first 10 minutes and a 300×10^3 W fire for the following 10 minutes [7] [8]. The NFPA standard room corner tests

requires the gas burner to produce a 40×10^3 W fire for the first 5 minutes and a 160×10^3 W fire for the next 10 minutes [10]. All of these room corner standards expose the tested specimen to a substantial fire, for a long duration. Fires of this magnitude will cause most combustible wall linings to ignite and the compartment will transition to flashover due to these conditions. In the standard tests, the gas burner is the primary force responsible for influencing flame spread along the corner-walls.

The main objective of this project's room corner tests were to compare material fire performance by focusing on the flame spread rate along the burning sample, with minimal influences from the burner. Thus, the burner conditions specified in the standard room corner test were modified. Rather than having the burner produce a fire throughout the entire test, the burner was specified to produce the minimum standard burner HRR of 40×10^3 W. The burner would then be turned off so that the flames would spread upwards at a rate dependent upon the flammability of the materials. The samples were subjected to the same burner fire size and duration, so that the performance of each material could be compared in an objective manner.

Preliminary testing was conducted to determine the minimum burner duration needed to achieve ignition and sustain flame spread during the room corner tests. It was found that exposing the samples to a 40×10^3 W for 165 s would meet this goal. Essentially, the square propane burner is intended to ignite the wall material and start the flame spread process. Once the burner is turned off, the fire will develop on its own. Modifying the burner conditions of the room corner test provides a more precise method to analyze the full-scale fire performance of these similar materials.

During both of the preliminary tests, the side-view video camera recorded the fire progression along the right corner-wall. These videos provided a good understanding of the single-sided width of the propane burner flame and the spreading corner-wall flame. It revealed that the air entrainment caused the flame from the propane burner to be pushed into the corner, as shown in Figure 20. It is estimated that the 25×10^3 W and 40 $\times10^3$ W propane burner flame occupied the first 75% of the burner width. This equates to a single-sided burner flame width of around 0.225 m.

Figure 20. Corner-wall propane burner fire and the effect of entrainment on the width of the flame

During the preliminary testing of the MDF samples, lateral flame spread did not occur prior to flames reaching the ceiling. In fact, it was observed that the single side flame width of the spreading corner-wall fire was slightly less than the burner width of 0.3 m. Several heat flux gauges were embedded in the walls during the actual open corner-walls tests to measure the thermal conditions from a spreading flame and or the

burner fire. The placement of those gauges with respect to the corner was determined based on information gained during these preliminary tests. During the open corner-wall flame spread and burner exposure tests, the heat flux gauges were conservatively placed 0.10 m from the corner of the wall. This location is less than half of the flame width and it ensures that the heat flux gauge was always located within the flame region of the burner fire and corner-wall fire.

2.4.3 Open Corner-Wall Flame Spread Experiments

The general set up for the corner-wall flame spread experiments is shown on Figure 21. During these experiments, the corner-wall assembly was directly underneath ATF's 1 MW Hood so that the HRR could be recorded based on the principal of oxygen-consumption. The heat flux gauges were located along the right wall, 0.10 m from the corner, based on the preliminary testing. The gauges were located at the following heights above the floor: 0.55 m, 0.80 m, 1.05 m, 1.30 m, 1.55 m, 1.80 m and 2.05 m. This translated to each heat flux gauge being at the following heights above the top of the propane gas burner: 0.196 m, 0.446 m, 0.696 m, 0.946 m, 1.196 m, 1.446 m and 1.696 m. The heat flux gauges were arranged only on the right wall because it is assumed that the heat transfer from the fire is symmetric with respect to the plane.

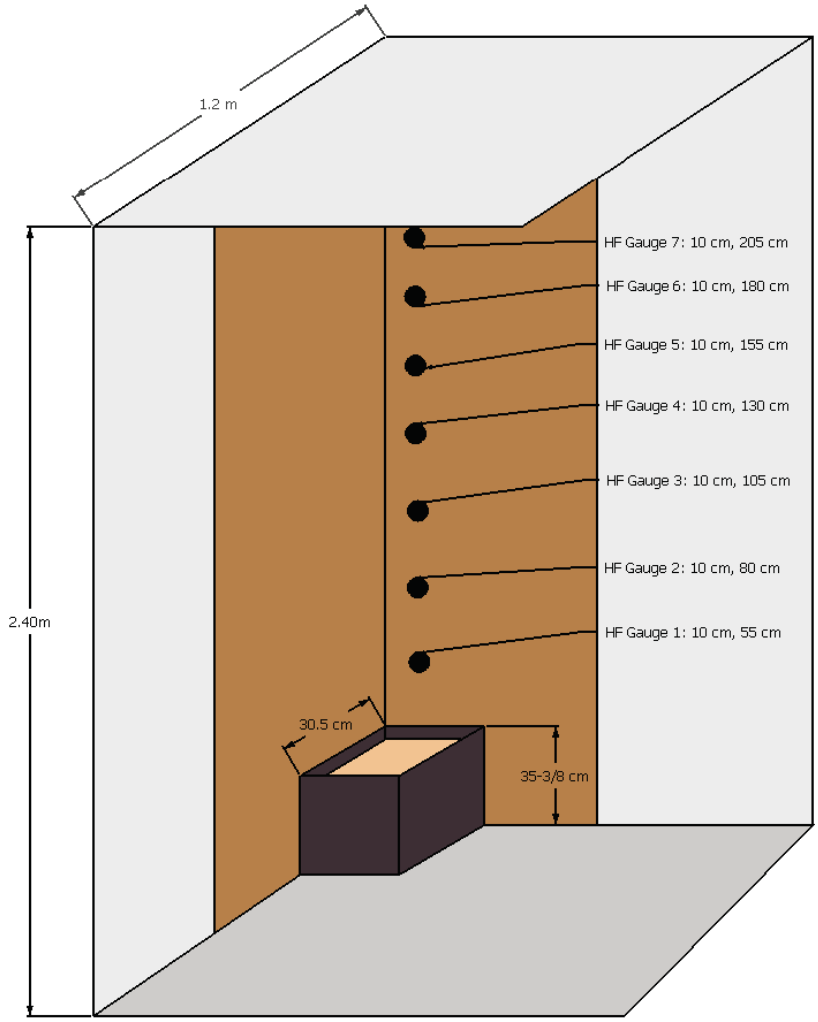

Figure 21. Flame spread experiments conducted in the open corner-wall assembly

All of the MDF samples were cut to be 0.61 m wide and 2.4 m tall and they were stapled to the walls so that samples met flush in the corner. Figure 22 shows the photos of the experimental setup for each sample. The corner-wall flame spread experiments were conducted once for each sample.

(a) Sample A (b) Sample B

(c) Sample C (d) Sample D

Figure 22. Pre-test open corner-wall flame spread tests: Image (a) shows Sample A, Image (b) shows Sample B, Image (c) shows Sample C and Image (d) shows Sample D

2.4.4 Burner Exposure Experiments

The next set of experiments conducted in the open corner-wall assembly was intended to characterize the heat flux from the propane gas burner when it produces a 25×10^3 W and 40×10^3 W fire. A 25×10^3 W burner fire was utilized during the open corner-wall flame spread experiments, and a 40×10^3 W burner fire was utilized during the room corner tests. Figure 23 provides a detailed image of the test setup. During these tests, the walls were only composed of gypsum wallboard. The heat flux gauges were arranged at varying heights along the right corner-wall. The heat flux gauges were arranged only on the right wall because it is assumed that the heat transfer from the fire is symmetric with respect to the plane. The heat flux gauges were spaced 0.10 m from the corner based on the preliminary testing. The 40×10^3 W burner fire produces a taller flame height compared to the 25×10^3 W burner fire. Thus, the heat flux gauges were spaced 0.125 m and 0.25 m apart during the 25×10^3 W and 40×10^3 W tests, respectively. Highly resolved measurements of the vertical flame heat flux distribution were obtained due to the selected vertical spatial distribution of the heat flux gauges.

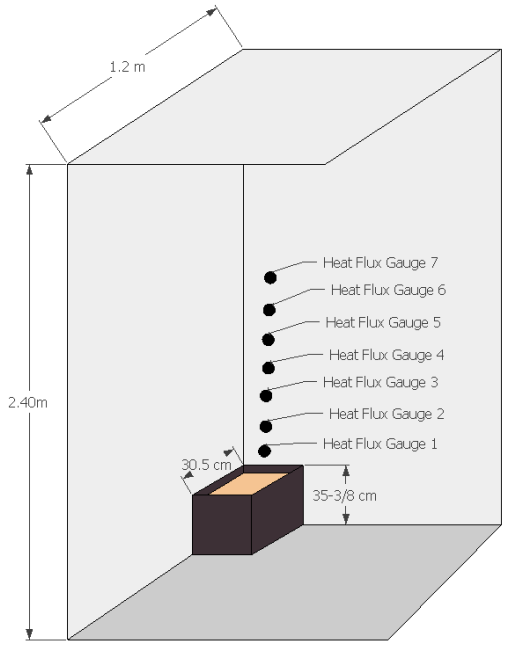

Figure 23. Corner-Wall 25 kW Propane Burner Tests Set-up

Prior to testing, the paper face of the gypsum wallboard was removed. If this was not done, the paper face of the gypsum wallboard would burn and therefore increase the fire size, flame length, which would affect the heat flux distribution. Three experiments were then conducted where the burner produced a 25×10^3 W fire for 420 s. Three more experiments were then conducted where the propane burner produced a 40×10^3 W fire.

2.4.5 Room Corner Tests

The standard room corner test was constructed under the 4 MW Hood at the ATF Fire Research Laboratory according to [7][8][10]. The compartment was built of wood framing with the following dimensions: 2.4 m × 3.6 m × 2.4 m. The doorway was 0.8 m × 2.0 m. Gypsum wallboard was installed along the walls and ceiling. The MDF samples were stapled to the gypsum along all the walls, except for the front wall where the door was located. The same square propane burner that was used during the open corner-wall tests, was also used during the room corner tests. This burner had the same

dimensions and utilized CP grade propane as the fuel. It was located in the far right corner of the compartment, flush against the corner-walls. 17 Schmidt-Boetler Heat Flux Transducers were utilized during each test. All of which had water circulating through them at 313 K. One 50×10^3 W m^{-2} capacity heat flux gauge was installed at the floor, according to the standard. The other gauges were installed along the corner-walls where the propane burner was located, flush with the sample surface. These heat flux gauges were embedded in both corner-walls at varying heights and distances from the corner. Table 2 provides the exact location of each heat flux gauge. These heat flux gauges are numbered from 1 to 17, starting with the gauge located closest to the burner along the right corner-wall. The heat flux gauges were arranged in this pattern to capture the vertical and horizontal heat flux distribution from the propane burner exposure and the corner-wall fire. The 4 MW Hood has the ability to measure compartment HRR with a combined standard uncertainty of 42 %, 4.6 % and 2.6 % at 50×10^3 W, 500×10^3 W and 1100×10^3 W, respectively [57]. A diagram of the room corner test is shown in Figure 24.

Table 2: Heat Flux Gauge Location during the Room Corner Tests

HF Gauge No.	Location	Height Above Burner [m]	Distance from Corner [m]	Capacity [W m^{-2}]
1	Right Wall	0.196	0.15	100×10^3
2	Right Wall	0.446	0.075	100×10^3
3	Right Wall	0.446	0.50	50×10^3
4	Right Wall	0.696	0.30	100×10^3
5	Right Wall	0.946	0.225	100×10^3
6	Right Wall	1.196	0.15	150×10^3
7	Right Wall	1.446	0.075	150×10^3
8	Right Wall	1.946	0.225	150×10^3
9	Left Wall	0.446	0.225	100×10^3
10	Left Wall	0.696	0.15	100×10^3
11	Left Wall	0.946	0.075	100×10^3
12	Left Wall	0.946	0.70	50×10^3
13	Left Wall	1.196	0.30	100×10^3
14	Left Wall	1.446	0.225	150×10^3
15	Left Wall	1.696	0.15	150×10^3
16	Left Wall	1.946	0.075	150×10^3
17	Floor	-	-	50×10^3

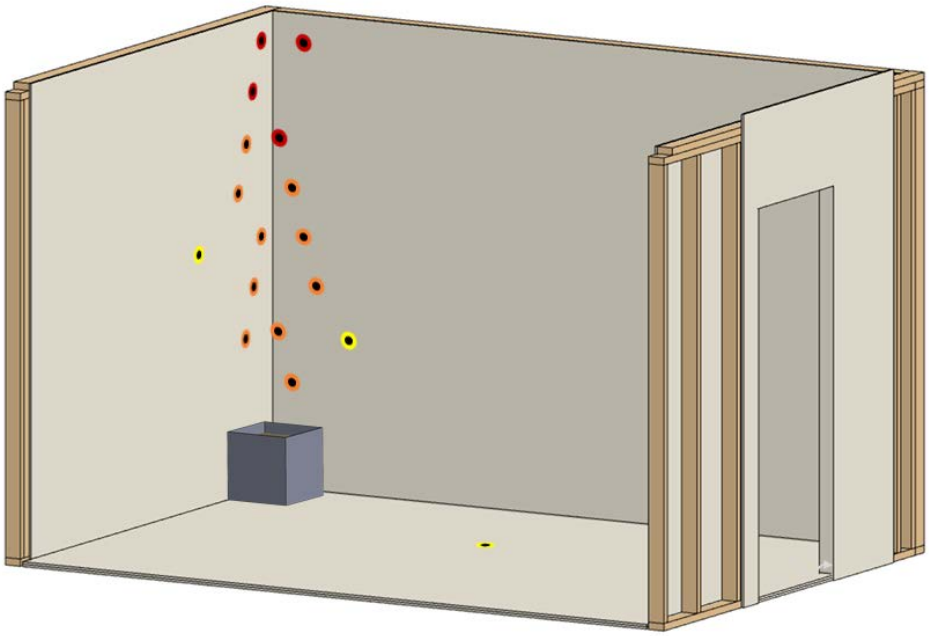

Figure 24. Diagram of the room corner test. Colored colors represent the location of the heat flux gauges. The red circles, orange circles and yellow circles represent 150 kW m^{-2}, 100 kW m^{-2} and 50 kW m^{-2} capacity heat flux gauges, respectively. The propane burner is located on the floor in the corner of the compartment, flush with the walls.

The room corner tests conducted in this project follow all the standard requirements, except for the burner duration. The burner duration is based on preliminary testing of each sample in the open-corner wall assembly, where the minimum duration needed to ensure ignition of all the samples was determined.

There were two tests conducted for each sample. Sample C was the only material where only one test was conducted. An exterior photo of the room corner test is provided in Figure 25. Interior pre-test photos of the room corner test is provided in Figure 26a, Figure 26b, Figure 26c and Figure 26d for each sample, respectively.

Figure 25. Room corner test conducted at the ATF Fire Research Laboratory

(a) Sample A

(b) Sample B

(c) Sample C

(d) Sample D

Figure 26. Pre-test photos of the interior in the room corner test. Image (a) provides a photo of Sample A, image (b) provides a photo of Sample B, image (c) provides a photo of Sample C and image (d) provides a photo of Sample D.

2.5 ThermaKin2D

The pyrolysis model, ThermaKin2D, was utilized in this project to obtain the chemical, thermal and optical material properties of the four samples and to predict full-scale flame spread in the corner of a room. ThermaKin2D is a flexible numerical solver that was designed to simulate the gaseous fuel production from a pyrolyzing material subjected to heat [58]. ThermaKin2D is able to simulate one-dimensional and two-dimensional pyrolysis by solving a series of mass and energy conservation equations, while conservation of momentum is introduced implicitly. In ThermaKin2D, materials are represented by components and each component is characterized by physical and

chemical properties. Each component must be specified as either a solid, liquid or a gas. These components undergo chemical reactions, which may occur in series or in parallel. Physical structures simulated in ThermaKin2D are defined by an initial temperature and material composition. The key governing equations are summarized as follows:

$$\frac{\partial \xi_j}{\partial t} = \sum_{i=1}^{Nr} \theta_i^j r_i - \frac{\partial J_j^x}{\partial x} - \frac{\partial J_j^y}{\partial y} + \frac{\partial}{\partial x}\left(\xi_j \int_0^x \frac{1}{\rho}\frac{\partial \rho}{\partial t} dx\right) \quad (9)$$

$$r_i = A_i \exp\left(-\frac{E_i}{RT}\right) \xi_k \xi_l \quad (10)$$

$$J_g^x = -\rho_g \lambda \frac{\partial(\xi_g/\rho_g)}{\partial x} \quad (11)$$

$$\sum_{j=1}^{N} \xi_j c_j \frac{\partial T}{\partial t} = \sum_{i=1}^{Nr} h_i r_i - \frac{\partial q_x}{\partial x} - \frac{\partial q_y}{\partial y} - \frac{\partial I_{ex}}{\partial x} + \frac{\partial I_{rr}}{\partial x} - \sum_{g=1}^{Ng} c_g \left(J_g^x \frac{\partial T}{\partial x} + J_g^y \frac{\partial T}{\partial y_j}\right) + c\rho \frac{\partial T}{\partial x} \int_0^x \frac{1}{\rho}\frac{\partial \rho}{\partial t} dx \quad (12)$$

$$q_x = -k \frac{\partial T}{\partial x} \quad (13)$$

$$\frac{\partial I_{ex}}{\partial x} = -I_{ex} \sum_{j=1}^{N} \alpha_j \xi_j \quad (14)$$

$$\frac{\partial I_{rr}}{\partial x} = \frac{\varepsilon \sigma T^4}{I_{ex}^0} - \frac{\partial I_{ex}}{\partial x} \quad (15)$$

The mass conservation statement is expressed for component j in Equation 9. ξ_j is the concentration of the component, which is in terms of mass per unit volume. The mass conservation statement accounts for all the chemical reactions that produce or consume component j. The first term on the right-hand-side is the reaction rate equation, Equation 10, the second and third term on the right-hand-side account for the mass flux of gas through the solid, Equation 11 and the fourth term represents the mass transfer

associated with expansion or contraction of the solid. The conservation of energy statement is provided Equation 12. The first term on the right-hand-side of Equation 12 accounts for the heat produced during each chemical reaction. The second and third term on the right-hand-side of the Equation 12 accounts for the conductive heat transfer through the solid object, which is determine in Equation 13. The fourth term on the right-hand-side of Equation 12 represents the radiative heat transfer from an external source, which is determined in Equation 14. The fifth term accounts for the re-radiative heat transfer from the material and this is determined in Equation 15. The sixth and seventh term in Equation 12 represent convective heat flow and the expansion and contraction of the solid material, respectively.

The symbols in the ThermaKin2D governing equations are defined as follows: *t* is the time, θ is the stoichiometric coefficient, ρ is the density, c is the heat capacity, h is the heat of reaction, A and E are the Arrhenius parameters: pre-exponential factor and activation energy, respectively, R is the universal gas constant, λ is the gas transfer coefficient, k is the thermal conductivity, α is the absorption coefficient of radiation, ε is the emissivity, σ is the Stefan-Boltzmann constant, and I_{ex}^{0} is the external radiation. x and y are the Cartesian coordinates. When h is positive, the reaction is exothermic. The density of the mixture is defined as one divided by the sum of the component mass fractions. The ThermaKin2D Technical Report provides a more detailed explanation of the governing equations, as well as the model verification and validation [58].

3. Experimental Results & Discussion

3.1 MCC

The HRR of each sample was recorded as function of the time and temperature and then scaled by the initial sample mass: HRR/m_0. The raw data from the five experiments were averaged together for each sample. The average test results for Sample A, Sample B, Sample C and Sample D are shown Figure 27a, Figure 27, Figure 27c and Figure 27d, respectively.

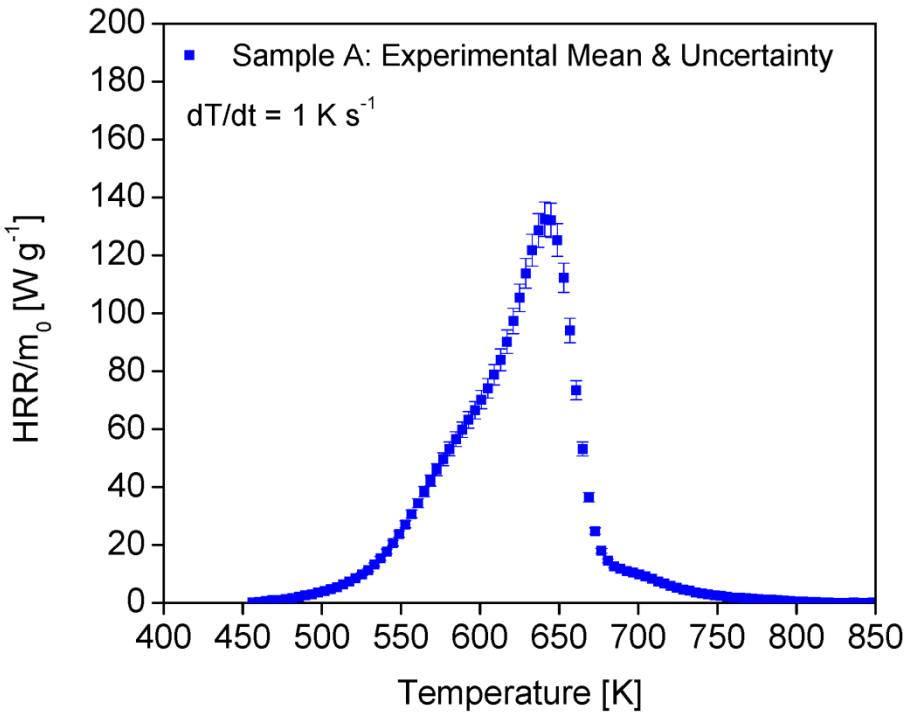

(a)

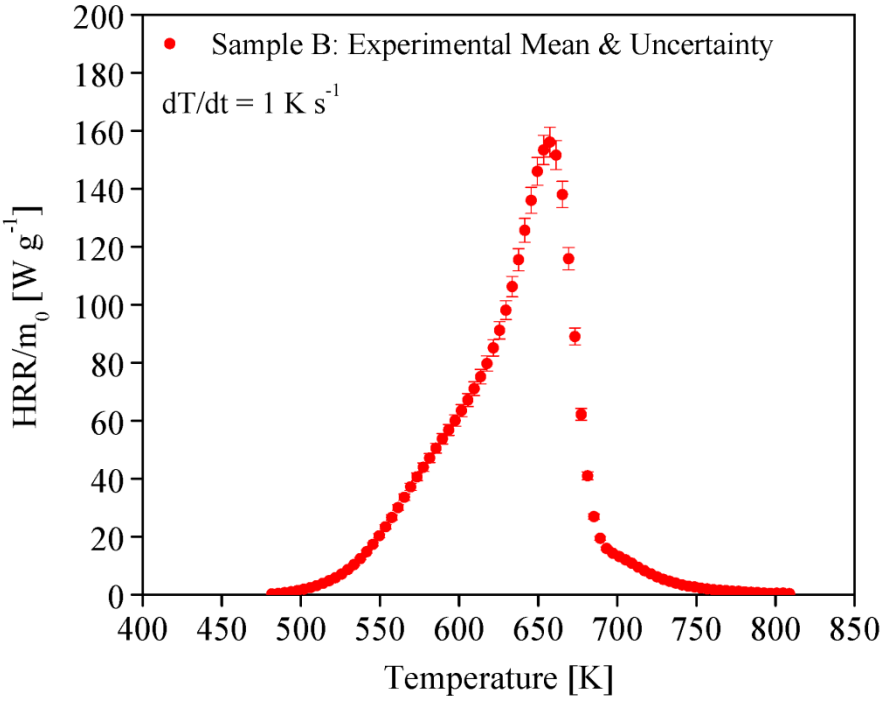
Sample B: Experimental Mean & Uncertainty
dT/dt = 1 K s-1
HRR/m0 [W g-1]
Temperature [K]
0
20
40
60
80
100
120
140
160
180
200
400
450
500
550
600
650
700
750
800
850

(b)

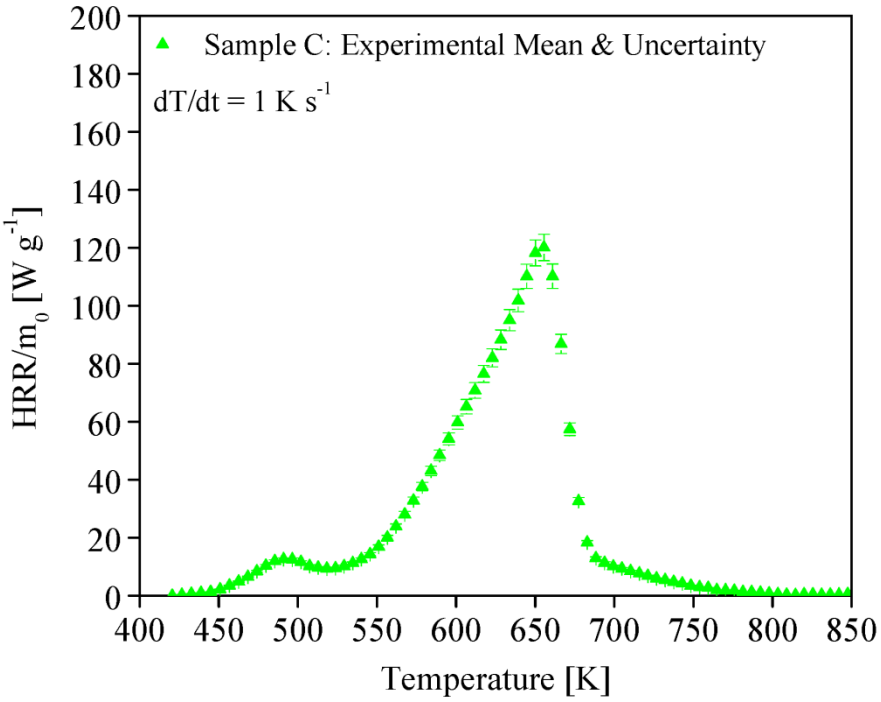
Sample C: Experimental Mean & Uncertainty
dT/dt = 1 K s-1
HRR/m0 [W g-1]
Temperature [K]
0
20
40
60
80
100
120
140
160
180
200
400
450
500
550
600
650
700
750
800
850

(c)

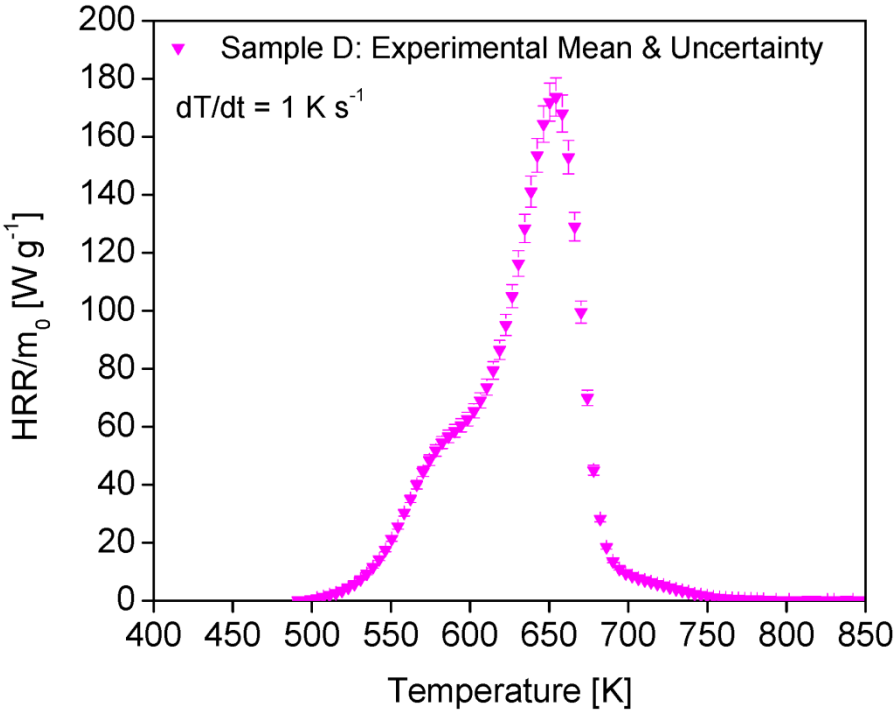

(d)

Figure 27. MCC experimental results - HRR/m_0 versus temperature for the five tests and the average of the five tests. Graph (a), graph (b), graph (c) and graph (d) provides average results from the tests of Sample A, Sample B, Sample C and Sample D, respectively.

The uncertainty calculated here are two standard deviations of the mean experimental values. The uncertainty in the average HRR/m_0 results are 4.5, 3.3, 3.8 and 3.8 for Sample A, Sample B, Sample C and Sample D, respectively.

The char yield was determined by dividing the char mass by the initial specimen mass. The total heat released was calculated to be the integral of the HRR curve from temperature of initial decomposition to the temperature of extinction and it was normalized by the initial mass. Equation 16 is used to determine the heat of complete combustion of the gaseous volatiles or effective heat of combustion (ΔH_{eff}). In Equation 16, the ΔH_{eff} is found by renormalizing the total heat released (THR) based on the initial

sample mass ($m_{initial}$) and the mass of gaseous volatiles produced during pyrolysis ($m_{volatiles}$).

$$\Delta H_{eff} = THR * \left(\frac{m_{initial}}{m_{volatiles}}\right) \quad (16)$$

Table 3 provides each sample's peak HRR/m_0, temperature of decomposition (T_{dec}), temperature when the peak HRR/m_0 occurs (T_{max}), THR, ΔH_{eff} and the char yield. All of the values reported in Table 3 are the average of the five experiments.

Table 3: Average MCC experimental results for Sample A, Sample B, Sample C and Sample D

Sample	Peak HRR/m_0 [W kg^{-1}]	T_{dec} [K]	T_{max} [K]	THR [J kg^{-1}]	ΔH_{eff} [J kg^{-1}]	Char Yield [%]
A	133.2×10^3	450	642	10.6×10^6	$12.8\times10^6 \pm 1.2$	17.5 ± 3.1
B	156.2×10^3	473	657	11.9×10^6	$13.9\times10^6 \pm 0.8$	14.4 ± 6.3
C	118.9×10^3	414	653	10.4×10^6	$12.6\times10^6 \pm 1.2$	17.6 ± 0.4
D	174.1×10^3	485	654	12.4×10^6	$14.1\times10^6 \pm 0.7$	11.6 ± 2.4

Sample C possessed the lowest decomposition temperature of 414 K, followed by Sample A at 450 K. Sample B had the second highest decomposition temperature at 473 K and Sample D had the highest decomposition temperature at 485 K. In that same order, Sample D produced the highest peak HRR/m_0 at 174.1×10^3 W kg^{-1}, followed by Sample B with the second highest peak HRR/m_0 at 156.2×10^3 W kg^{-1}. Sample A had the second lowest peak HRR/m_0 at 133.2×10^3 W kg^{-1} and Sample C had the lowest peak HRR/m_0 at 118.9×10^3 W kg^{-1}. Both Sample A and Sample C produce the highest percentage of char residue at 17.5 % and 17.6 %, respectively. While Sample B produces 14.6 % char and Sample D produce 11.6 % char. Each sample produced similar solid char that was porous and brittle. Figure 28 provides a general example of the char produced by these samples.

Figure 28. Char product post MCC experiment

Figure 29 compares the average HRR/m_0 for each sample as a function of the temperature. This graph demonstrates that both Sample A and Sample C begin decomposing prior to the Sample B and Sample D. While Sample B and Sample D produce the highest HRR/m_0 value.

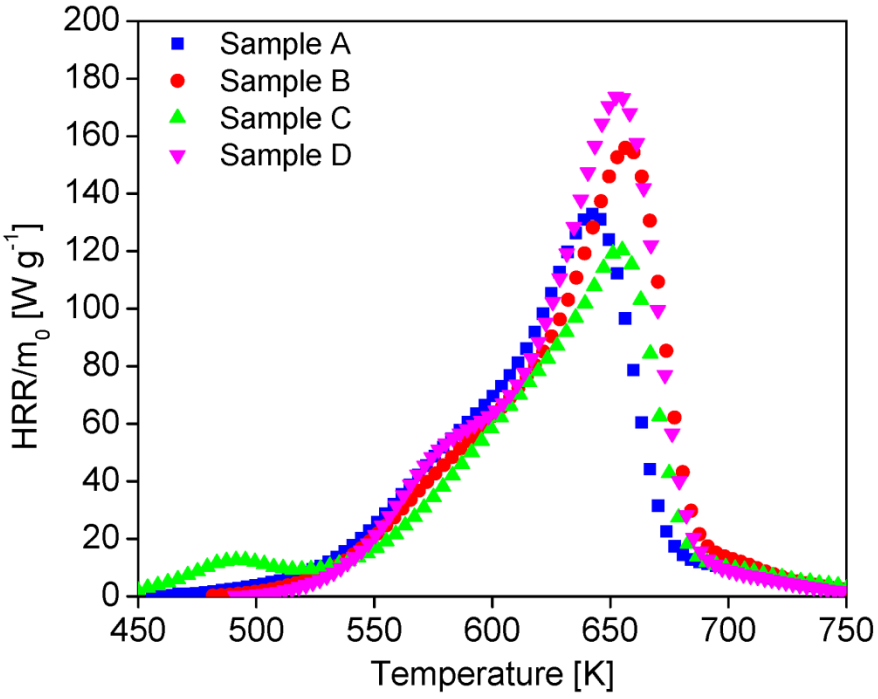

Figure 29. Average MCC experimental results for each sample - HRR/m_0 versus temperature

3.2 Cone Calorimeter

3.2.1 HRR and Effective Heat of Combustion

The HRR is calculated using Equation 8 and it is then divided by the area of the sample to determine the HRRPUA. The effective heat of combustion was calculated for each test based on Equation 9. The total heat released by the burning sample was divided by the total mass lost. This calculation was performed from ignition to the moment when flaming combustion becomes unstable. Smoldering combustion typically occurred once the flames transitioned to being unstable. At the end of this section, the mean ΔH_{eff} for each sample is reported in Table 4 and the uncertainty is two standard deviations of the mean.

The Sample A HRRPUA results from the cone calorimeter experiments performed at an incident heat flux of 20×10^3 W m^{-2}, 50×10^3 W m^{-2} and 80×10^3 W m^{-2} are provided in Figure 30a, Figure 30b, Figure 30c, respectively. Each plot provides the raw HRRPUA from the three tests that were performed at each of the incident heat fluxes. These graphs demonstrate that the time to ignition, the height of the first HRRPUA peak, location of the second HRRPUA peak and time to burnout was repeatable from test to test. Ignition obviously occurs once the HRR begins to rise. The moment when the flame transitions from a steady flame to an unsteady flame is marked on each graph. This provides the period of time when the effective heat of combustion was calculated. The flame becomes unstable at 720 s, 310 s and 229 s for the tests at 20×10^3 W m^{-2}, 50×10^3 W m^{-2} and 80×10^3 W m^{-2}, respectively. The ΔH_{eff} was calculated for each test and then averaged together. The mean ΔH_{eff} for Sample A is 11.27×10^6 J kg^{-1}.

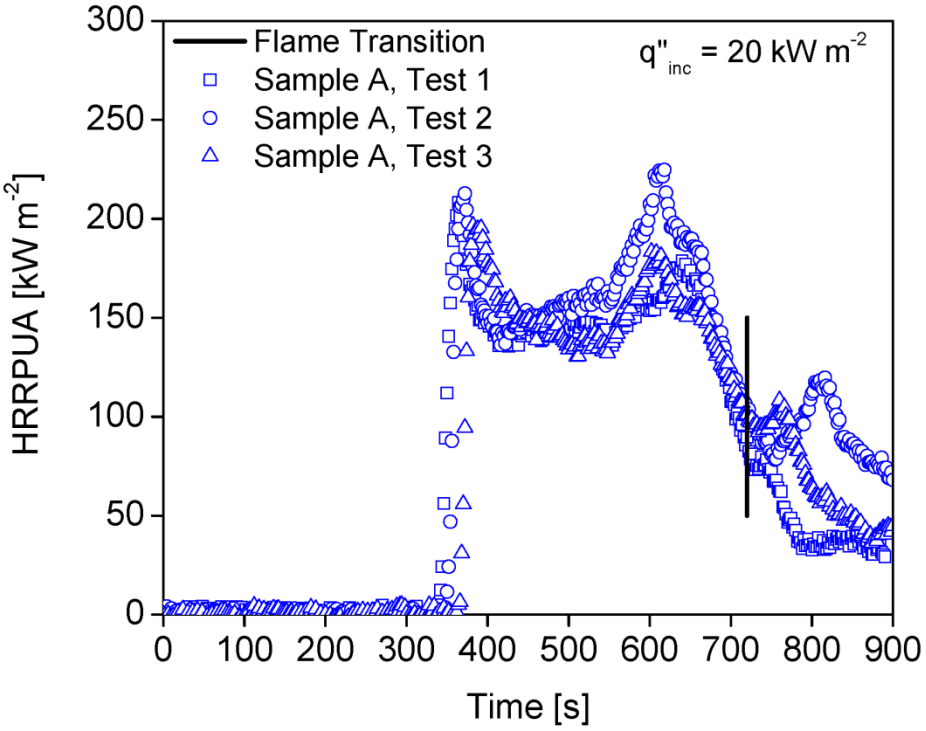
Flame Transition
Sample A, Test 1
Sample A, Test 2
Sample A, Test 3
q"inc = 20 kW m-2
HRRPUA [kW m-2]
Time [s]
0
50
100
150
200
250
300
0
100
200
300
400
500
600
700
800
900

(a)

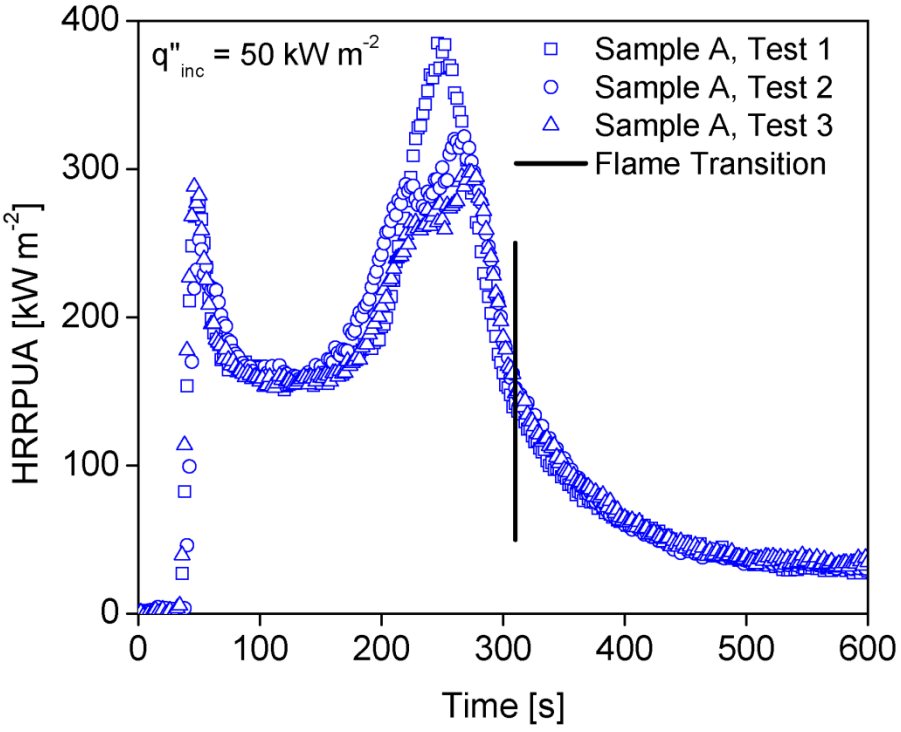
q"inc = 50 kW m-2
Sample A, Test 1
Sample A, Test 2
Sample A, Test 3
Flame Transition
HRRPUA [kW m-2]
Time [s]
0
100
200
300
400
0
100
200
300
400
500
600

(b)

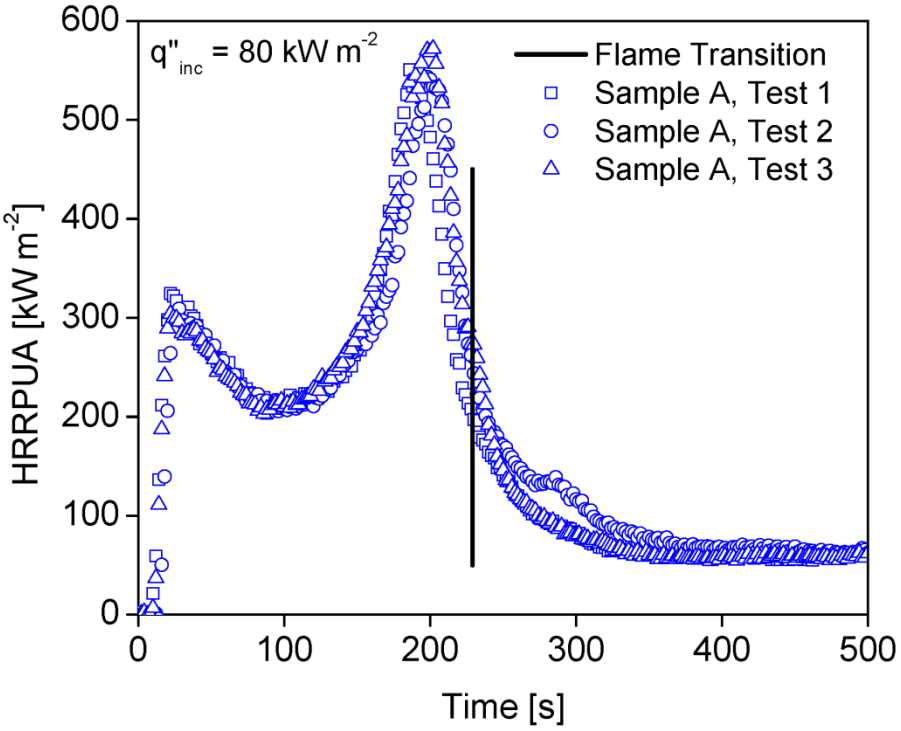

(c)

Figure 30. Cone Calorimeter Results - HRRPUA [kW/m^2] versus time for Sample A. Graph (a), graph (b) and graph (c) provides the raw data from the three tests conducted at 20×10^3 W m^{-2}, 50×10^3 W m^{-2} and 80×10^3 W m^{-2}, respectively

Sample B was also tested under the cone calorimeter at an incident heat flux of 20×10^3 W m^{-2}, 50×10^3 W m^{-2} and 80×10^3 W m^{-2}. The HRRPUA results are provided in Figure 31a, Figure 31b and Figure 31c, respectively. Each plot provides the raw HRR data from the three tests that were performed at each of the incident heat fluxes. The flame becomes unstable at 490 s, 219 s and 173 s for the tests at 20×10^3 W m^{-2}, 50×10^3 W m^{-2} and 80×10^3 W m^{-2}, respectively. The average ΔH_{eff} for Sample B is 11.67×10^6 J kg^{-1}.

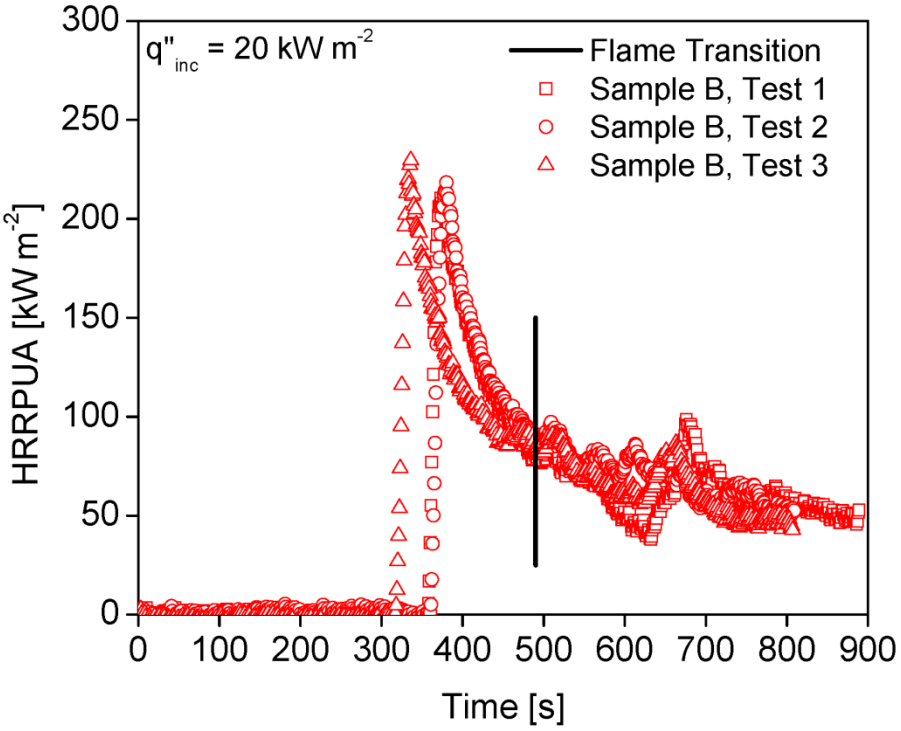
q"inc = 20 kW m-2
Flame Transition
Sample B, Test 1
Sample B, Test 2
Sample B, Test 3
HRRPUA [kW m-2]
Time [s]
0
50
100
150
200
250
300
0
100
200
300
400
500
600
700
800
900

(a)

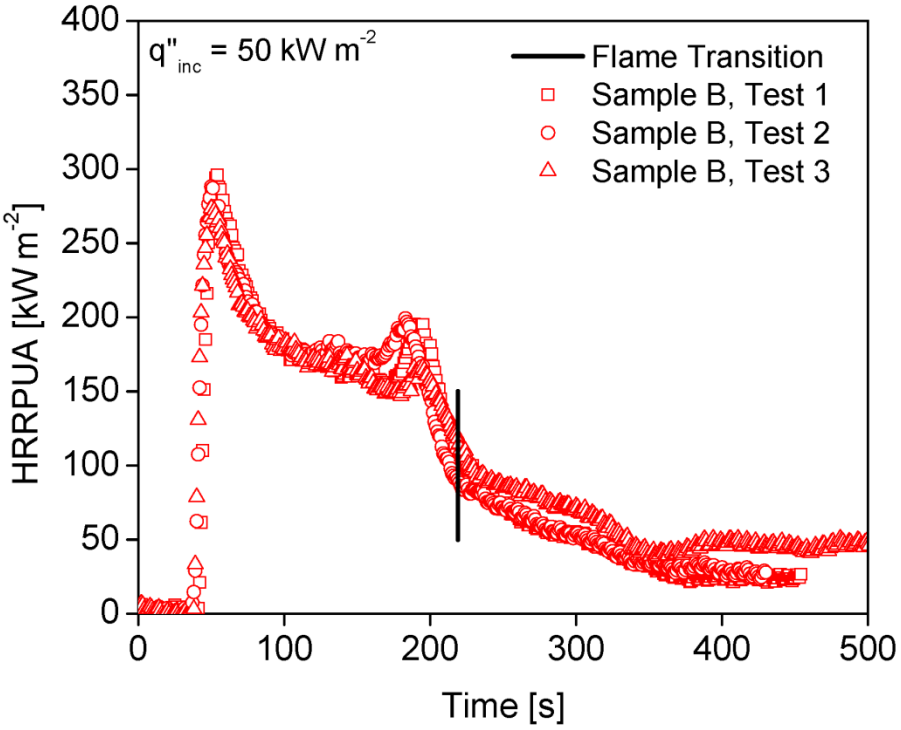
q"inc = 50 kW m-2
Flame Transition
Sample B, Test 1
Sample B, Test 2
Sample B, Test 3
HRRPUA [kW m-2]
Time [s]
0
50
100
150
200
250
300
350
400
0
100
200
300
400
500

(b)

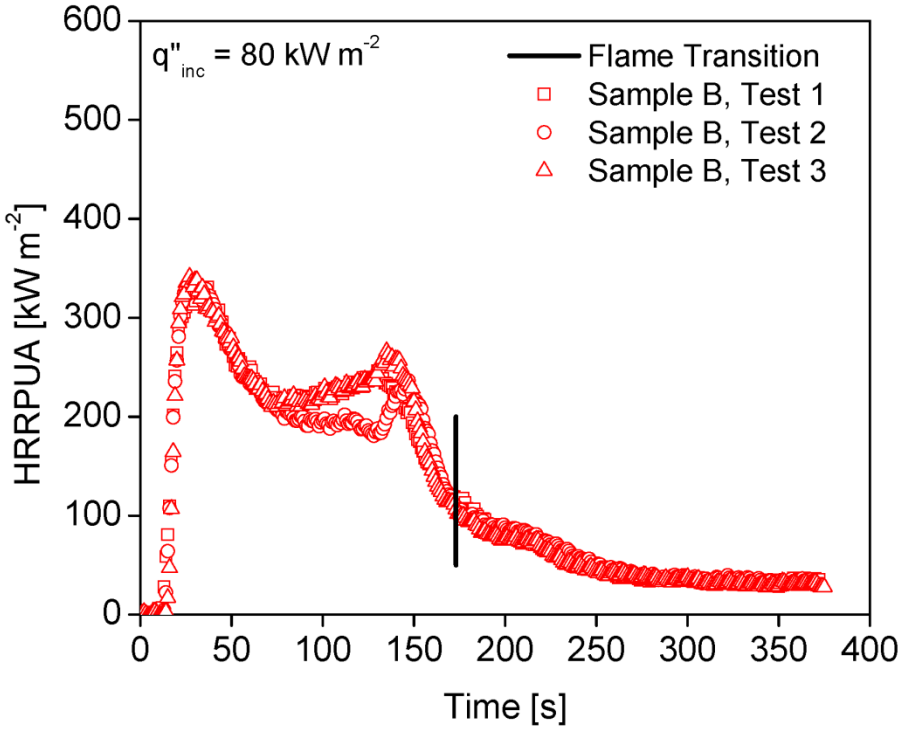

(c)

Figure 31. Cone Calorimeter Results - HRRPUA [kW/m^2] versus time for Sample B. Graph (a), graph (b) and graph (c) provides the raw data from the three tests conducted at 20×10^3 W m^{-2}, 50×10^3 W m^{-2} and 80×10^3 W m^{-2}, respectively

Sample C did not ignite at 20×10^3 W m^{-2}. Thus, it was tested under the cone calorimeter at the following incident heat flux conditions: 25×10^3 W m^{-2}, 50×10^3 W m^{-2} and 80×10^3 W m^{-2}. The HRRPUA results are provided in Figure 32a, Figure 32b and Figure 32c, respectively. Each plot provides the raw HRR data from the three tests, along with the moments when the flame becomes unstable. The flame becomes unstable at 311 s, 171 s and 145 s for the tests at 25×10^3 W m^{-2}, 50×10^3 W m^{-2} and 80×10^3 W m^{-2}, respectively. Sample C has an average ΔH_{eff} equal to 10.26×10^6 J kg^{-1}.

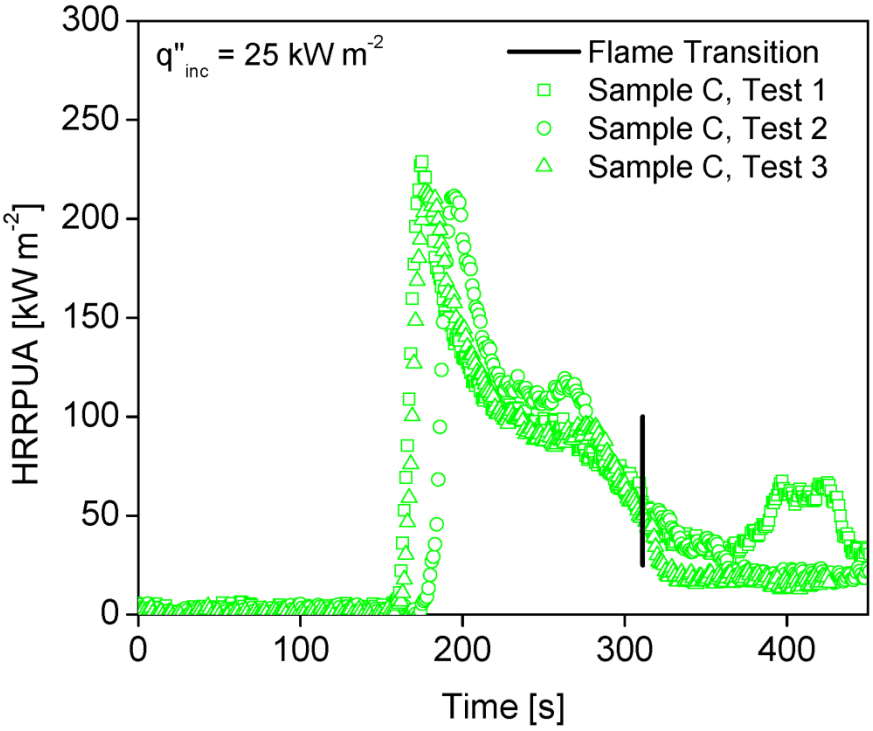
q"inc = 25 kW m-2
Flame Transition
Sample C, Test 1
Sample C, Test 2
Sample C, Test 3
HRRPUA [kW m-2]
Time [s]
0
50
100
150
200
250
300
0
100
200
300
400

(a)

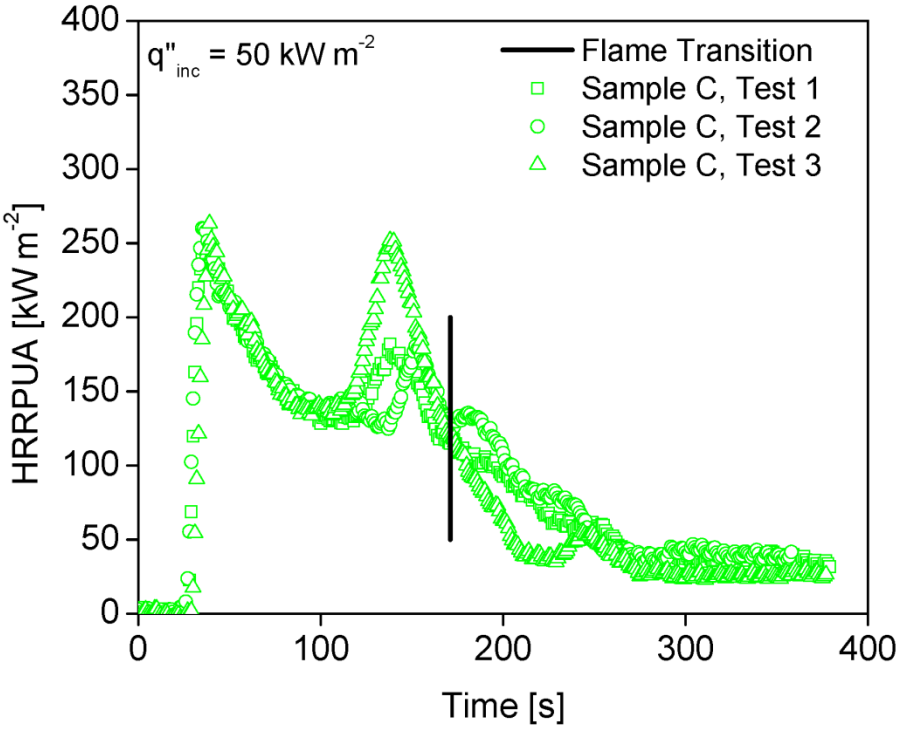
q"inc = 50 kW m-2
Flame Transition
Sample C, Test 1
Sample C, Test 2
Sample C, Test 3
HRRPUA [kW m-2]
Time [s]
0
50
100
150
200
250
300
350
400
0
100
200
300
400

(b)

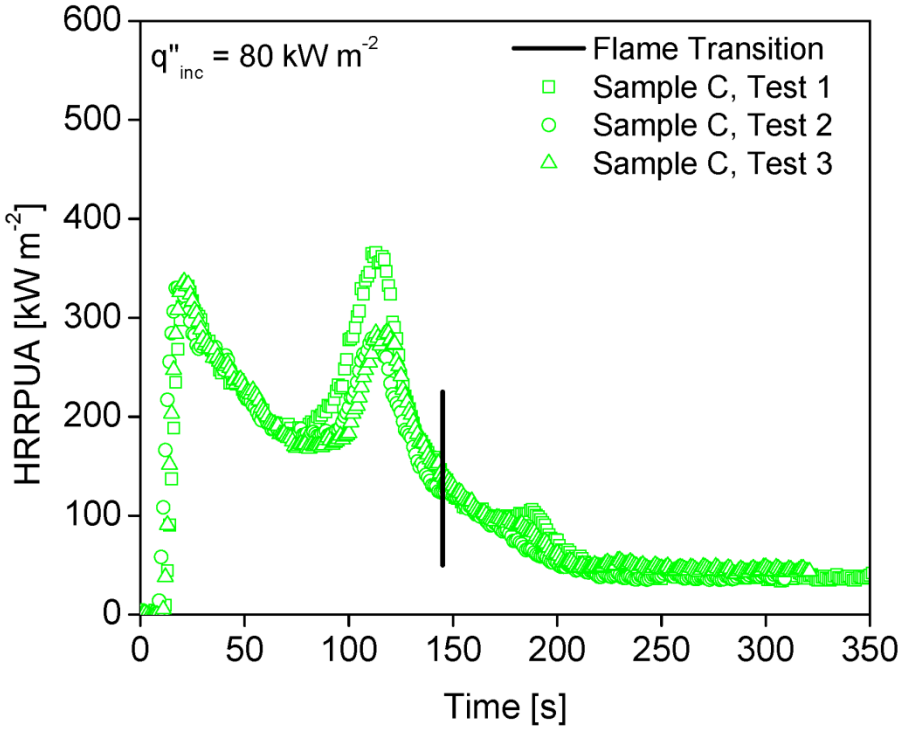

(c)

Figure 32. Cone Calorimeter Results - HRRPUA [kW/m^2] versus time for Sample C. Graph (a), graph (b) and graph (c) provides the raw data from the three tests conducted at 25×10^3 W m^{-2}, 50×10^3 W m^{-2} and 80×10^3 W m^{-2}, respectively

Sample D was tested under the cone calorimeter at an incident heat flux of 20×10^3 W m^{-2}, 50×10^3 W m^{-2} and 80×10^3 W m^{-2} and the HRRPUA results are provided Figure 33a, Figure 33b and Figure 33c, respectively. The raw HRR data is provided on each plot and the moment when the flames become unstable is marked. For Sample D, the flame becomes unstable at 428 s, 193 s and 151 s for the tests at 20×10^3 W m^{-2}, 50×10^3 W m^{-2} and 80×10^3 W m^{-2}, respectively. The average ΔH_{eff} for Sample D is 12.87×10^6 J kg^{-1}.

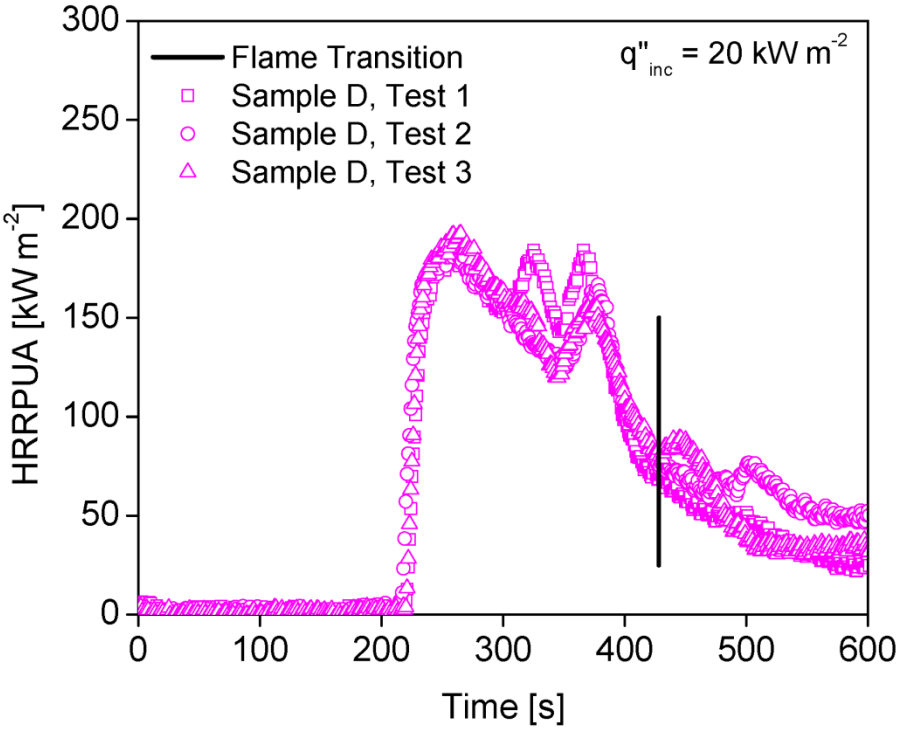
Flame Transition
Sample D, Test 1
Sample D, Test 2
Sample D, Test 3
q"inc = 20 kW m-2
HRRPUA [kW m-2]
Time [s]
0
50
100
150
200
250
300
0
100
200
300
400
500
600

(a)

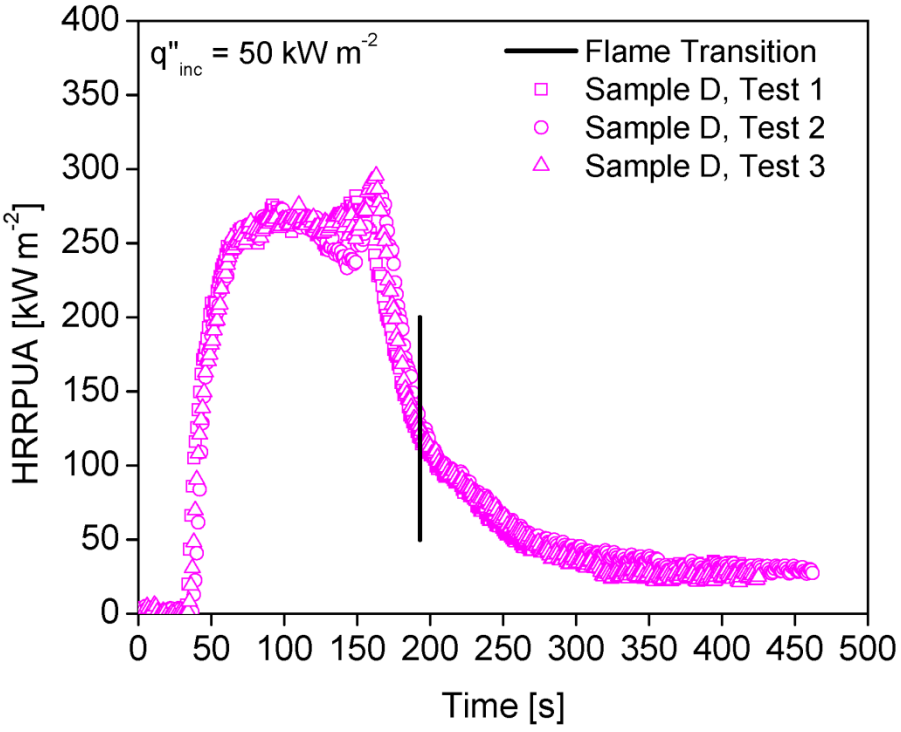
q"inc = 50 kW m-2
Flame Transition
Sample D, Test 1
Sample D, Test 2
Sample D, Test 3
HRRPUA [kW m-2]
Time [s]
0
50
100
150
200
250
300
350
400
0
50
100
150
200
250
300
350
400
450
500

(b)

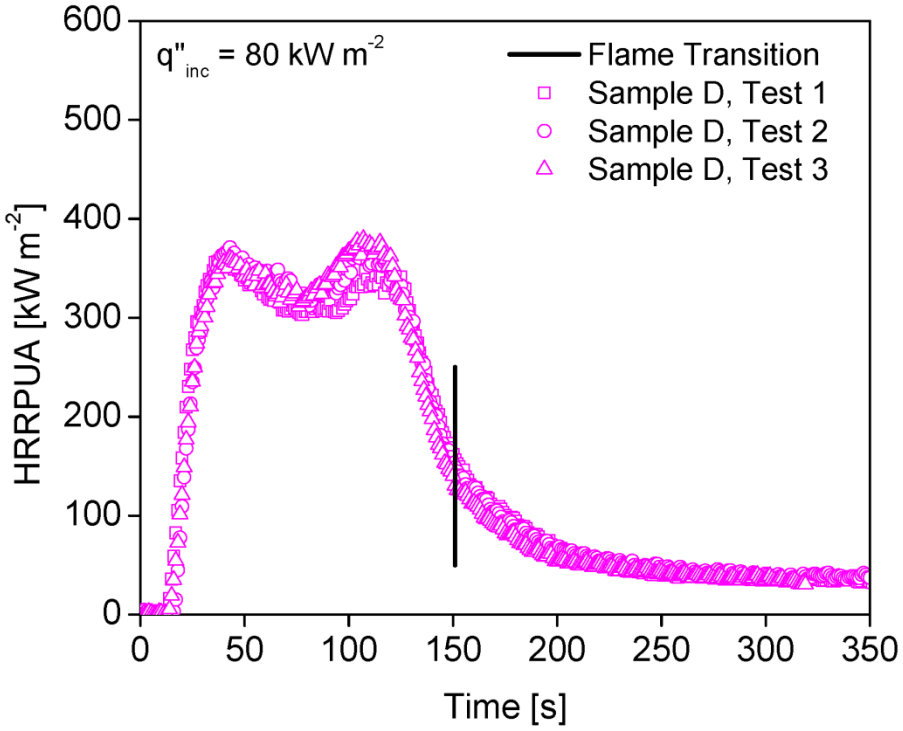

(c)

Figure 33. Cone Calorimeter Results - HRRPUA [kW/m^2] versus time for Sample D. Graph (a), graph (b) and graph (c) provides the raw data from the three tests conducted at 20×10^3 W m^{-2}, 50×10^3 W m^{-2} and 80×10^3 W m^{-2}, respectively

Table 4: Average Effective Heat of Combustion for each Sample based on Cone Calorimeter Testing

Sample Name	ΔH_{eff} [J kg^{-1}]
Sample A	$11.27\times10^6 \pm 2.5\times10^6$
Sample B	$11.67\times10^6 \pm 3.1\times10^6$
Sample C	$10.26\times10^6 \pm 9.0\times10^6$
Sample D	$12.87\times10^6 \pm 3.3\times10^6$

3.2.2 Char Density

After the experiment, once the sample holder was cool, the edge frame was removed and the charred specimen was weighed and analyzed. Figure 34 provides two images of the char produced during pyrolysis of Sample A in the cone calorimeter experiment. The first image shows the char while it rests on top of the gypsum, while the second image shows the char once it has been separated from the gypsum wallboard.

Unfortunately, the char density of Sample A was very difficult to analyze because the char possessed no solid structure. It was extremely porous, brittle and soft. Therefore, the char density of Sample A was approximated separately by performing a constant volume analysis, which is discussed in Section 4.2.2.

(a) (b)

Figure 34. Sample A char formation. The char remains on the gypsum wallboard in image (a), while the char has been separated from the gypsum wallboard in image (b)

Images of the Sample B char are provided in Figure 35. During pyrolysis, Sample B produces a char that was soft and brittle, much like the char produced by decomposition of Sample A. The Sample B char is also thin and it had the tendency to flake. Sample B's char density was difficult to measure due to the absence of a solid structure. Therefore, the char density of Sample B was also approximated through the constant volume analysis discussed in Section 4.2.2.

Figure 35. Sample B char formation

Unlike Sample A and Sample B, Sample C produces char that possesses a solid structure. Figure 36 provides a top-view and side-view image of the char produced by Sample C. The char density of Sample C was determined by measuring the mass, surface area and thickness of the char. The solid piece of char had a mass of 8.18×10^{-3} kg. The surface area of the char was measured to be 8.70×10^{-3} m^2. A caliper was used to measure the thickness of the char at 13 different locations. The average thickness of the char was 2.46×10^{-3} m. Assuming that the shape of the char can be approximated as a cube, the char volume was found by multiplying the average char thickness by the char surface area. The total char volume was 2.14×10^{-5} m^3. The char mass was divided by the char volume to find the char density. Sample C produced char that had a density of 382.4 kg m^{-3}.

(a) (b)

Figure 36. Sample C char formation. The top-view of the Sample C char is provided in image (a), while the side-view of char is shown in image (b)

Figure 37 provides a top-view image of the Sample D char. During pyrolysis, Sample D produced solid char that had the tendency to split into separate pieces. Each piece of char was carefully removed from the sample holder and the dimensions were recorded. The surface area was determined by representing each piece of char as a rectangle or a triangle. A caliper was used to determine the average thickness along each piece of char. Subsequently, the volume for each piece of char was calculated by multiplying the average thickness by the approximate surface area. This analysis was performed on all five pieces of char and the results are provided in Table 5. The combined total mass of the char was measured to be 5.6×10^{-3} kg. The char density was then calculated by dividing the mass by the volume. The final char density of Sample D is 247.4 kg m^{-3}.

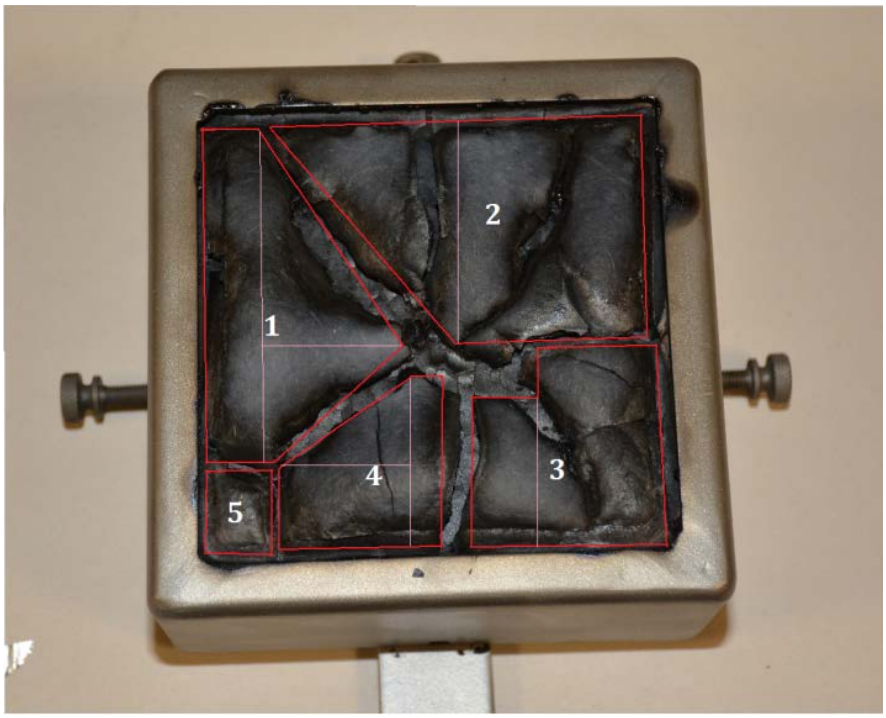

Figure 37. Sample D Char formation from the top-view. This image also includes the shape analysis of the pieces of char.

Table 5: Sample D Shape Analysis

Component Number	Total Area (m^2)	Average Thickness (m)	Total Volume (m^3)
1	29.35×10^{-4}	2.83×10^{-3}	8.307×10^{-6}
2	28.75×10^{-4}	2.34×10^{-3}	6.728×10^{-6}
3	17.40×10^{-4}	2.57×10^{-3}	4.472×10^{-6}
4	8.94×10^{-4}	2.53×10^{-3}	2.257×10^{-6}
5	3.70×10^{-4}	2.36×10^{-3}	0.873×10^{-6}
Total			22.637×10^{-6}

Even though the density of the sample changed during the cone calorimeter experiments, the staple restraining method did a good job of preventing the samples from swelling. There was a tendency for swelling to occur once the sample was removed from the cone calorimeter apparatus and placed under the fume hood to cool.

3.2.3 Flame Heat Flux

Six flame heat flux experiments were conducted in the cone calorimeter. The 35×10^{3} W m^{-2} of heat flux produced by the radiant heater was removed from the heat flux

gauge measurements to determine the flame heat flux. Figure 38a and Figure 38b provide a graphs displaying the flame heat flux when the gauge is positioned at the center and the side, respectively. As shown in Figure 38a, once the heat flux gauge shield was removed, the heat flux takes a few moments to reach a relatively steady state value. The heat flux gauge would maintain a steady state value for 12 s to 15 s. After which, a thin layer of condensation would form above the heat flux gauge similar to what is shown in Figure 39.

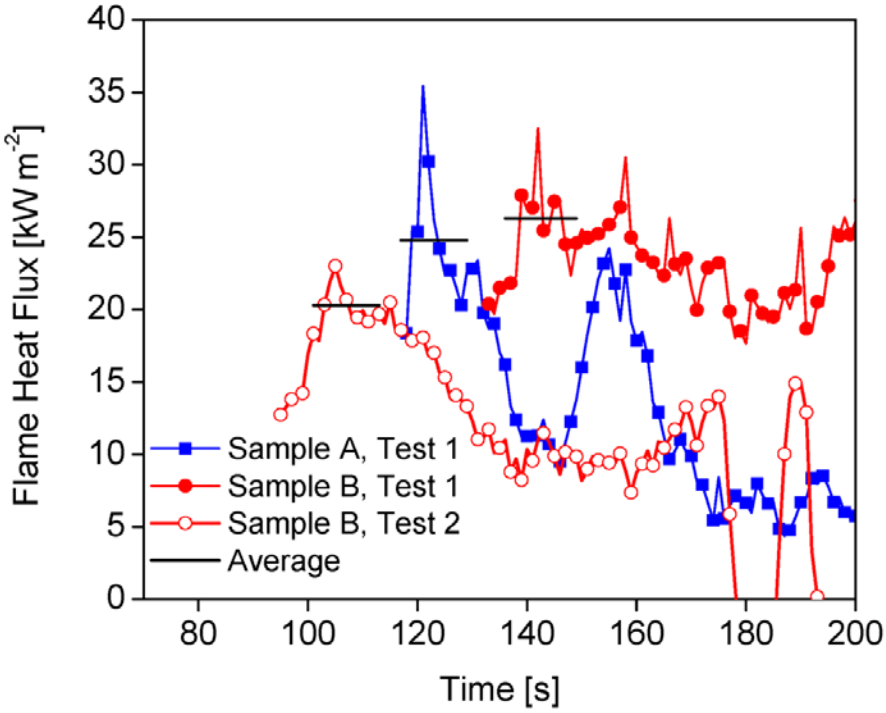

(a) Centered Heat Flux Gauge

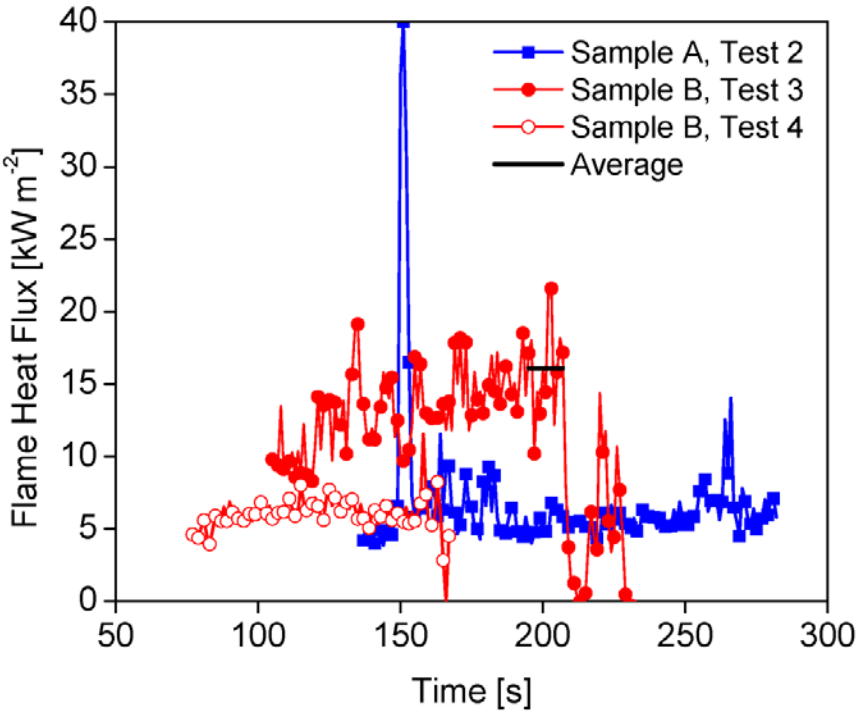

.

(b) Side Heat Flux Gauge

Figure 38. Flame heat flux measurements. Graph (a) shows the flame heat flux measurements when the heat flux gauge is located at the center of the sample and graph (b) displays the flame heat flux when the heat flux gauge is located at the side of the sample

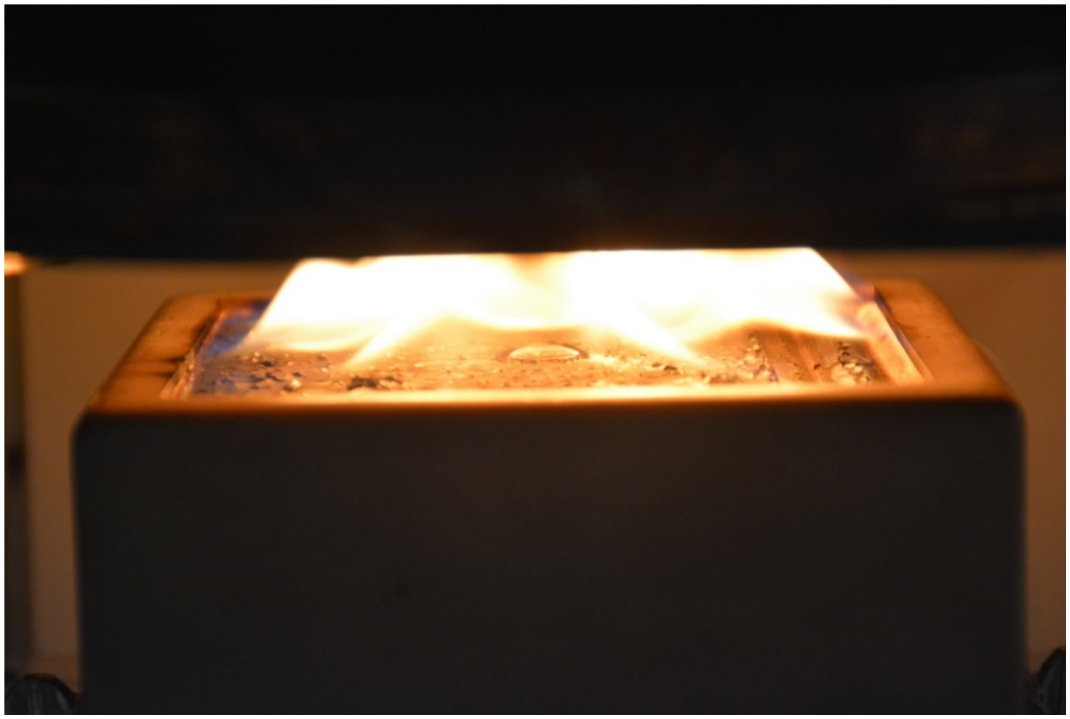

Figure 39. Condensation forming above the heat flux gauge during the flame heat flux experiments

Condensation had a significant effect on the heat flux gauge readings. Condensation formed on top of the heat flux gauge for all the tests except for Test 1 and Test 3 of Sample B. Once condensation forms on the heat flux gauge, the readings began to decrease at a significant rate to least a factor of 2. Therefore, a 12 s average was taken over the period when the gauge readings reached a steady state value. The 12 s average for each test is also displayed on each graph in Figure 38. Of the three experiments where the heat flux gauges were located at the side, the results from Test 3 of Sample B were the only heat flux gauge readings that are trustworthy. Figure 38b shows that both Sample A, Test 2 and Sample B, Test 4 produced an average heat flux of 5×10^3 W m^{-2}, which is well below the flame heat flux range reported in literature [59] [60]. During these tests, condensation was visible on top of the heat flux gauge immediately upon removal of the shield. The 12 s average was determined at the peak steady state measurements for Sample B, Test 3. The average side heat flux gauge reading from Sample B, Test 3 was 16.1×10^3 W m^{-2}. The average sample-centered heat flux gauge readings from Sample A, Test 1, Sample B, Test 1 and Sample B, Test 2 are 24.8×10^3 W m^{-2}, 26.3×10^3 W m^{-2} and 20.4×10^3 W m^{-2}, respectively. Averaging the three center heat flux gauge measurements together produces an average value of 23.8×10^3 W m^{-2}. Finally, the heat flux from the flame to the surface of the material can be determined by averaging the center and side gauge steady state heat flux measurements. The average flame heat flux is equal to 20.0×10^3 W m^{-2}. This value is consistent with flame heat flux values reported by Beaulieu and Dembsey [59] and Stoliarov et al [61]. Using the Advanced Flammability Measurements Apparatus, Beaulieu and Dembsey obtained flame heat flux values of 20×10^3 W $m^{-2} \pm 3\times10^3$ W m^{-2} for the sooting black PMMA.

Stoliarov et al performed inverse modeling of the cone calorimeter experiments to obtain flame heat flux values between 11×10^3 W m^{-2} to 24×10^3 W m^{-2} for a range of non-charring polymers. The cone calorimeter experiments will be modeled using the one-dimensional ThermaKin2D model. When the material ignites in the cone calorimeter model, the flame is represented as an additional radiant heat flux of 20×10^3 W m^{-2} added to the surface of the sample.

3.3 Open Corner-Wall Tests

3.3.1 Open Corner-wall Flame Spread Tests

The propane burner exposed Sample A to a 25×10^3 W fire for 345 s. After 345 s exposure time, the propane burner was turned off and the flames were allowed to propagate on their own. Throughout the test, the HRR and heat flux at the various heights were measured. The fire eventually spread to and extended along the ceiling. Once the flames protruded above the ceiling, the fire was suppressed and the test ended. After each test, the heat flux gauges were analyzed and they were covered in soot and sometimes residue. They were then cleaned, repainted and reinstalled. Luckily, the heat flux gauge measurements were made during early stages of flame spread. During this time frame, the heat flux gauges were most likely clean and relatively free of deposits. As opposed to the cone calorimeter heat flux gauge measurements, the heat flux data measured during the flame spread test did not seem to be affected by condensation. Its assumed that this is because the heat flux gauges are vertically oriented, and not horizontally oriented.

Figure 40 provides a graph displaying the gauge heat flux at each location and the total HRR as a function of time. The gauge heat flux and total HRR data was smoothed using a 20 s running average to reduce experimental noise. In Figure 40, the scale along the primary vertical axis is in terms of gauge heat flux, while the scale along the secondary vertical axis is in terms of HRR. Time is equal to zero seconds at the start of the test, when the burner was ignited. Small flamelets began emerging from the surface of the sample at 180 s which indicated that the sample had begun to ignite. After ignition, the HRR and flame height began to increase. The propane burner is turned off after 345 s, at which point the fire decreased in size until it reached a steady state value of 30×10^3 W at 381 s. Soon after this, the HRR began to increase and flames continued to spread upward. At 555 s, the fire was spreading along the ceiling. At 705 s, the fire began to protrude beyond the ceiling and the fire was suppressed using a pressurized water can moments later. All of these moments are shown in Figure 41.

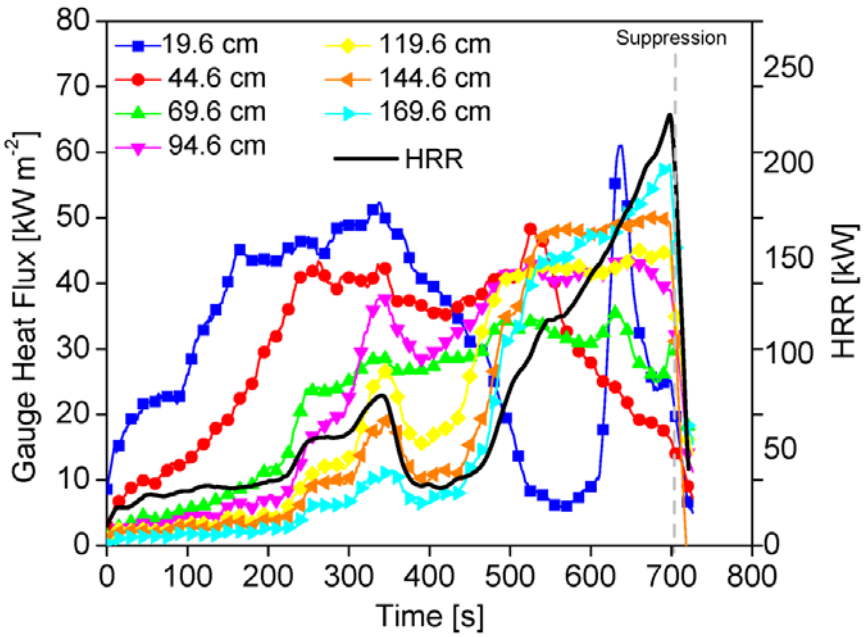

Figure 40. Flame spread experiments - Sample A: heat flux & HRR versus time

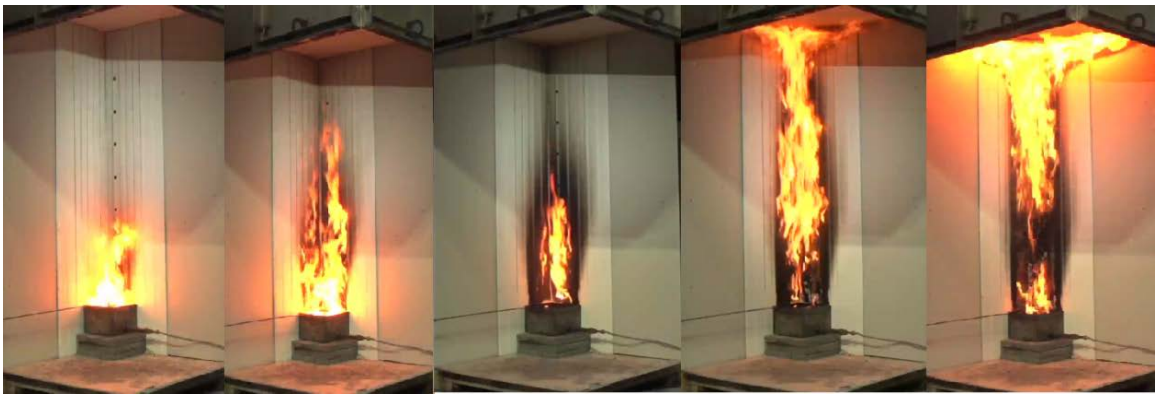

(a) (b) (c) (d) (e)

Figure 41. Sample A - Flame spread experiments. These photos were taken at (a) 180 s, (b) 345 s, (c) 381 s, (d) 555 s and (e) 705 s

The propane burner exposed Sample B to a 25×10^3 W fire for 227 s. Once the propane burner was turned off, the fire was allowed to propagate freely. Figure 42 provides a graph displaying the heat flux at each height, along with the HRR as a function of time. Sample B ignited around 110 s and the HRR began to increase steadily until the propane burner was turned off at 227 s. After the burner was turned off, the fire decreased in size until it steadied out to 28×10^3 W. At 245 s, the HRR and flame height began to increase. The flame spread vertically until the fire reached the ceiling at 347 s. At 533 s, the flames began to extend beyond the ceiling, at which point suppression occured. All of these moments are shown in Figure 43

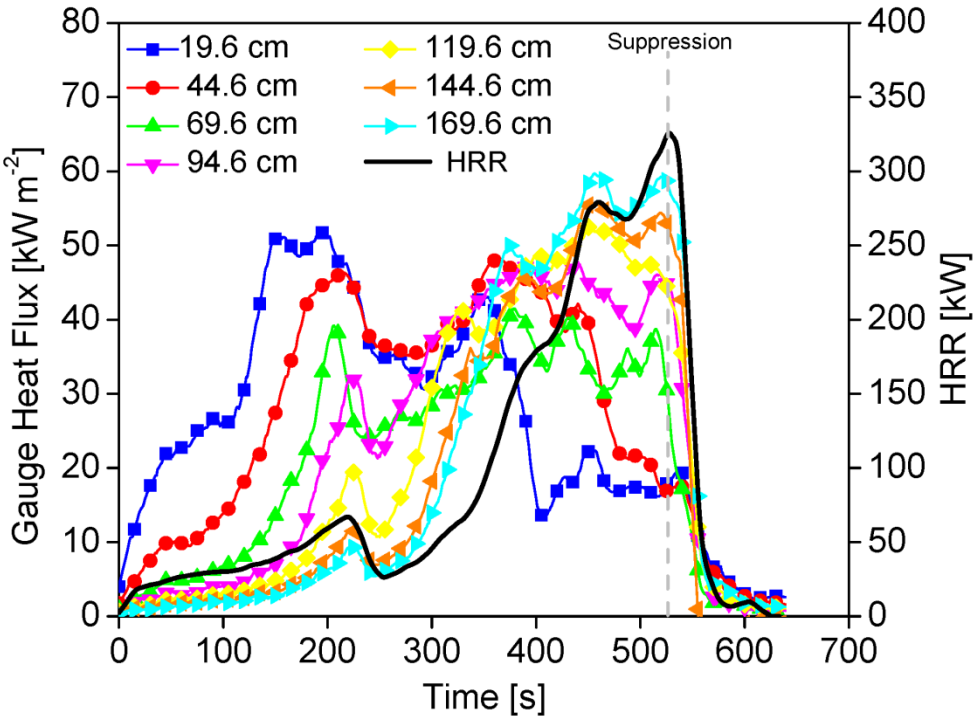

Figure 42. Flame spread experiments - Sample B: heat flux & HRR versus time

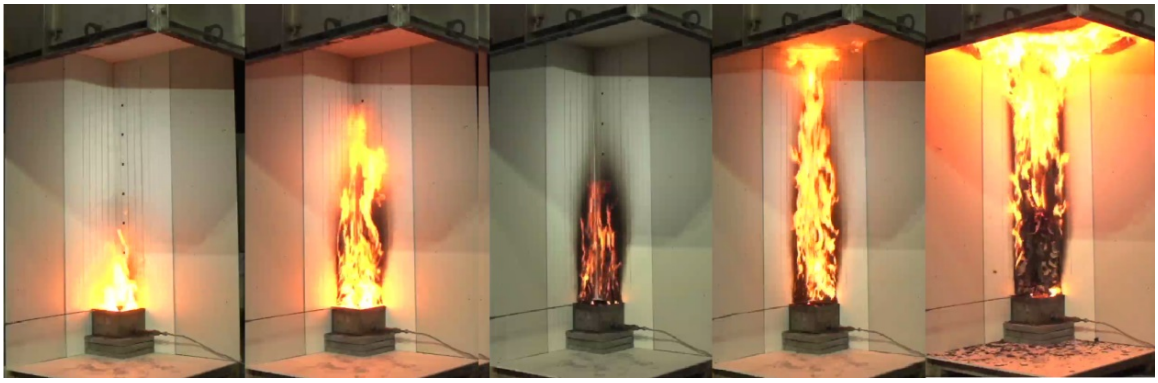

(a) (b) (c) (d) €

Figure 43. Sample B - Flame spread experiments. These photos were taken at (a) 110 s, (b) 227 s, (c) 245 s, (d) 347 s and (e) 533 s

Sample C was exposed to the propane burner fire for 293 s. Figure 44 provides a graph of the heat flux at each height above the burner, along with the corner-wall HRR as a function of time. During the experiment, Sample C ignited at 75 s, which caused both the HRR and the flame height increase in magnitude. The flame height reached the ceiling at 257 s and the burner was turned off at 293 s. After the burner was turned off,

the sample began to self-extinguish. At 306 s, the fire only exists in the corner of the room and burnout has occurred in the surrounding area. At 371, the fire self-extinguished. All these moments are shown in Figure 45.

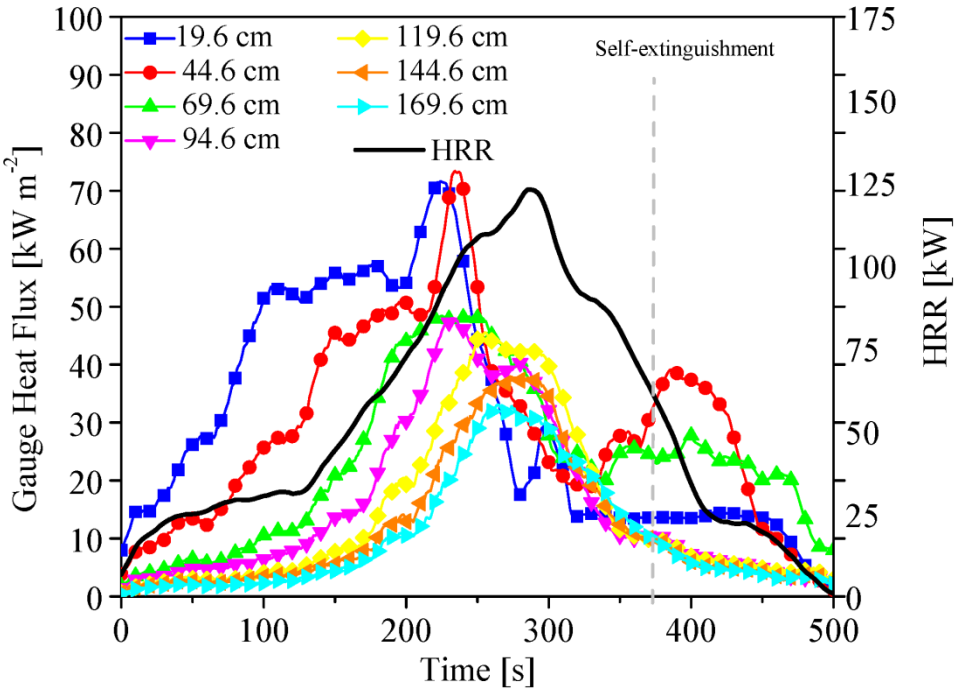

Figure 44. Flame spread experiments - Sample C: heat flux & HRR versus time

(a) (b) (c) (d) (e)

Figure 45. Sample C - Flame spread experiments. These photos were taken at (a) 75 s, (b) 257 s, (c) 293 s, (d) 306 s and (e) 371 s

The propane burner produced a 25×10^3 W fire for 250 s during the flame spread test on Sample D. Figure 46 provides the graph of the gauge heat flux measurements and corner-wall HRR versus time. Flamelets began to appear from the surface of Sample D at 110 s. The burner was turned off at 250 s. After the burner was turned off, the fire size decreased slightly prior to it beginning to grow again (272 s). The flames reached the ceiling at 282 s. The fire was extinguished after the flames were extending beyond the ceiling at 375 s. Images of these moments are provided in a sequence on Figure 47.

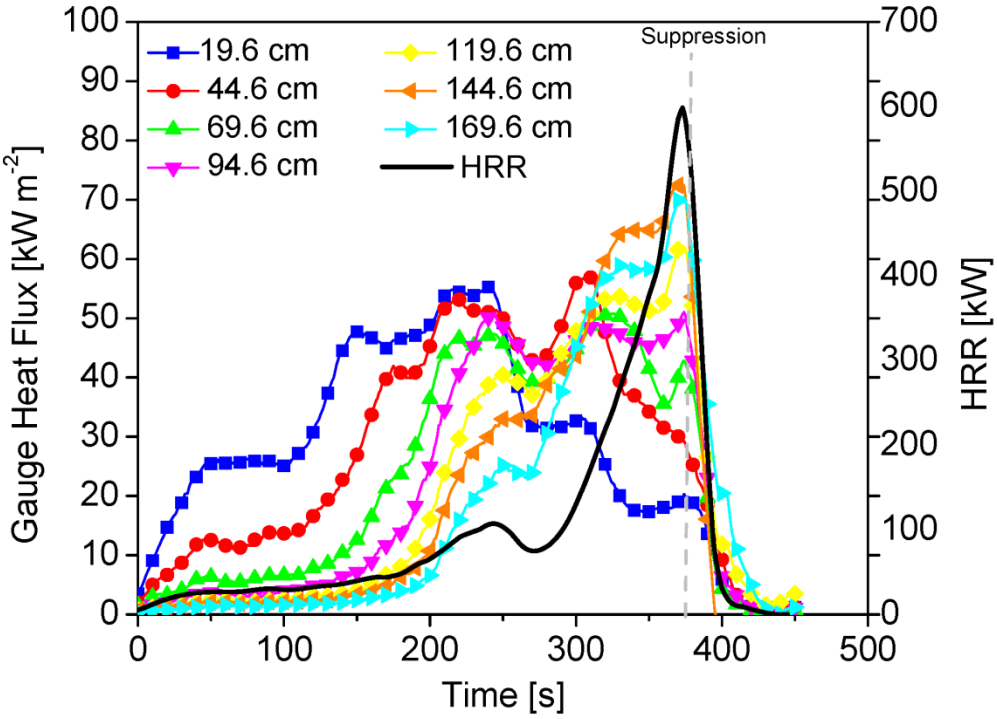

Figure 46. Flame spread experiments - Sample D: heat flux & HRR versus time

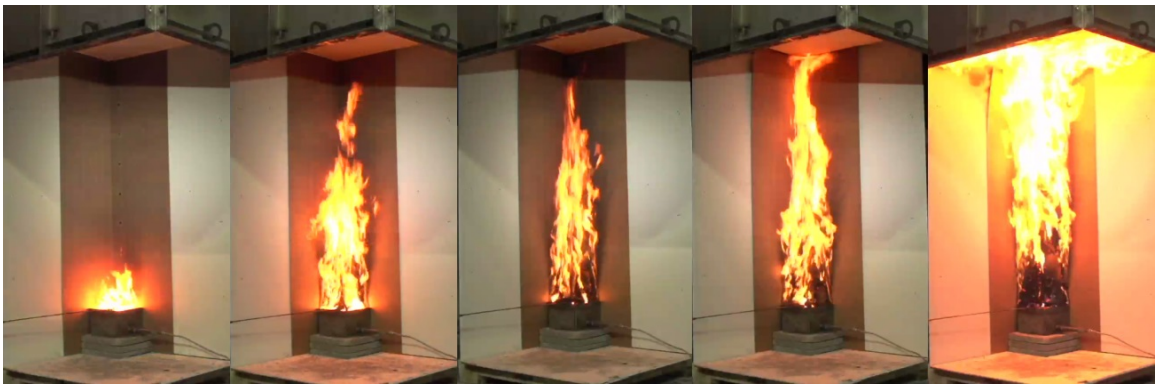

(a) (b) (c) (d) (e)

Figure 47. Sample D - Flame spread experiments. These photos were taken at (a) 110 s, (b) 250 s, (c) 272 s, (d) 282 s and (e) 375 s

The side-view video camera faced only the right wall to record the burning width. Still-frame images from the side-view camera perspective were captured at 5 s intervals. The still-frame images were analyzed visually and the distance from the corner to the edge of the luminous region was determined at various heights along the flame height. The single side burning width is plotted versus time for Sample A, Sample B, Sample C and Sample D in Figure 48. Sample A, Sample B and Sample D all continue burning once the propane burner was removed. During the experiment with Sample C, the fire slowly self-extinguished after the burner was removed. Figure 48 shows that the single side burning width is quite constant during flame spread. This indicates that there is minimal to no lateral flame spread occurring along these samples during this scenario. The mean single side burning width was determined by averaging the Sample A, Sample B and Sample D single side burning width over the first ten seconds after burner removal. It is assumed that the flame width is symmetric with respect to the corner. Therefore, the average total burning width was determined by doubling the mean single side burning width. The mean single side burning width is 0.251 m and the average total burning width is 0.502 m.

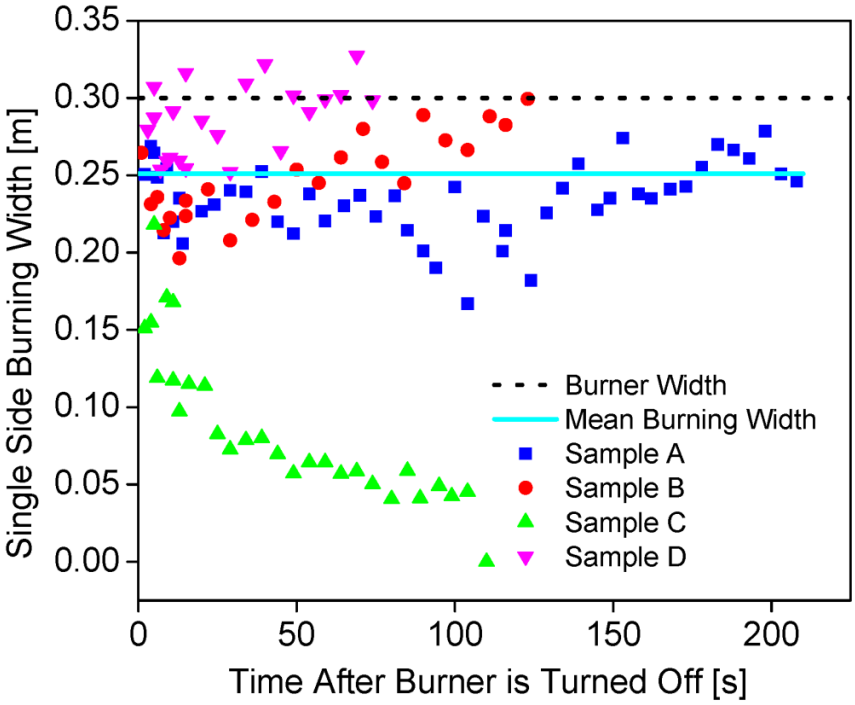

Figure 48. Burning width along the right corner-wall for all four samples from the moment the burner is turned off until the moment flames extend to the ceiling

For each experiment, the specified burner HRR of 25×10^3 W was subtracted from the total HRR measurements during the time period that the burner was on. This value was scaled based on the average total burning width to produce the heat release rate normalized by the burning width (Q'). Figure 49 is a graph displaying the Q' as a function of time for the four corner-wall experiments. This scaling technique provides a way to compare the full-scale fire performance of each sample based on the average amount of fuel burning. The two-dimensional pyrolysis model outputs the fuel production in terms of mass loss rate per unit width (MLR') and this can be converted to Q' based on the material's ΔH_{eff}. Scaling the flame spread experimental data provides a useful way to compare the model's prediction to the experimental results.

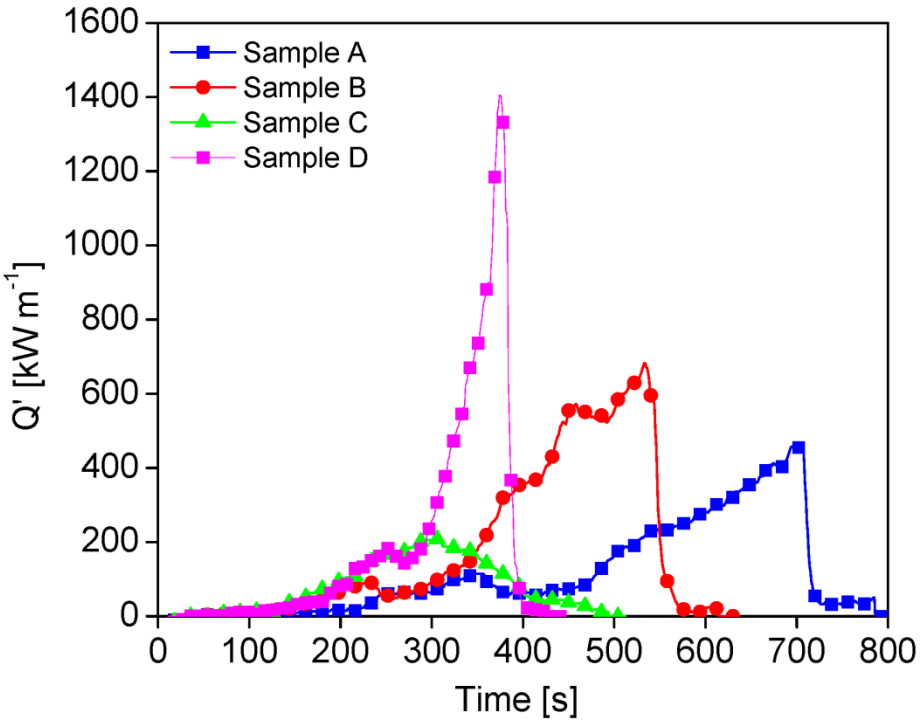

Figure 49. Corner-wall flame spread experiments - Q′, burner subtracted, versus time for all samples

3.3.2 25 kW Burner Exposure Tests

The raw heat flux gauge data at each height was averaged together for the three tests. Figure 50 displays the average heat flux measurements at each height over the course of the 400 s burner exposure. Figure 50 shows that the heat flux from the burner is highest in the regions closer to the burner. Subsequently, the heat flux decreases with vertical distance from the burner. During the first 60 s to 100 s the heat flux is transient. After the first 60 s to 100 s the heat flux become relatively steady.

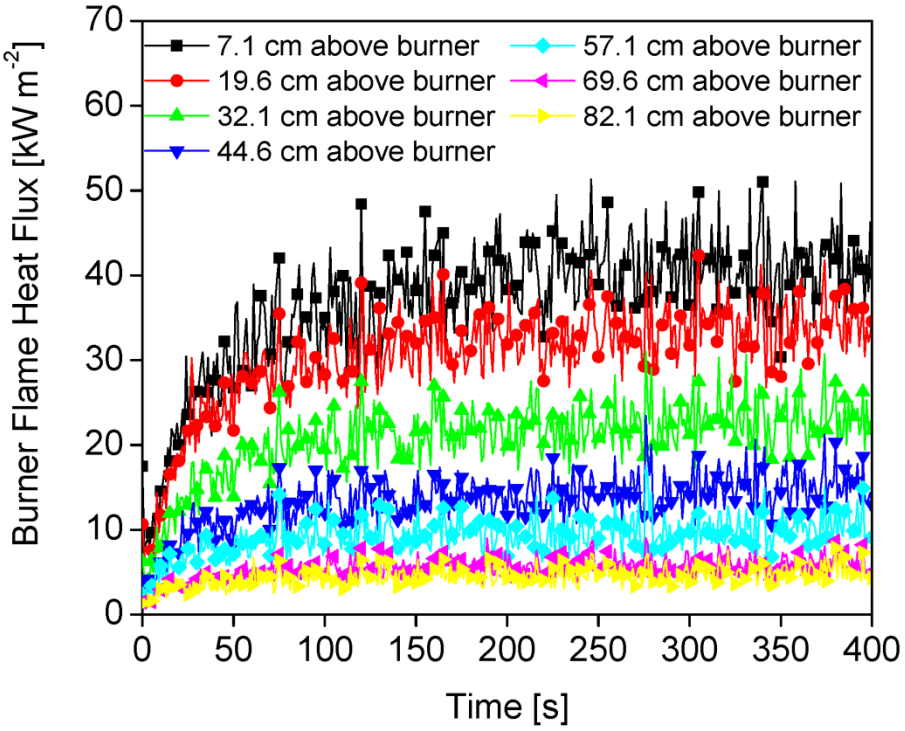

Figure 50. Average flame heat flux from the 25 kW square propane burner fire during the corner-wall experiments

3.3.3 40 kW Burner Exposure Experimental Results

The average heat flux readings at each height from the three tests where the propane burner produced a 40×10^3 W fire are show in Figure 51. The heat flux is the highest in the locations near the burner. The heat flux decreases with increasing height above the burner. The heat flux is transient during the first 30 s. After 30 s, the heat flux becomes relatively steady.

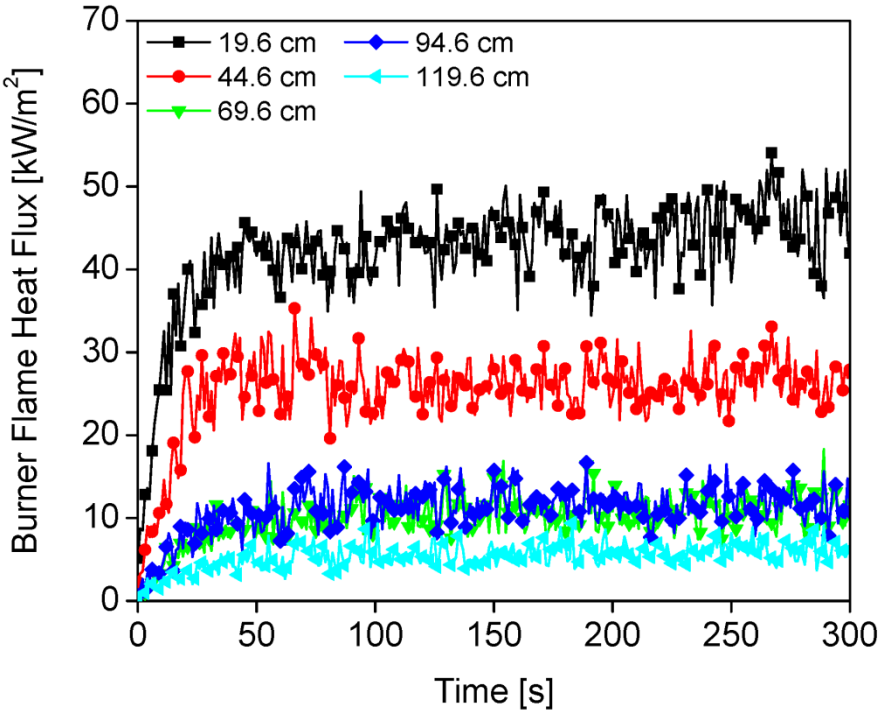

Figure 51. Average flame heat flux from the 40 kW propane burner fire during the corner-wall experiments

3.4 Room Corner Results

3.4.1 Compartment HRR

During the room corner tests, the square propane burner produced a 40×10^3 W fire for 165 s. After 165 s, the burner was turned off and the fire was allowed to propagate on its own. The fire would either continue to spread along the walls and ceiling until the compartment transitioned to flashover or, the combustible material would not support flame spread and the fire would self-extinguish. Throughout the test, the HRR and heat flux at the various heights were measured.

Figure 52 provides a plot of the compartment HRR measurements as a function of time for all seven room corner tests. The burner HRR of 40 kW was not subtracted from the HRR measurements on this graph. Both tests of Sample B and Sample D reached flashover. Sample C self-extinguished during its only test. Flashover was reached several minutes after the burner was turned off during Test 1 of Sample A. The fire self-extinguished during the second test of Sample A. According to NFPA 286, flashover has occurred when any two of the following conditions occur: HRR exceeding 1×10^6 W, heat flux at the floor exceeding 20×10^3 W m^{-1}, average upper layer temperature exceeding 873 K, flames exiting the doorway and autoignition of a paper target on the floor [10]. The time when flames have continuously extended beyond the doorway is listed in Table 6. Comparing Figure 52 and Table 6 shows that a compartment HRR of 1×10^6 W is a suitable criterion for determining flashover, as it corresponds wells to the moment when flames are extending beyond the compartment door.

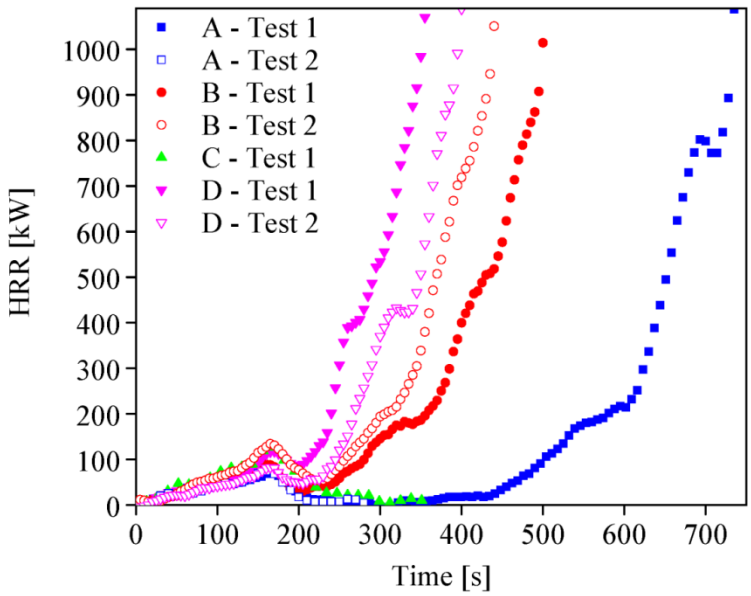

Figure 52. Room corner test - HRR, burner included, versus time

Table 6: Room Corner Test - Time to Flashover

Sample and Test Number	Time to Flashover [s]
Sample A - Test 1	717
Sample A - Test 2	Flashover did not occur
Sample B - Test 1	500
Sample B - Test 2	440
Sample C - Test 1	Flashover did not occur
Sample D - Test 1	345
Sample D - Test 2	410

The compartment HRR is the most important measurements taken during the room corner test. The specified burner HRR of 40 kW was subtracted from the compartment HRR measurements and normalized by the average burning width found during the open corner-wall flame spread tests. These graphs were utilized while validating the model's ability to simulate the room corner tests. Figure 53a, Figure 53b, Figure 53c and Figure 53d provides a plot of Q' versus time for the tests of Sample A, Sample B, Sample C and Sample D, respectively. Figure 53 is plotted from 0×10^3 W m^{-1} to 400×10^3 W m^{-1} to show the test results during the moment when the burner is first turned on until the moment when flames are spreading along the upper-wall and ceiling region. Amongst these tests, flames have reached the ceiling and are beginning to spread along the upper corner-wall region at fire sizes in the range of 220×10^3 W m^{-1} to 300×10^3 W m^{-1}. The ATF FRL reports an uncertainty of 42 %, 4.6 % and 2.6 % at 50×10^3 W, 500×10^3 W and 1100×10^3 W, respectively [57]. An uncertainty of 42 % was applied to the Q' measurements.

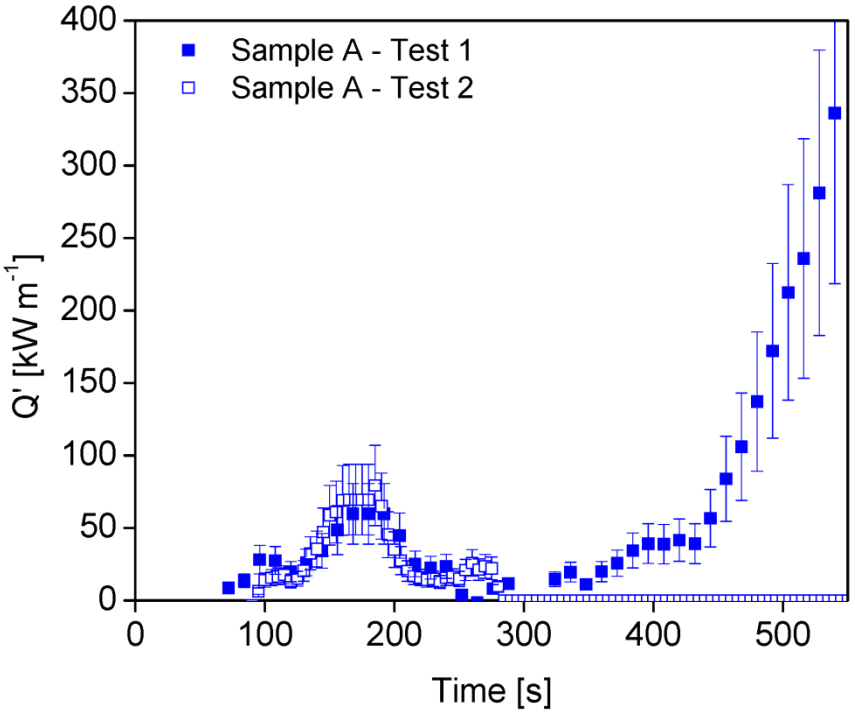
Sample A - Test 1
Sample A - Test 2
Q' [kW m-1]
Time [s]
0
50
100
150
200
250
300
350
400
0
100
200
300
400
500

(a)

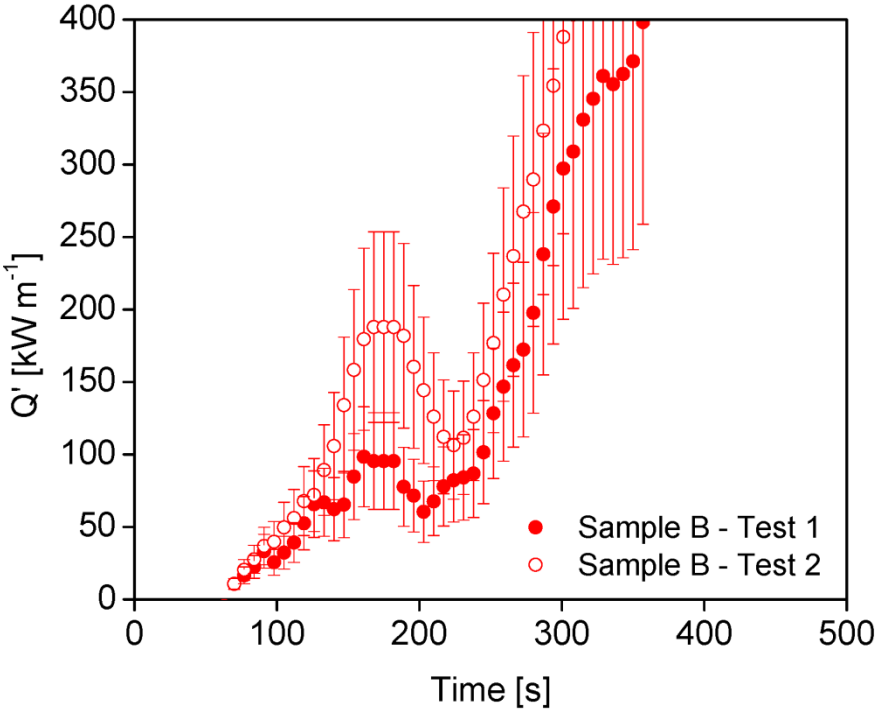
Sample B - Test 1
Sample B - Test 2
Q' [kW m-1]
Time [s]
0
50
100
150
200
250
300
350
400
0
100
200
300
400
500

(b)

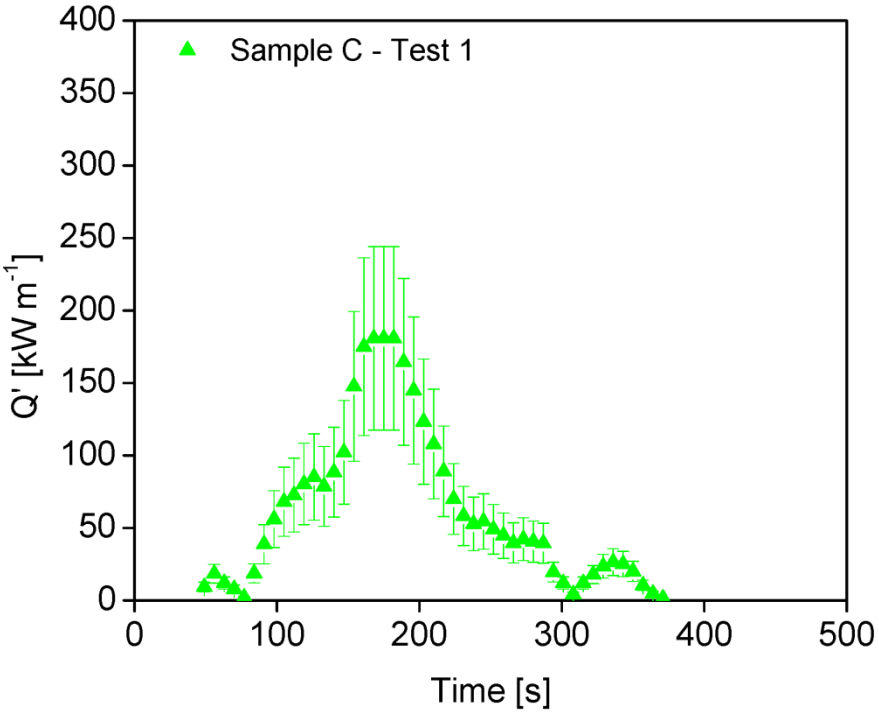
Sample C - Test 1
Q' [kW m-1]
Time [s]
0
50
100
150
200
250
300
350
400
0
100
200
300
400
500

(c)

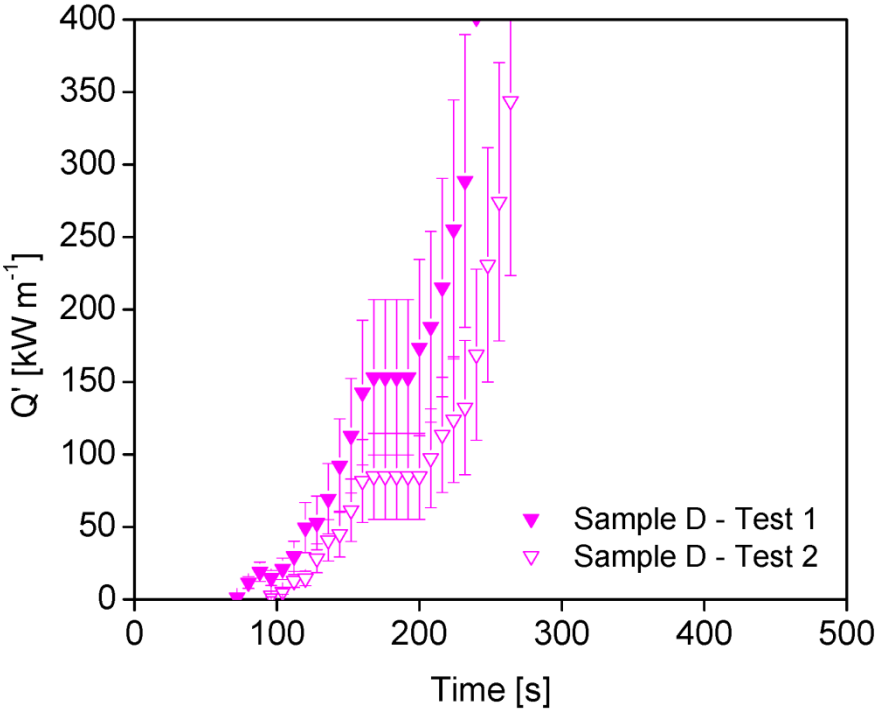
Sample D - Test 1
Sample D - Test 2
Q' [kW m-1]
Time [s]
0
50
100
150
200
250
300
350
400
0
100
200
300
400
500

(d)

Figure 53. Room corner tests - Q', burner subtracted, versus time. Graph (a), graph (b), graph (c) and graph (d) provides the test results for Sample A, Sample B, Sample C and Sample D, respectively

During the full-scale fire scenario, Sample D was the material that had the tendency to support flame spread the most compared to the other materials analyzed in this project. Sample B also supported flame spread and allowed the fire to continue to develop until the compartment reached flashover. Of the four materials, Sample A produced contradicting results. In the first test, it supported flame spread, while in the second test, it self-extinguished. It is believed that if Sample A was exposed to the propane burner for a few moments longer during Test 2, flames would have propagated until the compartment reached flashover. Sample C had the tendency to self-extinguish, as seen in both the open corner-wall tests and the room corner test. Only one test was performed for Sample C due to time restraints.

The heat flux gauge measurements were found to be dependent upon the distance from the corner. In the appendix, the heat flux gauge measurements were analyzed and a linear function was developed to represent the horizontal heat flux distribution during corner-wall flame spread.

4. Modeling and Optimization Procedure

4.1 Milligram-Scale Model & Optimization Procedure

4.1.1 MCC Model

MCC experiments were conducted to capture each sample's HRR/m_0, effective heat of combustion and char yield. During the MCC experiments, the milligram sized sample is linearly heated up at a rate of 1 K s^{-1}. As the sample heats up, it pyrolyzes, produces gaseous volatiles and they combust in the furnace. The sample's HRR/m_0 curve represents this process. The rate at which the sample pyrolyzes is controlled by the sample's kinetics. Since the MCC cannot directly measure the sample's kinetic parameters, inverse modeling was performed to determine the kinetic parameters. ThermaKin2D was utilized to simulate the MCC experiments and fit the HRR/m_0 curve by manually changing each sample's kinetic parameters (pre-expontential factor and activation energy). This optimization procedure provided the kinetic parameters for each sample, while accurately predicting the results of the MCC experiments.

The one dimensional mode of ThermaKin2D was used to model the MCC experiments. The sample was specified to be thermally thin so that it heats up uniformly. The initial temperature of the sample, as well as the top and bottom boundaries were set to 348 K; the initial temperature of the pyrolyzer. Once the simulation begins, the boundary temperature increases at a rate of 1 K s^{-1}. The convection coefficient is set to an arbitrarily high value to ensure that the internal temperature of the sample is uniform

with the outside boundaries. Mass transport occurs through the top surface is governed by a linear equation. The simulation ends once the temperature reaches 1023 K. The size of the computational grid is $\Delta x = 1\times10^{-6}$ m and the time step for each calculation is $\Delta t = 5\times10^{-3}$ s. The results still converged even when the grid size and time step were increased and decreased by a factor of two.

In the MCC ThermaKin2D model, the effects of heat and mass transport are negligible. The sample is made thermally thin, which removes all aspect of heat transfer through the sample. The gas transport coefficient is set to a value which allows the mass to exit the sample immediately once it is generated. Thus, the thermal and optical properties are irrelevant during the MCC model simulation. The model is only sensitive to the reaction's kinetic parameters, the stoichiometric coefficients and the effective heat of combustion. The stoichiometric coefficient comes from the char yield found during the MCC experiments. Both the char yield and the effective heat of combustion are reported in Table 3. The pyrolysis model produces an output file that provides the sample mass loss rate as a function of time and sample temperature. The mass loss rate is multiplied by the sample's effective heat of combustion gained from the MCC experiments and normalized by the initial mass to calculate the HRR/m_0.

During the MCC experiments, the pyrolysis rate is dependent upon the chemical kinetics of the sample. In chemistry, the rate at which chemical reactions occur is defined by Equation 17.

$$Reaction\ Rate = \gamma[B]^n \tag{17}$$

In Equation 17, (γ) is the rate constant, (B) is the species concentration of the reactant and (n) is the order of reaction for B. The rate constant is defined by the Arrhenius equation, Equation 18.

$$\gamma = A \exp\left(-\frac{E}{R\,T}\right) \tag{18}$$

The Arrhenius equation states that the rate constant is based on the pre-exponential factor (A), the activation energy (E), the universal gas constant, (R) and the temperature (T). The pre-exponential factor is defined as the frequency factor in terms of [s^{-1}]. The activation energy is described as the minimum amount of energy required to start the reaction and it has units of [J mol^{-1}]. Both the pre-exponential factor and the activation energy are material dependent. The universal gas constant is equal to 8.314 J K^{-1} mol^{-1}. During the MCC experiment, the temperature corresponds to the pyrolysis temperature which is influenced by the heating rate. Overall, the rate of pyrolysis is dependent upon the Arrhenius parameters, the concentration of the species, the order of the reaction and the temperature.

Previous research has been performed to quantify the chemical kinetics that occur during the decomposition of MDF [62] [63] [64]. Current research methods approximate the pyrolysis of materials by grouping the many chemical reactions into a group of apparent reaction schemes that best fit thermal degradation experimental data. One of the goals of this research project is to determine how many chemical reactions are needed to accurately fit the MCC and cone calorimeter experimental data. An optimization procedure becomes much more difficult as more chemical reactions are introduced. Therefore, three separate reaction models were created for each sample. The models

differed based on the complexity of the reaction schemes. The simplest model contained one first-order chemical reaction. Next, a more advanced model was introduced that contains two consecutive first-order reactions. Finally, the most advanced model contained three parallel first-order reaction statements.

The simplest model used to define the decomposition of the sample was a single first-order chemical reaction, also known as the "1 Reaction Model". The general formula for the single first-order chemical reaction statement is provided in Equation 19.

$$Sample \rightarrow \theta_C * Char + (1 - \theta_C) * Gas \quad (19)$$

The $Sample$ is the virgin material prior to decomposition. Once the $Sample$ undergoes decomposition, it produces $Char$ and Gas. $Char$ is the solid product formed during condensed-phase pyrolysis and Gas is the gaseous volatile produced during pyrolysis. The stoichiometric coefficient for the char yield with respect to the initial virgin material (θ_C) was discovered during the MCC experiments.

The next model used to simulate the decomposition of the samples is two consecutive first-order reactions, also known as the "2 Reaction Model". The general formula for the more advanced, two consecutive reaction equations is presented in Equation 20a and Equation 20b. In this formula, the first reaction produces a solid $Intermediate$ component and gaseous volatiles. The Intermediate component then undergoes a reaction where it produces solid char and more gaseous volatiles. These reactions occur in series. Both the stoichiometric coefficients of the intermediate with respect to the initial virgin sample (θ_I) and char with respect to the intermediate

component (θ_{CI}) had to be specified so that the model yielded a final char that matched the experimental results. This was verified using Equation 21.

$$Sample \rightarrow \theta_I * Intermediate + (1 - \theta_I) * Gas \quad (20a)$$

$$Intermediate \rightarrow \theta_{CI} * Char + (1 - \theta_{CI}) * Gas \quad (20b)$$

$$\theta_C = \theta_I * \theta_{CI} \quad (21)$$

The third and final reaction model utilized in this project incorporates three parallel reactions. Each set of kinetic parameters are equal amongst the four samples and they are based on literature values of MDF [62]. Li et al., associates one reaction with each component of MDF. In this project, it is assumed that the four samples have similar composition, but the mass fraction of each component differs amongst the samples. Thus, it is reasonable to apply the kinetic values and stoichiometric coefficient of MDF found in the literature to the materials studied in this project. The optimization procedure was performed for each sample by changing the initial mass fraction of each component until the model best fits the experimental results. The general formula for the three parallel reaction statement is provided in Equation 22a, Equation 22b and Equation 22c.

$$Component_1 \rightarrow \theta_1 * Char + (1 - \theta_1) * Gas \quad (22a)$$

$$Component_2 \rightarrow \theta_2 * Char + (1 - \theta_2) * Gas \quad (22b)$$

$$Component_3 \rightarrow \theta_3 * Char + (1 - \theta_3) * Gas \quad (22c)$$

$$Sample = \Upsilon_1 * Component_1 + \Upsilon_2 * Component_2 + \Upsilon_3 * Component_3 \quad (23a)$$

$$\Upsilon_1 + \Upsilon_2 + \Upsilon_3 = 1 \quad (23b)$$

The virgin sample is composed of three components, all of which possess a percentage of the initial sample mass, (Υ). As shown in Equation 23a and Equation 23b, all of the components have a Υ which add up to 1. These parallel reactions occur simultaneously and they each produce solid char and gaseous volatiles.

The Arrhenius parameters and the stoichiometric coefficients for each reaction come from a paper authored by Li et al [62]. In this paper, the authors define a set of parallel reactions for the decomposition of MDF. An optimization procedure was performed to determine the kinetic parameters of the MDF by fitting the experimental TGA test data. The "Search I" pre-exponential factor, activation energy, char yield and initial mass fraction for resin, hemicellulose and cellulose provide the closest match to the MCC experimental results. Table 7 provides the kinetic values of the three parallel reactions used to describe the degradation of the samples in this project.

Table 7: Kinetic parameters implements into the three parallel reaction scheme

Properties	Component 1: Cellulose	Component 2: Hemicellulose	Component 3: Resin
A [1 s^{-1}]	7.94×10^{13}	1.26×10^{12}	6.31×10^{11}
E [J mol^{-1}]	1.92×10^{5}	1.57×10^{5}	1.30×10^{5}
θ [-]	0.29	0.09	0.09
Υ [%]	35.7	39.3	10.0

4.1.2 MCC Optimization Procedure

The MCC optimization procedure began by first modeling a single first-order chemical reaction. The initial guess of Arrhenius parameters for both the single and two consecutive first-order reaction schemes is based on a paper by Stoliarov et al. [65]. The authors of this paper analyzed the literature reported property values for a wide range of

polymers and determined the average pre-exponential factor and activation energy to be 1e14 1 s^{-1} and 2.18e5 J mol^{-1}, respectively. Table 8 defines the reaction equation for each sample being specified in the first MCC model. The individual char yield for each sample was determined during the MCC experiments and reported in Table 3.

Table 8: Kinetic parameters specified for the first attempt single reaction MCC model

Sample	Chemical Equation	Pre-exponential Factor [s^{-1}]	Activation Energy [J mol^{-1}]
A	Sample $\rightarrow$ 0.175*Char + 0.825*Gas	1×10^{14}	2.18×10^{5}
B	Sample $\rightarrow$ 0.144*Char + 0.856*Gas		
C	Sample $\rightarrow$ 0.1764*Char + 0.8236*Gas		
D	Sample $\rightarrow$ 0.1156*Char + 0.8844*Gas		

The ThermaKin2D MCC model was utilized to simulate the pyrolysis of each sample using the average kinetic parameters as the initial guess. In Figure 54, the HRR/m_0 results from the original model is compared to the experimental average for each sample. Figure 54 shows that the original Model over predicts the HRR/m_0 and the decomposition temperature for each sample. Since all the samples have the same kinetic parameters, each model predicts that the decomposition temperature occurs at the same temperature. The height of the HRR/m_0 curve depends upon the char yield and the effective heat of combustion. When a sample has a greater char yield, it produces less gaseous volatiles and thus the HRR/m_0 is lower. While on the other hand, if a sample has a lower char yield, it produces more gaseous volatiles and therefore the HRR is higher. Also, when a sample has a higher effective heat of combustion, it will produce more heat during combustion. The opposite is also true.

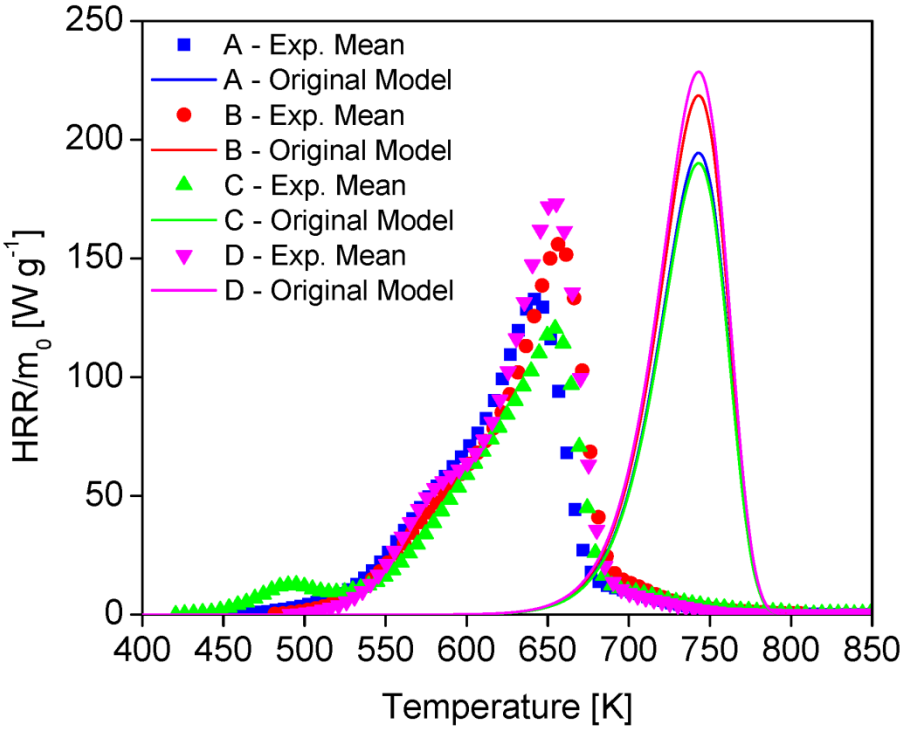

Figure 54. The MCC experimental average compared to the model first attempt using average polymer kinetic parameters

Figure 54 demonstrates that the average Arrhenius parameters were unable to accurately predict the HRR/m_0 curve. Thus, an optimization procedure was initiated to determine the Arrhenius parameters that could best predict the experimental HRR/m_0 curve during sample pyrolysis. The optimization procedure was performed according to the guide provided by Li [66]. This guide is provided in Table 9. It was initially developed to fit TGA/DSC experiments, but was altered in this project to work for the MCC experiments. This optimization guide advises the user to utilize Equation 24 and Equation 25 to shift the curve.

Table 9: Guide to fitting the MCC HRR/m_0 curve [66]

Desired Change to the HRR/m_0 Curve	Procedure
Shift peak to higher temperature	Increase T_{max} and recompute A and E using Eq. 26 and Eq.27
Shift peak to lower temperature	Decrease T_{max} and recompute A and E using Eq. 26 and Eq.27
Increase Peak Height	Increase E and re-compute A using Eq. 27
Decrease Peak Height	Decrease E and re-compute A using Eq. 27

$$E = \frac{e\ R\ T_{max}^2 \frac{HRR_{max}}{m_0}}{(1-\theta)\frac{dT}{dt}} \tag{24}$$

$$A = \frac{e\ HRR_{max}}{m_0}\ e^{\frac{E}{R\,T_{max}}} \tag{25}$$

In Equation 24 and Equation 25, e is the base of the natural logarithm, R is the universal gas constant, $\frac{dT}{dt}$ is the MCC linear heating rate, θ is the stoichiometric coefficient of the char and m_0 is the initial sample mass. HRR_{max} is the maximum HRR and T_{max} is the decomposition temperature at which the maximum HRR occurs. The MCC optimization guide provides a specific methodology for shifting the height and location of the HRR/m_0 curve by simply adjusting the maximum decomposition temperature and the activation energy and then re-computing Equation 24 or Equation 25. A simpler rule for fitting the HRR/m_0 curve is presented in Table 10. Both guides were utilized to fit the MCC experimental data and determine the kinetics parameters for all the samples and each of their reactions.

Table 10: Simple Guide to Fitting the MCC HRR/m_0 Curve

Desired Change to the HRR/m_0 Curve	Procedure
Shift peak to higher temperature	$\downarrow A\ \uparrow E$
Shift peak to lower temperature	$\uparrow A\ \downarrow E$
Increase Peak Height	$\uparrow A\ \uparrow E$
Decrease Peak Height	$\downarrow A\ \downarrow E$

The MCC optimization procedure was performed for the four samples using the 1 Reaction Model. The accuracy of the HRR/m_0 fit was determined by calculating the

coefficient of determination (R^2). Table 11 provides the optimized Arrhenius values, stoichiometric char yield and coefficient of determination for the four samples.

Table 11: MCC optimization - Kinetic parameters utilized in the single first-order reaction scheme

	A [s^{-1}]	E [J mol^{-1}]	Char Yield [%]	R^2
Sample A	1.44×10^{7}	1.04×10^{5}	17.50	0.91
Sample B	5.81×10^{7}	1.15×10^{5}	14.40	0.93
Sample C	4.8×10^{6}	1.019×10^{5}	17.64	0.91
Sample D	2.8×10^{8}	1.2225×10^{5}	11.56	0.93

Figure 55 provides the finalize optimization for each sample's 1 Reaction Model. Figure 55 compares the model's prediction of HRR/m_0 vs temperature to the experimental results. These graphs demonstrate that a single first-order reaction scheme is able to accurately predict the decomposition temperature and peak HRR/m_0 for the four samples. The R^2 value for all these fits are above 90 %.

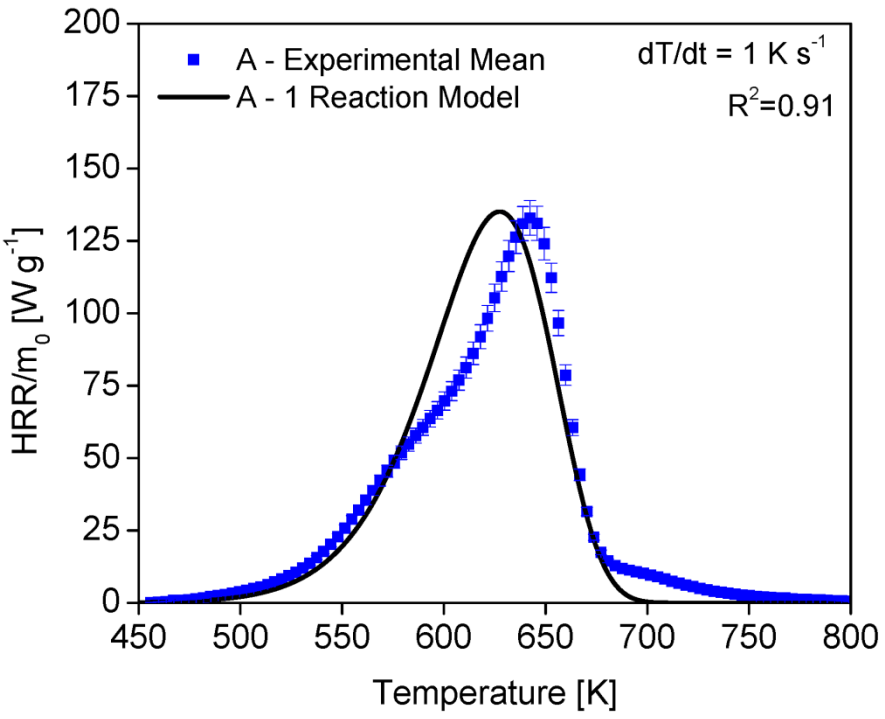

(a)

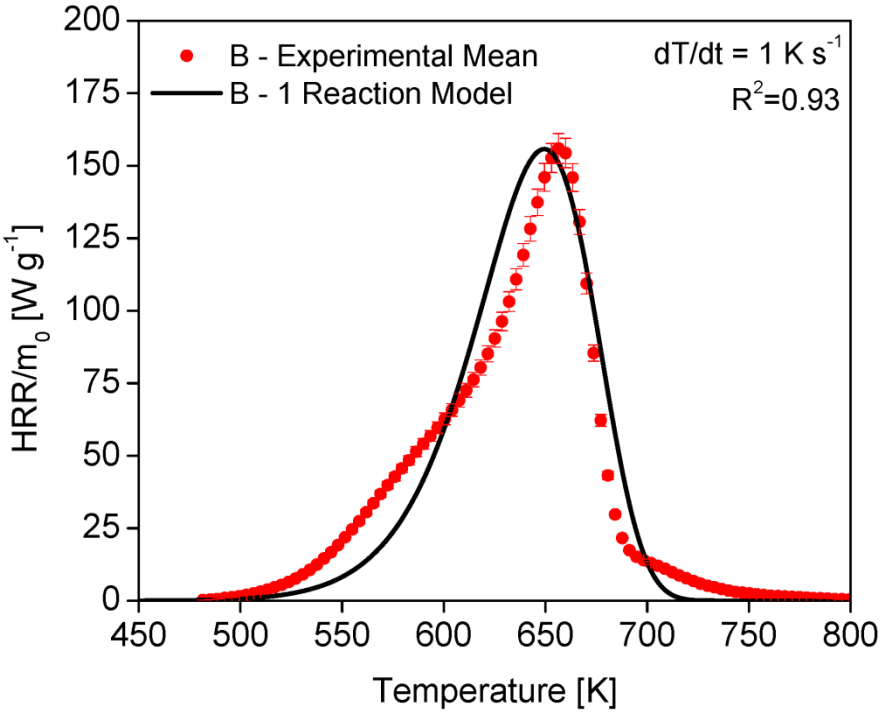
B - Experimental Mean
B - 1 Reaction Model
dT/dt = 1 K s-1
R2=0.93
HRR/m0 [W g-1]
Temperature [K]
0
25
50
75
100
125
150
175
200
450
500
550
600
650
700
750
800

(b)

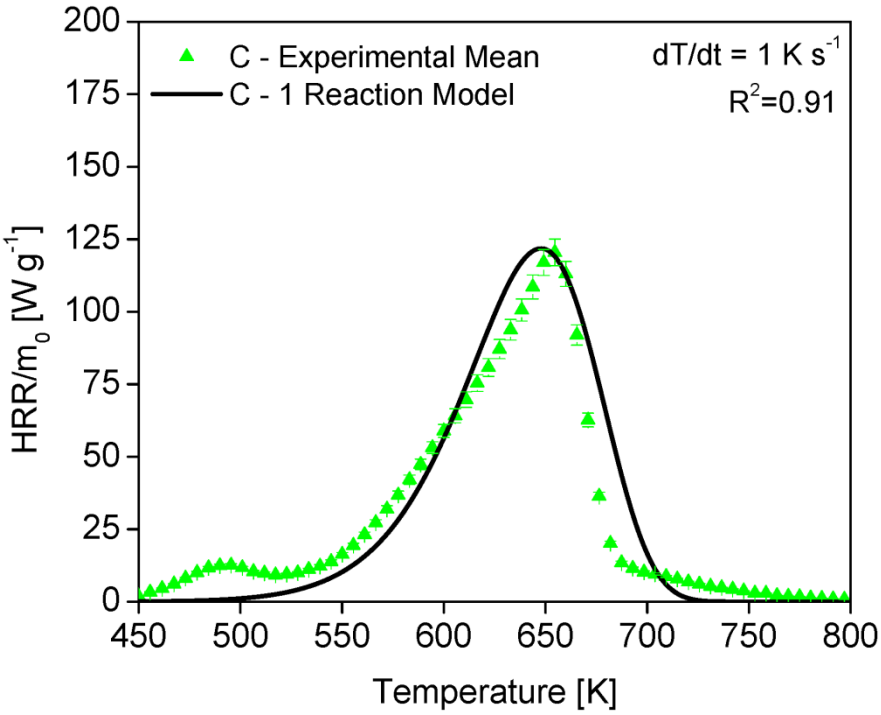
C - Experimental Mean
C - 1 Reaction Model
dT/dt = 1 K s-1
R2=0.91
HRR/m0 [W g-1]
Temperature [K]
0
25
50
75
100
125
150
175
200
450
500
550
600
650
700
750
800

(c)

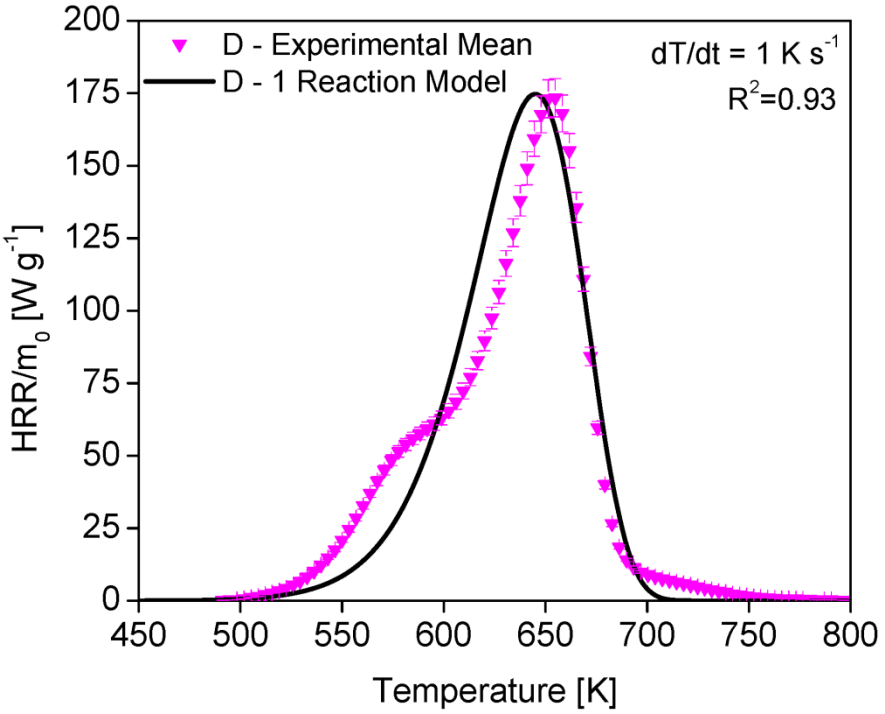

(d)

Figure 55. MCC Optimization - The experimental average HRR/m_0 curve for each sample is compared to the model's prediction using the final set of optimized kinetic parameters. The model utilizes a single first-order chemical reaction to describe the decomposition of the samples. Graph (a), graph (b), graph (c) and graph (d) provides the final fit for Sample A, Sample B, Sample C and Sample D, respectively

The 1 Reaction Model was able to adequately fit the experimental HRR/m_0 curve. Once the coefficient of determination was maximized for the single reaction scheme, a second reaction was introduced according to Equation 20. The fit becomes more precise once a second reaction is incorporated and the Arrhenius parameters and stoichiometric coefficients are optimized. Table 12 provides the final set of Arrhenius values, stoichiometric char yield and coefficient of determination for the four samples that utilize the 2 Reaction Model.

Table 12: MCC Optimization: Two Consecutive Reactions - Kinetic Parameters

	Reaction Number	A [1 s^{-1}]	E [J mol^{-1}]	Stoichiometric Yield [%]	R^2
Sample A	1st	2.6×10^{7}	9.99×10^{4}	70.64	0.99
	2nd	1.8×10^{11}	1.55×10^{5}	24.77	
Sample B	1st	9.5×10^{7}	1.06×10^{5}	80.00	0.98
	2nd	1.4×10^{10}	1.45×10^{5}	17.99	
Sample C	1st	3.0×10^{7}	8.34×10^{4}	94.00	0.96
	2nd	9.9×10^{6}	1.05×10^{5}	18.77	
Sample D	1st	9.87×10^{8}	1.15×10^{5}	83.00	0.99
	2nd	1.95×10^{10}	1.45×10^{5}	13.93	

Figure 56 provides the model prediction compared to the experimental results based on the final set of optimized kinetic parameters for all four samples. Each sample decomposes based on a reaction scheme containing two consecutive first-order reactions. Figure 56 demonstrates that the 2 Reaction Model is able to fit the decomposition temperature, peak HRR/m_0 and overall shape of the experimental data with a great deal of accuracy. The R^2 value for all these fits are between 96% and 99%.

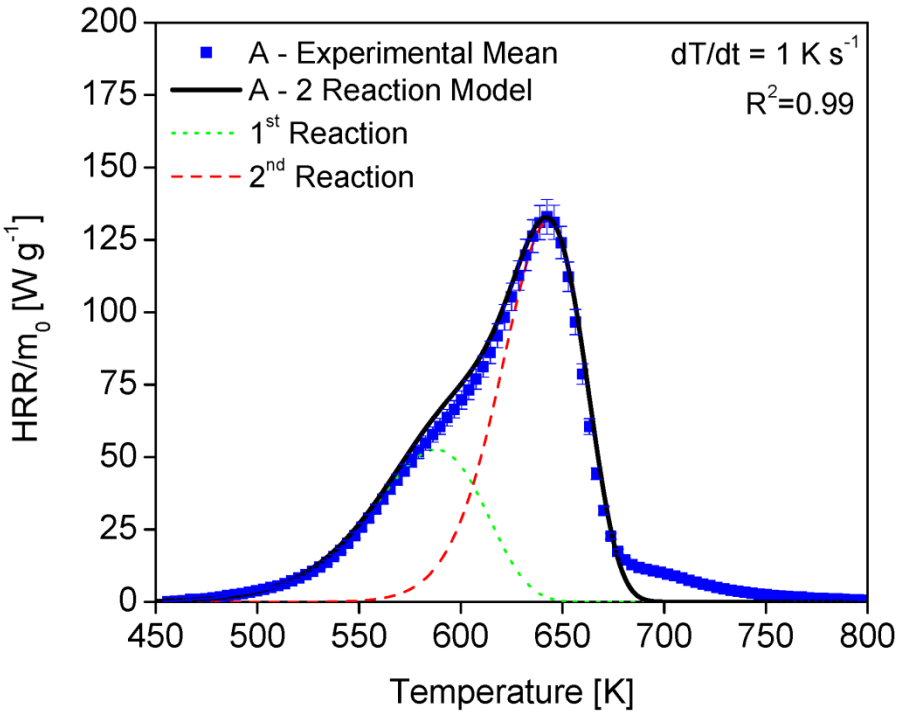

(a)

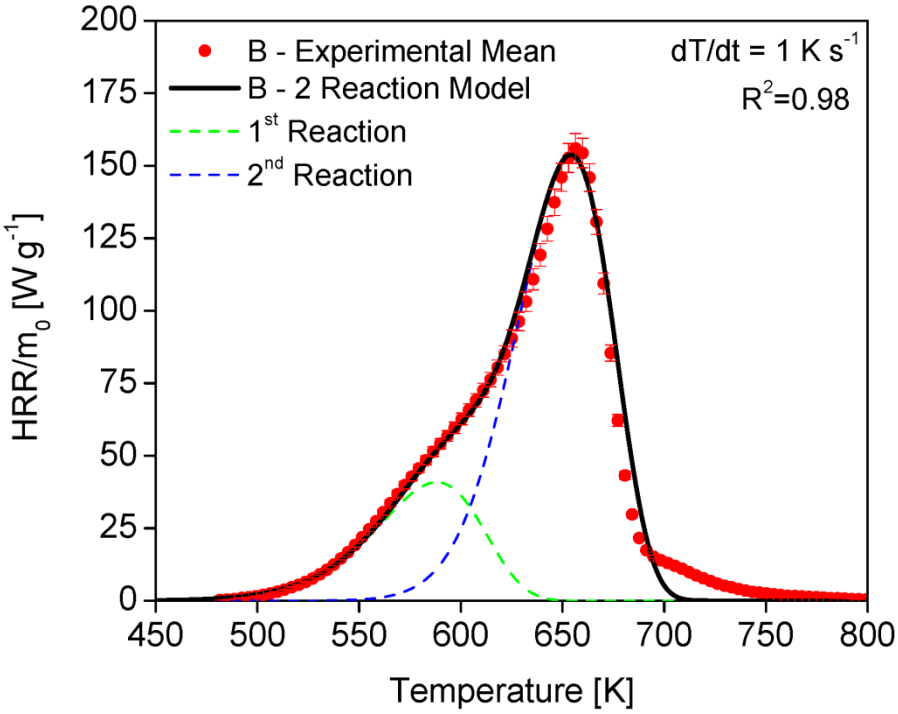
B - Experimental Mean
B - 2 Reaction Model
1st Reaction
2nd Reaction
dT/dt = 1 K s-1
R2=0.98
HRR/m0 [W g-1]
Temperature [K]
0
25
50
75
100
125
150
175
200
450
500
550
600
650
700
750
800

(b)

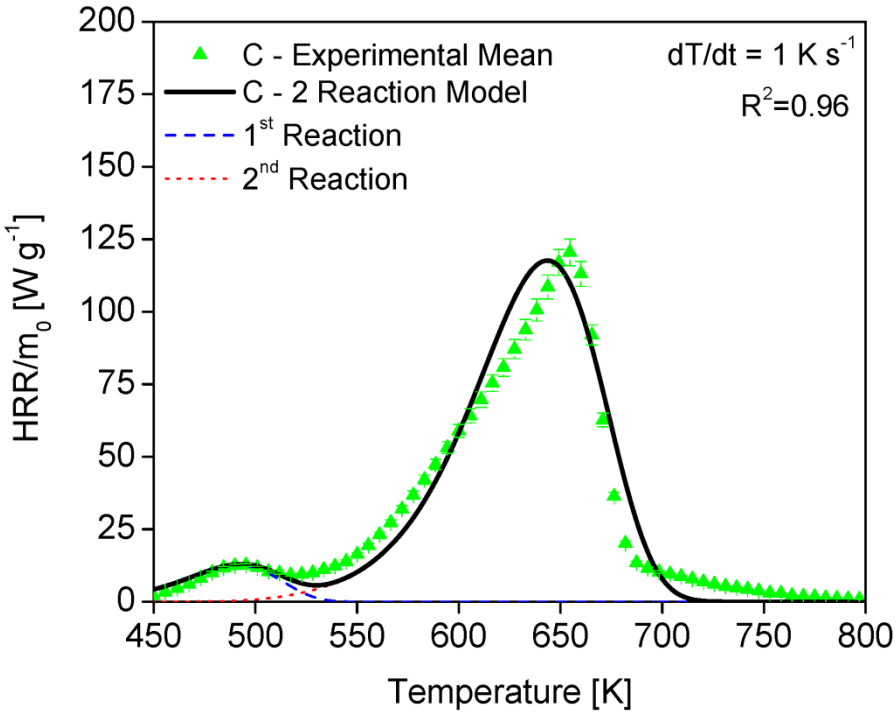
C - Experimental Mean
C - 2 Reaction Model
1st Reaction
2nd Reaction
dT/dt = 1 K s-1
R2=0.96
HRR/m0 [W g-1]
Temperature [K]
0
25
50
75
100
125
150
175
200
450
500
550
600
650
700
750
800

(c)

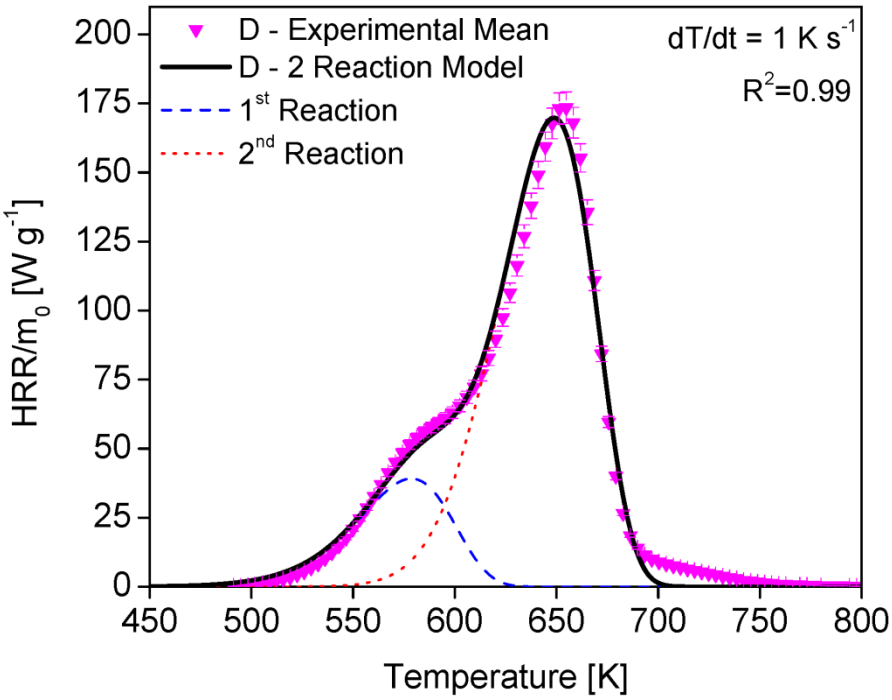

(d)

Figure 56. MCC Optimization - The experimental average HRR/m_0 curve for each sample is compared to the model's prediction using the final set of optimized kinetic parameters. The model utilizes two consecutive first-order chemical reactions to describe the decomposition of the samples. Graph (a), (b), (c) and (d) provides the final fits for Sample A, Sample B, Sample C and Sample D, respectively, as well as their individual reactions.

A set of three parallel single-order reactions were then utilized to fit the MCC experimental data. Table 13 provides the kinetics parameters for the three parallel reactions. In this optimization procedure, the stoichiometric coefficients and Arrhenius parameters are kept constant, while the initial mass fraction (ϒ) is optimized to produce the best fit. The goal of this optimization procedure is to determine whether or not the kinetic parameters found in literature could accurately fit MCC data based on simply altering the initial mass fraction of the various components. Of all the articles that define the kinetics of MDF, the kinetic parameters presented in reference [62] "Search I" provide the best initial fit to the MCC results. The optimization procedure is performed

for the three parallel reaction scheme by manually adjusting the ϒ of the three components, while ensuring that the sum of the initial mass fraction equals 1. Table 13 provides the optimized set of ϒ that provide the highest R^2 value for the fit of Sample A, Sample B, Sample C and Sample D. The kinetic parameters match the values reported in Table 7.

Table 13: MCC Optimization - Three Parallel Reactions

	Component	ϒ [-]	Char Yield [%]	R^2
A	Cellulose	0.26	23.0	0.70
	Hemicellulose	0.71		
	Resin	0.03		
B	Cellulose	0.20	24.0	0.94
	Hemicellulose	0.78		
	Resin	0.02		
C	Cellulose	0.28	22.0	0.91
	Hemicellulose	0.67		
	Resin	0.05		
D	Cellulose	0.17	25.0	0.88
	Hemicellulose	0.83		
	Resin	0.00		

Figure 57 presents the final fit of the HRR/m_0 curve for Sample A, Sample B, Sample C and Sample D. Figure 57 shows that the 3 Reaction Model provides an adequate fit of the HRR/m_0 curve for Sample B and Sample C. Both the R^2 value for Sample B and Sample C are 0.94 and 0.91, respectively. The three parallel reaction scheme for Sample D produces a good fit that has an R^2 equal to 0.88. While, the reaction scheme is unable to produce a good fit for Sample A ($R^2 = 0.70$).

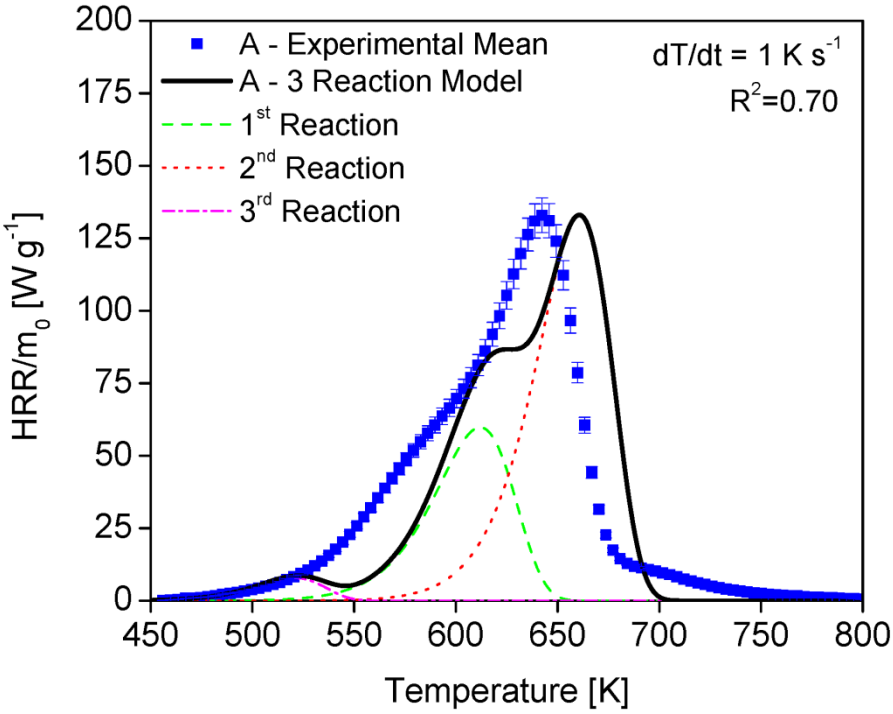
A - Experimental Mean
A - 3 Reaction Model
1st Reaction
2nd Reaction
3rd Reaction
dT/dt = 1 K s-1
R2=0.70
HRR/m0 [W g-1]
Temperature [K]
0
25
50
75
100
125
150
175
200
450
500
550
600
650
700
750
800

(a)

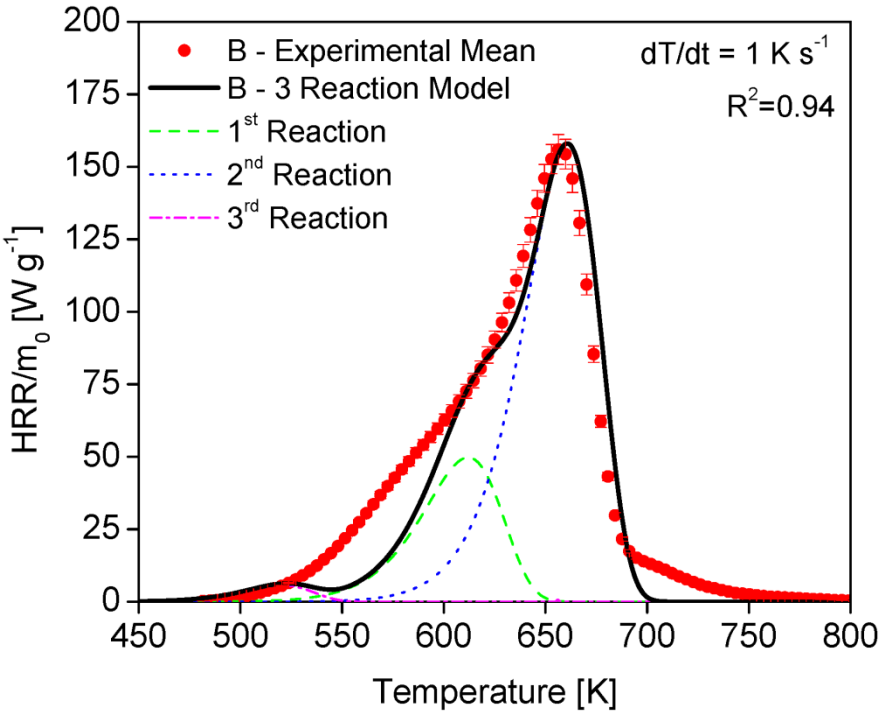
B - Experimental Mean
B - 3 Reaction Model
1st Reaction
2nd Reaction
3rd Reaction
dT/dt = 1 K s-1
R2=0.94
HRR/m0 [W g-1]
Temperature [K]
0
25
50
75
100
125
150
175
200
450
500
550
600
650
700
750
800

(b)

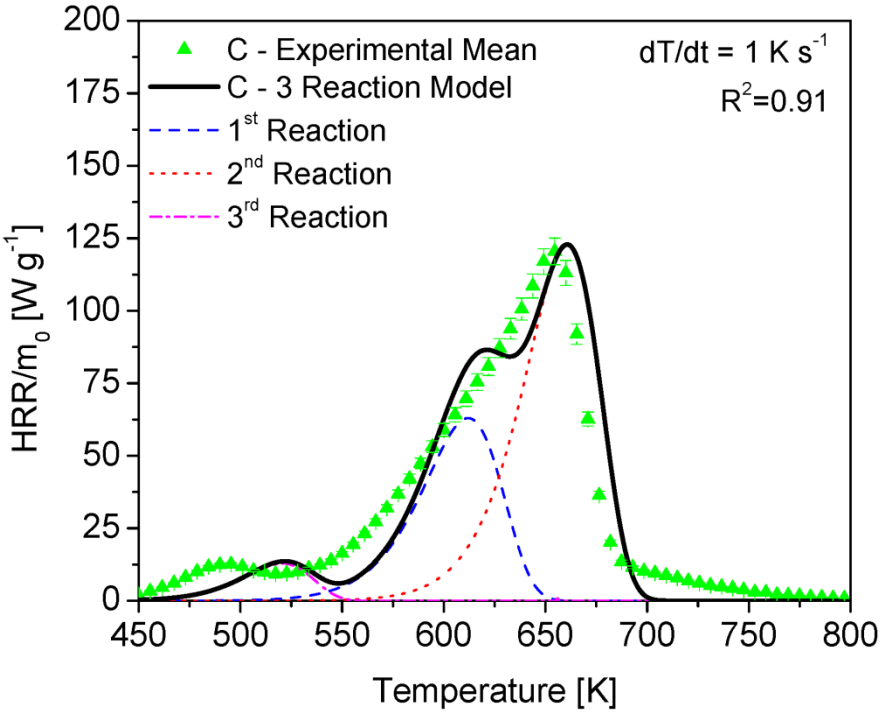
C - Experimental Mean
C - 3 Reaction Model
1st Reaction
2nd Reaction
3rd Reaction
dT/dt = 1 K s-1
R2=0.91
HRR/m0 [W g-1]
Temperature [K]
0
25
50
75
100
125
150
175
200
450
500
550
600
650
700
750
800

(c)

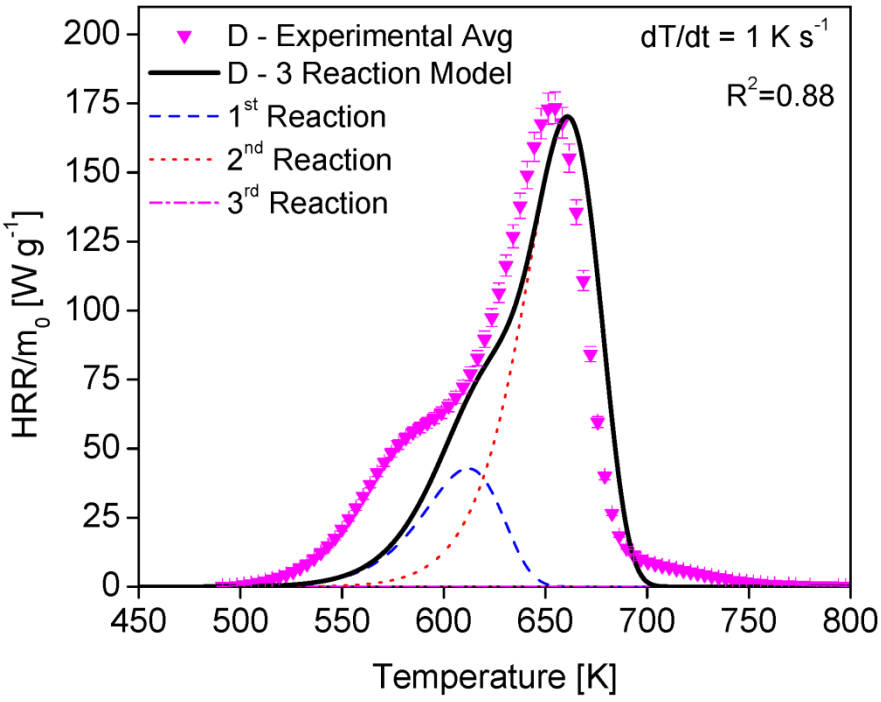
D - Experimental Avg
D - 3 Reaction Model
1st Reaction
2nd Reaction
3rd Reaction
dT/dt = 1 K s-1
R2=0.88
HRR/m0 [W g-1]
Temperature [K]
0
25
50
75
100
125
150
175
200
450
500
550
600
650
700
750
800

(d)

Figure 57. MCC Optimization - The experimental average HRR/m_0 curve for each sample is compared to the model's prediction using the final set of optimized initial mass fractions. The model utilizes three parallel first-order chemical reactions to describe the decomposition of the samples. Graph (a), (b), (c) and (d) provides the final fits for Sample A, Sample B, Sample C and Sample D, respectively, as well as their individual reactions.

The single reaction scheme produces a good fit, with a R^2 value between 91 % and 93%. The two consecutive reaction scheme produces a great fit that has an R^2 value between 96 % and 99 %. Simply introducing one more reaction enables the user to improve the model's fit to the experimental data. While the three parallel reaction scheme based on literature values produces a good fit for some of the sample, it also produces an inadequate fit for the other samples. The 3 Reaction Model produces fits that have a R^2 value between 70 % and 93 %. Of the three proposed reactions schemes, the 2 Reaction model produces the best fit, followed by the 1 Reaction Model, and lastly the 3 Reaction Model.

Moving forward, only two of the reaction schemes will be further utilized in this project: the 1 Reaction Model and 2 Reaction Model. The 3 Reaction Model based on literature kinetic values is too inconsistent for further use. Both of these schemes will be incorporated into the cone calorimeter model to determine the remaining thermal, optical and chemical properties of each sample.

4.2 Bench-Scale Model & Optimization Procedure

4.2.1 Cone Calorimeter Model

First, the cone calorimeter model developed in ThermaKin2D will be presented, along with its assumptions. Next, the cone calorimeter optimization procedure is discussed. In this part, the initial properties of the sample, char, gas and any intermediate

components will be provided, as well as the minimum and maximum range for these properties. Lastly, the final results of the optimization procedure are presented. This chapter identifies the final set of sample properties that will be utilized for the flame spread modeling.

The cone calorimeter model was constructed in ThermaKin2D under the one dimensional mode. Thermakin2D requires a complete set of material properties which represent the sample, its char and any intermediate component that are relevant during the reaction. Each component (virgin sample, intermediate, char and gas) need the following parameters: the state of the component (solid, liquid or gas), density, heat capacity, thermal conductivity, gas transport coefficient, emissivity and absorption coefficient. Each reaction requires the following: stoichiometric coefficients, the Arrhenius parameters (pre-exponential factor and activation energy) and the heat of reaction.

The conditions the sample is subjected to during the cone calorimeter experiments are represented by a boundary condition within the model. Therefore a detailed description of this boundary condition is also needed. The top surface of the cone calorimeter model was defined by the incident radiative heat flux ($q"_{inc}$) equal to 20×10^3, 25×10^3, 50×10^3 or 80×10^3 W m^{-2}, T_∞ equal to 300 K and convective heat transfer coefficient (h_c) equal to 10 W m^{-2} K^{-1}. The sample and gypsum are defined by their material properties and the thickness (τ). Figure 58a provides the pre ignition diagram of the cone calorimeter model constructed in ThermaKin2D and Figure 58b provides the post ignition boundary conditions. The gaseous volatiles produced during the pyrolysis are specified to leave the top surface of the material. Mass transport of the gaseous species occurs at a rate that will not inhibit the flow of gaseous species through the

material. Once the mass loss rate reaches the specified critical mass flux, ignition occurs and an additional radiative heat flux of 20×10^3 W m^{-2} is provided to the surface of the sample. The details discussing the additional flame heat flux were provided in Section 3.2.3. After ignition occurs, it is assumed that the flame covers the entire surface and therefore the convective heat transfer at the surface is eliminated. The bottom surface is treated as an insulated boundary where no mass transport occurs, the heat transfer coefficient is zero, flames do not exist and the surrounding temperature is 300 K.

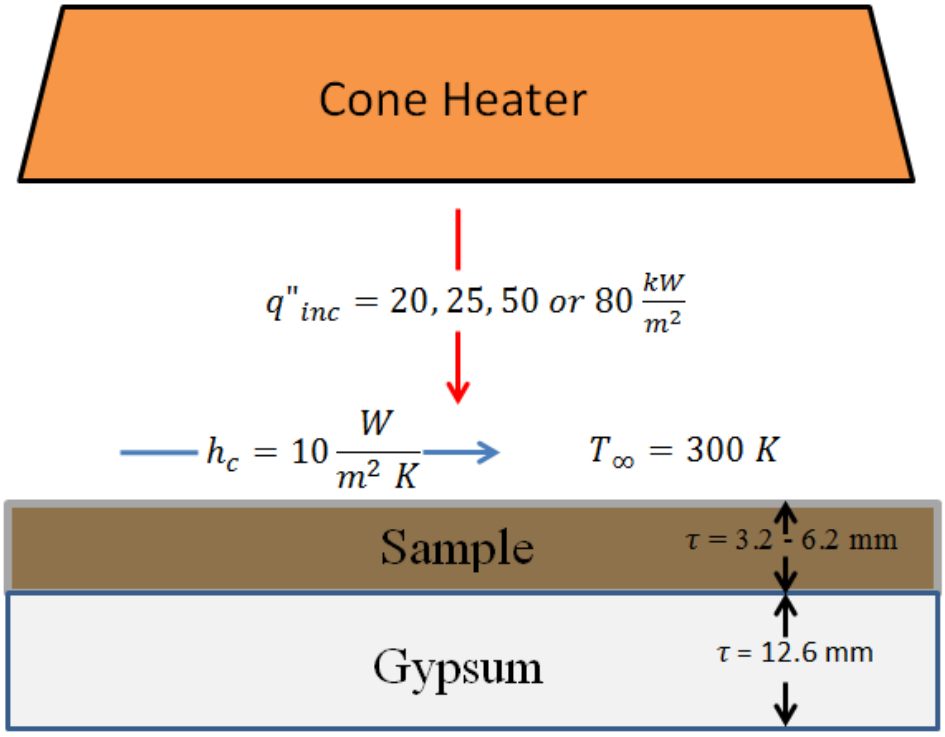

(a) Pre-ignition Boundary Conditions

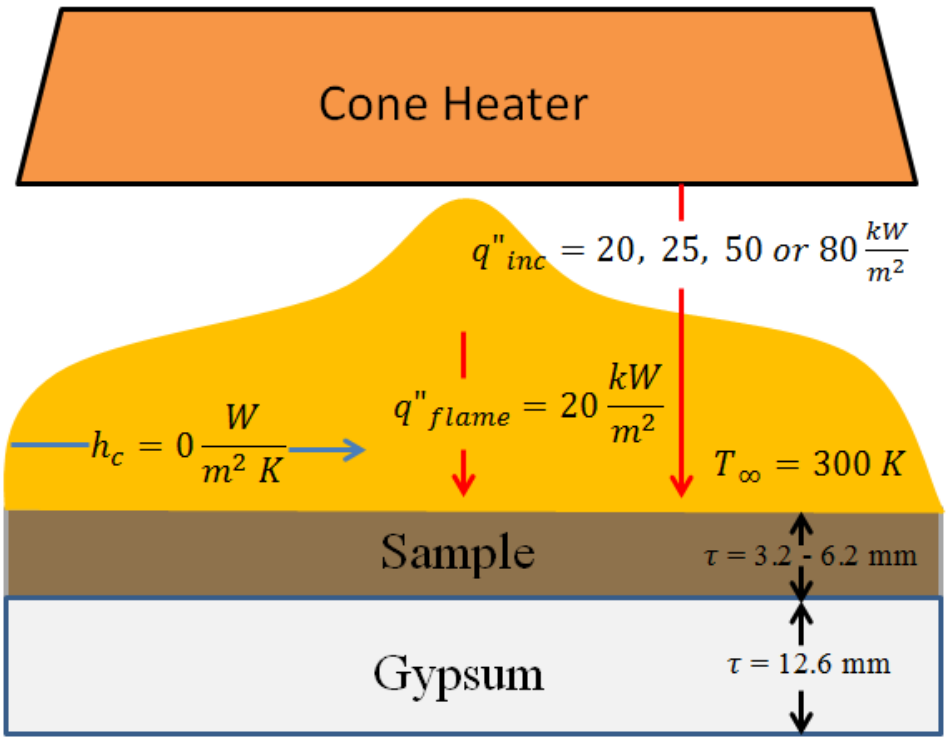

(b) Post ignition Boundary Conditions

Figure 58. ThermaKin2D cone calorimeter model and diagram. Image (a) provides the pre ignition boundary conditions, while image (b) provides the post ignition boundary conditions

The critical mass flux is an important parameter that is responsible for simulating flaming combustion above the surface of the material. When the mass loss rate of the volatile species reaches the specified critical mass flux, ignition is simulated and the flame boundary condition is turned on, thus subjecting the sample surface to additional 20×10^3 W m^{-2} of radiative heat flux. Lyon and Quintiere demonstrated through experiments and a theoretical analysis that that transient ignition occurs for a range of polymers at a virtual HRR needed for ignition (HRR^*) of 21×10^3 W m^{-2} $\pm$ 6×10^3 W m^{-2} [67]. The critical mass flux needed for ignition ($\dot{m}''_{crit}$) is determined based on Equation 26.

$$\dot{m}''_{crit} = \frac{HRR^*}{\Delta h_{eff}} \quad (26)$$

The critical mass flux is an important parameter that effects the time to ignition. It was determined for each sample by applying the effective heat of combustion value that was determined from the cone calorimeter experiments. The critical mass flux was another parameter that was altered during the optimization procedure by working within the acceptable range of HRR^* values (21×10^3 W m^{-2} $\pm$ 6×10^3 W m^{-2}).

There are a few more assumptions made during the pyrolysis modeling. These include assuming that the sample is perfectly flush on top of the gypsum and that the samples have a constant effective heat of combustion. During cone calorimeter sample preparation, the MDF sample was stapled to the gypsum wallboard. It is assumed that the MDF wallboard lays flush on top of the gypsum wallboard because there is no separation distance that can be seen between the two materials as shown in Figure 59.

Figure 59. MDF sample ontop of the gypsum wallboard

Also, the ThermaKin2D output file provides the mass loss rate of gaseous volatiles per unit area of the sample. Therefore, the mass loss rate per unit area needs to

be converted to HRRPUA so that the cone calorimeter model results could be compared to the experimental data. Equation 27 is used to convert the mass loss rate per unit area to HRRPUA by multiplying the mass loss rate per unit area ($\dot{m}$") by the effective heat of combustion value for each sample. The analysis of the cone calorimeter experiments in Section 3.2.1 provides a constant effective heat of combustion value for each sample.

$$HRRPUA = \dot{m}" * \Delta h_{eff} \quad (27)$$

During the cone calorimeter experiments, the side and back surface of the MDF sample and gypsum combination was sealed using aluminum foil. Fiberfrax insulation was also positioned under sample within the sample holder. This insured that the MDF surface was flush at the top of the sample holder edge frame. Only the MDF sample and the 0.0126 m of gypsum was included during the ThermaKin2D cone calorimeter modeling to save on computational time. Including the back surface Fiberfrax insulation and the aluminum foil did not alter the modeling results.

The model was evaluated at the following cell size and time step: Δx = 2.5e-5 m and Δt = 0.005 s. When the grid size and the time step were increased and decreased by a factor of two, the model results did not change, indicating convergence.

4.2.2 Cone Calorimeter Material Properties

The MCC experiments provided the stoichiometric char yield and the MCC optimization procedure provided the pre-exponential factor and the activation energy of each reaction. The thickness of each individual sample was measured using a caliper. The mass was divided by the average thickness to determine the sample density at

ambient temperature. The effective heat of combustion for each sample was derived from an analysis of the cone calorimeter experiments, previously discussed in Section 3.2.1. The char density for Sample C and Sample D was determined based on cone calorimeter testing and this was discussed in Section 3.2.2. When two consecutive reactions were specified, the intermediate density was specified to be the average of the virgin density and the char density. As discussed in Section 3.2.2, Sample A and Sample B were both unique materials that produced soft, brittle, ash-like char, which were difficult to analyze. During the cone calorimeter experiments, the height of the sample changed very little because the staples and edge frame restrained the samples. Since the staples prevented the sample from expanding, the sample structure was assumed to maintain a constant volume, while the mass and density decreased. Therefore, the char density of Sample A and Sample B was approximated by multiplying the initial sample density by the stoichiometric coefficient for either the intermediate reaction or the char producing reaction as shown in Equation 28a, Equation 28b and Equation 28c. Equation 28a was used to determine the char density when one single chemical reaction is specified. Equation 28b was utilized to find the char density of the sample when two consecutive chemical reactions are specified. Equation 28c was used to determine the intermediate density of the sample when two consecutive reactions are specified. This is referred to as the "constant volume analysis".

$$\rho_c = \rho_v * \theta_C \tag{28a}$$

$$\rho_c = \rho_v * \theta_I * \theta_C \tag{28b}$$

$$\rho_i = \rho_v * \theta_I \tag{28c}$$

The complete set of measured and mathematically estimated properties for the 1 Reaction Model and the 2 Reaction Model are provided in Table 14 and Table 15, respectively.

Table 14: Measured and Estimated Material Properties for the 1 Reaction Model

Parameters	Sample A	Sample B	Sample C	Sample D	Reference
Virgin Material					
Thickness [m]	6.2×10^{-3}	4.1×10^{-3}	3.6×10^{-3}	3.2×10^{-3}	Physical Measurement
Density [kg m^{-3}]	1089.4	889.3	888.8	1080.2	Physical Measurement
Pre-Exponential Factor [s^{-1}]	1.44×10^{7}	5.81×10^{7}	4.8×10^{6}	2.8×10^{8}	MCC Optimization
Activation Energy [J mol^{-1}]	1.04×10^{5}	1.15×10^{5}	1.02×10^{5}	1.2225×10^{5}	MCC Optimization
ΔH_{eff} [J kg $^{-1}$]	11.27×10^{6}	11.67×10^{6}	10.26×10^{6}	12.87×10^{6}	Cone Calorimeter Experiments
Char					
θ_C [%]	17.50	14.40	17.64	11.56	MCC Experiments
Density [kg m^{-3}]	190.7	128.1	382.4	255.0	Constant Volume Analysis or Cone Calorimeter Experiments

Table 15: Measured and Estimated Material Properties for the 2 Reaction Model

Parameters	Sample A	Sample B	Sample C	Sample D	Reference
Virgin Material Properties					
Thickness [m]	6.2×10^{-3}	4.1×10^{-3}	3.6×10^{-3}	3.2×10^{-3}	Physical Measurement
Density [kg m^{-3}]	1089.4	889.3	888.8	1080.2	Physical Measurement
θ_{CI} [%]	70.64	80.00	94.00	83.00	MCC Optimization
Pre-Exponential Factor [s^{-1}]	2.6×10^{7}	9.5×10^{7}	3.0×10^{7}	9.9×10^{8}	MCC Optimization
Activation Energy [J mol^{-1}]	9.99×10^{4}	1.06×10^{5}	8.34×10^{4}	1.15×10^{5}	MCC Optimization
ΔH_{eff} [J kg $^{-1}$]	11.27×10^{6}	11.67×10^{6}	10.26×10^{6}	12.87×10^{6}	Cone Calorimeter Experiments
Intermediate Material Properties					
Density [kg m^{-3}]	769.6	711.5	635.6	667.5	Constant Volume Analysis or Mean of Virgin & Char
θ_I [%]	24.77	17.99	18.77	13.93	MCC Optimization
Char					
θ_C [%]	17.50	14.40	17.64	11.56	MCC Experiments
Density [kg m^{-3}]	190.6	128.0	382.4	255.0	Constant Volume Analysis or Cone Calorimeter Experiments

The remaining thermal, optical and chemical properties that need to be determined are the k, c, ε and α, h and $\dot{m}''_{crit}$ of the virgin sample, char product and the intermediate component utilized during the 2 Reaction Model. These properties were determined for each sample by performing an optimization procedure using the

ThermaKin2D cone calorimeter model. The cone calorimeter model was simulated simultaneously at the three incident heat flux conditions and each individual property was manually adjusted until the model's prediction matched the experimental HRRPUA measurements. Beginning the cone calorimeter optimization procedure requires an initial guess for the unknown material properties, as well as the minimum and maximum range for which each property can be adjusted. The MDF samples analyzed in this project are composed of various types of wood products bound by resin. A thorough literature review of polymers, MDF and wood products was performed to obtain the initial guess and the lower and upper bounds for each property. Having a precise optimization ranged based on literature values ensures that the final set of material properties are realistic. The gypsum properties are also presented in this section. All the material properties are temperature independent, except for the thermal conductivity of char. This optimization procedure was separately performed for each sample's 1 Reaction Model and 2 Reaction Model. A total of 8 optimization procedures were performed.

The virgin polymer properties are based on a paper authored by Stoliarov et al. where the literature was reviewed to obtain the thermal, optical and chemical properties for a wide range of many synthetic polymers [65]. The mean and standard deviation for each property value was calculated. Table 16 provides each properties average value, as well as the lower and upper bound obtained during the literature review. These polymers produce char and their properties are independent of temperature. In this paper, ThermaKin2D was used to perform a sensitivity analysis on each property to determine its relative importance during pyrolysis modeling.

Table 16: Average, Lower Bound and Upper Bound Polymer Properties [65]

Property	Lower Boundary	Average Value	Upper Boundary
Thermal Conductivity [W m^{-1} K^{-1}]	0.11	0.24	0.42
Heat Capacity [J kg^{-1} K^{-1}]	1700	2300	2900
Emissivity [-]	0.75	0.88	0.94
Absorption coefficient [m^2 kg^{-1}]	0.6	3.0	10.8
Heat of reaction [J kg^{-1}]	-7×10^5	-1.3×10^6	-2.5×10^6

The samples analyzed in this project produce between 11.6 % and 17.6 % char. In his dissertation, Li tested 15 common polymers to determine their various properties for condensed phase modeling [66]. A large body of his work focused on determining the properties of char. Li performed simultaneous thermal gravimetric analysis - differential scanning calorimetry (TGA-DSC) tests, as well as controlled atmosphere pyrolysis apparatus (CAPA) tests to obtain the chemical properties for each reaction and the thermal properties of the virgin material and its char. Li produced 8 temperature dependent heat capacity equations for the char of the various polymers. An average equation for the heat capacity of char was developed by fitting the data with a linear expression. A single temperature independent value for the heat capacity of char was determined to be 1500 J kg^{-1} K^{-1} by evaluating the expression from 600 K to 1000 K, the temperature range at which char is formed. Li determined the absorption coefficient of the materials by placing a thin piece of each sample between a cone heater and a heat flux gauge to measure the transmitted heat flux. Using the Beer-Lambert law, the absorption coefficient was determined for the virgin sample, intermediate component and char to be between 1.36 m^2 kg^{-1} and 100 m^2 kg^{-1}. Li also reviewed the literature to determine the emissivity of the materials. He claimed that when char is formed, it has a similar emissivity to graphite, which is reported to be 0.86 [68]. Li also states that the heat capacity of all gaseous decomposition products should be 1.8×10^3 J kg^{-1} K^{-1}, which is the average heat capacity of various hydrocarbons decomposing from 400 K to 500 K.

Li, Fleischmann and Spearpoint analyzed MDF to determine expressions for the thermal properties of the virgin sample its char product [69]. The heat capacity was found using the DSC tests. The virgin MDF heat capacity expression was evaluated from ambient temperature, 300 K to the peak decomposition temperature, 1000 K. The lower and upper bounds for the heat capacity of MDF is 1100 and 2900 J kg^1 K^{-1}.

Another paper by Li, Pau, Hou and Ji was utilized to estimate the heats of reaction for MDF [63]. In this paper, MDF was tested using the TGA-DSC to obtain the kinetic parameters and the heats of reaction of the individual components. There were two major endothermic reactions that occurred during decomposition. The MDF resin is reported to have the highest heat of reaction of -5.3×10^5 J kg^{-1}, while cellulose is responsible for the lowest heat of reaction at -1.5×10^5 J kg^{-1}.

In Gronli's dissertation, a literature review, experiments and modeling were performed to obtain the chemical, thermal and optical properties of different types of wood [70]. Gronli cites a book by Raznjevic, who determined the lower and upper bounds for the thermal conductivity of variety of virgin wood products to be 0.08 W m^{-1} K^{-1} and 4.20 W m^{-1} K^{-1}, respectively. Gronli also cities a paper by Havens et al. regarding TGA-DSC experiments on pine and oak, where the heats of reaction was determined to be between -1.1×10^5 J kg^{-1} and 2.0×10^5 J kg^{-1} [71].

In McKinnon's thesis, a pyrolysis model was developed to simulate the flaming combustion of cardboard [60]. Cardboard is a lignocellulosic material general composed of cellulose, hemicellulose and lignin, similar to MDF. McKinnon approximates the thermal conductivity of char as a temperature dependent expression based on the

radiation diffusion approximation [60]. The radiation diffusion approximation assumes that conductive heat transfer through the char is driven by radiation. Equation 29 provides the radiation diffusion correlation utilized to determine the thermal conductivity of char (k_c).

$$k_c = \beta T^3 \tag{29}$$

The char thermal conductivity is based on a user-controlled constant (β) and temperature to the third power. McKinnon used a β value between 1.5×10^{-10} and 1.5×10^{-9}. McKinnon also found that cardboard had an emissivity of 0.70.

The MDF samples were backed by the gypsum wallboard during the cone calorimeter experiments and the full-scale experiments. Therefore, both the thermal and optical properties of gypsum must also be specified for the bench-scale and full-scale pyrolysis models. Ultralight gypsum wallboard used during the cone calorimeter tests were carefully weighed on a scale and measured using a caliper to obtain the mass and dimensions. The thickness of the gypsum at room temperature is 1.26×10^{-2} m. The density at room temperature was calculated to be 480.6 kg m^{-3} by dividing the mass by the cubic volume. The thermal conductivity and heat capacity were selected from a literature review of Rahmanian's dissertation regarding the thermal and mechanical properties of gypsum wallboard during fire conditions [72]. Gypsum wallboard is non fire-rated much like the gypsum wallboard utilized during this project. Rahmanian provided the effective thermal conductivity of gypsum wallboard for a range of temperature conditions and this graph is shown in Figure 60a. Since most of the properties are temperature independent, one thermal conductivity value was selected to

characterize the gypsum wallboard. The lowest thermal conductivity value was selected (0.1 W m^{-1} K^{-1}) because the MDF is not perfectly flush on top of the gypsum. Presumably, there are a few small air pockets between the bottom of the sample and the top of the gypsum. At elevated temperatures, air possesses a very low thermal conductivity. The lowest possible value of the gypsum thermal conductivity was selected to account for this imperfection. Rahmanian also provides the heat capacity of gypsum which is also based her analysis of the literature. Figure 60b shows the heat capacity of gypsum over a range temperature conditions. Rahmanian states that the room temperature heat capacity is 950 J kg^{-1} K^{-1} and that the two peaks in heat capacity are due to "two dehydration reactions" [72]. Once again, our goal is to use constant material properties and therefore a gypsum heat capacity of 950 J kg^{-1} K^{-1} was selected. The gypsum was provided with an arbitrarily high absorption coefficient (1000 m^2 kg^{-1}) so that it is represented as a non-transparent object that absorbs all the radiation at its surface. The model was simplified by providing gypsum with an emissivity of 0, which makes the back surface of the gypsum adiabatic.

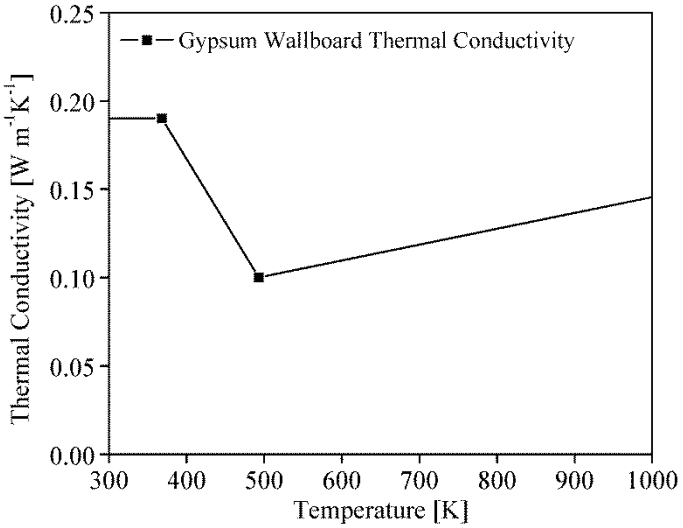

(a)

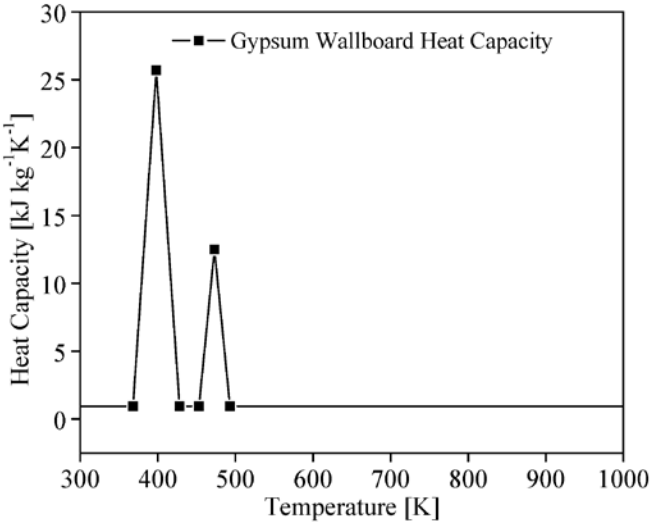

(b)

Figure 60. Gypsum thermal properties. Graph (a) provides a graph of the gypsum thermal conductivity and Graph (b) provides a graph of the gypsum heat capacity

This general procedure for obtaining the sample material properties is intended to be applied to any type of material, not just MDF. The literature review by Stoliarov et al. analyzed a wide range of polymers consistently used in modern-day applications [65]. Therefore, the initial guess, as well as the minimum and maximum range for which the virgin material properties can be adjusted is based on the average polymer properties and their lower and upper bounds reported in Table 16. When an intermediate component and reaction was introduced for the 2 Reaction Model, the initial properties of the intermediate component matched the initial properties of the virgin sample.

Some adjustments to the initial guess and the bounds were made based on the property values found during the literature review. The lower bound for the thermal conductivity of polymers was reported to be 0.11 W m^{-1} K^{-1}. Gronli found that some wood products have thermal conductivity values as low as 0.08 W m^{-1} K^{-1} [70]. Therefore, the minimum range for the virgin sample and intermediate component was

lowered to 0.07 W m^{-1} K^{-1} to provide 10% more room for improvement. The lower bound polymer heat capacity was reported to be 1700 J kg^{-1} K^{-1}. Li et al. showed that MDF could have a heat capacity as low as 1100 J kg^{-1} K^{-1} and thus, the adjustable range was altered accordingly [69]. The lower range for the emissivity of polymers is 0.75. McKinnon showed that his lignocellulosic material had an emissivity of 0.70 [60]. Therefore, the lower range of the virgin sample and intermediate component's emissivity was adjusted to 0.70. The upper bound for the virgin sample, intermediate component and char absorption coefficient was adjusted to 100 m^2 kg^{-1}, to reflect the work by Li [66]. The initial guess for the char absorption was set to 10 m^2 kg^{-1} to better represent the non-transparency of char. Li et al. and Gronli both showed that the heat of reaction for MDF and wood is endothermic and much lower than the minimum range reported for polymers [63] [70]. The lower bound polymer heat of reaction was first utilized because -7e5 J mol^{-1} is much closer to the reported heat of reaction for wood and MDF. Theoretically, some reactions will have zero heat of reaction. Therefore, the lower bound for the heat of reaction was adjusted to 0. The radiation diffusion approximation was used to represent the char thermal conductivity. A midrange value of 5×10^{-10} was utilized as the initial guess for β. The lower and upper bounds for β was set to 1×10^{-10} and 1×10^{-9}, based on McKinnon's β value [60]. Table 17 provides the initial guess used during the cone calorimeter optimization procedure. Table 17 also provides the minimum and maximum range for which these properties can be changed during the optimization procedure. All of these properties are independent of temperature, except for the char thermal conductivity.

Table 17: Cone Optimization Adjustable Properties: Initial Property Value and Adjustable Range

Property	Initial Value	Minimum Range	Maximum Range
Virgin Sample			
Thermal Conductivity [W m^{-1} K^{-1}]	0.24	0.07	0.42
Heat Capacity [J kg^{-1} K^{-1}]	2300	1100	2900
Emissivity [-]	0.88	0.70	0.94
Absorption coefficient [m^2 kg^{-1}]	3	0.6	100
Ignition Mass Flux [kg s^{-1} m^{-2}]	$m''_{crit} = \frac{21 \times 10^3}{\Delta H_{eff}}$	$m''_{crit} = \frac{15 \times 10^3}{\Delta H_{eff}}$	$m''_{crit} = \frac{27 \times 10^3}{\Delta H_{eff}}$
Heat of Reaction [J kg^{-1}]	-7×10^5	0	-2.5×10^6
Intermediate Component			
Thermal Conductivity [W m^{-1} K^{-1}]	0.24	0.07	0.42
Heat Capacity [J kg^{-1} K^{-1}]	2300	1100	2900
Emissivity [-]	0.88	0.70	0.94
Absorption coefficient [m^2 kg^{-1}]	3	0.6	100
Heat of Reaction [J kg^{-1}]	-7×10^5	0	-2.5×10^6
Char			
Thermal Conductivity [W m^{-1} K^{-1}]	$5\times10^{-10}*T^3$	$1\times10^{-10}*T^3$	$1\times10^{-9}*T^3$
Absorption coefficient [m^2 kg^{-1}]	10	0.6	100

Lastly, there are several non-adjustable material properties. These include the measured or estimated properties reported in Table 14 and Table 15, as well as the properties of gypsum wallboard. They also include the heat capacity and emissivity of char and the heat capacity of the gaseous volatiles. The char heat capacity and emissivity is set to 1500 J kg^{-1} K^{-1} and 0.86, respectively, while the gaseous volatiles heat capacity is 1.8 J kg^{-1} K^{-1} [66]. The initial analysis indicates that the modeling results were not impacted by changes to these parameters. Therefore, the average literature values were used and not adjusted in order to reduce the amount of unknown parameters and simplify the optimization procedure.

4.2.3 Cone Calorimeter Model Initial Attempt

The initial component property values provided in Table 17 were implemented into the cone calorimeter model to begin the optimization procedure. The prediction of HRRPUA for the initial model attempt is compared to the experimental results for each

sample's 1 Reaction Model and 2 Reaction Model in Figure 61, Figure 62, Figure 63 and Figure 64 for Sample A, Sample B, Sample C and Sample D, respectively.

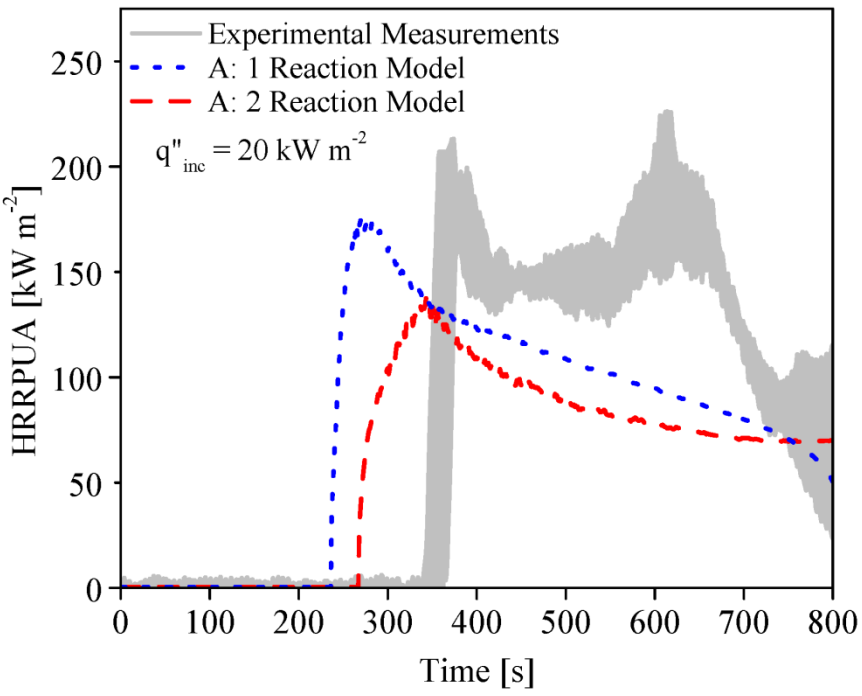

(a)

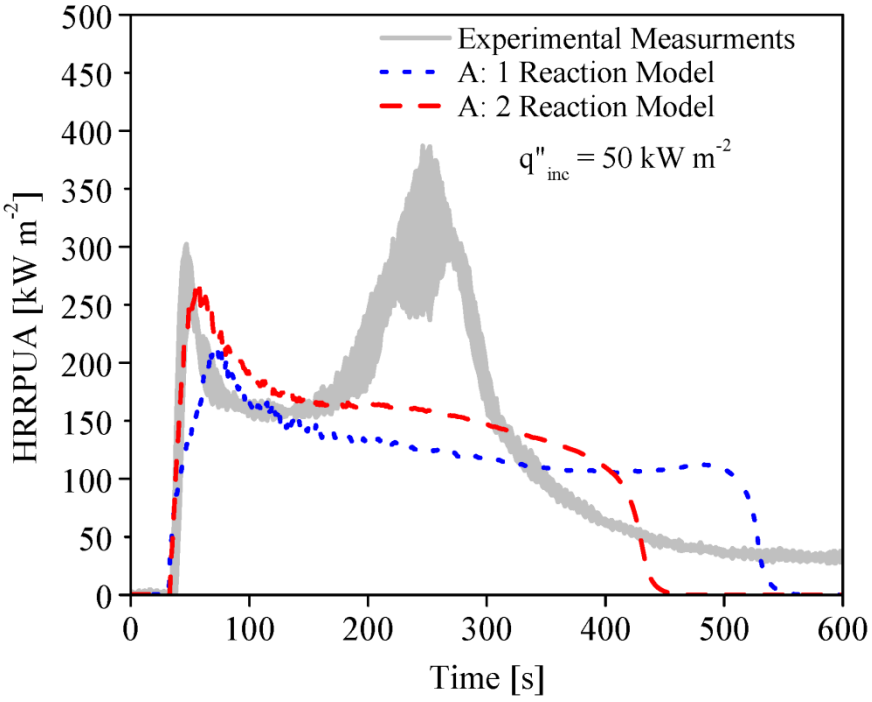
Experimental Measurments
A: 1 Reaction Model
A: 2 Reaction Model
q"inc = 50 kW m-2
HRRPUA [kW m-2]
Time [s]
0
50
100
150
200
250
300
350
400
450
500
0
100
200
300
400
500
600

(b)

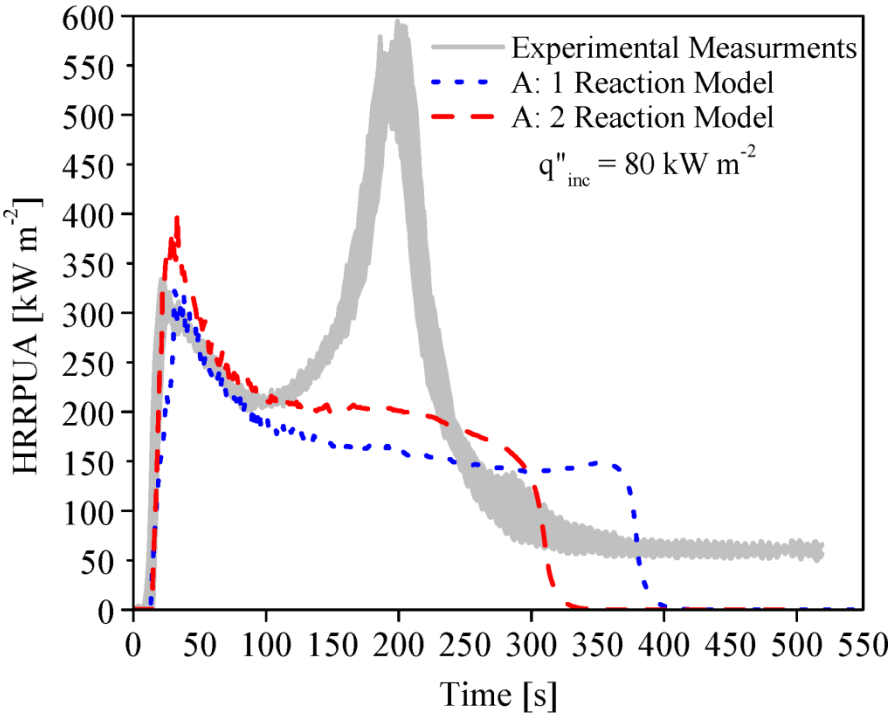
Experimental Measurments
A: 1 Reaction Model
A: 2 Reaction Model
q"inc = 80 kW m-2
HRRPUA [kW m-2]
Time [s]
0
50
100
150
200
250
300
350
400
450
500
550
600
0
50
100
150
200
250
300
350
400
450
500
550

(c)

Figure 61. Sample A cone calorimeter model initial prediction of the single reaction and two consecutive reactions compared to the experimental measurements. The experiments and models were conducted at 20 kW/m^2, 50 kW/m^2 and 80 kW/m^2 in graph (a), graph (b) and graph (c), respectively

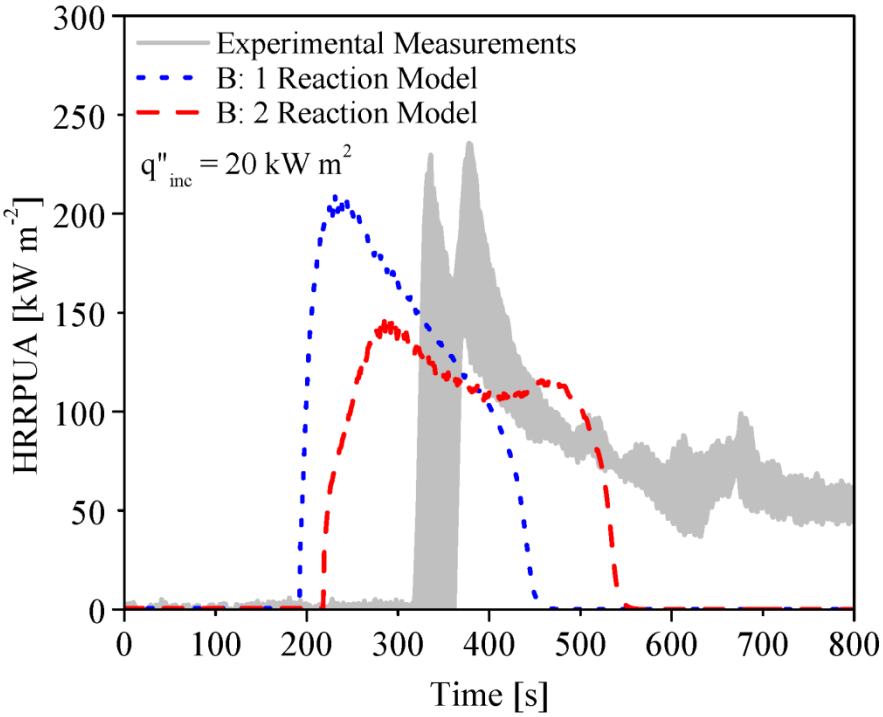

(a)

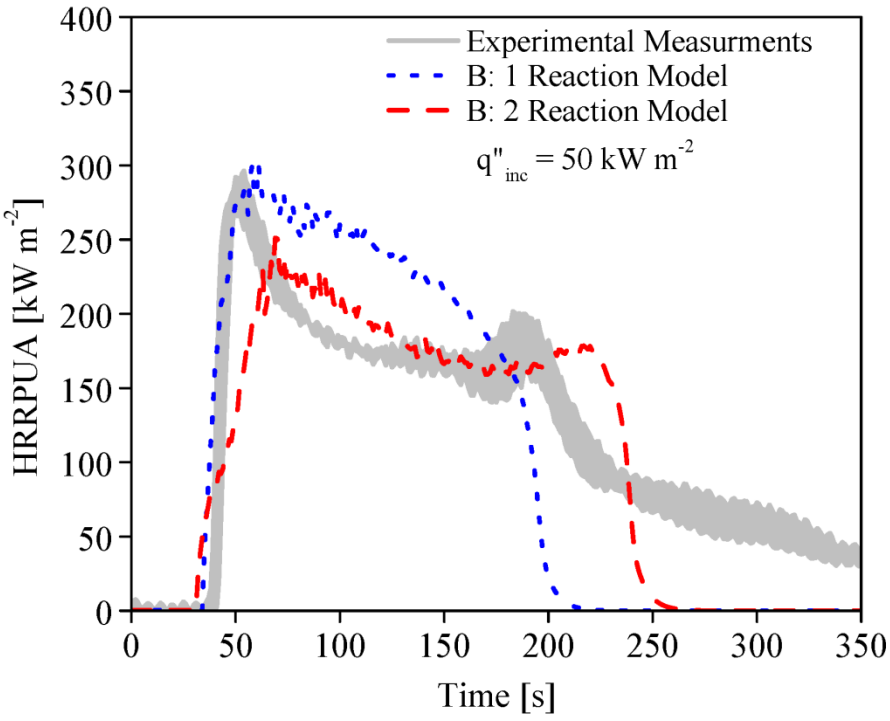
Experimental Measurments
B: 1 Reaction Model
B: 2 Reaction Model
q"inc = 50 kW m-2
HRRPUA [kW m-2]
Time [s]
0
50
100
150
200
250
300
350
400

(b)

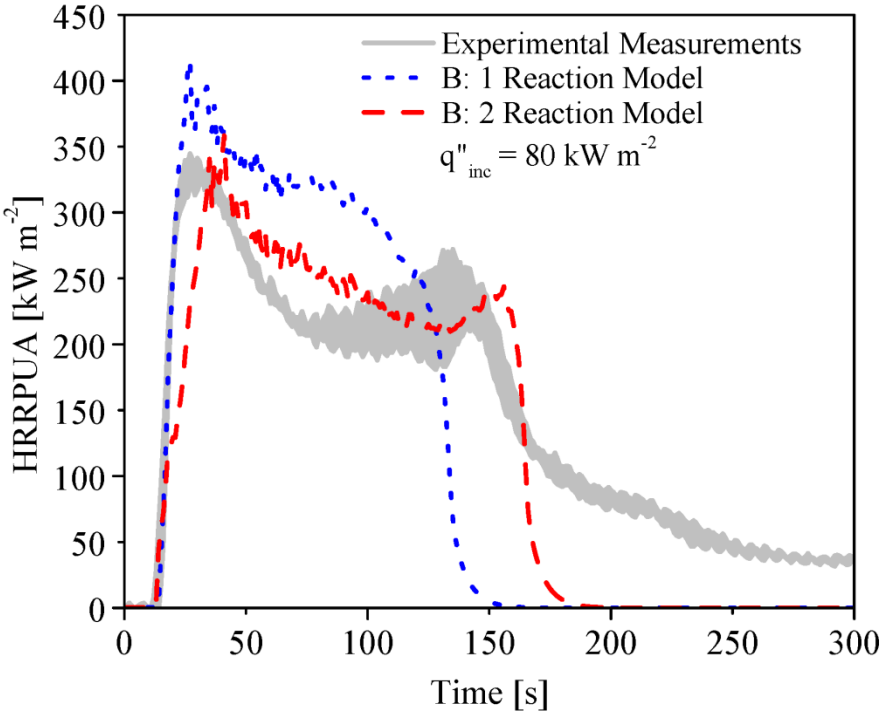
Experimental Measurements
B: 1 Reaction Model
B: 2 Reaction Model
q"inc = 80 kW m-2
HRRPUA [kW m-2]
Time [s]
0
50
100
150
200
250
300
350
400
450

(c)

Figure 62. Sample B cone calorimeter model initial prediction of the single reaction and two consecutive reactions compared to the experimental measurements. The experiments and models were conducted at 20 kW/m^2, 50 kW/m^2 and 80 kW/m^2 in graph (a), graph (b) and graph (c), respectively

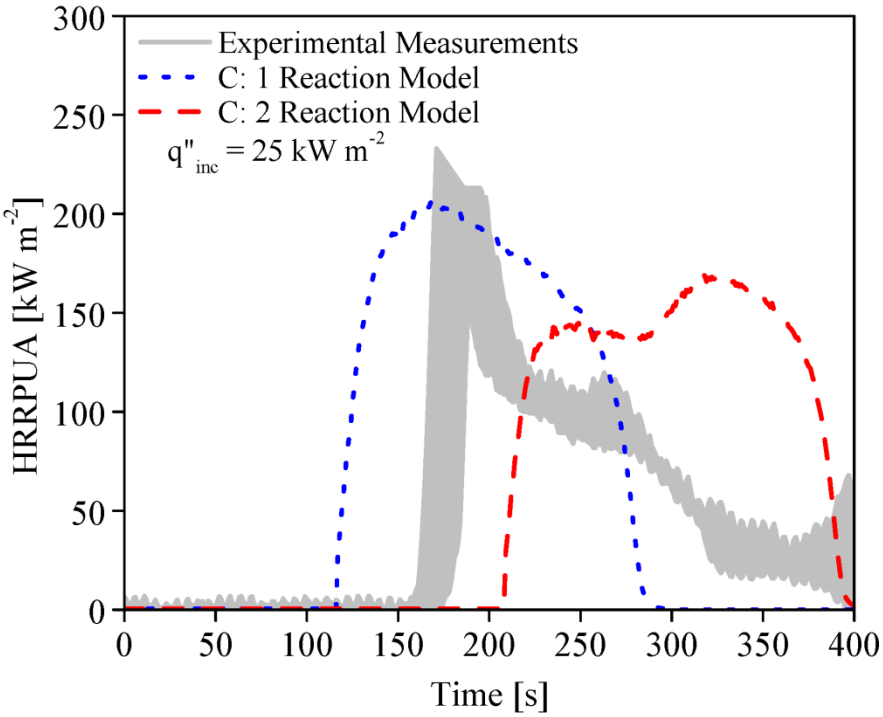

(a)

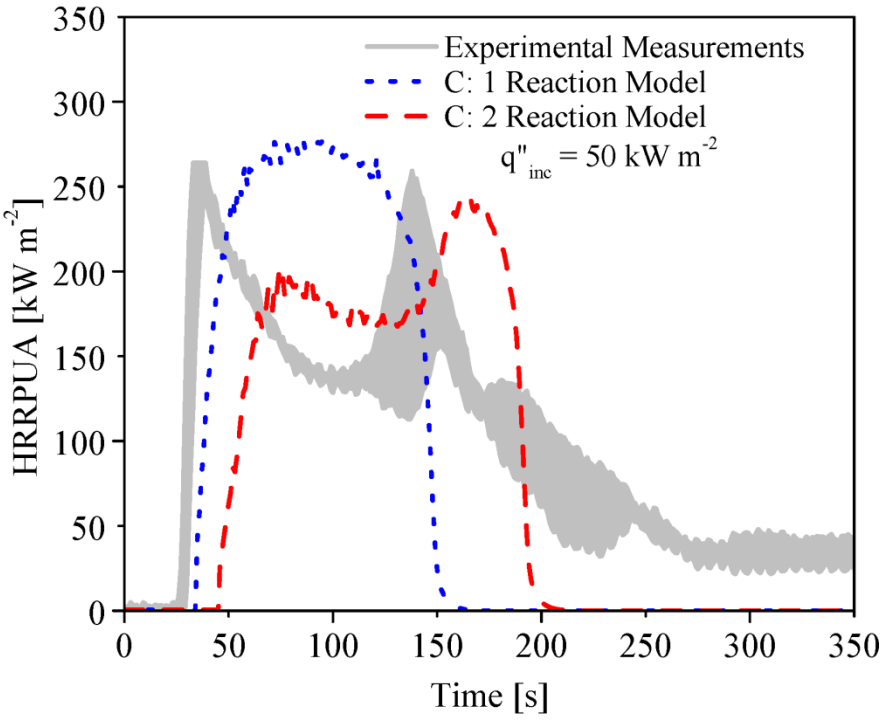
Experimental Measurements
C: 1 Reaction Model
C: 2 Reaction Model
q"inc = 50 kW m-2
HRRPUA [kW m-2]
Time [s]
0
50
100
150
200
250
300
350

(b)

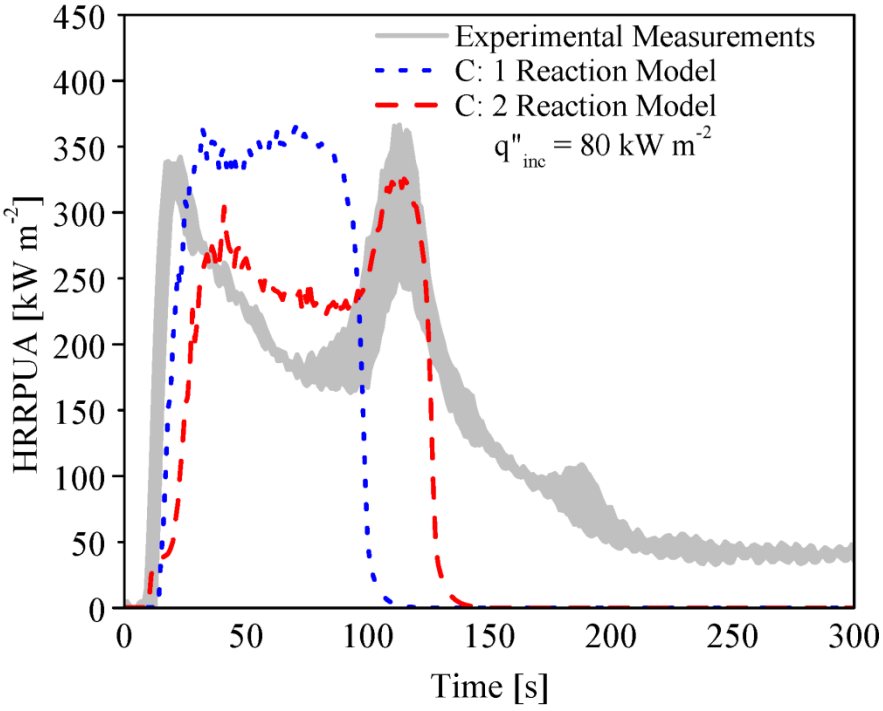
Experimental Measurements
C: 1 Reaction Model
C: 2 Reaction Model
q"inc = 80 kW m-2
HRRPUA [kW m-2]
Time [s]
0
50
100
150
200
250
300
350
400
450

(c)

Figure 63. Sample C cone calorimeter model initial prediction of the single reaction and two consecutive reactions compared to the experimental measurements. The experiments and models were conducted at 25 kW/m^2, 50 kW/m^2 and 80 kW/m^2 in graph (a), graph (b) and graph (c), respectively

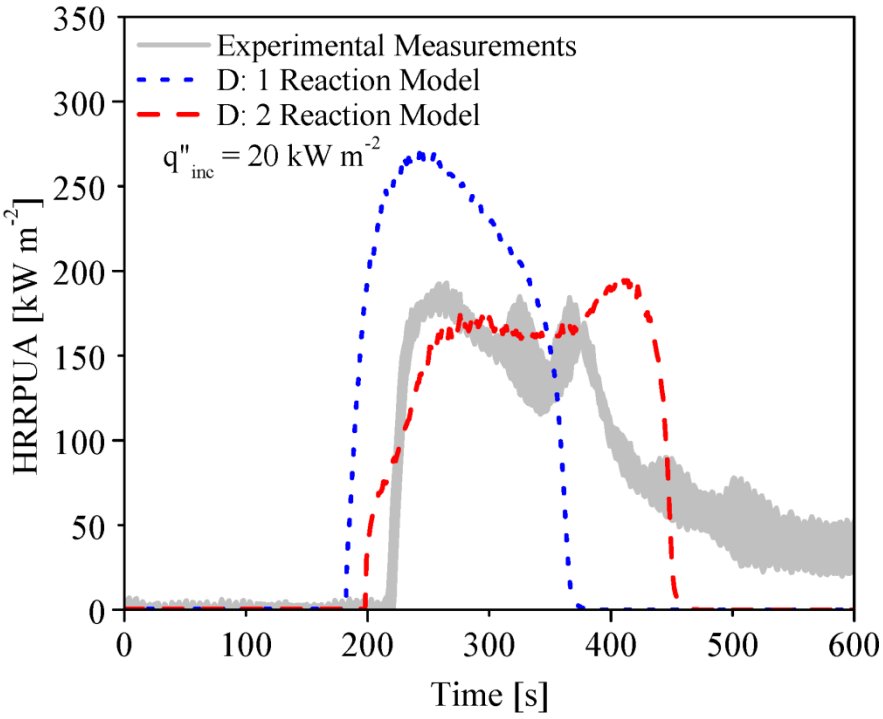

(a)

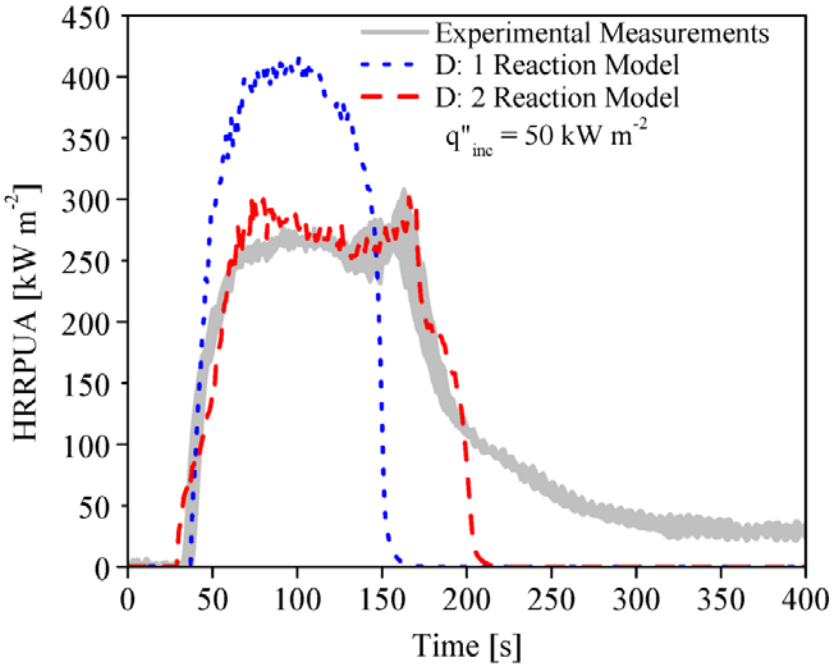

(b)

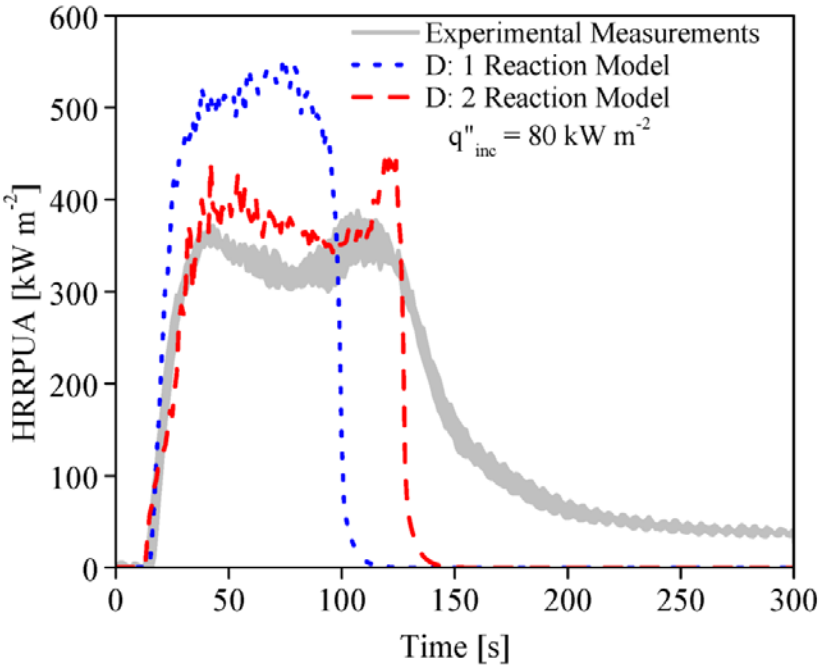

(c)

Figure 64. Sample D cone calorimeter model initial prediction of the single reaction and two consecutive reactions compared to the experimental measurements. The experiments and models

were conducted at 20 kW/m^2, 50 kW/m^2 and 80 kW/m^2 in graph (a), graph (b) and graph (c), respectively

The material properties utilized in the initial cone calorimeter model are based on the discussion of the measured and estimated properties, average polymer properties and literature values discussed in Section 4.2.2. The initial model does a decent job of predicting the cone calorimeter experiments. At the lower incident heat flux conditions, the models are systematically under predicting the ignition time. At higher incident heat flux conditions, the 2 Reaction Model does a decent good at predicting the HRRPUA curves for Sample B and Sample D. Both reaction models are unable to predict the second HRR peak for Sample A and aspects of the HRRPUA curve for Sample C. Overall, the fits of both reaction models must be improved. In the following section, the optimization procedure will be discussed in which the sample properties are adjusted to better fit the HRRPUA curves for all heat flux conditions.

4.2.4 Cone Calorimeter Optimization Procedure

The goals of the optimization procedure was to simultaneously simulate the cone calorimeter model at each incident heat flux and perform a manual iteration by individually changing the desired properties until the model's prediction of HRRPUA matched the experimental results. In some cases the entire HRRPUA curve could not be matched. Since the project objective is to model flame spread, the optimization procedure was tailored so that the most important aspects of the HRRUPA curve were matched. The following approach was utilized: first match the time to ignition, followed by the height and shape of the first HRRPUA peak, then the time to the transition to smoldering and lastly the time and shape of the second HRRPUA peak. During upward

flame spread scenario, the heat flux from the burner and or the flame produce heat flux conditions between 0 W m^{-2} to 55×10^3 W m^{-2}. While the heat flux does increase to a higher range once the room approaches flashover conditions, it is not the predominant conditions these samples face during the initial stages of fire development in the room corner scenario. Thus, the most important incident heat flux condition to match were the lower conditions (20×10^3 W m^{-2} and 25×10^3 W m^{-2}), followed by incident heat flux at 50×10^3 W m^{-2}, and then the heat flux at 80×10^3 W m^{-2}.

As shown in Table 17, the 1 Reaction Model contained 8 unknown parameters, while the 2 Reaction Model contained 11 unknown parameters. The cone calorimeter optimization procedure was first performed for each sample's 1 Reaction Model because it contains the least amount of unknown parameters. Next, the properties were determined for the sample's 2 Reaction Model. Prior to beginning the optimization procedure, a sensitivity analysis was performed to understand the influence each property possessed. Combining that knowledge with the sensitivity analysis performed in Stoliarov et al. [65], an optimization guide was developed to better assist those interested in utilizing this approach. This guide is provided in Table 18. The cone calorimeter optimization guide was developed by determining the sensitivity of the HRRPUA results to changes in the thermal and optimal properties of the virgin and char components. A hypothetical material was created based on the initial property values reported in Table 17. All the measured material properties were calculated to be the average value of the four samples analyzed in this project. The properties of this hypothetical material are as follows; thickness, virgin thermal conductivity (k_v), virgin heat capacity (c_v), virgin emissivity (e_v), virgin absorption coefficient (a_v), heat of reaction (H), critical mass flux for

ignition (m''_{crit}), char thermal conductivity (k_c), char heat capacity (c_c), char emissivity (e_c) and char absorption coefficient (a_c) are equal to 4.3×10^{-3} m, 0.24 W m^{-1} K^{-1}, 2300 J kg^{-1} K^{-1}, 0.88, 3 m^2 kg^{-1}, 7×10^5 J kg^{-1}, 2.33×10^{-3} kg m^{-2} s^{-1}, $5\times10^{-10}\times T^3$ W m^{-1} K^{-1}, 1500 J kg^{-1} K^{-1}, 0.86, and 10 m^2 kg^{-1}, respectively. Each thermal and optical property was changed 25% to assess the impact this change had on the ignition time, burnout time, and HRR curve. Table 18 provides a guide detailing how to influence certain aspects of the HRR curve based on which parameters are most impactful.

Table 18: Cone Calorimeter Optimization Guide

External Heat Flux Conditions	Desired Change
	↑ **t_{ign}**
20×10^3 W m^{-2}	↓ e_v > ↑ c_v > ↑ m''_{crit} > ↑ H > ↑ k_v
50×10^3 W m^{-2}	↓ e_v > ↑ c_v > ↑ k_v
80×10^3 W m^{-2}	↓ e_v > ↑ c_v > ↑ k_v
	↓ **t_{ign}**
20×10^3 W m^{-2}	↓ c_v > ↑ e_v > ↓ m''_{crit} > ↓ k_v > ↓ H
50×10^3 W m^{-2}	↓ c_v > ↑ e_v > ↓ k_v
80×10^3 W m^{-2}	↓ c_v > ↑ e_v > ↓ k_v
	↑ **HRR_{1st}**
20×10^3 W m^{-2}	↓ H > ↑ k_v = ↓ c_v = ↑ e_c > ↓ a_v
50×10^3 W m^{-2}	↓ H > ↑ e_c > ↓ c_v > ↑ k_v > ↑ e_v = ↓ a_v
80×10^3 W m^{-2}	↓ H > ↓ c_v > ↑ c_e = ↑ e_v > ↓ a_v
	↓ **HRR_{1st}**
20×10^3 W m^{-2}	↑ H > ↓ e_c > ↓ k_v = ↑ v_c
50×10^3 W m^{-2}	↑ H > ↑ v_c = ↓ e_c > ↓ e_v
80×10^3 W m^{-2}	↑ H > ↓ e_c > ↑ c_v > ↓ e_v > ↑ a_v = ↑ k_v
	↑ **HRR_{2nd}**
20×10^3 W m^{-2}	↓ a_c > ↑ k_c
50×10^3 W m^{-2}	↓ H > ↓ a_c > ↑ k_v
80×10^3 W m^{-2}	↓ H > ↓ a_c > ↑ k_c > ↑ k_v = ↑ e_c
	↓ **HRR_{2nd}**
20×10^3 W m^{-2}	↓ k_c
50×10^3 W m^{-2}	↓ k_c > ↓ k_v > ↑ a_v
80×10^3 W m^{-2}	↓ k_c > ↓ k_v
	→ **HRR_{1st}**
All Conditions	↓c_a > ↓ e_v = ↑ c_v > ↑ k_v > ↑ H
	← **HRR_{1st}**
All Conditions	↓ c_v > ↑ e_v > ↓ k_v > ↓ H

4.2.5 Cone Calorimeter Optimization Results

Many of Sample A's properties had to be altered to achieve a satisfactory fit of the experimental curves. Figure 65a, Figure 65b and Figure 65c provide the final HRRPUA predictions from the cone calorimeter model of Sample A's 1 Reaction Model and 2 Reaction Model at an incident heat flux of 20×10^3 W m^{-2}, 50×10^3 W m^{-2} and 80×10^3 W m^{-2}, respectively. In these figures, the model's prediction is compared to the experimental results. Table 19 provides the final set of material properties for Sample A. All of these properties are within the minimum and maximum property ranges.

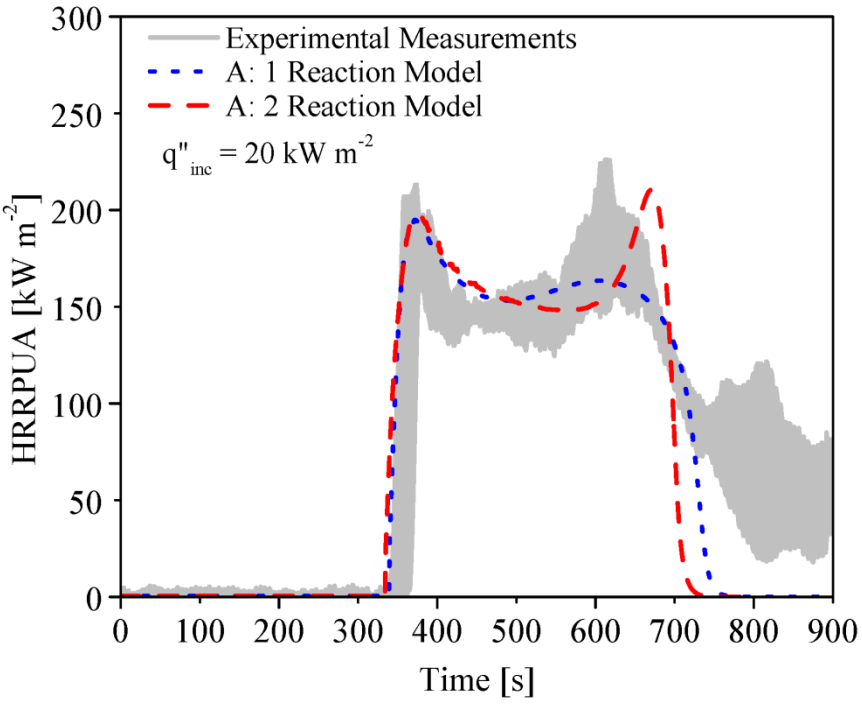

(a)

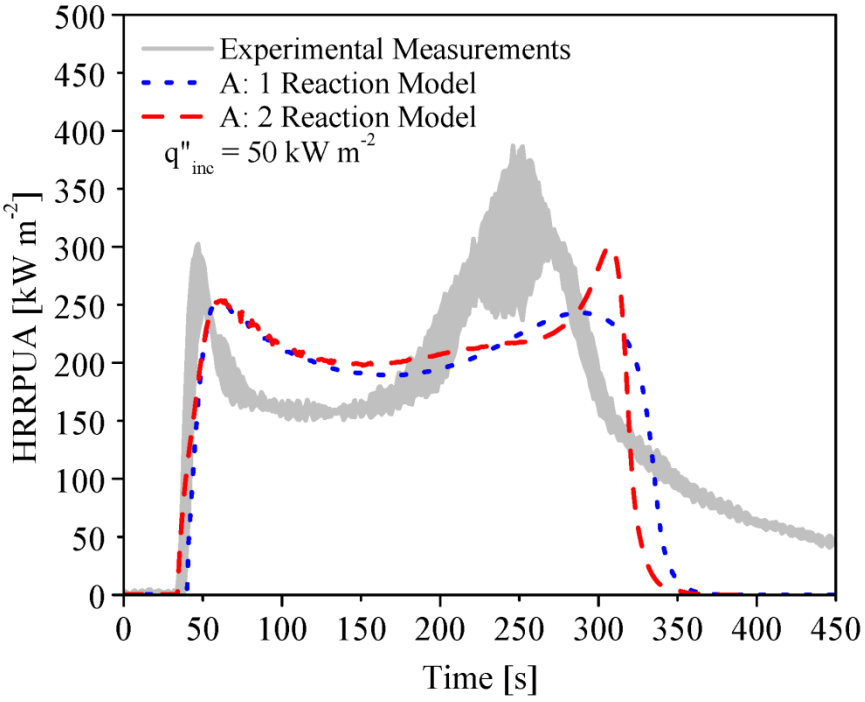
Experimental Measurements
A: 1 Reaction Model
A: 2 Reaction Model
q"inc = 50 kW m-2
HRRPUA [kW m-2]
Time [s]
0
50
100
150
200
250
300
350
400
450
500

(b)

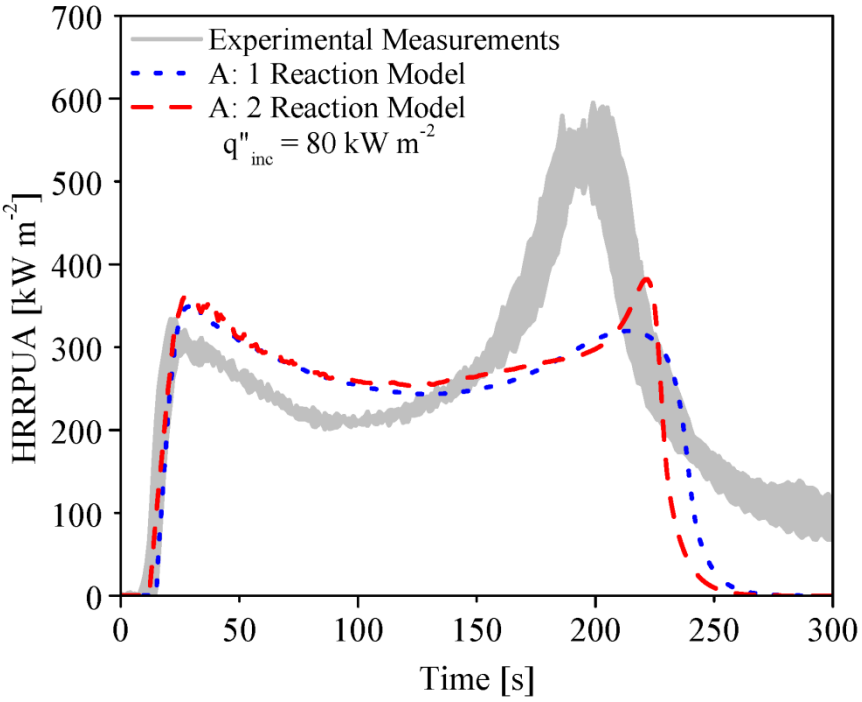
Experimental Measurements
A: 1 Reaction Model
A: 2 Reaction Model
q"inc = 80 kW m-2
HRRPUA [kW m-2]
Time [s]
0
50
100
150
200
250
300
400
500
600
700

(c)

Figure 65. Sample A cone calorimeter final model prediction of the single reaction and two consecutive reactions compared to the experimental measurements. The experiments and models were conducted at 20 kW/m^2, 50 kW/m^2 and 80 kW/m^2 in graph (a), graph (b) and graph (c), respectively

Table 19: Sample A - Final Set of Optimized Properties

Virgin Material Properties			
Parameter	**1 Reaction**	**2 Reactions**	**Reference**
Thickness [m]	0.0062		Physically Measured
Density [kg m^{-3}]	1089.4		
Thermal Conductivity [W m^{-1} K^{-1}]	0.2	0.235	Cone Optimization
Heat Capacity [J kg^{-1} K^{-1}]	2900	2550	
Emissivity [-]	0.82	0.88	
Absorption coefficient [m^2 kg^{-1}]	20	25	
Ignition Mass Flux [kg s^{-1} m^{-2}]	2.22×10^{-3}	2.40×10^{-3}	
Heat of Reaction [J kg^{-1}]	-3×10^{5}	-4×10^{5}	
θ_C or θ_I [%]	17.50	70.64	MCC Experiments/ MCC Optimization
Pre-Exponential Factor [s^{-1}]	1.44×10^{7}	2.6×10^{7}	MCC Optimization
Activation Energy [J mol^{-1}]	1.04×10^{5}	9.99×10^{4}	
ΔH_{eff} [J kg^{-1}]	11.27×10^{6}		Cone Calorimeter Experiments
Intermediate Material Properties			
Density [kg m^{-3}]	-	769.7	Constant Volume Analysis
Thermal Conductivity [W m^{-1} K^{-1}]	-	0.324	Cone Optimization
Heat Capacity [J kg^{-1} K^{-1}]	-	1500	
Emissivity [-]	-	0.86	
Absorption coefficient [m^2 kg^{-1}]	-	30	
Heat of Reaction [J kg^{-1}]	-	-1×10^{5}	
θ_{CI} [%]	-	24.77	MCC Optimization
Pre-Exponential Factor [s^{-1}]	-	1.80×10^{11}	
Activation Energy [J mol^{-1}]	-	1.55×10^{5}	
Char Material Properties			
Density [kg m^{-3}]	190.6	190.6	Constant Volume Analysis
Thermal Conductivity [W m^{-1} K^{-1}]	$9.5\times10^{-10}*T^3$	$9\times10^{-10}*T^3$	Cone Optimization
Absorption coefficient [m^2 kg^{-1}]	35	20	
Heat Capacity [J kg^{-1} K^{-1}]	1500		Literature
Emissivity [-]	0.86		

Figure 66a, Figure 66b and Figure 66c provide the final HRRPUA curves for the 1 Reaction Model and 2 Reaction Model for Sample B compared to the experimental results. Table 20 provides the final set of properties for both models. All of these properties are within the acceptable range.

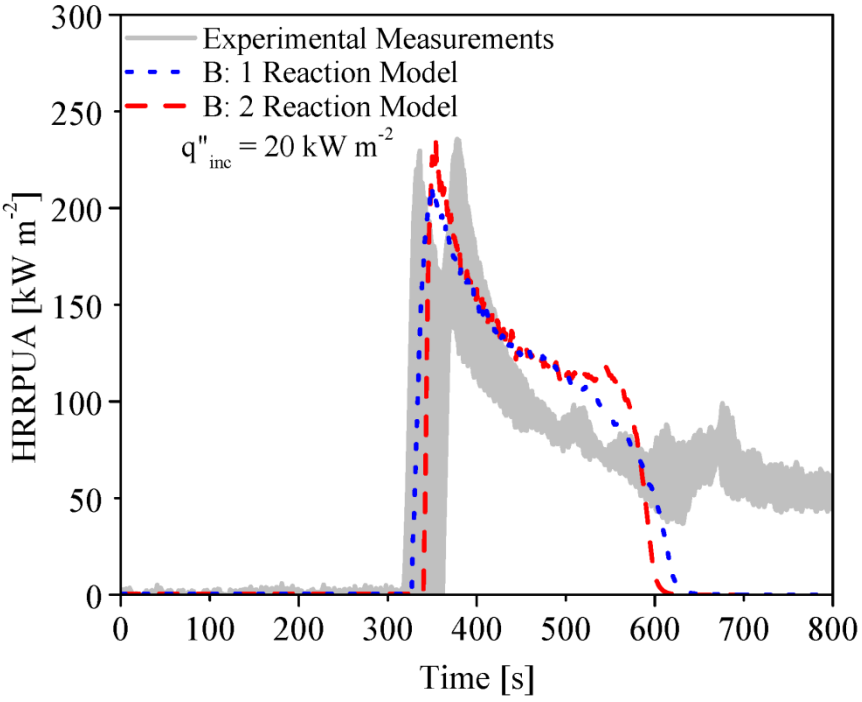
Experimental Measurements
B: 1 Reaction Model
B: 2 Reaction Model
q"inc = 20 kW m-2
HRRPUA [kW m-2]
Time [s]
0
50
100
150
200
250
300
0
100
200
300
400
500
600
700
800

(a)

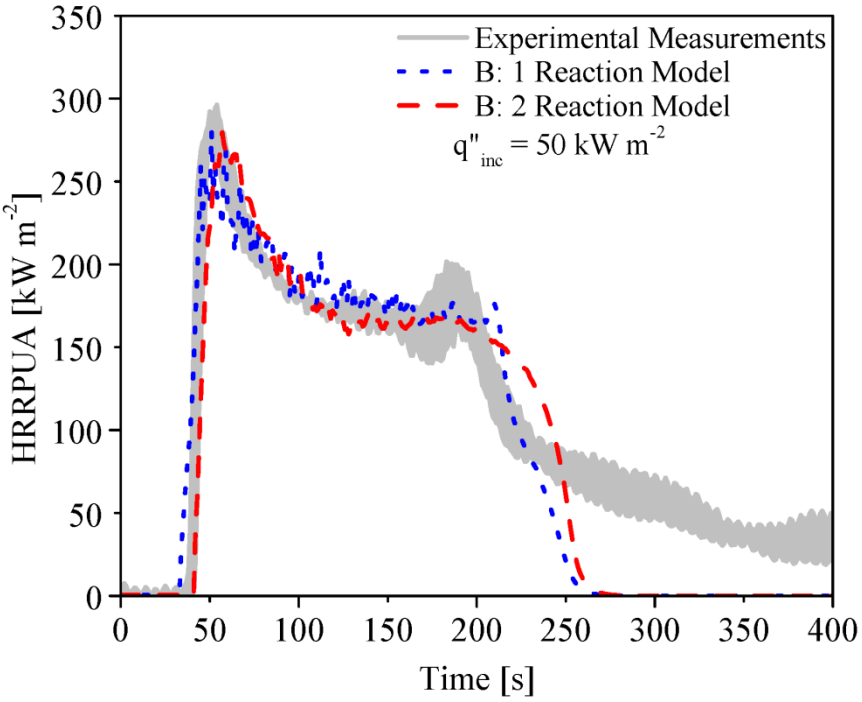
Experimental Measurements
B: 1 Reaction Model
B: 2 Reaction Model
q"inc = 50 kW m-2
HRRPUA [kW m-2]
Time [s]
0
50
100
150
200
250
300
350
0
50
100
150
200
250
300
350
400

(b)

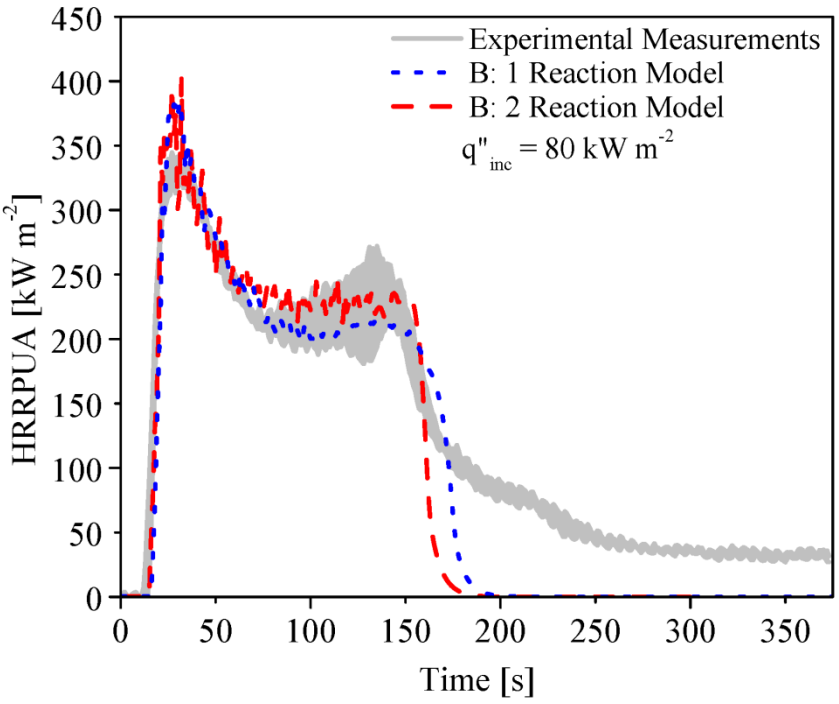

(c)

Figure 66. Sample B cone calorimeter final model prediction of the single reaction and two consecutive reactions compared to the experimental measurements. The experiments and models were conducted at 20 kW/m^2, 50 kW/m^2 and 80 kW/m^2 in graph (a), graph (b) and graph (c), respectively

Table 20: Sample B Final Set of Optimized Properties

Virgin Material Properties			
Parameter	**1 Reaction**	**2 Reactions**	**Reference**
Thickness [m]	0.0041		Physically Measured
Density [kg m^{-3}]	889.3		
Thermal Conductivity [W m^{-1} K^{-1}]	0.13	0.175	Cone Optimization
Heat Capacity [J kg^{-1} K^{-1}]	2900	2850	
Emissivity [-]	0.71	0.77	
Absorption coefficient [m^2 kg^{-1}]	5	4	
Ignition Mass Flux [kg s^{-1} m^{-2}]	2.33×10^{-3}		
Heat of Reaction [J kg^{-1}]	-4×10^{5}	3×10^{5}	
θ_C or θ_I [%]	14.40	80.00	MCC Experiments/ MCC Optimization
Pre-Exponential Factor [s^{-1}]	5.81×10^{7}	9.50×10^{7}	
Activation Energy [J mol^{-1}]	1.15×10^{5}	1.06×10^{5}	
ΔH_{eff} [J kg^{-1}]	11.67×10^{6}		Cone Calorimeter Experiments
Intermediate Material Properties			
Density [kg m^{-3}]	-	711.5	Constant Volume Analysis
Thermal Conductivity [W m^{-1} K^{-1}]	-	0.0725	Cone Optimization
Heat Capacity [J kg^{-1} K^{-1}]	-	1720	
Emissivity [-]	-	0.72	

Absorption coefficient [m^2 kg^{-1}]	-	10	
Heat of Reaction [J kg^{-1}]	-	-2.5×10^5	
θ_{CI} [%]	-	17.99	MCC Optimization
Pre-Exponential Factor [s^{-1}]	-	1.40×10^{10}	
Activation Energy [J mol^{-1}]	-	1.445×10^5	
Char Material Properties			
Density [kg m^{-3}]	128.0	128.0	Constant Volume Analysis
Thermal Conductivity [W m^{-1} K^{-1}]	$2.5\times10^{-10}*T^3$	$3\times10^{-10}*T^3$	Cone Optimization
Absorption coefficient [m^2 kg^{-1}]	10	10	
Heat Capacity [J kg^{-1} K^{-1}]	1500		Literature
Emissivity [-]	0.86		

Figure 67a, Figure 67b and Figure 67c provide the final HRRPUA curves for the 1 Reaction Model and 2 Reaction Model for Sample C at 25×10^3 W m^{-2}, 50×10^3 W m^{-2} and 80×10^3 W m^{-2}, respectively. In these figures, the ThermaKin2D model predictions are compared to the experimental results. Table 21 provides the final set of properties for Sample C using a 1 Reaction Model and 2 Reaction Model. All of these properties are within the acceptable ranges.

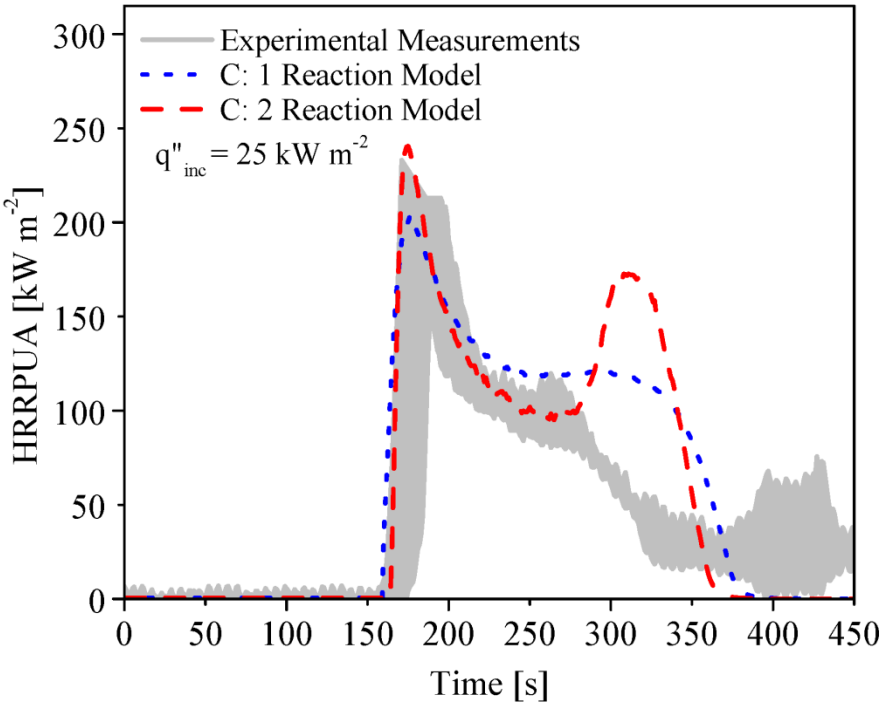

(a)

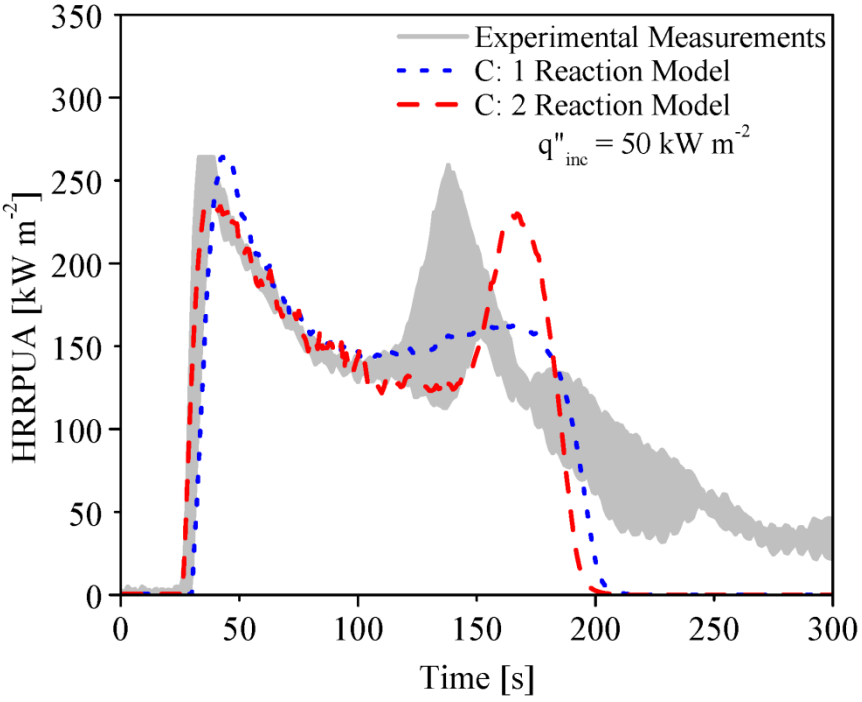
Experimental Measurements
C: 1 Reaction Model
C: 2 Reaction Model
q"inc = 50 kW m-2
HRRPUA [kW m-2]
Time [s]
0
50
100
150
200
250
300
350

(b)

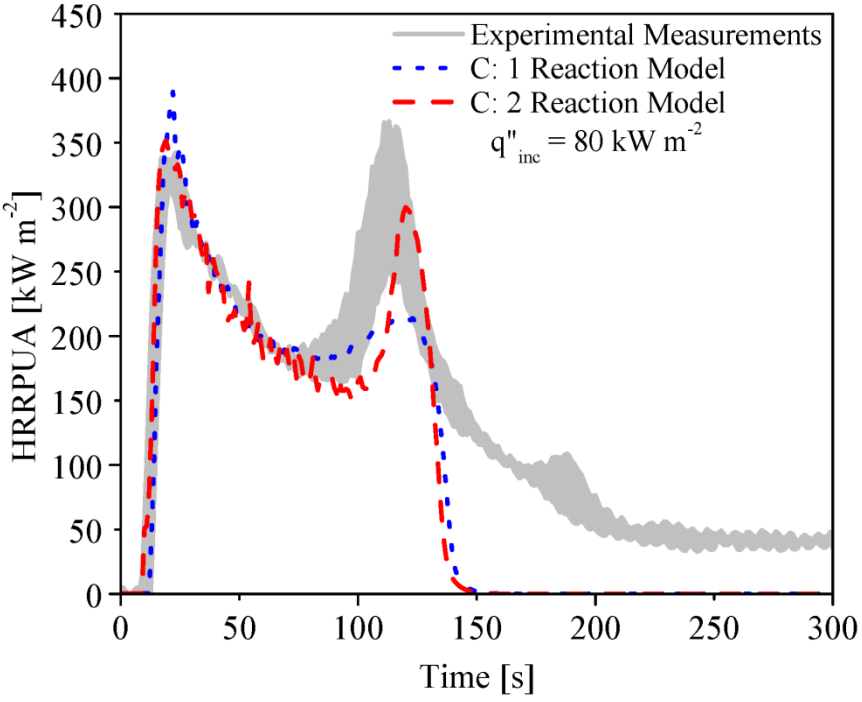
Experimental Measurements
C: 1 Reaction Model
C: 2 Reaction Model
q"inc = 80 kW m-2
HRRPUA [kW m-2]
Time [s]
0
50
100
150
200
250
300
350
400
450

(c)

Figure 67. Sample C cone calorimeter final model prediction of the single reaction and two consecutive reactions compared to the experimental measurements. The experiments and models were conducted at 25 kW/m^2, 50 kW/m^2 and 80 kW/m^2 in graph (a), graph (b) and graph (c), respectively

Table 21: Sample C Final Set of Optimized Properties

Virgin Material Properties			
Parameter	**1 Reaction**	**2 Reactions**	**Reference**
Thickness [m]	0.0036		Physically Measured
Density [kg m^{-3}]	888.8		
Thermal Conductivity [W m^{-1} K^{-1}]	0.095	0.081	Cone Optimization
Heat Capacity [J kg^{-1} K^{-1}]	2900	2600	
Emissivity [-]	0.725	0.88	
Absorption coefficient [m^2 kg^{-1}]	7	1.5	
Ignition Mass Flux [kg s^{-1} m^{-2}]	2.64×10^{-3}		
Heat of Reaction [J kg^{-1}]	-1.5×10^{5}	-5.5×10^{5}	
θ_C or θ_I [%]	17.64	94.00	MCC Experiments/ MCC Optimization
Pre-Exponential Factor [s^{-1}]	4.8×10^{6}	3×10^{7}	
Activation Energy [J mol^{-1}]	1.019×10^{5}	8.34×10^{4}	
ΔH_{eff} [J kg^{-1}]	10.26×10^{6}		Cone Calorimeter Experiments
Intermediate Material Properties			
Density [kg m^{-3}]	-	635.6	Mean of Virgin Sample & Char
Thermal Conductivity [W m^{-1} K^{-1}]	-	0.15	Cone Optimization
Heat Capacity [J kg^{-1} K^{-1}]	-	1500	
Emissivity [-]	-	0.84	
Absorption coefficient [m^2 kg^{-1}]	-	50	
Heat of Reaction [J kg^{-1}]	-	-5e3	
θ_{CI} [%]	-	18.77	MCC Optimization
Pre-Exponential Factor [s^{-1}]	-	9.93×10^{6}	
Activation Energy [J mol^{-1}]	-	1.049×10^{5}	
Char Material Properties			
Density [kg m^{-3}]	382.4	382.4	Cone Calorimeter Tests
Thermal Conductivity [W m^{-1} K^{-1}]	1.25×10^{-10}*T^3	1×10^{-10}*T^3	Cone Optimization
Absorption coefficient [m^2 kg^{-1}]	15	10	
Heat Capacity [J kg^{-1} K^{-1}]	1500		Literature
Emissivity [-]	0.86		

Figure 68a, Figure 68b and Figure 68c provide the final HRRPUA curves for the 1 Reaction Model and 2 Reaction Model for Sample D at 20×10^3 W m^{-2}, 50×10^3 W m^{-2} and 80×10^3 W m^{-2}, respectively. The ThermaKin2D model predictions are compared to the experimental results at each incident heat flux. Table 22 provides the final set of

properties for Sample D using the 1 Reaction Model and 2 Reaction Model. All of these properties are within the acceptable range.

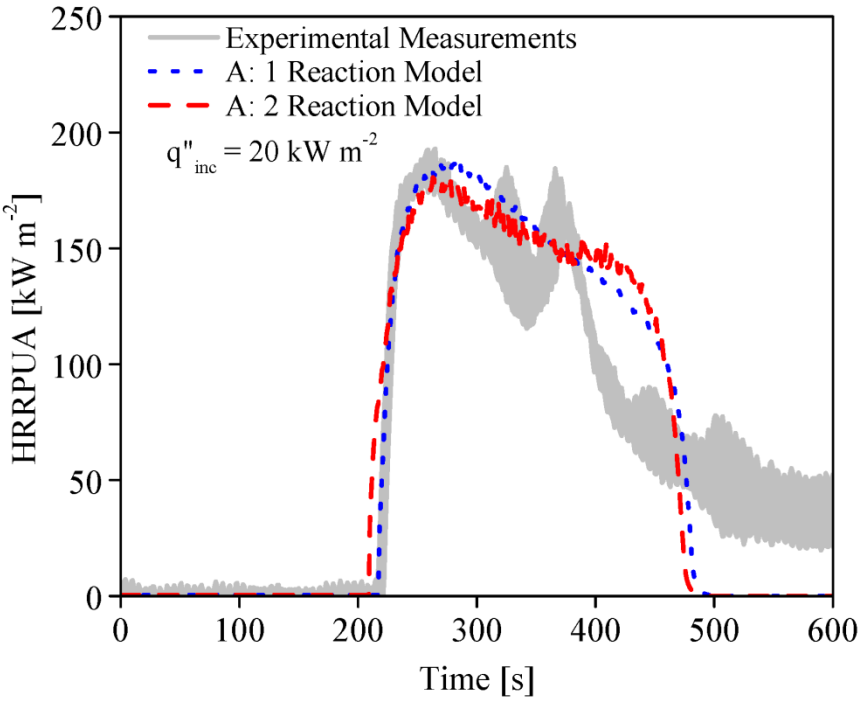

(a)

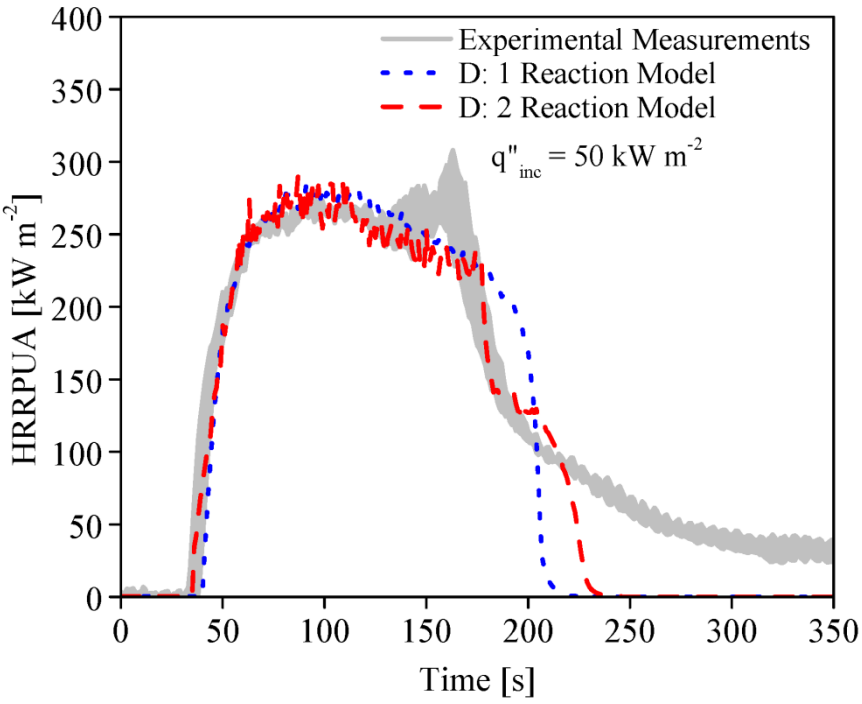
Experimental Measurements
D: 1 Reaction Model
D: 2 Reaction Model
q"inc = 50 kW m-2
HRRPUA [kW m-2]
Time [s]
0
50
100
150
200
250
300
350
400

(b)

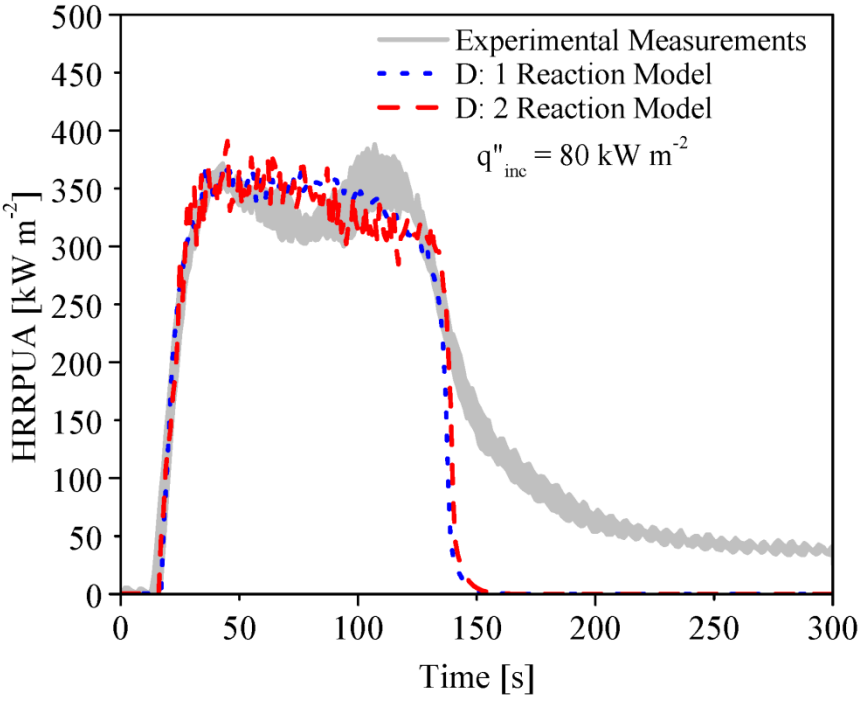
Experimental Measurements
D: 1 Reaction Model
D: 2 Reaction Model
q"inc = 80 kW m-2
HRRPUA [kW m-2]
Time [s]
0
50
100
150
200
250
300
350
400
450
500

(c)

Figure 68. Sample D cone calorimeter final model prediction of the single reaction and two consecutive reactions compared to the experimental measurements. The experiments and models were conducted at 20 kW/m^2, 50 kW/m^2 and 80 kW/m^2 in graph (a), graph (b) and graph (c), respectively

Table 22: Sample D Final Set of Properties

Virgin Material Properties			
Parameter	**1 Reaction**	**2 Reactions**	**Reference**
Thickness [m]	0.0032		Physically Measured
Density [kg m^{-3}]	1080.2		
Thermal Conductivity [W m^{-1} K^{-1}]	0.22	0.28	Cone Optimization
Heat Capacity [J kg^{-1} K^{-1}]	2650	2650	
Emissivity [-]	0.91	0.88	
Absorption coefficient [m^2 kg^{-1}]	3	4	
Ignition Mass Flux [kg s^{-1} m^{-2}]	2.13×10^{-3}	1.89×10^{-3}	
Heat of Reaction [J kg^{-1}]	-1.2×10^{6}	-4×10^{5}	
θ_C or θ_I [%]	11.56	83.00	MCC Experiments/ MCC Optimization
Pre-Exponential Factor [s^{-1}]	2.8×10^{8}	9.87×10^{8}	
Activation Energy [J mol^{-1}]	1.2225×10^{5}	1.15×10^{5}	
ΔH_{eff} [J kg^{-1}]	12.87		Cone Calorimeter Tests
Intermediate Material Properties			
Density [kg m^{-3}]	-	667.5	Mean of Virgin Sample & Char
Thermal Conductivity [W m^{-1} K^{-1}]	-	0.147	Cone Optimization
Heat Capacity [J kg^{-1} K^{-1}]	-	1500	
Emissivity [-]	-	0.80	
Absorption coefficient [m^2 kg^{-1}]	-	10	
Heat of Reaction [J kg^{-1}]	-	-7×10^{5}	
θ_{CI} [%]	-	13.93	MCC Optimization
Pre-Exponential Factor [s^{-1}]	-	1.95×10^{10}	
Activation Energy [J mol^{-1}]	-	1.45×10^{5}	
Char Material Properties			
Density [kg m^{-3}]	255		Cone Calorimeter Experiments
Thermal Conductivity [W m^{-1} K^{-1}]	$4e\times10^{-10}*T^3$	$2e\times10^{-10}*T^3$	Cone Optimization
Absorption coefficient [m^2 kg^{-1}]	13	10	
Heat Capacity [J kg^{-1} K^{-1}]	1500		Literature
Emissivity [-]	0.86		

4.2.6 Cone Calorimeter Optimization Analysis

The accuracy of each model can be quantified by using Equation 30 to determine the relative difference (ς) between the model prediction and the experimental average. During the flame spread modeling, either the 1 Reaction Model or 2 Reaction Model will be employed. Defining the relative difference enables the user to determine which

reaction model is more accurate for each sample. Table 23 provides the results of the relative difference analysis.

$$\varsigma = \frac{\sum|HRR_{exp,avg,i} - HRR_{model,i}|}{N * HRR_{exp,mean}} * 100 \quad (30)$$

In Equation 30, the $HRR_{exp,avg,i}$ is the experimental mean of the 3 experiments at each individual time step minus the $HRR_{model,i}$ which is the model HRR each time step. All this is divided by the number of data points (N) and the experimental mean HRR ($HRR_{exp,mean}$). The experimental uncertainty was also determined and compared to the relative difference analysis in Table 23.

Table 23: Relative Difference between the Model's Prediction And the Average Experimental Result, Along with the Experimental Uncertainty

Sample	Condition (W m^{-2})	1 Reaction Model	2 Reaction Model	Experimental Uncertainty
A	20×10^3	8.7 %	13.1 %	9.5
	50×10^3	22.8 %	24.7 %	10.0
	80×10^3	27.2 %	30.2 %	8.3
B	20×10^3	8.3 %	10.5 %	15.0
	50×10^3	6.5 %	5.9 %	9.1
	80×10^3	17.5 %	21.0 %	8.4
C	25×10^3	18.8 %	14.4 %	22.9
	50×10^3	10.2 %	9.8 %	13.8
	80×10^3	21.1 %	25.2 %	13.6
D	20×10^3	10.0 %	9.1 %	7.0
	50×10^3	5.7 %	5.9 %	10.2
	80×10^3	9.7 %	10.8 %	10.6

For each sample, several manual iterations of all the properties were required to best match the experimental HRRPUA results. Sample A was the most difficult sample to optimize due to the second HRR peak. The second peak is predominately due to the effects of the back surface and material swelling. During a majority of the cone calorimeter experiments, the staples did an adequate job of preventing swelling. Sample A began to deform and swell around the staples at the time when the second HRR peak was developing. This characteristic is very difficult to model and it is outside the scope

of this project. Overall, both models for Sample A were able to adequately predict all the characteristics of the HRR curve at 20×10^3 W m^{-2}. Both models were also able to predict time to ignition and the height of the first HRR peak at 50×10^3 W m^{-2} and 80×10^3 W m^{-2}. The models were unable to adequately predict the second HRR peak at 50×10^3 W m^{-2} and 80×10^3 W m^{-2}. The uncertainty in the cone calorimeter experiments are 9.5, 10.0 and 8.3 at 20×10^3 W m^{-2}, 50×10^3 W m^{-2} and 80×10^3 W m^{-2}, respectively. On average the relative difference between the model and the experimental HRRPUA is nearly double the experimental uncertainty. The relative difference analysis shows that the 1 Reaction Model was slightly better at predicting the average experimental results.

The optimization procedure was quite successful for Sample B at all the incident heat flux conditions. The model predictions were able to predict the time to ignition, height and shape of the first HRR peak, the time and height of the second HRR peak and time to burnout for all the conditions. Time to burnout was not adequately predicted at 20×10^3 W m^{-2} for both Sample B models. Compared to the experimental uncertainty, the model is able to predict the experimental results with a lower relative difference at 20×10^3 W m^{-2} and 50×10^3 W m^{-2}. At 80 W m^{-2} the model does have a higher relative difference compared to the experimental uncertainty. Reviewing the relative difference analysis of the Sample B models shows that the 1 Reaction Model is slightly more accurate for two of the three conditions.

The optimization procedure was also successful for Sample C. Both models were accurately able to predict the time to ignition and the height and shape the first HRR peak at all the incident heat flux conditions. The time to transition to smoldering was accurately predicted for both models at 50×10^3 W m^{-2} and 80×10^3 W m^{-2}. The 1

Reaction model slightly over predicts the second half of the HRR curve at 20×10^3 W m^{-2}, it matches the second half of the HRR curve at 50×10^3 W m^{-2} and it slightly under predicts the second half of the HRR curve at 80×10^3 W m^{-2}. The Sample C 2 Reaction Model was able to accurately predict the height of the second HRR peak at 50×10^3 W m^{-2} and 80×10^3 W m^{-2}. This is evident in the relative difference analysis, which shows that the more complex model is more accurate than the simple model for two of the three conditions. At 20×10^3 W m^{-2}, the model unrealistically predicts a second HRR peak. Overall, these models were able to accurately match the experimental HRR curves, even though this sample produced two distinct HRR peaks. The difference between the model's prediction and the experimental results are comparable to the experimental uncertainty for all the conditions.

Sample D was the most successful cone calorimeter optimization procedure. The time to ignition, height and shape of the first HRR peak was accurately predicted for both models at all the heat flux conditions. The time to burnout was predicted for both models at 50×10^3 W m^{-2} and 80×10^3 W m^{-2} and it was over predicted for both models at 20×10^3 W m^{-2}. There was also a slight second HRR peak for all the heat flux conditions. The models predict the second HRR peak but at the lower bounds. The relative difference analysis shows that both models predict accurate results that are near or within the experimental uncertainty.

The relative difference analysis demonstrates that for a majority of the conditions, the 1 Reaction Model and 2 Reaction Model produce comparable predictions. The next phase of this project involves modeling each samples full-scale fire performance during corner-wall flame spread. The set of properties for the 1 Reaction Model will be utilized

because the optimization procedures for the 1 Reaction Model was simpler since it had less unknown properties to determine. Also, the simulation time increases as more reactions are specified. Overall, using the more complex model did not truly improve the accuracy of the cone calorimeter predictions. When conducting either a MCC or cone calorimeter optimization procedure, it is recommended to use the more efficient, 1 Reaction Model to obtain the desired properties.

4.3 Full-Scale Model

4.3.1 Burner Exposure Model

The full-scale flame spread model requires two submodels to describe the thermal conditions from the burner exposure fire and the spreading flame. The thermal conditions from these two fires are characterized by the flame heat flux. Due to the large and turbulent nature of the fire, the heat flux from the exposure fire and the spreading flame was specified to be radiation driven. In this section the burner exposure submodel will be discussed. In the following section, the flame spread model will be derived.

During both the open corner-wall tests and the room corner tests, a square burner produces a fire that subjects the corner-walls to the heat flux conditions shown in Figure 50 and Figure 51. A boundary condition is specified in ThermaKin2D to represent the one-dimensional vertical heat flux distribution from the burner fire. First, a set of empirical equations were derived to represent the burner flame heat flux as a function of height above the burner. Second, the empirical equation was implemented into the model and validated by comparing the experimental results to the model's prediction.

In ThermaKin2D, the heat flux boundary condition are represented mathematically as a set of linear equations that are a function of the height above the

burner. The heat flux boundary condition was separated into two phases in order to accurately model the propane burner heat flux in time and space. The first phase represents the transient increase in heat flux. During the 25×10^3 W burner exposure, the fire was transient over the first 60 s. During the 40×10^3 W burner exposure, the fire was transient over the first 30 s. The second phase represents the steady state heat flux. The steady state heat flux must be characterized as a function of the height above the burner. Figure 69a and Figure 69b display the average heat flux measurements at each height for the 25×10^3 W and 40×10^3 W burner exposure fire, respectively. ThermaKin2D has the ability to represent the heat flux boundary condition using three sets of three linear equations. The average experimental measurements were fit using three linear equations for the 25×10^3 W fire and two linear equations for the 40×10^3 W fire. The linear equations were extrapolated prior to the lowest heat flux gauge and beyond the tallest heat flux gauge. The linear set of equations describing the steady state burner flame heat flux from a 25×10^3 W fire and a 40×10^3 W fire is shown in Equation 31 and Equation 32.

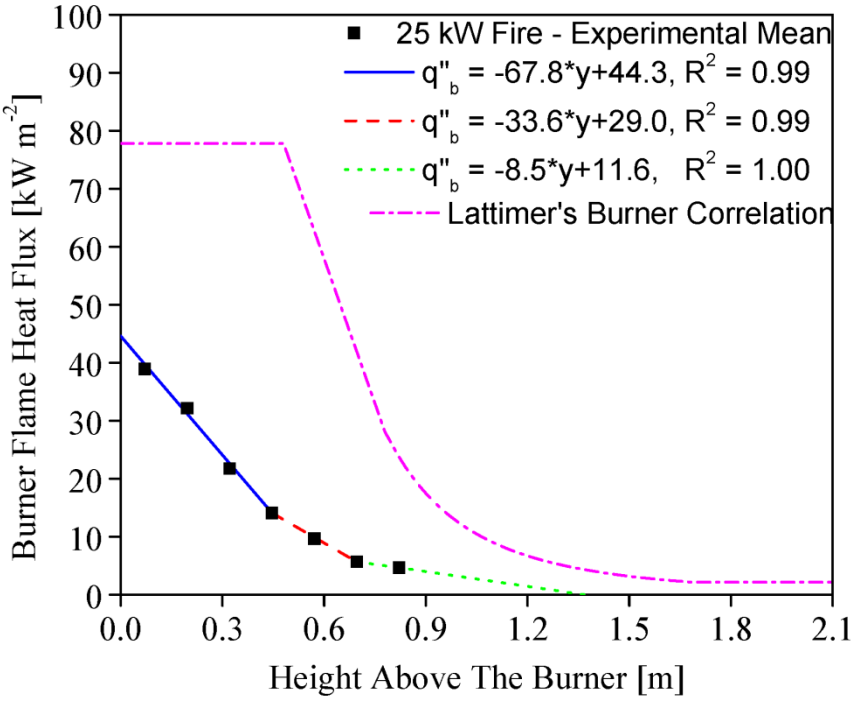

(a) 25 kW burner fire

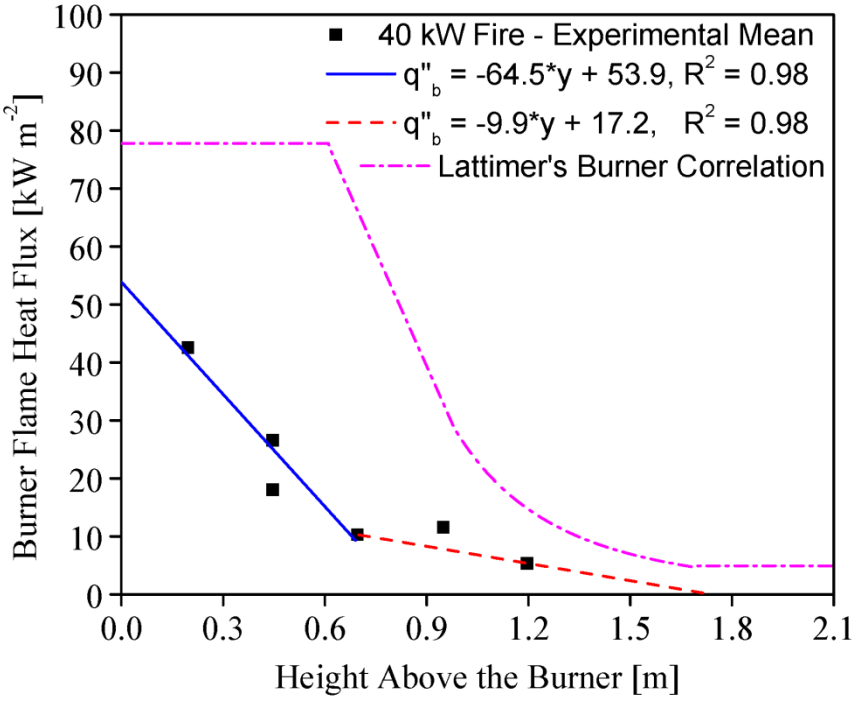

(b) 40 kW burner fire

Figure 69. Steady state square propane burner heat flux exposure as a function of height. A set of linear equations fit the experimental data. Graph (a) shows 25 kW fire exposure located 0.10 m from the corner and graph (b) provides the 40 kW fire exposure located 0.10 m from the corner

$$q"_b = \begin{cases} -67.8 * y + 44.3, & 0 < y \leq 0.446\ m \\ -33.6 * y + 29.0, & 0.446\ m < y \leq 0.696\ m \\ -8.5 * y + 11.6, & 0.626\ m < y \leq 1.37\ m \end{cases} \quad (31)$$

$$q"_b = \begin{cases} -64.5 * y + 53.9, & 0 < y \leq 0.696\ m \\ -9.9 * y + 17.2, & 0.696\ m < y \leq 1.739\ m \end{cases} \quad (32)$$

Equation 7 was used to plot Lattimer's heat flux correlations for a square burner producing a 25×10^3 W and a 40×10^3 W fire as shown in Figure 69a and Figure 69b, respectively. Lattimer's correlations were determined at 0.10 m from the corner. Lattimer's correlations over predict the experimental heat flux measurements determined during this project.

The set of burner flame heat flux equations are implemented into ThermaKin2D in order to validate the model's ability to accurately predict the experimental heat flux measurements. In ThermaKin2D, the transient phase of the burner flame heat flux is defined by linearly increasing the heat flux from 0 W m^{-2} to the steady state heat flux value. After the transient phase, the heat flux is kept steady. Figure 70a and Figure 70b display the mean experimental heat flux from the 25×10^3 W burner fire at the various heights compared to the model's prediction of the burner flame heat flux. Figure 70c and Figure 70d compare the mean experimental heat flux from the 40×10^3 W fire compared to the model's prediction.

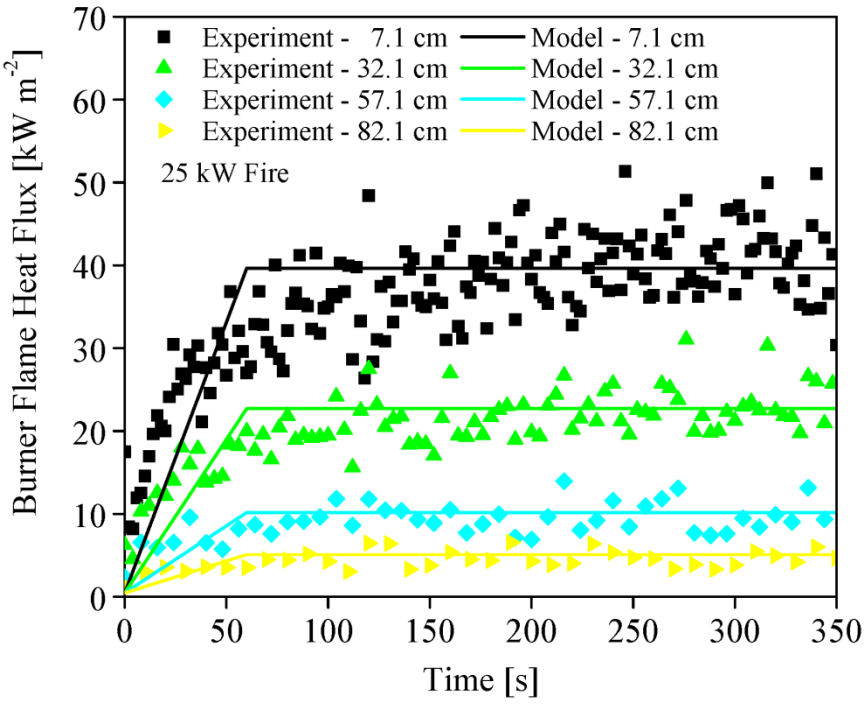
Experiment - 7.1 cm
Model - 7.1 cm
Experiment - 32.1 cm
Model - 32.1 cm
Experiment - 57.1 cm
Model - 57.1 cm
Experiment - 82.1 cm
Model - 82.1 cm
25 kW Fire
Burner Flame Heat Flux [kW m-2]
Time [s]
0
10
20
30
40
50
60
70
0
50
100
150
200
250
300
350

(a)

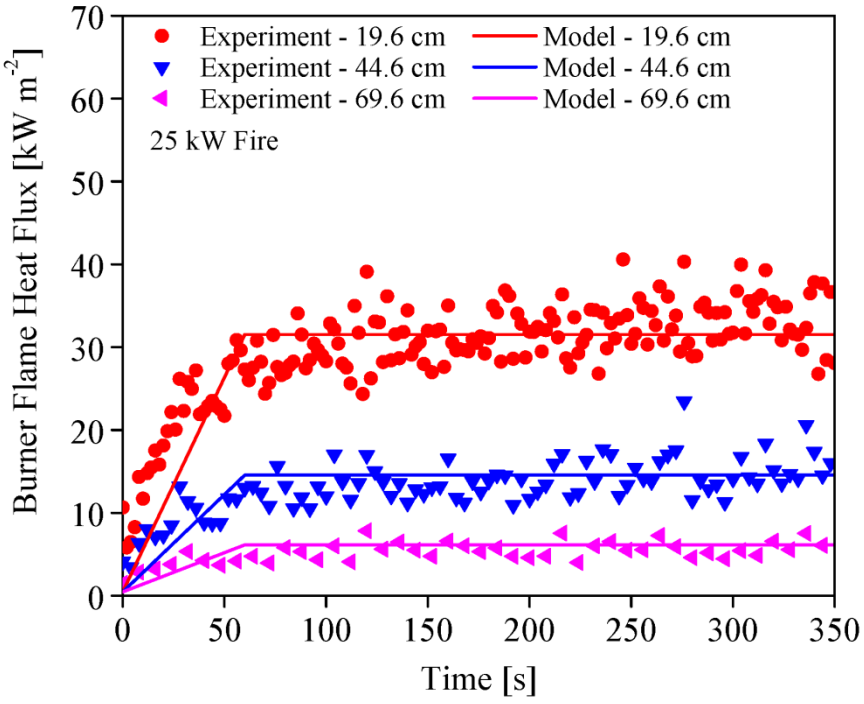
Experiment - 19.6 cm
Model - 19.6 cm
Experiment - 44.6 cm
Model - 44.6 cm
Experiment - 69.6 cm
Model - 69.6 cm
25 kW Fire
Burner Flame Heat Flux [kW m-2]
Time [s]
0
10
20
30
40
50
60
70
0
50
100
150
200
250
300
350

(b)

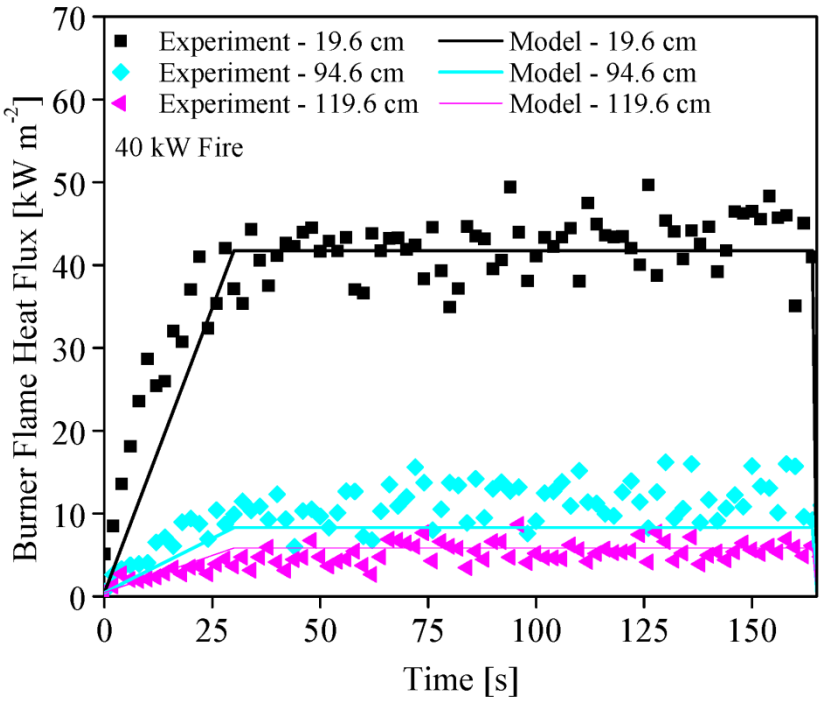
Experiment - 19.6 cm
Experiment - 94.6 cm
Experiment - 119.6 cm
Model - 19.6 cm
Model - 94.6 cm
Model - 119.6 cm
40 kW Fire
Burner Flame Heat Flux [kW m-2]
Time [s]
0
10
20
30
40
50
60
70
0
25
50
75
100
125
150

(c)

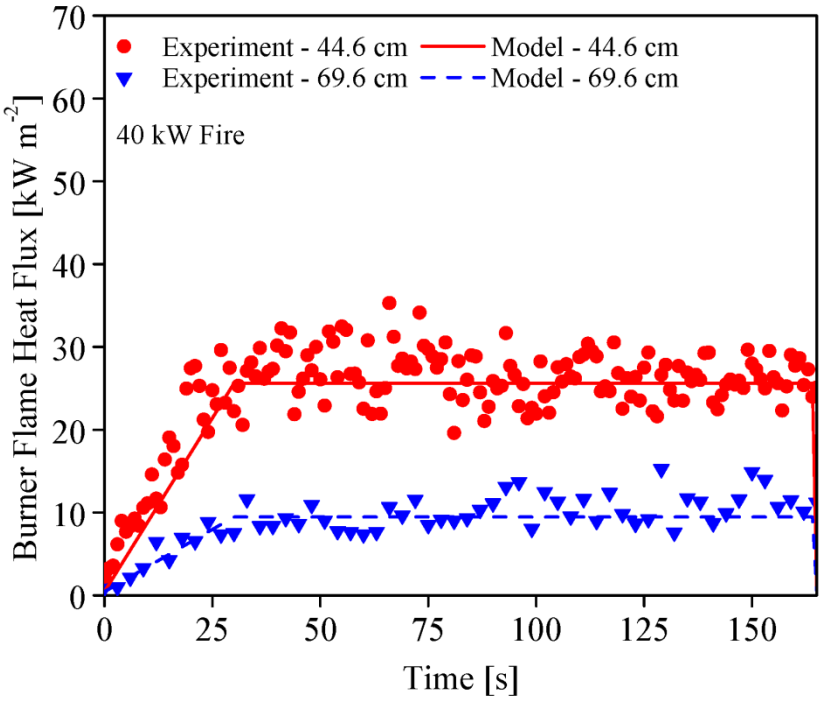
Experiment - 44.6 cm
Experiment - 69.6 cm
Model - 44.6 cm
Model - 69.6 cm
40 kW Fire
Burner Flame Heat Flux [kW m-2]
Time [s]
0
10
20
30
40
50
60
70
0
25
50
75
100
125
150

(d)

Figure 70. Burner flame heat flux validation - experimental mean compared to the model prediction at varying heights. Graph (a) and graph (b) show the 25 kW validation study at different heights. Graph (c) and graph (d) show the 40 kW validation study at different heights

4.3.2 Leventon & Stoliarov Flame Heat Feedback Model

A model was developed in ThermaKin2D to simulate full-scale flame spread in the corner of a compartment. Thus, a flame heat feedback model is needed to represent the heat flux from a spreading flame to the surface of the burning corner-walls. The corner-wall flame heat feedback model was developed based on an analysis of the open corner-wall flame spread tests of Sample A, Sample B and Sample D. The framework of this flame heat feedback model is based on the work by Leventon and Stoliarov [73]. Leventon and Stoliarov developed a flame heat feedback model which determines the flame height and heat flux based on the width-normalized mass loss rate $\left(\frac{dm'}{dt}\right)$ of PMMA. This flame heat feedback model was created based on experiments conducted at the University of Maryland. During these tests, PMMA was carefully ignited using a non-premixed propane burner, and flames were allowed to spread along the vertically oriented sample. The PMMA samples were 0.05 m wide and the sample heights ranged from 0.03 m to 0.20 m. The heat flux was measured using a 9.5×10^{-3} m water-cooled Schmidt Boetler heat flux gauge that was embedded in the sample, flush with the surface. During each test, a single heat flux gauge was located at one of the following heights: 0.03 m, 0.04 m, 0.05 m, 0.075 m, 0.10 m, 0.125 m, 0.15 m and 0.175 m. The burning sample was arranged on top of a scale to determine the mass loss rate during flame spread. These experiments produced highly resolved measurements of the vertical heat flux distribution from a flame to a vertically oriented surface.

The objective of their research was to produce a flame heat feedback model for concurrent flow upward flame spread. The framework of their flame model is presented in Equation 33, Equation 34, Equation 35 and Equation 36.

$$q"_{steady} = \begin{cases} 40 \times 10^3\ Wm^{-2},\ y \leq 0.05\ m \\ 34\ \times 10^3\ Wm^{-2},\ y > 0.05\ m \end{cases} \quad (33)$$

$$y_f = a\left(\frac{dm'}{dt}\right)^b + c \quad (34)$$

$$y^* = \frac{y+y_0}{y_f+y_0} \quad (35)$$

$$q"_{flame} = \begin{cases} q"_{steady}, & y \leq y_f \\ \left(\alpha_f \times q"_{steady}\right)\left(e^{-\ln(\alpha_f)\times(y^*)^2}\right), & y > y_f \end{cases} \quad (36)$$

In their analysis, the steady state flame heat flux was found to be 40×10^3 W m^{-2} near the base of the flame and 34×10^3 W m^{-2} in the mid to upper flame region. A piece-wise function was used to represent the steady state flame heat flux as shown in Equation 33. Next, the flame height was quantitatively determined based on heat flux measurements. Flame height was selected once the heat flux measurement at each gauge location was within 97.5 % of the steady state heat flux. A power-law function was then used to develop a correlation for the flame height as a function of the $\frac{dm'}{dt}$ Equation 34. a, b and c are empirical constants derived from fitting the experimental curve of flame height versus the sample $\frac{dm'}{dt}$ and they are equal to 189.2, 0.4592 and -6.905, respectively. In Equation 34, flame height is in terms of centimeters and $\frac{dm'}{dt}$ is in terms of [g cm^{-1} s^{-1}]. Next, Leventon and Stoliarov created a dimensionless equation for the length scale.

Equation 35 is the normalized length scale equation which was based on the vertical distance above the base of the flame (y), the flame height (y_f) and an empirical constant (y_0). Equation 36 was developed to represent the vertical heat flux distribution. The first expression in Equation 36 states that the heat flux is at its peak steady value within the flame height region ($y \leq y_f$). The second expression in Equation 36 states that the heat flux decays beyond the flame height ($y > y_f$). This expression incorporates the normalized length scale and an empirical constant (α_f) which are altered to fit the experimental data. Combining these expressions together creates a flame heat flux model that can be used to determine the heat flux at any height based on the mass loss rate from a burning material. Leventon and Stoliarov found that the model's prediction of heat flux fit the experimental measurements best when the following empirical values were used for y_0 and α_f: 0.0375 m and 1.794, respectively.

More recently, Korver tested a wide range of polymers and showed that this flame heat feedback model could be scaled using the sample's effective heat of combustion to accurately predict the flame heat flux distribution during flame spread along a flat vertical wall [74].

4.3.3 Corner-wall Flame Heat Feedback Model

The framework of the Leventon and Stoliarov flame heat feedback model is incorporated into ThermaKin2D as a boundary condition to represent the additional heat flux from a flame spreading along a vertical surface. In this project, flame spread experiments were conducted in an open corner-wall configuration, while the HRR, burning width and flame heat flux were measured. An empirical flame height and

vertical heat flux equation for flame spread in the corner of a room was developed using the framework of the flame heat feedback model.

During the corner-wall flame spread tests, the incident heat flux from the flame to the vertical surface was measured using water-cooled Schmidt Boelter heat flux gauges. These gauges were located 0.10 m from the corner along the right wall at the following heights above the top of the burner: 0.196 m, 0.446 m, 0.696 m, 0.946 m, 1.196 m, 1.443 m and 1.696 m. It is assumed that the heat flux distribution from the fire is symmetric with respect to the corner. Figure 71a, Figure 71b and Figure 71c show the raw heat flux gauge readings at each height for the test of Sample A, Sample B and Sample D, respectively. The graphs begin once the propane gas burner was turned off and the graphs end prior to suppression. The Sample C test results were not included in this analysis because burnout occurred while the propane burner was on, which caused the fire to self-extinguishing a few moments later. Figure 72 shows the thin fire in the corner of walls moments after the propane burner was turned off, but prior to extinguishment.

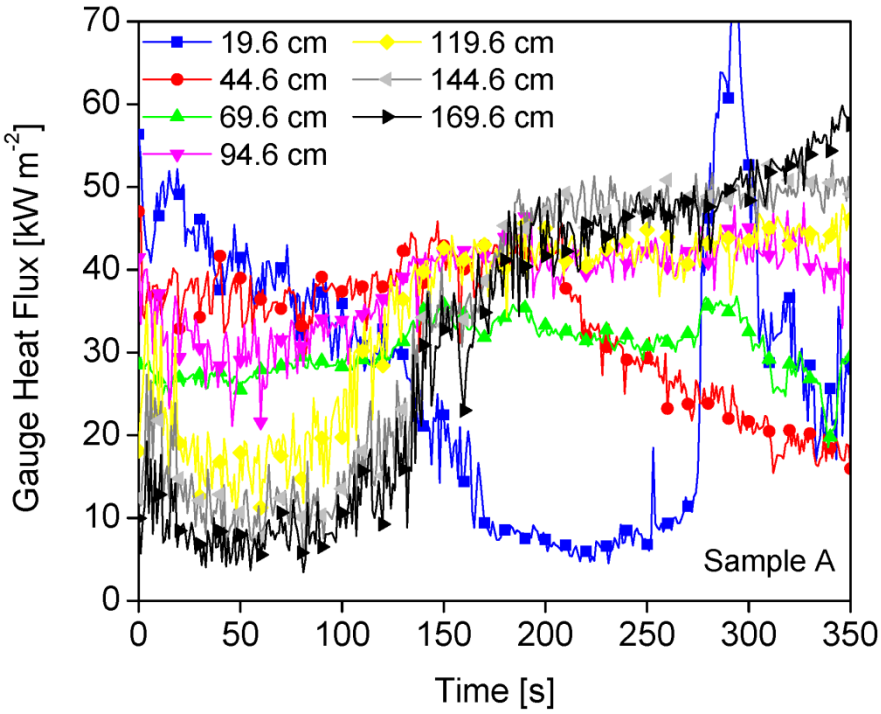
19.6 cm
44.6 cm
69.6 cm
94.6 cm
119.6 cm
144.6 cm
169.6 cm
Sample A
Gauge Heat Flux [kW m-2]
Time [s]
0
10
20
30
40
50
60
70
0
50
100
150
200
250
300
350

(a)

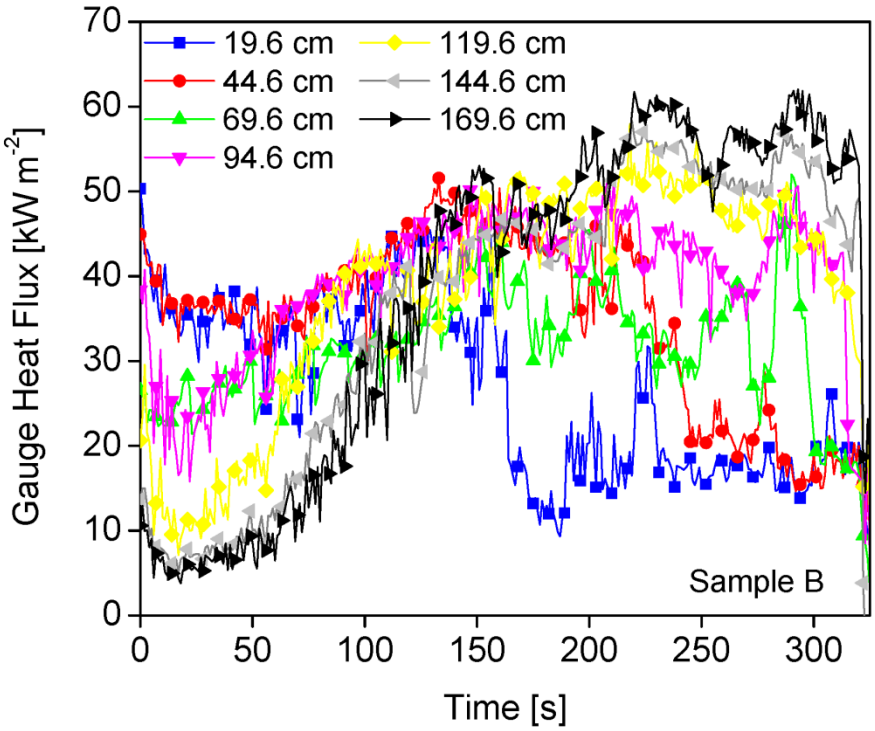
19.6 cm
44.6 cm
69.6 cm
94.6 cm
119.6 cm
144.6 cm
169.6 cm
Sample B
Gauge Heat Flux [kW m-2]
Time [s]
0
10
20
30
40
50
60
70
0
50
100
150
200
250
300

(b)

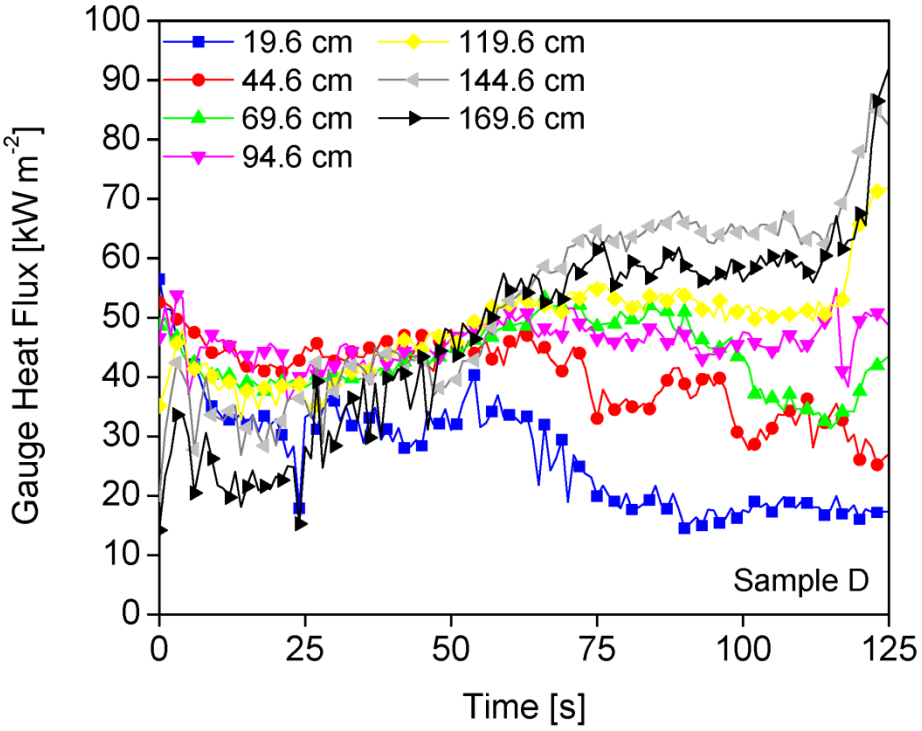

(c)

Figure 71. Raw heat flux gauge measurements during the open corner-wall flame spread measurements starting from the moment the burner is turned off until the suppression. Graph (a), graph (b) and graph (c) provides the gauge heat flux measurements at the various heights and 0.10 m from the corner for Sample A, Sample B and Sample D, respectively

Figure 72. Open corner-wall flame spread experiments - Sample C a few moments after the burner is turned off

When the burner was off, the flames began to spread upwards. During this time, the fire size is at its lowest and the flames appeared to be turbulent and thin. This can be seen in Figure 43c. Figure 71 demonstrates that the flame heat flux measurements are lower when the fire is small and the flames are first spreading. As the fire grew larger, the flames became increasingly turbulent and thicker. This corresponds to an increase in flame heat flux. Once the flames cover the heat flux gauge, the heat flux measurements reach a relatively steady value between 35×10^3 W m^{-2} and 50×10^3 W m^{-2}. As the fire grows large enough the flames began spreading along the ceiling and upper corner-wall region, the flame heat flux increases to (45×10^3 W m^{-2} - 65×10^3 W m^{-2}) at heights above

1.2 m. These observations of the upper-layer effects are extremely similar to what Dillion found during his heat flux measurements within the ISO 9705 compartment [30].

During the corner-wall flame spread for the Sample A and Sample D tests, the MDF wallboard expanded around the heat flux gauge located 0.196 m above the burner. The expansion of the wallboard blocked heat transfer from the flame and caused the heat flux measurements to quickly decrease. Also, there was systematic error in the measurements from the heat flux gauge located 0.696 m above the burner during the Sample A and Sample B flame spread tests. During these tests, the heat flux gauge measurements were well below the other gauge readings, even though the gauge was within the flame region. The Sample A and Sample D heat flux gauge measurements located at 0.196 m above the burner were removed from the flame spread analysis, as well as the Sample A and Sample B heat flux gauge measurements located 0.696 m above the burner.

The goal of this analysis is to develop a flame spread model for when fire is spreading along a combustible wall in the corner of a room, but prior to ceiling flame spread. Once flames are spreading along the ceiling, the fire and smoke layer begin reradiating back to the surface of the wall paneling. This complication is not desired in this version of flame spread model. Therefore, this flame spread analysis begins after the propane burner is turned off, when the fire size is at the lowest Q'. This analysis ends once flames begin spreading along the ceiling. These moments were determined visually for each test. For Sample A, the flame spread analysis begins at 74 s and ends at 210 s. The flame spread analysis begins at 24 s and ends at 120 s for the test of Sample B. The flame spread analysis starts at 21 s and ends at 48 s for the test of Sample D. Images of

these moments are provided in Figure 73a, Figure 73b, Figure 73c, Figure 73d, Figure 73e and Figure 73f for Sample A, Sample B and Sample D respectively. The raw heat flux gauge readings were smoothed using a 20 s running average and fit by a 2^{nd} to 5^{th} order polynomial equation to reduce experimental noise. Figure 74a, Figure 74b and Figure 74c show the heat flux gauge measurements for Sample A, Sample B and Sample D, respectively from the time when the fire size is the smallest up until when flames begin spreading along the ceiling and upper wall region.

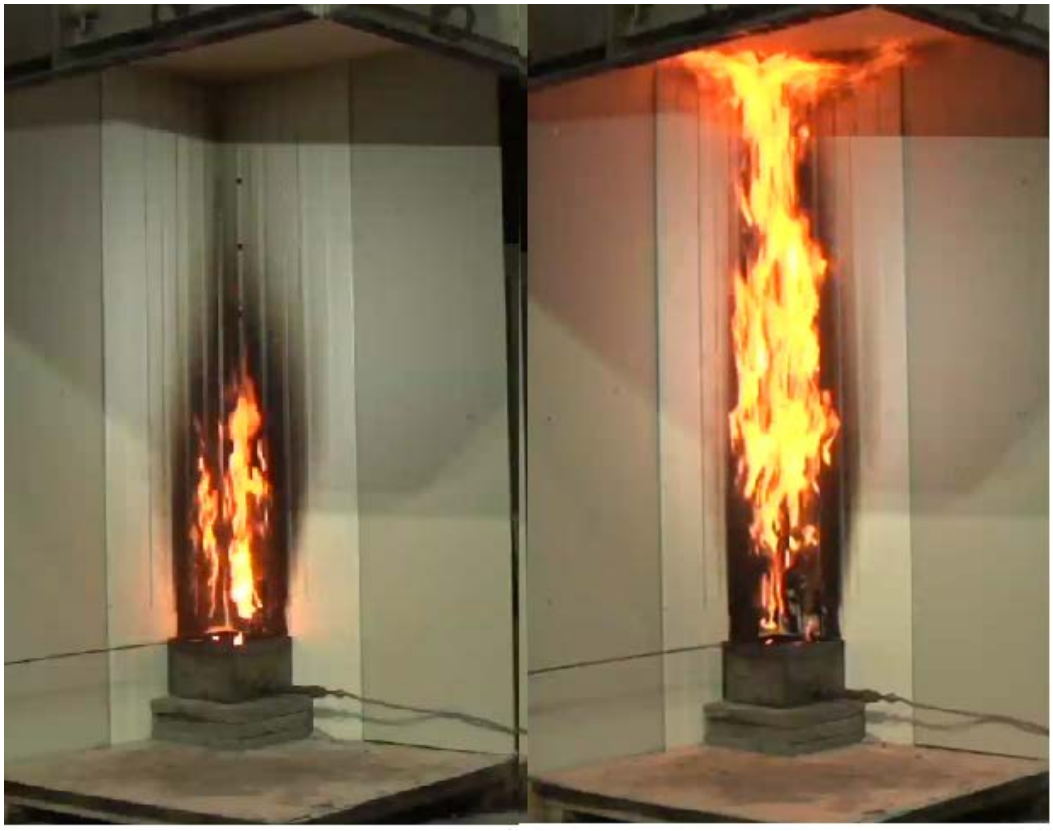

(a) Sample A - 74 s (b) Sample A - 210 s

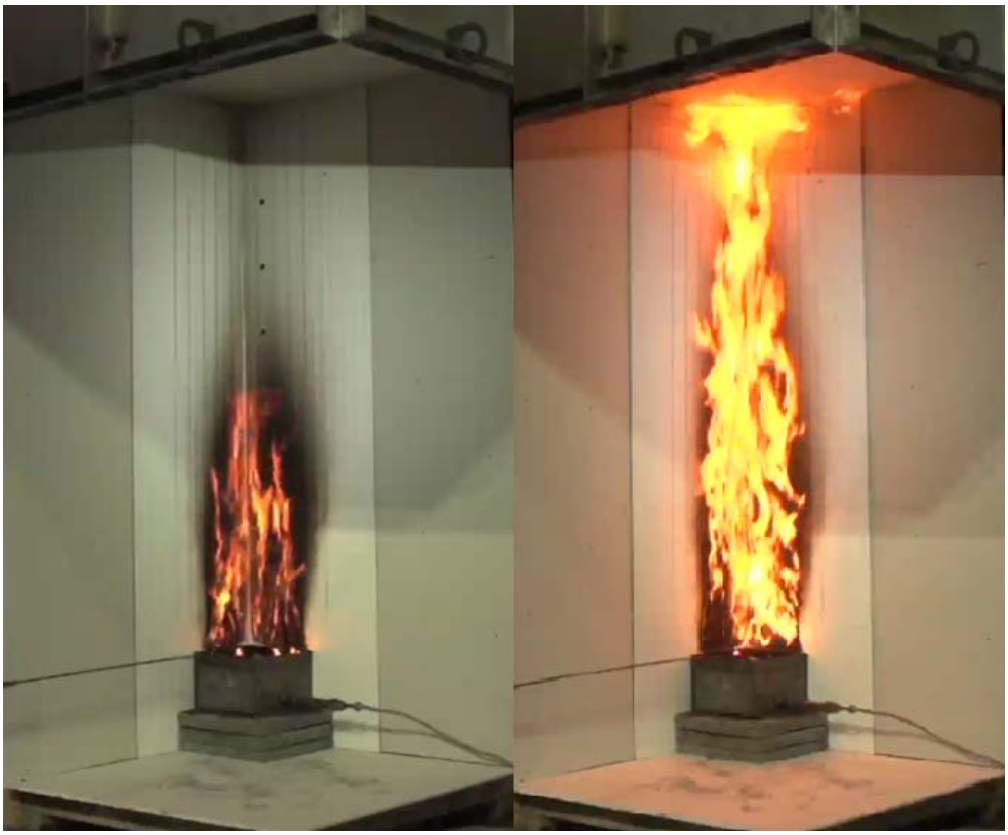

(c) Sample B - 24 s (d) Sample B - 120 s

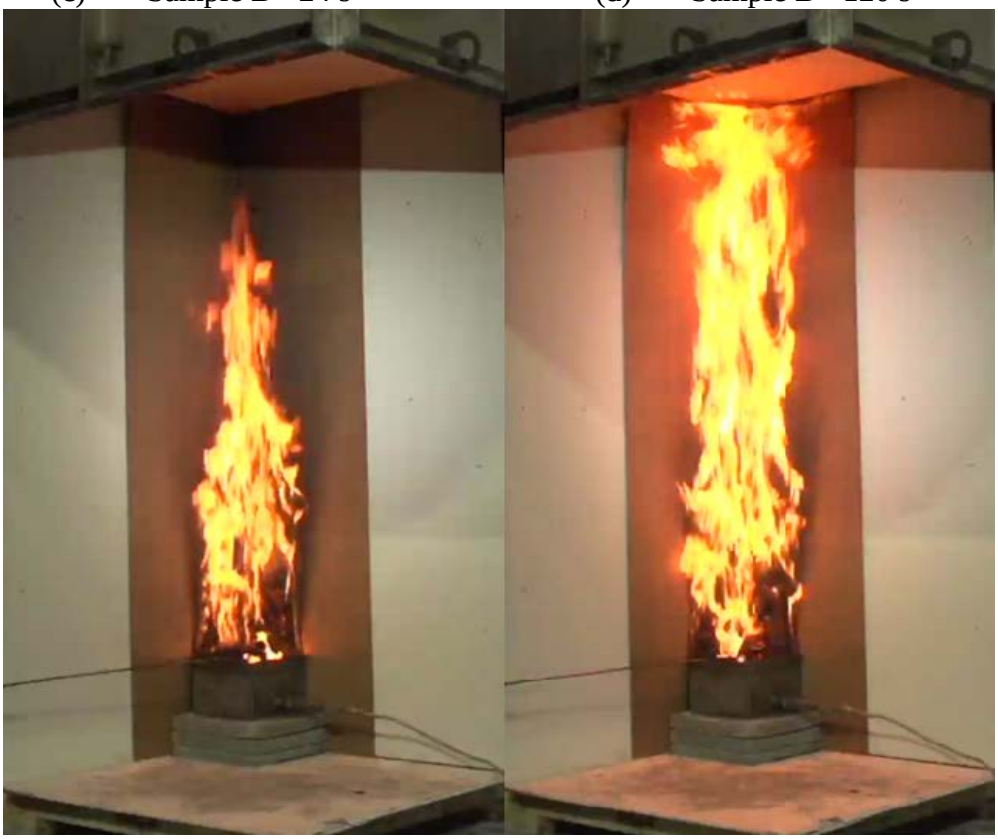

(e) Sample D - 21 s (f) Sample D - 48 s

Figure 73. Open corner-wall flame spread experiments. Image (a) and image (b) provide a picture of the fire at 74 s and 210 s during the Sample A experiment. Image (c) and image (d) provide a picture of the fire at 24 s and 120 s during the Sample B experiment. Image (e) and image (f) provide a picture of the fire at 21 s and 48 s during the Sample D experiment.

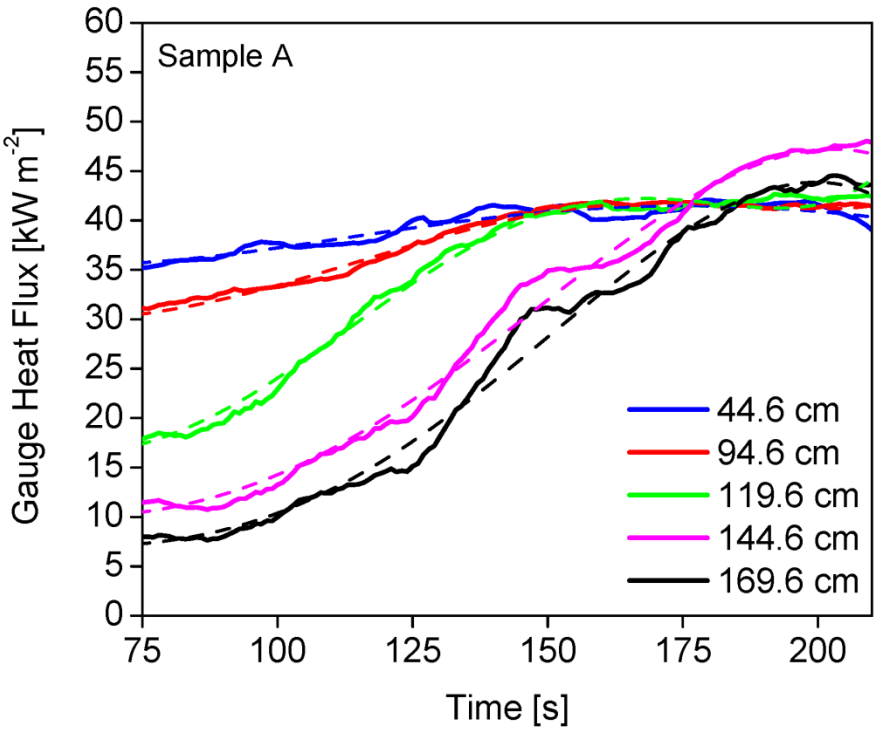

(a)

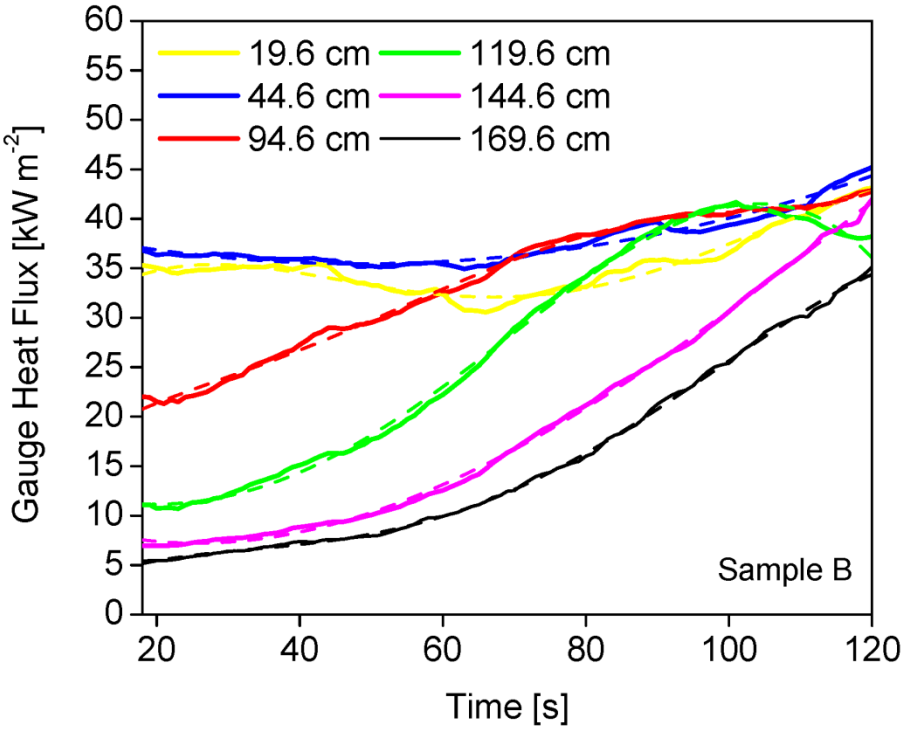
19.6 cm
119.6 cm
44.6 cm
144.6 cm
94.6 cm
169.6 cm
Sample B
Gauge Heat Flux [kW m-2]
Time [s]
0
5
10
15
20
25
30
35
40
45
50
55
60
20
40
60
80
100
120

(b)

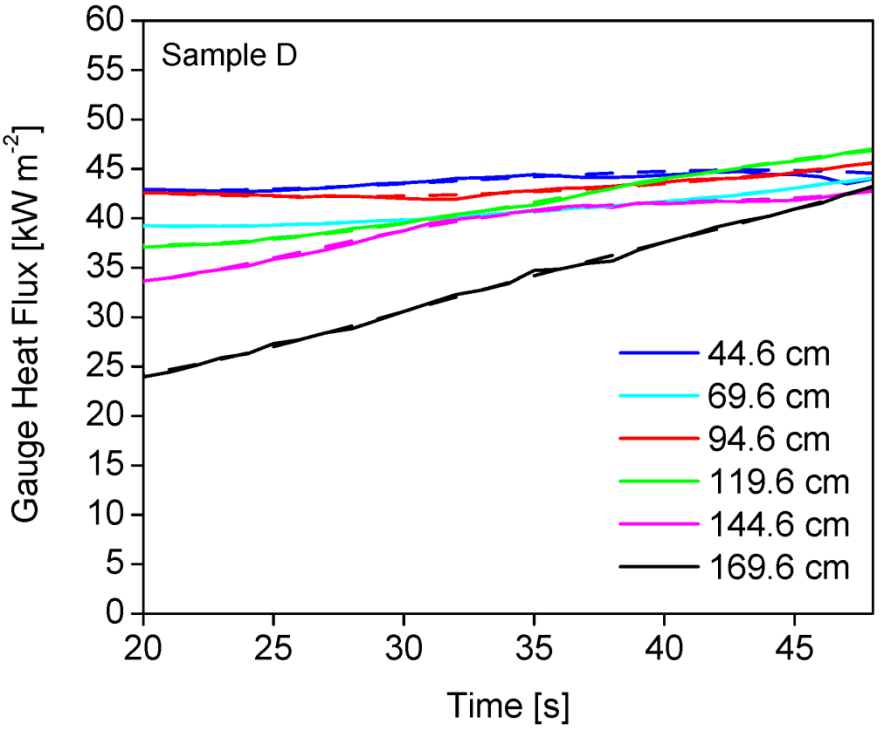
Sample D
44.6 cm
69.6 cm
94.6 cm
119.6 cm
144.6 cm
169.6 cm
Gauge Heat Flux [kW m-2]
Time [s]
0
5
10
15
20
25
30
35
40
45
50
55
60
20
25
30
35
40
45

(c)

Figure 74. Gauge heat flux reading during upward flame spread in the open corner-wall tests of Sample A (graph a), Sample B (graph b) and Sample D (graph c) at varying heights above the burner

The peak steady state heat flux during upward flame spread was determined by averaging each individual heat flux gauge reading over a 15 s time period beginning when the gauge reading reached a relatively steady value. If a heat flux gauges did not reach steady state, then it was not included in the analysis. Table 24 identifies each heat flux gauge that was included in the steady state heat flux analysis, the time frame when the steady state heat flux was averaged and the mean steady heat flux. Figure 75 provides a plot of the steady heat flux versus the height above the burner for all the tests. During upward corner-wall flame spread, the peak steady state heat flux is independent of the height above the burner. The mean steady state peak heat flux was found to be 42×10^{3} W m^{-2}.

Table 24: Peak Heat Flux Analysis

Test	Heat Flux Gauge Height above the Burner [m]	Averaging Period [s]	Mean Steady Heat Flux [W m^{-2}]
Sample A	0.446	144 - 159	40.8×10^{3}
	0.946	150 - 165	41.9×10^{3}
	1.196	154 - 169	41.5×10^{3}
	1.446	193 - 208	47.3×10^{3}
	1.696	193 - 208	44.5×10^{3}
Sample B	0.196	100 - 115	40.0×10^{3}
	0.446	82 - 97	39.5×10^{3}
	0.946	93 - 108	41.2×10^{3}
	1.196	94 - 109	42.1×10^{3}
Sample D	0.446	23 - 38	43.8×10^{3}
	0.696	27 - 42	40.5×10^{3}
	0.946	26 - 41	42.7×10^{3}
	1.196	26 - 41	40.6×10^{3}
	1.446	28 - 43	41.2×10^{3}

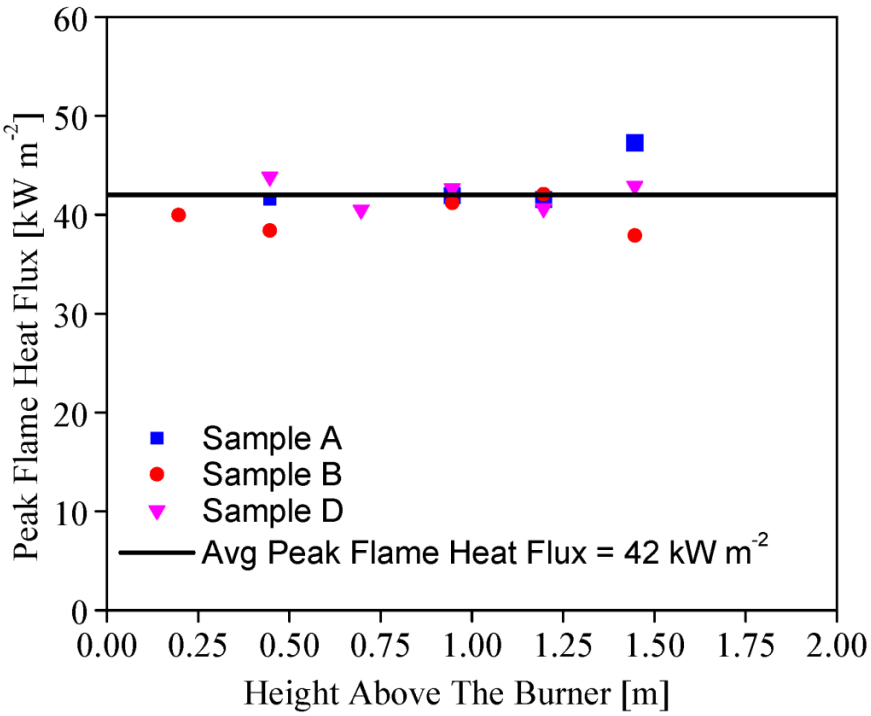

Figure 75. Peak steady flame heat flux

Flame height is commonly defined as the distance from the base of the flame to either the continuous flame region or the flame tip region. Lattimer defines the continuous flame region as the height where flames are always visually present and he defines the flame tip region as the highest location where flames were visually present [33]. Historically, both of these are measured qualitatively through visual observation. While, in this study, the flame height was obtained quantitatively, based on the heat flux measurements at each height. The flame height is defined as the distance from the base of the flame to the highest location where the measured heat flux is within 85 % of the steady heat flux (42×10^3 W m^{-2}). Figure 76 displays the development of flame height as a function of the Q' from each experiment. A power law function was used to fit the

experimental data and create a correlation that determines the flame height in the corner of a room based on the fire size Equation 37.

$$y_f = a(Q')^b + c \tag{37}$$

The units of flame height and Q' are [m] and [kW m^{-1}]. This correlation depends on three empirical constants used to fit the experimental data: a, b and c which are equal to -10.3, -0.2457 and 4.349, respectively. Figure 76 plots the flame height model for corner-wall flame spread, as well as Lattimer's continuous flame height correlation (Equation 4) and Leventon & Stoliarov's flame height equation for upward flame spread along a vertical sample of PMMA (Equation 34). Qualitatively, Lattimer's flame height correlation is very similar to the flame height correlation developed in this project, even though the two were created using different measuring techniques. Lattimer's flame height correlation was based on visual observation, while this flame height correlation is based on heat flux measurements. During the open corner-wall experiments, measurements of the fire size were made as low as 27×10^3 W or 54×10^3 W m^{-1}. Therefore, the power law function is extrapolated at lower fire sizes until it reaches the x-intercept on the graph in Figure 76. The x-intercept is also known as the critical heat release rate normalized by the flame width (Q'_{crit}). It is an important parameter during modeling because it dictates when the flame is produced. Though, Leventon & Stoliarov's flame height correlation is for a flat vertical wall, their correlation demonstrates that the flame acts differently at smaller fire sizes. This is something that the current flame height correlation does not account for because flame measurements were not made at lower fire sizes. The two other flame height correlations presented on

Figure 76 are represented over the range of fire sizes that were measured during their respected experiments.

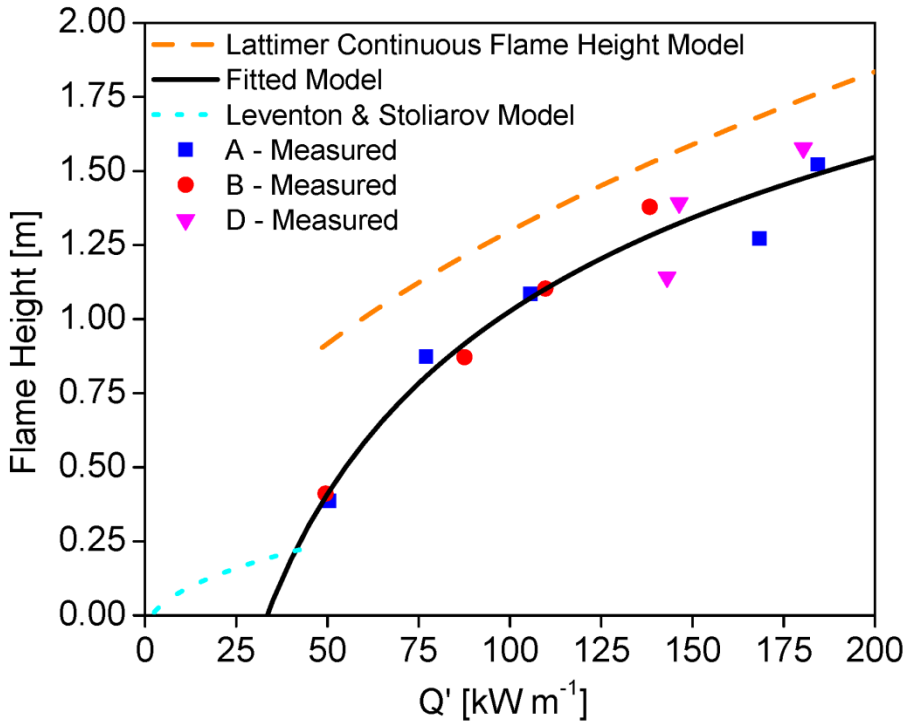

Figure 76. Corner-wall flame height as a function of the fire size

The framework of Leventon & Stoliarov's flame feedback model will be utilized in this project to define one set of equations that provide the flame height and heat flux distribution along a combustible wall material in the corner of the room during vertical flame spread. It is assumed that the incident heat flux is uniform within the flame height region and then it decays beyond the flame height. The peak steady state flame heat flux within the flame height region was determined to be 42×10^{3} W m^{-2} and the flame height correlation was derived based on empirical data and presented in Equation 37. In ThermaKin2D, the base of the flame is the lowest height in which the critical mass flux

for ignition is achieved. The critical mass flux for ignition is a parameter that was determined for each sample during the cone calorimeter optimization.

The last component that needs to be resolved is the vertical heat flux distribution beyond the flame height. Equation 35 and Equation 36 were utilized to fit the heat flux gauge data at the various vertical heights as a function of the Q'. The y_0 and α_f terms in Equation 35 and Equation 36 are then altered until the model accurately predicts the vertical heat flux distribution as a function of the height and fire size. The flame heat feedback model is able to achieve the best fit of the experimental heat flux data when y_0 is equal to 1 m and α_f is equal to 3. Figure 77a, Figure 77b, Figure 77c, Figure 77d, Figure 77e and Figure 77f display the experimental gauge heat flux measurements compared to the flame heat flux model predictions at the following elevations above the propane burner: 0.196 m, 0.446 m, 0.946 m, 1.196 m, 1.446 m and 1.696 m, respectively.

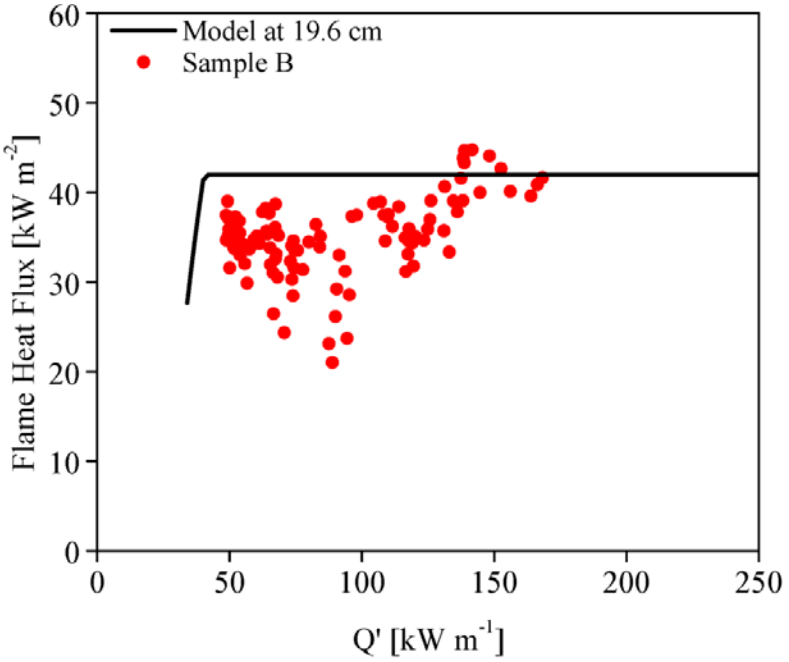

(a)

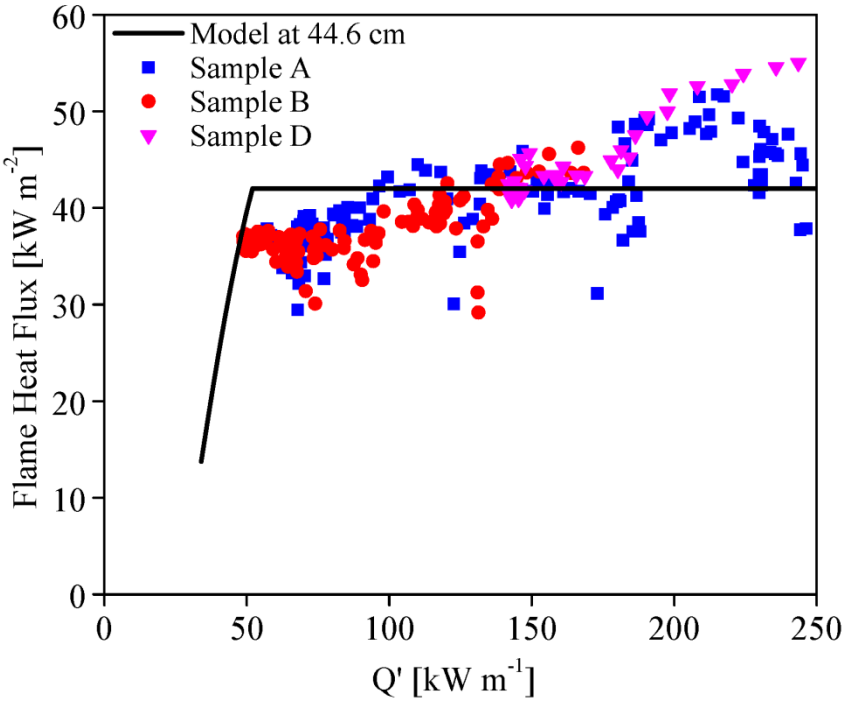
Model at 44.6 cm
Sample A
Sample B
Sample D
Flame Heat Flux [kW m-2]
Q' [kW m-1]
0
10
20
30
40
50
60
0
50
100
150
200
250

(b)

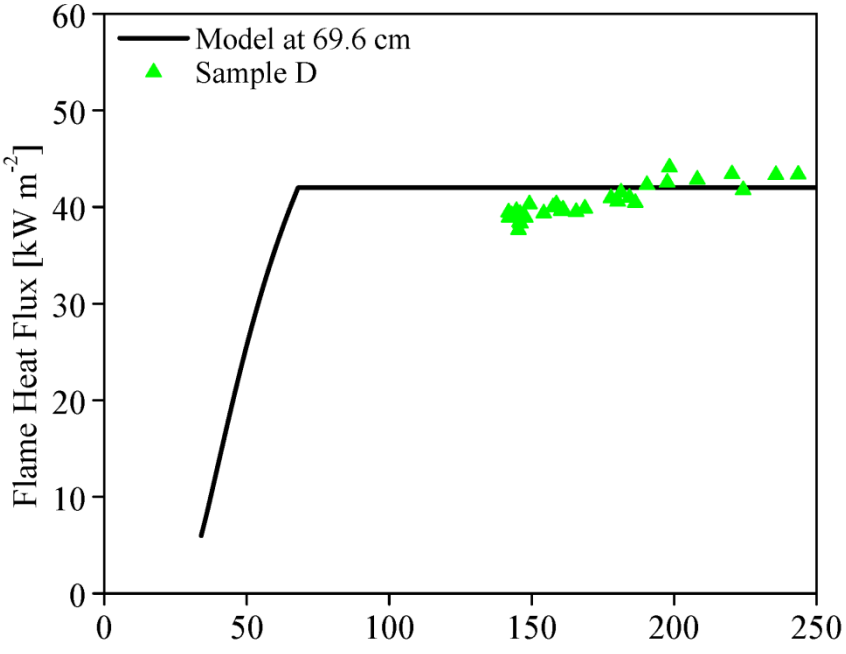
Model at 69.6 cm
Sample D
Flame Heat Flux [kW m-2]
0
10
20
30
40
50
60
0
50
100
150
200
250

(c)

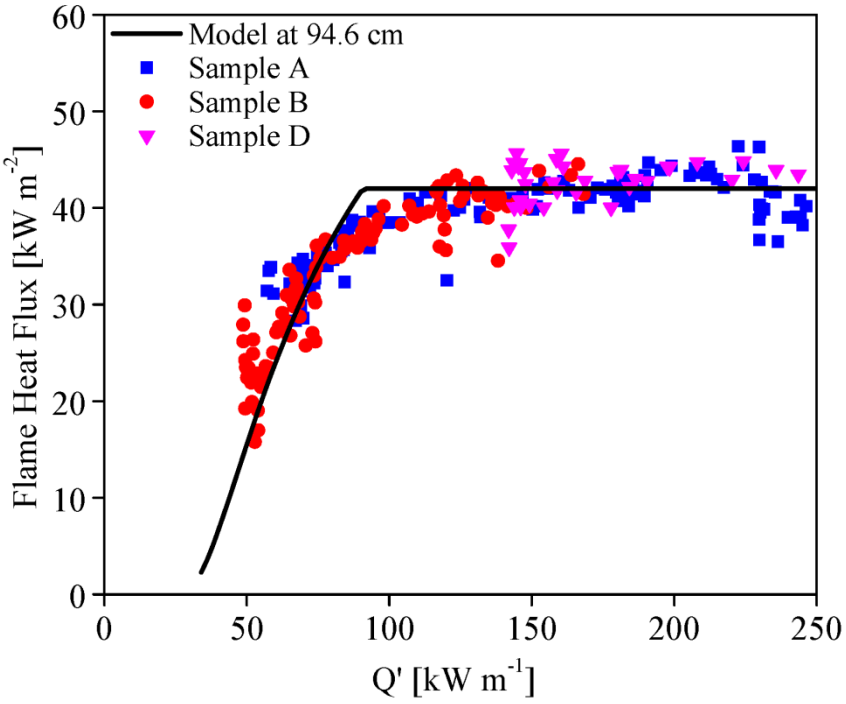
Model at 94.6 cm
Sample A
Sample B
Sample D
Flame Heat Flux [kW m-2]
Q' [kW m-1]
0
10
20
30
40
50
60
0
50
100
150
200
250

(d)

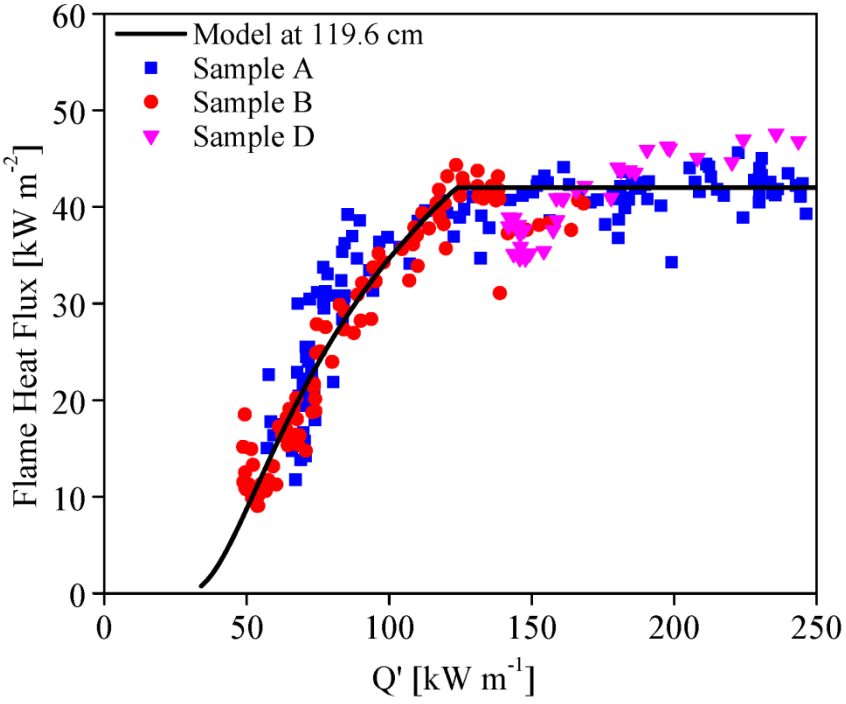
Model at 119.6 cm
Sample A
Sample B
Sample D
Flame Heat Flux [kW m-2]
Q' [kW m-1]
0
10
20
30
40
50
60
0
50
100
150
200
250

(e)

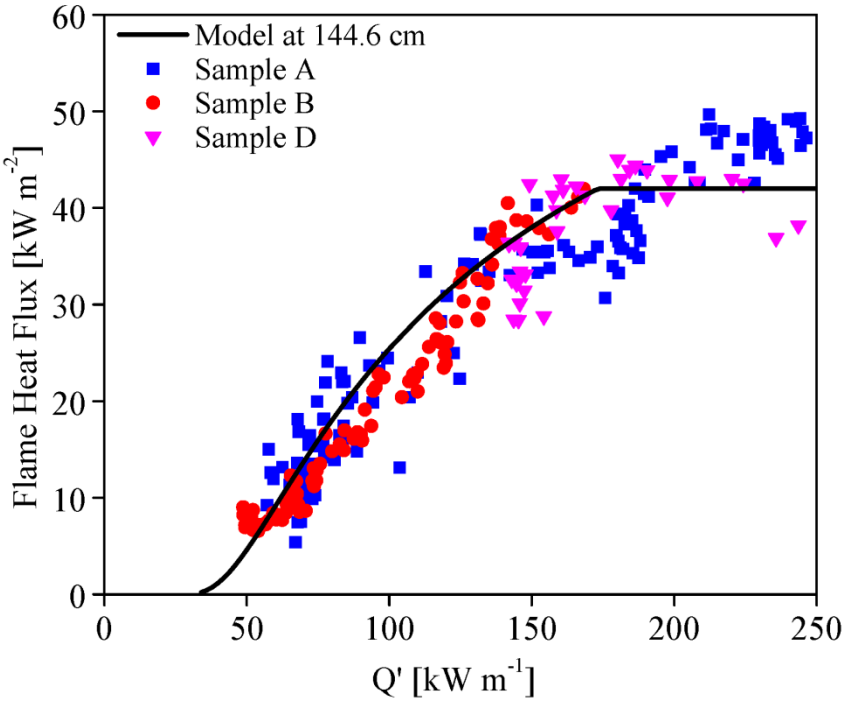
Model at 144.6 cm
Sample A
Sample B
Sample D
Flame Heat Flux [kW m-2]
Q' [kW m-1]
0
10
20
30
40
50
60
0
50
100
150
200
250

(f)

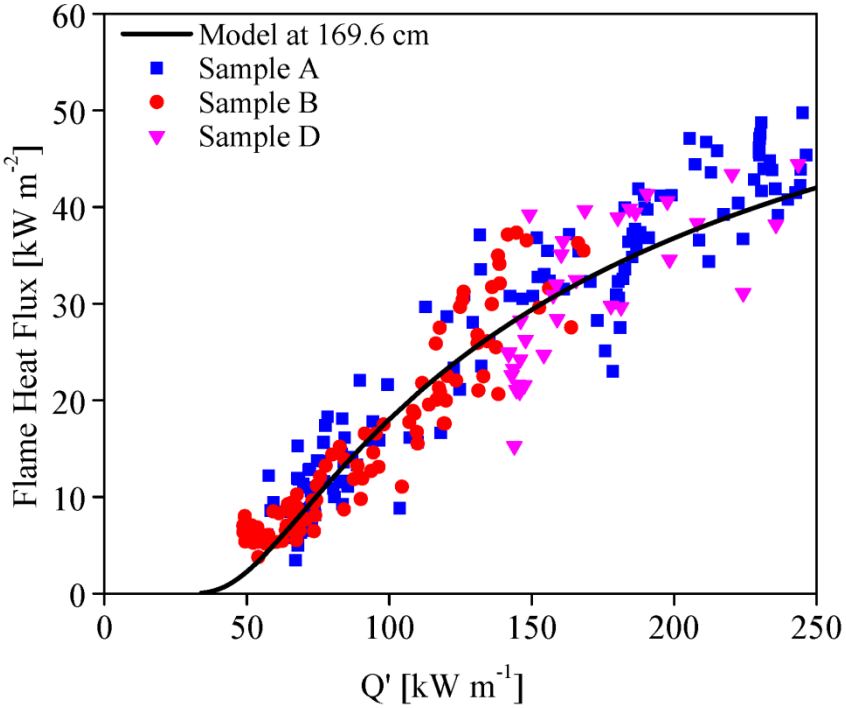
Model at 169.6 cm
Sample A
Sample B
Sample D
Flame Heat Flux [kW m-2]
Q' [kW m-1]
0
10
20
30
40
50
60
0
50
100
150
200
250

(g)

Figure 77. Flame heat feedback model for corner-wall flame spread. Graph (a), graph (b), graph (c), graph (d), graph (e), graph (f) and graph (g) provide the flame heat flux as a function of the fire size for Sample A, Sample B and Sample D at 0.196 m, 0.446 m, 0.696 m, 0.946 m, 1.196 m, 1.446 m and 1.696 m, respectively

Qualitatively, Figure 77 shows that at lower fire sizes, the flame height is shorter and thus the heat flux is the highest in the lower region where the flame height occupies. As the fire produces more heat, the flame height increases and the heat transfer rate increases along the region higher on the wall. The selected values for the empirical constants (α_f and y_0) provided the lowest mean absolute deviation from the model's predictions of the experimental measurements. The mean absolute deviation of the flame heat feedback model is of 3.5 W m^{-2}.

Figure 77 shows that the flame heat feedback model works very well for fire sizes larger than 50×10^3 W m^{-1}, when the fire was fully turbulent. Since only large-scale flame spread experiments were performed, measurements of the heat flux from a fire were not made at fire sizes less than 50×10^3 W m^{-1}. Therefore, the model is robust during fully turbulent flame spread. While, the model is not well resolved at intermediate sized fires, during the period when flames are transitioning from laminar to turbulent flow. Since there is no data at lower fire sizes, the x-intercept of the flame height expression is based on extrapolating the power law function. The x-intercept is a very important parameter that dictates ignition during the "simulated ignition scenario" in ThermaKin2D. When the fire size reaches the critical heat release rate normalized by the flame width (Q'_{crit}), the flame height expression becomes positive and the flame is allowed to spread upwards.

4.4 Full-scale Simulations

4.4.1 Open Corner-wall Model Setup

In the room corner scenario, vertical flame spread in the corner of the room is the most important aspect controlling the rate of fire development and the time it takes to reach flashover. Therefore, the goal of this project is to simulate the initial stages of upward flame spread along the walls in the room corner scenario. The open corner-wall experiments were modeled first because the Q' measurements were much more accurate during these tests.

ThermaKin2D was utilized to simulate the open corner-wall experiments for each sample. The model was designed by specifying the external heat flux exposure from the 25×10^3 W fire according to durations listed in Table 1. The corner-wall flame heat feedback model was established in the model and the final set of properties for each sample was implemented. These properties are reported in Table 19 through Table 22. During each simulation, the thickness of the sample was material specific. The sample was backed by 0.0126 m of gypsum wallboard with the properties specified in Section 4.2.2. The sample was 2.05 m tall, which is the difference between the ceiling height and the burner height. The initial temperature of the materials were specified to be 300 K. Mass transfer occurs only through the front surface. The random radiation absorption algorithm was utilized. The dimensions of the modeling grid are as follows: $\Delta x = 5\times10^{-5}$ m, $\Delta y = 0.01$ m and $\Delta t = 0.01$ s. Increasing or decreasing the integration parameters by a factor 2 yields converging results.

Two ignition scenarios were assessed during the open corner-wall modeling. The first ignition scenario is titled "Simulated Ignition". In this model, ignition is simulated once the Q' value exceeds 33.4×10^3 W m^{-1}, the Q'_{crit} of the corner-wall flame height expression (Equation 37). The flame height is only positive when the Q' value is above 33.4×10^3 W m^{-1}. Once ignition occurs, the flame is allowed to spread along the vertical surface and the heat flux from the spreading flame is added to the heat flux from the burner. This ignition scenario nearly doubles the surface heat flux while both the burner is on and the flame is spreading.

The second ignition scenario is titled "Prescribed Ignition". While the combustible wall is pyrolyzing, it produces gaseous volatiles that are consumed by the burner fire. This scenario assumes that the flame structure is constant while the burner is on and that the wall is subjected to similar thermal conditions. This creates a condition where the corner-wall flame does not contribute to the surface heat flux and flames do not travel upwards prior to the burner being removed. The goal of this approach is to improve the accuracy of the model by keeping the flame heat flux consistent with the heat flux measurements recorded during the experiment. Both ignition scenarios are viewed as the minimum and maximum heat flux scenarios that would occur while the burner is on.

4.4.2 Open Corner-wall Model Results & Discussion

The rate at which fire develops and spreads upward along the corner-walls is quantified in terms of Q'. The model's predictions of Q' is compared to the experimental measurements for each simulation in Figure 78a, Figure 78b, Figure 78c and Figure 78d

for Sample A, Sample B, Sample C and Sample D, respectively. In both the experimental results and the model prediction, the burner fire size of 25 $\times 10^3$ W was not included in the Q' readings, during the period of time when the burner was on. These graphs simply compare the rate at which fire is developing along the vertical surface. The ThermaKin2D simulations titled "Simulated Ignition" utilize the first approach where ignition occurs based on the Q'_{crit} of the flame height expression and the flame heat flux is added to the burner heat flux. The ThermaKin2D simulations titled "Prescribed Ignition" utilize the second approach where the flame turns on once the burner is removed.

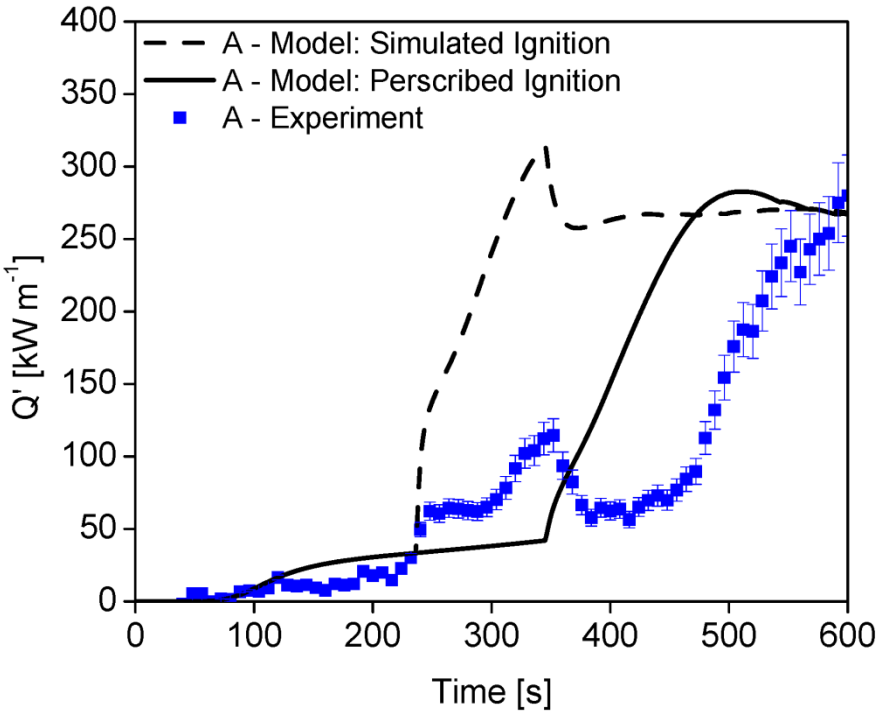

(a)

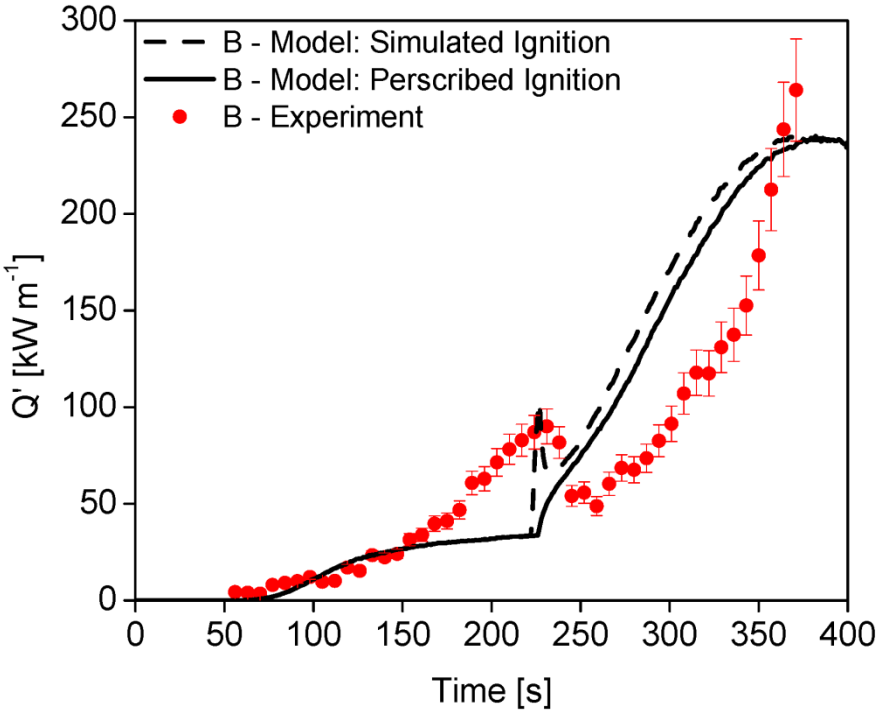
B - Model: Simulated Ignition
B - Model: Perscribed Ignition
B - Experiment
Q' [kW m-1]
Time [s]
0
50
100
150
200
250
300
350
400

(b)

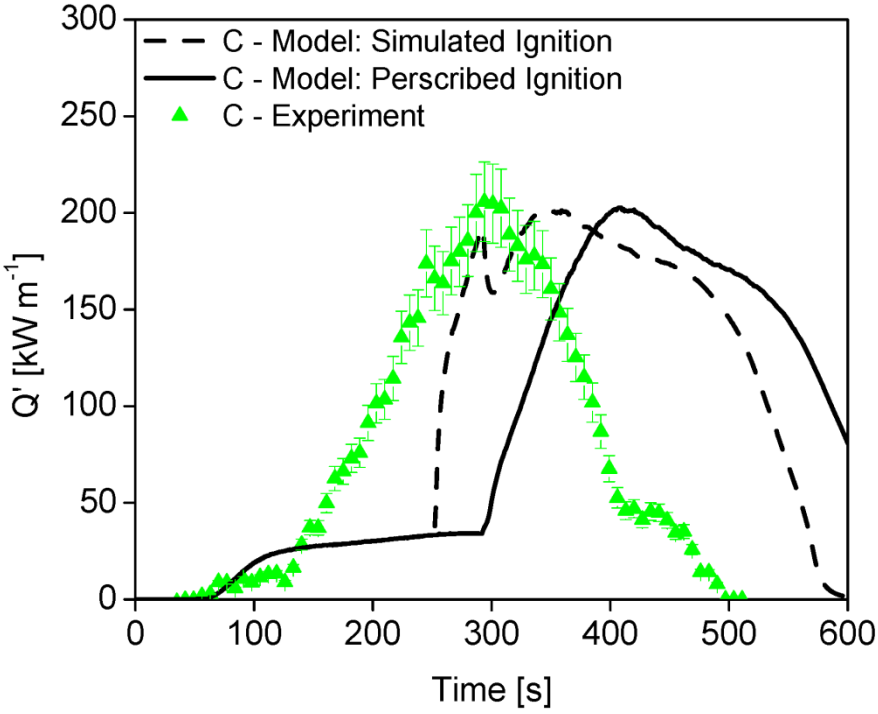
C - Model: Simulated Ignition
C - Model: Perscribed Ignition
C - Experiment
Q' [kW m-1]
Time [s]
0
100
200
300
400
500
600

(c)

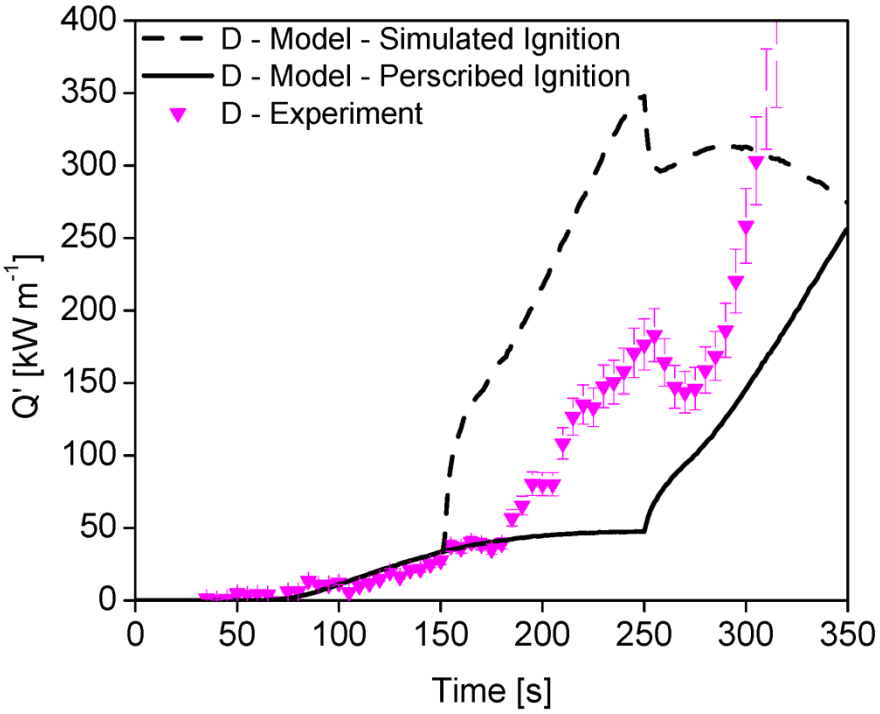

(d)

Figure 78. Open Corner-wall Simulations. Graph (a), graph (b), graph (c) and graph (d) present the model predictions compared to the experimental results of Sample A, Sample B, Sample C and Sample D, respectively. The burner fire size of 25 kW was removed from the experimental results, as well as the models prediction

The open corner-wall model is able to qualitatively predict the fire growth rate very well. Unfortunately, it does a poor job of predicting the time at which the fire growth begins. For both models of Sample A and Sample B, the simulations predict early upward flame spread. The Sample C models qualitatively predict that the flames spread upwards but eventually self-extinguish. The Sample D simulated ignition model over predicts the time at which upward flame spread occurs, while the prescribed ignition scenario under predicts the time at which upward flame spread occurs. A major reason why the open corner-wall model does a poor job of predicting the timing of fire growth is because the flame heat feedback model was developed based on large-scale flame spread experiments. The dynamics of flame spread were captured well at large fire sizes but

poorly at small fire size. This is evident in the validation study of the flame heat feedback model shown on Figure 77.

Overall, the prescribed ignition scenario does a better job of predicting the rate of fire development during the open corner-wall tests. Moving forward, the room corner tests are simulated using the prescribed ignition scenario.

4.4.3 Room Corner Model Setup

During the room corner tests, the MDF samples were stapled to the walls of the compartment and exposed to a 40×10^3 W corner fire for 165 s. These room corner tests provide an objective comparison of the full-scale material fire performance because the samples were exposed to the same burner conditions.

Two-dimensional simulations of the room corner tests were conducted using ThermaKin2D. Four simulations were performed to analyze the fire performance of each sample during a corner-wall fire. The model was designed by specifying the external heat flux exposure from the 40×10^3 W fire for 165 s, establishing the corner-wall flame heat feedback model and implementing the final set of properties for each sample. These properties are reported in Table 19 through Table 22. The prescribed ignition model was utilized during the room corner models.

Much like the open-corner wall model, each sample was backed by 0.0126 m of gypsum wallboard, with the properties specified in Section 4.2.2. The samples were also 2.05 m tall. The ambient temperature of the materials was specified to be 300 K. Mass transfer occurs only through the front surface. The random radiation absorption

algorithm was utilized. The heat transfer from the exposure fire and during flame spread is specified to be radiation driven. The dimensions of the modeling grid are as follows: $\Delta x = 5\times10^{-5}$ m, $\Delta y = 0.01$ m and $\Delta t = 0.01$ s. Increasing or decreasing the integration parameters by a factor 2 yields converging results.

4.4.4 Room Corner Model Results & Discussion

The model's predictions of Q' are compared to the experimental measurements for each simulation in Figure 79a, Figure 79b, Figure 79c and Figure 79d for Sample A, Sample B, Sample C and Sample D, respectively. In these graphs, the Q' does not include the burner HRR of 40×10^{3}.

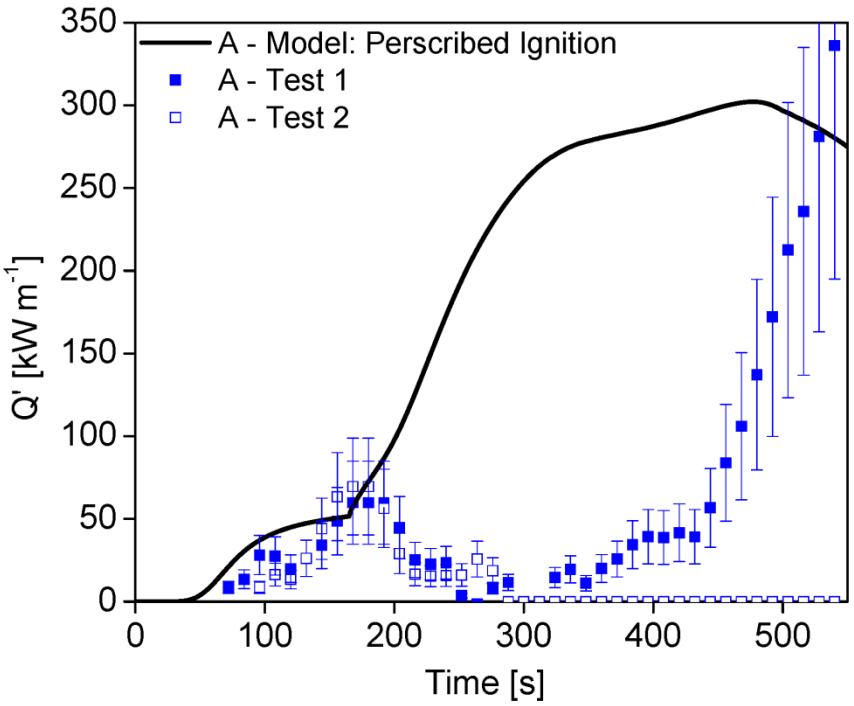

(a)

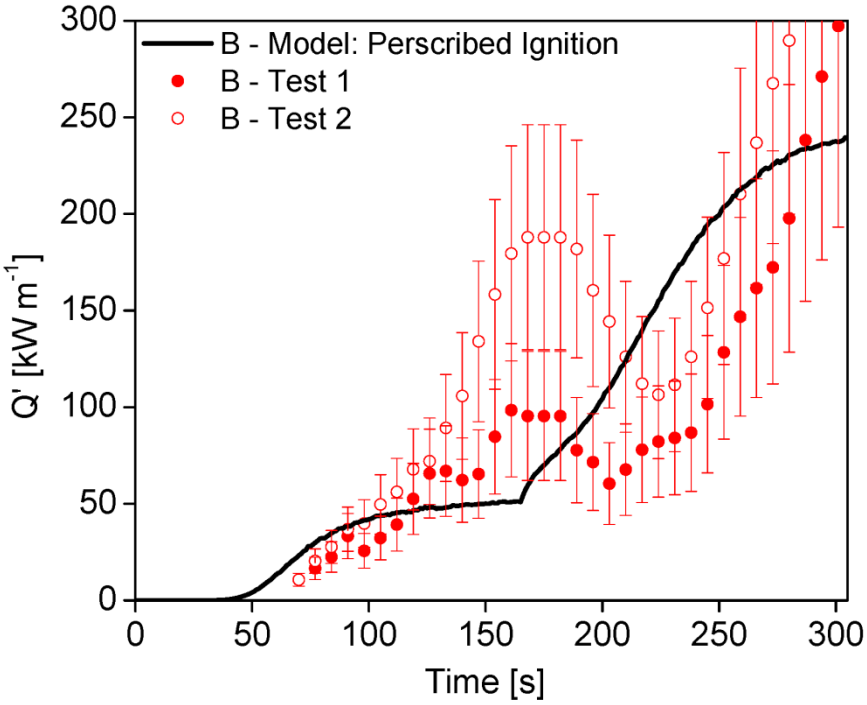
B - Model: Perscribed Ignition
B - Test 1
B - Test 2
Q' [kW m-1]
Time [s]
0
50
100
150
200
250
300

(b)

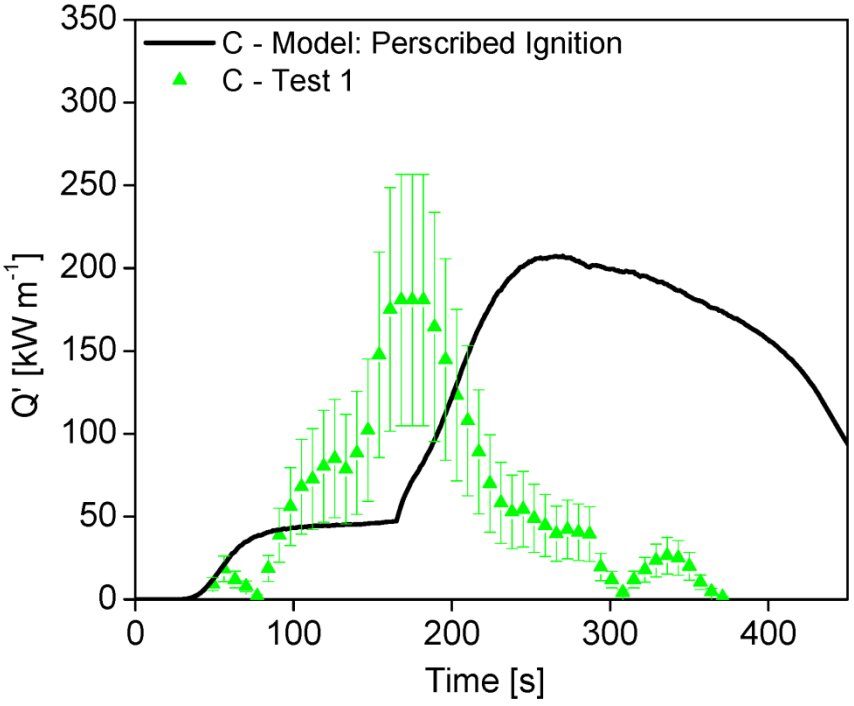
C - Model: Perscribed Ignition
C - Test 1
Q' [kW m-1]
Time [s]
0
50
100
150
200
250
300
350
400

(c)

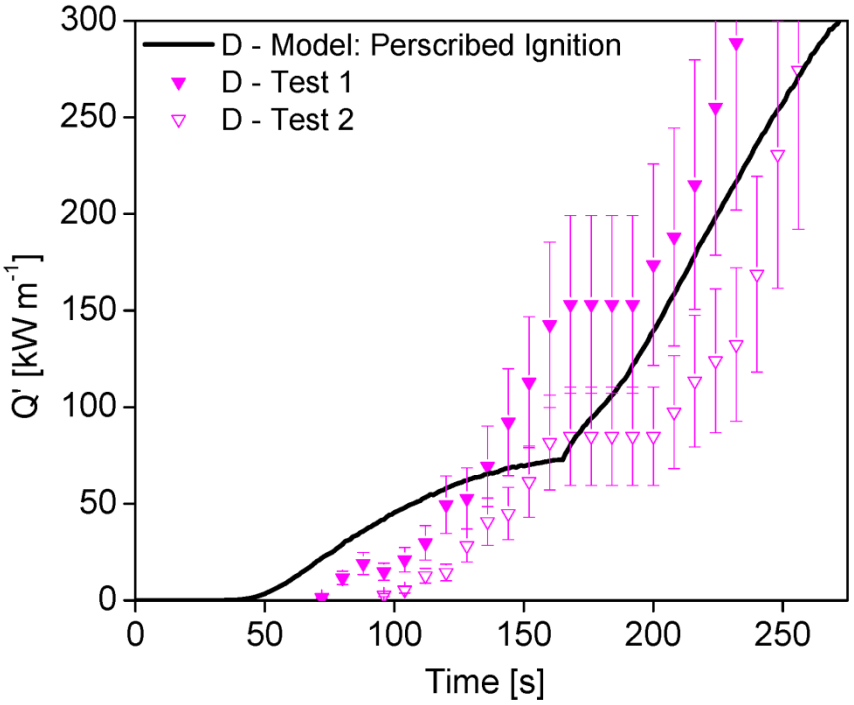

(d)

Figure 79. Room Corner Simulations. Graph (a), graph (b), graph (c) and graph (d) present the model predictions compared to the experimental results of Sample A, Sample B, Sample C and Sample D, respectively. The burner HRR was removed from the Q' measurements

ThermaKin2D does a good job predicting the experimental results for Sample D. The model slightly under predicts the ignition time, but does an excellent job of predicting the fire growth rate. The Sample B model is able to obtain an adequate fit of the experimental results. It under predicts the fire size while the burner is on. Once the burner fire is turned off, the fire develops slightly faster than the experimental results show.

For Sample A and Sample C, ThermaKin2D does a good job to qualitatively predict the fire growth rate. But, the model does a poor job of predicting the time at which fire growth began. During the experiments, Sample A either self-extinguished once the burner was removed or the flames neared extinction and then eventually spread

upwards. The model predicts that the flames spread upwards soon after the burner is removed. Of all the samples, the model predictions are the worst for Sample A. The room corner model quantitatively predicts how Sample C performed during the full-scale tests. Out of the four materials, the model predicts that Sample C produces the lowest Q'. The model simulates that the fire spreads upward, peaking at the ceiling and then the fire eventually self-extinguishing. Sample A and Sample C were the most difficult materials to test because they had the tendency to self-extinguish once the burner was removed.

It is believed that the material properties representing Sample B and Sample D enabled the user to more accurately simulate their full-scale fire performance. The ThermaKin2D cone calorimeter model was able to accurately simulate all of the cone calorimeter results for Sample B and Sample D. The average relative difference between the experimental mean and the model prediction for the 1 Reaction Model of Sample B and Sample D were 10.8 % and 8.5 %, respectively. At its best, ThermaKin2D cone calorimeter model was able to obtain a fit of the Sample A and Sample C cone calorimeter results with a 19.6 % and 16.7 % relative difference, respectively. It is speculated that having material properties which better represent Sample A and Sample C would improve the results of the full-scale simulations.

The major reason why the timing of the fire growth rate is not accurate is because the corner-wall flame heat feedback model is not well resolved at intermediate sized fires. The initial stages of flame spread is highly dependent on the flame heat feedback model at fire sizes of 50×10^3 W m^{-1} and lower. The model predictions would be improved once intermediate-scale flame spread measurements are made and incorporated into the flame heat feedback model.

Due to the limitations of the pyrolysis model, both the flame heat feedback model and the linear set of equations characterizing the burner exposure are one-dimensional. The full-scale model would become more accurate once two-dimensional heat flux models are incorporated.

4.5 Full-scale Comparison Criteria

The goal of this project was to predict and compare how similar materials performance relative to one another during the room corner tests. In order to do this, full-scale flame spread simulations of each sample were conducted using the ThermaKin2D room corner model. The model was able to subject the wall material to heat flux conditions that represented the 40×10^3 W exposure fire. After the fire from the burner was turned off, the model simulates upward flame spread. The fire performance of each sample in this simulation was compared based on the following criteria.

The most important aspect of the room corner scenario is the rate at which flames spread to the ceiling. It is also important to this project because upward flame spread is completely dependent upon material flammability. Once the flames begin spreading along the upper corner-walls, a smoke layer rapidly forms and heat is transferred to the surrounding combustible surfaces at a significant rate. After this, the compartment becomes ventilation limited, and the fire growth rate is dependent upon the size of the compartment opening.

During the room corner experiments, flames had spread to the ceiling and along the upper corner-walls at fire sizes between 220×10^3 W m^{-1} and 300×10^3 W m^{-1}. An image of the 300×10^3 W m^{-1} fire during the Sample B room corner test is shown in

Figure 80. Earlier in Section 3.4, Figure 52 and Figure 53 demonstrate how the fire size increases exponentially once the flames spread to the ceiling. During the five room corner tests where compartment flashover was achieved, it took between 225 s and 525 s for the fire to spread to the ceiling. During those same tests, it took between 100 s and 175 s for the compartment to reach flashover once flames had reached the ceiling. This time dependence demonstrates how important upward flame spread is. Essentially, flashover is eminent once flames reach and establish themselves at the ceiling.

Figure 80. Room corner test: Sample B Test 2 - image of the fire size at 300×10^3 W m^{-1}

300×10^3 W m^{-1} is a good criteria for defining how quickly flames spread to the ceiling of the compartment. After the simulation reaches this value, it is assumed that the fire would continue to grow exponentially until the compartment reaches flashover. The fire never spreads to the ceiling during the room corner tests where the fire self-extinguished. Thus, if the fire never reached 220×10^3 W m^{-1}, then it is assumed that the compartment would not reach flashover because the fire self-extinguished.

The fire performance of each sample is predicted and compared to one another based on the rate at which the fire develops to 300×10^3 W m^{-1}. The fire development rate (FDR) is calculated as the slope of the line beginning once the burner is turned off, up until moment when the fire size reaches 300×10^3 W m^{-1}. The peak Q' value is utilized if the model simulations do not reach 300×10^3 W m^{-1}. Equation 38 is used to define the FDR for the simulations and experiments.

$$FDR = \frac{Q'_{peak} - Q'_{b,off}}{t_{peak} - t_{b,off}} \tag{38}$$

Equation 38 states that the FDR is calculated based on the Q'_{peak}, which is either 300×10^3 W m^{-1} or the peak Q', the $Q'_{b,off}$, the fire size when the burner is turned off, t_{peak}, the time at which Q'_{peak} is determined and $t_{b,off}$, the time when the burner is turned off. If the model predicts that the fire size never reaches a value of 220×10^3 W m^{-1} then it is assumed that the compartment never reaches flashover due to the fire self-extinguishing. Table 25 provides the calculations of the FDR for the room corner model simulations and experimental average.

Table 25: Fire Performance Comparison Tool

	Fire Development Rate	
	Experimental Mean	Model Simulation
Sample A	0.7	0.8
Sample B	0.9 - 1.5	1.3
Sample C	Self-extinguish	Self-extinguish
Sample D	2.2 - 2.3	2.1

The FDR was calculated individually for each experiment where the flames continued to spread after burner removal. Sample B and Sample D both had two tests where the compartment reached flashover. FDR was calculated for both of these tests and their values are present in Table 25 as a range. Sample A had only one test where

flames sustained themselves after the burner was removed. The fire development rate is reported as the slope of this individual test. Sample C is classified as "self-extinguished" because the fire could not sustain itself after the burner was removed.

The FDR is also calculated for all the samples based on the room corner simulations. The model FDR calculations compare well with the experimental FDR values and ranges. Much like the experimental results, the model simulations show that the fire grows the slowest for Sample A, at a medium rate for Sample B and the quickest for Sample D. Both the experiments and the predictions for Sample C indicate that flashover does not occur because the fire size does not spread to the ceiling. Sample C had a Q'_{peak} of 205×10^3 W m^{-1} and a FDR of 1.7 prior to self-extinguishment. The FDR is a good criteria for classifying how hazardous the materials are. A database can be built which ranks the materials according to their FDR values. Sample D is the most hazardous material, Sample B is the second most hazardous material, Sample A is ranked as the third most hazardous material and Sample C is classified as the least hazardous material because it self-extinguishes. The FDR calculations shown in Table 25 validate the procedure presented in this project as an appropriate method for predicting and comparing the fire performance of similar materials in a full-scale fire scenario.

4.6 MCC Derived Properties for Full-scale Modeling

ThermaKin2D requires the user to input 18 properties that characterize the virgin sample, the char it produces and the reaction that occurs during pyrolysis. This project has identified a specific procedure for obtaining these properties based on milligram-scale and bench-scale testing in order to perform large-scale simulations using

ThermaKin2D. It assumes that the fire investigator has enough material to conduct both milligram-scale and bench-scale tests. The procedure requires the user to conduct MCC and cone calorimeter experiments and inversely model these experiments through an optimization procedure to obtain the necessary material properties needed for pyrolysis modeling. The cone calorimeter optimization procedure is much more tedious than the MCC optimization procedure due to the amount of unknown parameters that need to be determined and the multiple incident heat flux conditions that must be simulated. Eliminating the cone calorimeter experiments and optimization procedure would simplify this process greatly and it may be necessary due to the fire investigator not having enough material to perform multiple bench-scale tests. Therefore, room corner simulations were conducted using only the properties derived from the MCC experiments and the kinetics found during the MCC optimization procedure. Since this procedure is intended to be used for any type of material, the thermal and optical properties for the virgin sample are based on the average polymer properties identified in Table 16. A 1 Reaction model is specified, in which the virgin sample produces char and gaseous volatiles upon decomposition. The properties of the gaseous volatilies match the virgin sample, except for the heat capacity, which is 1.8×10^{3} J kg^{-1} K^{-1}. The properties of the char are based on the same analysis utilized during the material properties cone calorimeter optimization section, Section 4.3.2. Here, the char density was determined through the constant volume analysis, the char thermal conductivity is based on the radiation absorption approximation which utilizes the mean β value of 5×10^{-10}, the char absorption coefficient is 10 m^{2} and the char emissivity is 0.86. The simplified procedure for obtaining the key material properties are reported in Table 26. This table either

provides the average polymer property or the methodology to obtain the individual parameter. These properties are implemented into the ThermaKin2D room corner model to simulate flame spread in the corner of a room.

Table 26: Material Properties Derived from MCC Experiments & Literature Review

Virgin Sample Material Properties	
Parameter	**Input Value or Reference**
Thickness [m]	Measured
Density [kg m^{-3}]	
Thermal Conductivity [W m^{-1} K^{-1}]	0.24
Heat Capacity [J kg^{-1} K^{-1}]	2300
Emissivity [-]	0.88
Absorption coefficient [m^2 kg^{-1}]	3
Ignition Mass Flux [kg s^{-1} m^{-2}]	$21\times10^3/\Delta H_{eff}$
Heat of Reaction [J kg^{-1}]	-1.3×10^6
Char Yield [-]	MCC Experiment
Effective Heat of Combustion [J kg^{-1}]	
Pre-Exponential Factor [s^{-1}]	MCC Optimization
Activation Energy [J mol^{-1}]	
Char Material Properties	
Density [kg m^{-3}]	Constant Volume Analysis
Thermal Conductivity [W m^{-1} K^{-1}]	5×10^{-10} T^3
Absorption coefficient [m^2 kg^{-1}]	10
Heat Capacity [J kg^{-1} K^{-1}]	1500
Emissivity [-]	0.86

The FDR was calculated for each room corner simulation in which the material properties were obtained using the approach where the material properties were derived from milligram-scale testing and a literature review. These values are reported in Table 27 in the column titled “MCC Derived Properties”. The “MCC & Cone Derived Properties” utilizes the more tedious procedure to obtain the material properties.

Table 27: Fire Development Rate - Comparison of the Experimental Mean to the Model Prediction

Sample	Experimental Mean	MCC & Cone Derived Properties	MCC Derived Properties
Sample A	0.7	0.8	0.9
Sample B	0.9 - 1.5	1.3	1.7
Sample C	Self-extinguish	Self-extinguish	1.5
Sample D	2.2 - 2.3	2.1	2.5

When the MCC Derived Property approach was used to predict the full-scale fire performance of each sample, the model shows that none of the samples self-extinguishes because the Q'_{peak} is atleast 220×10^3 W m^{-1} for all the simulations. Using this approach, the model is unable to predict that Sample C self-extinguishes. Besides that, the FDR values of the MCC Derived Property model compares well with the experimental FDR values. The thermal and optical properties are not characterized with as much accuracy since the MCC Derived Property approach uses literature values. Therefore, the more efficient approach is not as accurate as the MCC & Cone Derived Property approach. Even though this approach was slightly less accurate, it was still able to appropriately compare the relative fire performance of the four similar materials based upon the FDR calculation.

5. Conclusion

5.1 Summary

Even though the various products of MDF wood-paneling have the same name and have a similar composition, they do not burn the same way during a fire. The small-scale and large-scale experiments conducted during this project demonstrate how differently each one of these materials performs in the various fire scenarios. This shows how critical it is for the fire investigator to select the right exemplar material to use during the reconstructive fire test.

The goal of this project was to create a procedure for obtaining the properties of several similar materials through milligram-scale and bench-scale testing and comparing their full-scale fire performance in the room corner test. Milligram-scale and bench-scale experiments were performed on four different types of MDF wall paneling. MCC experiments were conducted at a heating rate of 1 K s^{-1} and the cone calorimeter experiments were performed at (20×10^3 W m^{-2} - 25×10^3 W m^{-2}), 50×10^3 W m^{-2} and 80×10^3 W m^{-2}. The MCC experiments produced the char yield and the HRR/m_0 as a function of the pyrolysis temperature for each sample. The cone calorimeter experiments provided the sample's effective heat of combustion, char density and HRRPUA. Additional research was conducted using the cone calorimeter to determine the most effective sample restraining method and the flame heat flux upon ignition. A MCC and cone calorimeter model was developed using ThermaKin2D. An optimization procedure

was performed by inversely modeling the experimental MCC and cone calorimeter HRR results to obtain the effective thermal, chemical and optical properties for each sample, their char and any intermediate components that react during pyrolysis. A simple single chemical reaction was able to accurately predict the MCC and cone calorimeter experiments at each incident heat flux condition. This procedure requires the fire investigator to have enough material to conduct multiple bench-scale experiments.

Full-scale experiments were performed in the open corner-wall configuration and the room corner test. The first set of tests performed in the open corner-wall configuration subjected a noncombustible corner-wall surface to a fire created by a square propane burner producing a 25×10^3 W and 40×10^3 W fire. Linear sets of equations were derived to characterize the one-dimensional vertical heat flux distribution from the square burner exposure fires. The second set of open corner-wall tests involved exposing the MDF wallboard samples to the 25×10^3 W square burner fire. The materials eventually ignited and the square burner fire was turned off. The fire was allowed to spread upwards and the HRR and flame heat flux was measured. The flame height was measured quantitatively while the burning width was measured visually. These experiments led to the development of a one-dimensional flame heat feedback model for corner-wall fires. The flame heat feedback model defines a set of correlations for the flame height as a function of the fire size, the peak heat flux over the flame height region and the heat flux distribution beyond the flame height. The peak heat flux during corner-wall flame spread was 42×10^3 W m^{-2}.

The standard room corner test requires the corner burner to produce a large fire which exposes the wall and ceiling materials to extreme thermal conditions. The entire

fire growth process is driven by the burner when it produces a fire with such a magnitude. Therefore, the burner conditions of the standard room corner test were modified by exposing the wall linings to a shorter burner duration, 40×10^3 W for 165 s, so that the fire performance of the materials could be better analyzed. Full-scale room corner tests were performed for each sample.

The goal of this project was to simulate the most important aspect of the room corner fire scenario, upward flame spread in the corner of the compartment. This is a phenomenon that researchers have been attempting to simulate for decades. It is especially important in this project because upward flame spread is completely dependent upon the flammability of the material. Once flames spread to the ceiling, other aspects control the rate of fire growth. The smoke layer reradiates heat to the surrounding wall and ceiling surfaces. Eventually, the compartment becomes ventilation limited and the compartment opening dictates the fire development rate.

ThermaKin2D was utilized to model the room corner tests by implementing the complete set of sample properties, the corner-wall flame heat feedback model and the linear equations representing the burner heat flux. The model predictions are compared to the experimental results for each sample. The model was able to accurately predict the fire performance of Sample B and Sample D, the most flammable materials. The model was also able to qualitatively predict the rate of fire growth for Sample A and Sample C. Unfortunately, it was unable to predict the time at which fire growth occurred. The timing of fire growth is highly dependent upon the flame heat feedback model at intermediate sized fires. The flame heat feedback model was developed based on large turbulent fires, and it is not resolved for intermediate sized fire.

A set of criteria was developed which successful compares the full-scale fire performance of each sample. This criteria relies on one key parameter, fire development rate, to determine the rate at which flames spread to the ceiling of the compartment once the fire from the square burner is removed. The fire development rate is a useful parameter for defining how hazardous the materials are.

During some fire investigations, an investigator will not be able to collect enough material for bench-scale testing. Therefore, a simplified approach was explored for obtaining the necessary material properties needed to model the full-scale tests in ThermaKin2D. It only requires the user to perform MCC experiments and an optimization procedure to obtain the sample's kinetics, char yield and effective heat of combustion. Rather than performing cone calorimeter tests and the optimization procedure, the thermal and optical properties are selected based on literature values of the average polymer. The properties gained through the MCC derived property approach were implemented into the ThermaKin2D room corner model to predict how each sample performed relative to one another. The fire development rate analysis was applied to this set of simulations. It was determined that this approach is not as accurate as the previous mentioned procedure in which the complete set of material properties were obtained based on MCC and cone calorimeter tests. But, it is still able to rank how these four samples perform relative to one another.

A fire investigator will be able to better select materials for their reconstructive fire test based on the modeled full-scale fire performance of candidate materials compared to the exemplar material found during the fire investigation. Overall, this

procedure is expected to improve a fire investigator's ability to perform accurate reconstructive fire tests.

5.2 Future Research

A new optimization procedure was created for obtaining the key scientific material properties needed to accurately model condensed-phase decomposition. In order to classify this procedure as a valid tool for engineering application, future researchers will need to perform various bench-scale experiments that measure the material properties and compare their values to the ones discovered during the optimization procedure.

To date, there has been limited research that analyzes flame spread along combustible materials in the corner-wall configuration. Modeling the ignition and early stages of corner-wall flame spread depends heavily upon the flame height correlation and its Q'_{crit}. Further corner-wall flame spread experiments should be conducted on various materials and at lower fire sizes. This would make the flame heat feedback model more robust and improve its accuracy. The corner-wall flame heat feedback model is currently a one-dimensional model. A two-dimensional corner-wall flame heat feedback model could improve the model predictions.

In this project, material fire performance was only simulated in the corner-wall scenario. This procedure can be adapted to other flame spread and ignition scenarios. Examples of other flames spread scenarios include: upward flame spread along a vertical wall and horizontal flame spread along upright and flat surfaces. Examples of ignition scenarios include point source heating and various types of exposure fires.

Appendix A. Horizontal Heat Flux Analysis

The heat flux from the flame to the surface was measured during the room corner tests at varying heights above the gas burner and distances away from the corner. These measurements were used to verify the peak heat flux measurements recorded during the open corner-wall flame spread experiments. They will also provide an understanding of how the heat flux changes with increasing distance from the corner.

The peak steady state heat flux was determined for all the tests where the compartment transitioned to flashover. A 60 s average was calculated for each heat flux gauge once the gauge reached a relatively steady value. The average peak heat flux at 0.075 m, 0.15 m, 0.225 m and 0.30 m away from the corner is 41.0×10^3 W m^{-2}, 31.1×10^3 W m^{-2}, 18.1×10^3 W m^{-2} and 5.8×10^3 W m^{-2}. Figure 81 displays the horizontal heat flux distribution at varying heights and locations. This graph demonstrates that the heat flux from the flame decreases with increasing distance from the corner. The heat flux decreases by a factor of three from 0.225 m to 0.30 m. This justifies the assumption that the average burning width from the open corner-wall experiments applies to the room corner tests.

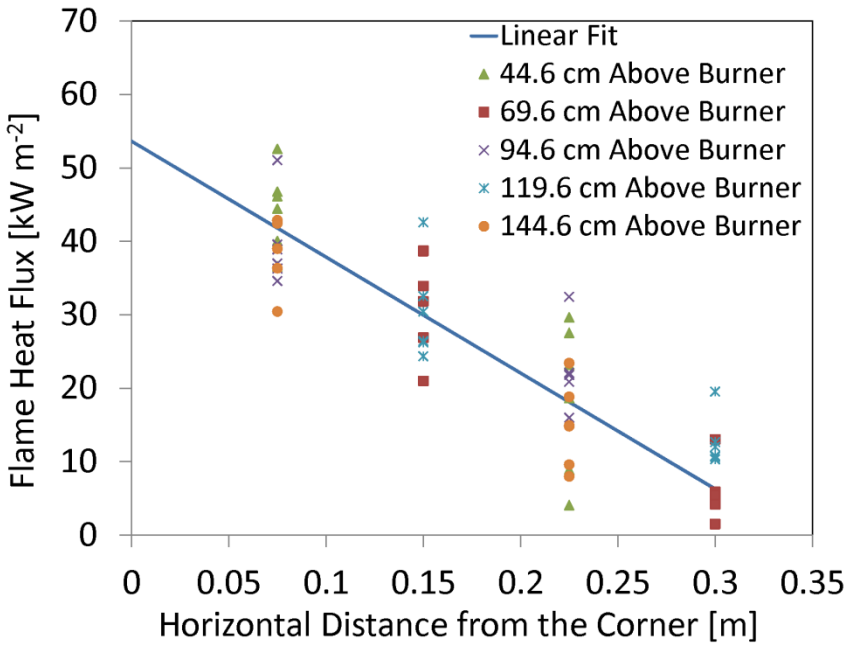

Figure 81. Horizontal heat flux distribution during the room corner tests

The average heat flux data at the four horizontal distances from the corner (x_h) were fit with a linear expression. The horizontal heat flux distribution expression is provided in Equation 39.

$$q"_{flame} = -157.9x_h + 53.6 \quad (39)$$

Appendix B. ThermaKin2D Scaling Analysis

The corner-wall flame heat feedback model reported in Equation 37 determines the flame height in terms of [m] as a function of the Q', which in terms of [W m^{-1}]. The solid phase pyrolysis model operates in terms of mass flux from the surface of the sample, not heat released. Therefore, Equation 37 must be scaled from Q' to $\left(\frac{dm'}{dt}\right)$ using the material specific effective heat of combustion. Equation 40a and Equation 40b provides a set of equations which determine the flame height correlation as a function of $\left(\frac{dm'}{dt}\right)$.

$$y_f = a^* \left(\frac{dm'}{dt}\right)^b + c \tag{40a}$$

$$a^* = a\left(\Delta H_{eff}\right)^b \tag{40b}$$

Further scaling must be performed so that the flame height correlation can be inputted into ThermaKin2D. The ThermaKin2D flame height correlation is provided in Equation 41a and Equation 41b. a' is calculated by multiplying the a^* by the critical mass flux, which is the power of b.

$$y_f = a' \left(\frac{dm'}{dt}\right)^b + c \tag{41a}$$

$$a' = a^* (m''_{crit})^b \tag{41b}$$

Appendix C. ThermaKin2D Input Files

Thermakin2D requires the user to set up two files; a components file and a conditions files. The components file defines the material properties of each component and characterizes the chemical reactions. Table 19, Table 20, Table 21 and Table 22 define the properties utilized in the components file for Sample A, Sample B, Sample C and Sample D, respectively. The same properties are utilized during the MCC model, cone calorimeter model and full-scale models. During the MCC model, the thermal and optical properties are irrelevant because the thermally-thin mode is utilized.

The conditions file defines the geometry, boundary conditions, computational grid, integration parameters and output details. An example of the Sample A conditions file for the MCC, cone calorimeter model at an incident heat flux of 50×10^3 W m^{-2}, open corner-wall and room corner model is shown below.

ThermaKin2D MCC Model: Sample A - 1 K/s

OBJECT TYPE: 1D

OBJECT STRUCTURE
****

THICKNESS: 0.00001
TEMPERATURE: 348.15
MASS FRACTIONS:
Sample 1

OBJECT BOUNDARIES
****

TOP BOUNDARY

MASS TRANSPORT: YES
Sample_Gas LIN 0.05 0

OUTSIDE TEMP TIME PROG: 348.15 1
CONVECTION COEFF: 100000

EXTERNAL RADIATION: NO

FLAME: NO

BOTTOM BOUNDARY

MASS TRANSPORT: No

OUTSIDE TEMP TIME PROG: 348.15 1
CONVECTION COEFF: 100000

EXTERNAL RADIATION: NO

FLAME: NO

INTEGRATION PARAMETERS
****

ELEMENT SIZE: 1e-6
TIME STEP: 0.005
DURATION: 675

OUTPUT FREQUENCY:
ELEMENTS: 10
TIME STEPS: 200

ThermaKin2D Cone Calorimeter Model: Sample A - 50 kW m^{-2}

OBJECT TYPE: 1D

OBJECT STRUCTURE
****

THICKNESS: 0.0062
TEMPERATURE: 300
MASS FRACTIONS:
Sample 1

THICKNESS: 0.0126
TEMPERATURE: 300
MASS FRACTIONS:
Gypsum 1

OBJECT BOUNDARIES
****

TOP BOUNDARY

MASS TRANSPORT: YES
Sample_Gas LIN 0.05 0

OUTSIDE INIT TEMP: 300
OUTSIDE HEAT RATE: 0 0 0 0
CONVECTION COEFF: 10

EXTERNAL RADIATION: YES
TIME PROG1: 50000 0 450
TIME PROG2: 0 0 0
REPEAT: NO
ABSORPTION MODE: RAND

FLAME: YES
IGNITION MASS FLUXES:
Sample_Gas 2.22e-3
OUTSIDE TEMP: 2270
CONVECTION COEFF: 0
RADIATION: 20000

BOTTOM BOUNDARY

MASS TRANSPORT: NO

OUTSIDE INIT TEMP: 300
OUTSIDE HEAT RATE: 0 0 0 0
CONVECTION COEFF: 0

EXTERNAL RADIATION: NO

FLAME: NO

INTEGRATION PARAMETERS
****

ELEMENT SIZE: 2.5e-5
TIME STEP: 0.005
DURATION: 450

OUTPUT FREQUENCY:
ELEMENTS: 1
TIME STEPS: 200

ThermaKin2D Open Corner-wall Prescribed Ignition Model: Sample A
OBJECT TYPE: 2D

OBJECT STRUCTURE
****

FROM BOTTOM:
LAYER LENGTH: 2.05

FROM FRONT:
THICKNESS: 0.0062
TEMPERATURE: 300
MASS FRACTIONS:
Sample 1

THICKNESS: 0.0126
TEMPERATURE: 300
MASS FRACTIONS:
Gypsum 1

OBJECT BOUNDARIES
****

FRONT BOUNDARY

MASS TRANSPORT: YES
Sample_Gas LIN 0.05 0

EXTERNAL HEAT FLUX 1: YES
START & END TIMES: 0 60
RAMP: UP
MODE: RAD
POSITION DEPEND1: 44284 -67828 0.446
POSITION DEPEND2: 29028 -33595 0.696
POSITION DEPEND3: 11613 -8474.7 1.37

EXTERNAL HEAT FLUX 2: YES
START & END TIMES: 60 345
RAMP: HOLD
MODE: RAD
POSITION DEPEND1: 44284 -67828 0.446
POSITION DEPEND2: 29028 -33595 0.696
POSITION DEPEND3: 11613 -8474.7 1.37

EXTERNAL HEAT FLUX 3: NO

FLAME: YES
START TIME: 345
IGNITION MASS FLUXES:
Sample_Gas 2.22e-3
FLAME LENGTH: 4.349 -4.66961 -0.2457
HEAT FLUX MODE: RAD
HEAT FLUX INSIDE: 42000 2.05 0
HEAT FLUX BELOW: 1e10
HEAT FLUX ABOVE: 3.0 1

BACKGROUND TEMP: 300
RADIAT ABSORPT MODE: RAND

BACK BOUNDARY

MASS TRANSPORT: NO

EXTERNAL HEAT FLUX 1: NO

EXTERNAL HEAT FLUX 2: NO

EXTERNAL HEAT FLUX 3: NO

FLAME: NO

BACKGROUND TEMP: 300
RADIAT ABSORPT MODE: RAND

INTEGRATION PARAMETERS
****

LAYER SIZE: 0.05
ELEMENT SIZE: 5e-5
TIME STEP: 0.01
DURATION: 838

OUTPUT FREQUENCY:
LAYERS: 1
ELEMENTS: 94
TIME STEPS: 100

ThermaKin2D Room Corner Model: Sample A

OBJECT TYPE: 2D

OBJECT STRUCTURE
****

FROM BOTTOM:
LAYER LENGTH: 2.05

FROM FRONT:
THICKNESS: 0.0062
TEMPERATURE: 300
MASS FRACTIONS:
Sample 1

THICKNESS: 0.0126
TEMPERATURE: 300
MASS FRACTIONS:
Gypsum 1

OBJECT BOUNDARIES
****

FRONT BOUNDARY

MASS TRANSPORT: YES
Sample_Gas LIN 0.05 0

EXTERNAL HEAT FLUX 1: YES
START & END TIMES: 0 30
RAMP: UP
MODE: RAD
POSITION DEPEND1: 53870 -64545 0.696
POSITION DEPEND2: 17187 -9880.1 1.740
POSITION DEPEND3: 0 0 2.05

EXTERNAL HEAT FLUX 2: YES
START & END TIMES: 30 165
RAMP: HOLD
MODE: RAD
POSITION DEPEND1: 53870 -64545 0.696
POSITION DEPEND2: 17187 -9880.1 1.740
POSITION DEPEND3: 0 0 2.05

EXTERNAL HEAT FLUX 3: NO

FLAME: YES
START TIME: 165
IGNITION MASS FLUXES:
Sample_Gas 2.22e-3
FLAME LENGTH: 4.349 -4.66961 -0.2457
HEAT FLUX MODE: RAD
HEAT FLUX INSIDE: 42000 2.05 0
HEAT FLUX BELOW: 1e10
HEAT FLUX ABOVE: 3.0 1

BACKGROUND TEMP: 300
RADIAT ABSORPT MODE: RAND

BACK BOUNDARY

MASS TRANSPORT: NO

EXTERNAL HEAT FLUX 1: NO

EXTERNAL HEAT FLUX 2: NO

EXTERNAL HEAT FLUX 3: NO

FLAME: NO

BACKGROUND TEMP: 300
RADIAT ABSORPT MODE: RAND

INTEGRATION PARAMETERS
****

LAYER SIZE: 0.05
ELEMENT SIZE: 5e-5
TIME STEP: 0.01
DURATION: 720

OUTPUT FREQUENCY:
LAYERS: 1
ELEMENTS: 94
TIME STEPS: 100

Bibliography

[1] Fires in the U.S. 2013, National Fire Protection Association, http://www.nfpa.org/research/reports-and-statistics/fires-in-the-us. [8.7.2015].

[2] NFPA 921, Guide for Fire and Explosion Investigations, National Fire Protection Association, Quincy, MA, (2013).

[3] ASTM Standard E1354-13, Standard Test Method for Heat and Visible Smoke Release Rates for Materials and Products Using an Oxygen Consumption Calorimeter , ASTM International, West Conshohocken, Pa (2014).

[4] ASTM Standard E162-15, Standard Test Method for Surface Flammability of Materials Using a Radiant Heat Energy Source, ASTM International, West Conshohocken, Pa (2012).

[5] ASTM Standard E1321-13, Standard Test Method for Determining Material Ignition and Flame Spread Properties, ASTM International, West Conshohocken, Pa (2013).

[6] ASTM Standard E84, Standard Test Method for Surface Burning Characteristics of Building Materials, ASTM nternational, West Conshohocken, Pa (2013).

[7] ASTM Standard E2257-13a, Standard Test Method for Room Fire Test of Wall and Ceiling Materials and Assemblies, ASTM nternational, West Conshohocken, Pa (2013).

[8] ISO Standard 9705, Fire Tests - Full-scale room test for surface products, Internal Standards Organization, Switzerland, (1993).

[9] NFPA 265, Standard Method of Tests for Evaluating Room Fire Growth Contribution of Textile Wall Coverings, National Fire Protection Association, Quincy, MA.

[10] NFPA 286 Standard Methods of Fire Tests for Evaluating Contribution of Wall and Ceiling Interior Finish to Room Fire Growth, National Fire Protection Association, Quincy, MA, (2006).

[11] Information about Room Corner Test, SP Technical Research Institute of Sweden, http://www.sp.se/en/index/services/firetest_building/firetest_bu%C3%ADlding/iso_9705_room_corner_test/Sidor/default.aspx. [7.10.2015].

[12] Wickstrom, U., Goransson, U., Prediction of Heat Rlease Rates of Surface Materials in Large Scale Fire Test Based on Cone Calorimeter Results, *J. Test. Eval.*, vol. 15, no. 6, pp. 364 – 370, (1987).

[13] Ostman, B., Nussbaum, R., Correlation Between Small-scale Rate Of Heat Release And Full-scale Room Flashover For Surface Linings, *Fire Saf. Sci.*, vol. 2, pp. 823–832, (1989).

[14] Quintiere, J. G., A Simulation Model for Fire Growth on Materials Subject to a RoomCorner Test, *Fire Sa*, vol. 20, pp. 313 – 339, (1993).

[15] Wade, C., A New Engineering Tool for Evaluating the Fire Hazard in Rooms, (1999).

[16] Lattimer, B. Y., Hunt, S. P., Wright, M., Beyler, C., Corner fire growth in a room with a combustible lining, *Fire Saf. Sci.*, pp. 419–430, (2003).

[17] Sundstrom, B., The Development of a European Fire Classification System for Building Products Test Methods and Mathematical Modelling, Lund University, (2007).

[18] Quintiere, J. Q., Lian, D, Inherent Flammability Parameters - Room Corner Test, *Proc. Fire Mater.*, vol. 33, pp. 377 – 393, (2009).

[19] Janssens, M., Huczek, J., Gomez, C., Modeling of the Performance of GRP Panels in the ISO 9705 Room Test, *Compos. Polycon*, (2009).

[20] Grexa, O., Dietenberger, M. a., White, R.H., Reaction-to-Fire of Wood Products and Other Building Materials, Madison, WA, (2012).

[21] Saito, K., Quintiere, J. G., Williams, F, Upward turbulent flame spread, *Fire Saf. Sci. First Int. Symp.*, pp. 75–86, (1986).

[22] Icove, D., DeHaan, J., Haynes, G., *Forensic Fire Scene Reconstruction*. Upper Saddle River: Pearson Education, Inc., (2013).

[23] Karlsson, B., Quintiere, J.G., *Enclosure Fire Dyanmics*. Boca Raton: CRC Press LLC., (2000).

[24] Lattimer, B. Y. , "Heat Fluxes from Fires to Surfaces" in *SFPE Handbook of Fire Protection Engineering, 4th ed.*, (2008), pp. 2.303 – 2.334.

[25] Williamson, R., Revenaugh, A., Mowrer, F., Ignition Sources In Room Fire Tests And Some Implications For Flame Spread Evaluation, *Fire Saf. Sci.*, vol. 3, pp. 657 – 666, (1991).

[26] Kokkala, M. A., Characteristics of a Flame in an Open Corner of Walls, London, (1993).

[27] Tran, H. C., Janssens, M. L., Modeling the Burner Source Used in the ASTM Room Fire Test, *J. Fire Prot. Eng.*, vol. 5, pp. 53 – 66, (1993).

[28] Quintiere, J. G., Cleary, T.G., Heat Flux from Flames to Vertical Surfaces, *Fire Technol.*, vol. 30, no. 2, pp. 209 – 231, (1994).

[29] Ohlemiller, T., Cleary, T., Shields, J., Effects of ignition confitions on upward flame spread on a composite material in a corner configuration, *Fire Saf. J.*, vol. 31, pp. 331 – 344, (1998).

[30] Dillon, S., Analysis of the ISO 9705 Room/Corner Test: Simulations, Correlations and Heat Flux Measurements, (1998).

[31] Hasemi, Y., Yoshida, M., Takashima, S., Kikuchi, R.,Yokobayashi, Y., Flame length and Flame Heat Transfer Correlations in Corner-Wall and Corner-wall-ceiling Configurations, *Interflame'96*, (1995).

[32] Qian, C., Saito, K., An Empirical Model For Upward Flame Spread Over Vertical Flat And Corner Walls, *Fire Saf. Sci.*, vol. 5, pp. 285–296, (1997).

[33] Lattimer, B. Y. , Sorathia, U., Thermal Characteristics of Fires in a Noncombustible Corner, *Fire Saf. J.*, vol. 38, no. 8, pp. 709–745, (2003).

[34] Lattimer, B. Y., Sorathia, U., Thermal Characteristics of Fires in a Combustible Corner, *Fire Saf. J.*, vol. 38, no. 8, pp. 747–770, (2003).

[35] Janssens, M., Module 6 - Heat Release Rate Tests II, University of Maryland, ENFP652: Fire Assessment Methods, in *University of Maryland, ENFP652: Fire Assessments Methods*, (2013).

[36] Dillon, S. E., Kim, W.H., Quintiere, J.G., Determination of Properties and the Prediction of the Energy Release Rate of Materials in the ISO 9705 Room Corner Test, Washington, D.C., (1998).

[37] Beyler, C., Hunt, S., Lqbal, N., Williams, F., A Computer Model Of Upward Flame Spread On Vertical Surfaces, *Fire Saf. Sci.*, vol. 5, pp. 297–308, (1997).

[38] Wade, C. A., BRANZFIRE 2008 Compilation of Verification Data, New Zealand, (2008).

[39] Private correspondense, James Lord, (2015) .

[40] Sun, L, Wang, F., Xie, Y., Feng, J., Wang, Q, The combustion performance of medium density fiberboard treated with fire retardant microspheres, *BioResources*, vol. 7, no. 1, pp. 593–601, (2012).

[41] Huynh, V. C. M., Flame Spread Measurements of New Zealand Timber Using An Adaptation of the Cone Calorimeter Apparatus, University of Canterbury, NZ, (2003).

[42] White, R. H.. Sumathipala, K, Cone Calorimeter Tests of Wood Composites, *Proc. Fire Mater. 2013 Conf.*, pp. 401–412, (2013).

[43] Hasemi, Y., Yoshida, M., Heat Release Rates Measured By the Cone Calorimeter and Intermediate Scale Electrical Radiant Panels, in *Thirteenth Meeting of the UJNR Panel on Fire Research and Safety*, (1997), pp. 225 – 234.

[44] American Forrest & Paper Association, Inc., Flame Spread Performance of Wood Products, (1997).

[45] Georgia Pacific, LLC, Decorative Finish Panels, (2014) http://www.buildgp.com/wc-purimpressions-mdf, [6.5.15].

[46] Decorative Panels International, Beadboard, (2014) http://www.decpanels.com/products/beadboard, [6.5.15].

[47] Georgia Pacific, LLC, Decorative Finish Panels, (2014) http://www.buildgp.com/wc-springfield-hickory, [6.5.15].

[48] Eucatex North America, Eucaboard Plain Hardboard. http://www.eucatex.com.br/en/hardboard/product?id=29, [6.5.15]

[49] United States Gypsum Company, USG SHEETROCK Brand UltraLight Panels MSDS, (2011).

[50] Lyon, R. E., Walters, R., A Microscale Combustion Calorimeter, Atlantic City, NJ, (2002).

[51] ASTM D7309: Standard Test Method for Determining Flammability Characteristics of Plastics and Other Solid Materials Using Microscale Combustion", ASTM International, West Conshohocken, Pa.

[52] Lyon, R. E., Walters, R., Stoliarov, S. I., Safronava, N., Principles and Practices of Microscale Combustion Calorimetry. Federal Aviation Administration -, Atlantic City, NJ, (2013).

[53] Huggett, C, Estimation of rate of heat release by means of oxygen consumption measurements, *Fire Mater.*, vol. 4, no. 2, pp. 61–65, (1980).

[54] ISO 5660-1: Reaction-to-fire tests - Heat release, smoke production and mass loss rate -- Part 1: Heat release rate (cone calorimeter method), International Standards Association, Switzerland, (2002).

[55] Babrauskas, V., *SFPE Handbook of Fire Protection Engineering*, 4th ed. Quincy, MA: National Fire Protection Association, (2008).

[56] Bureau of Alcohol, Tobacco, Firearms and Explosives Fire Research Laboratory, Technical Reference: Fire Products Collector - 1 MW Square TR011a.

[57] Bureau of Alcohol, Tobacco, Firearms and Explosives Fire Research Laboratory, Technical Reference: Fire Products Collector - 4 MW TR011c.

[58] Stoliarov, S. I., Leventon, I. T., Lyon, R. E., Two-Dimensional Model of Burning for Pyrolyzable Solids, Atlantic City, NJ, (2013).

[59] Beaulieu, P. a., Dembsey, N. a., Effect of oxygen on flame heat flux in horizontal and vertical orientations, *Fire Saf. J.*, vol. 43, no. 6, pp. 410–428, (2008).

[60] McKinnon, M. B., Development of a Model for Flaming Combustion of Double-Wall Corrugated Cardboard, University of Maryland College Park, College Park, (2012).

[61] Stoliarov, S. I., Crowley, S., Lyon, R.E., Linteris, G.T., Prediction of the burning rates of non-charring polymers, *Combust. Flame*, vol. 156, no. 5, pp. 1068–1083, (2009).

[62] Li, K, Huang, X, Fleischmann, C., Rein, G., Ji, J., Pyrolysis of Medium Density Fibreboard: Optimized Search for Kinetic Scheme and Parameters via Genetic Algorithm Driven by Kissinger's Method, *Energy & Fuels*, vol. 28, pp. 6130 – 6139, (2014)

[63] Li, K. Y., Pau, D.S.W, Hou, Y.N., Ji, J., Modeling pyrolysis of charring materials: Determining kinetic properties and heat of pyrolysis of medium density fiberboard, *Ind. Eng. Chem. Res.*, vol. 53, pp. 141–149, (2014).

[64] Becidan, M., Várhegyl, G., Hustad, J.E., Skreiberg, O, Thermal decomposition of biomass wastes. A kinetic study, *Ind. Eng. Chem. Res.*, vol. 46, no. 8, pp. 2428–2437, (2007).

[65] Stoliarov, S. I., Safronava, N., Lyon, R.E., The effect of variation in polymer properties on the rate of burning, *Fire and Materials*, vol. 33, no. 6. pp. 257–271, (2009).

[66] Li, J, A Multiscale Approach To Parameterization of Burning Models for Polymeric Materials, University of Maryland, (2014).

[67] Lyon, R.E, Quintiere, J.Q, Criteria for piloted ignition of combustible solids, *Combust. Flame*, vol. 151, no. 4, pp. 551–559, (2007).

[68] Matsumoto, T., Ono, A, Specific Heat Capacity and Emissivity Measurements of Ribbon-shaped Graphite Using Pulse Current Heating, *Intern. J. Thermophys.*, vol. 16, pp. 267 – 275, (1995).

[69] Li, K. Y. , Fleischmann, C.M., Spearpoint, M.J., Determining thermal physical properties of pyrolyzing New Zealand medium density fibreboard (MDF), *Chem. Eng. Sci.*, vol. 95, pp. 211–220, (2013).

[70] Gronli, M.G., A Theoretical and Experimental Study of the Thermal Degradation of Biomass., The Norwegian University of Science and Technology, Trondheim, Norway, (1996).

[71] Havens, J. A., Hashemi, L, Welker, J.R., A Mathematical Model of the Thermal Decomposition of Wood, *Combust. Sci. Technol.*, vol. 5, pp. 91 – 98, (1972).

[72] Rahmanian, I., Thermal and Mechanical Properties of Gypsum Boards and Their Influences on Fire Resistance of Gypsum Board Based Systems, University of Manchester, (2011).

[73] Leventon, I.T., Li, J., Stoliarov, S.I., A flame spread simulation based on a comprehensive solid pyrolysis model coupled with a detailed empirical flame structure representation, *Combust. Flame*, (2015).

[74] Korver, K., A Generalized Model for Wall Flame Heat Flux During Upward Flame Spread on Polymers, University of Maryland College Park, (2015).